BUBBLE GROWTH DYNAMICS

IN BOILING

By

Anthony James Robinson

A Thesis

Submitted to the Faculty of Graduate Studies

in Partial Fulfilment of the Requirements for

the Degree

Doctor of Philosophy

McMaster University

BUBBLE GROWTH DYNAMICS

IN BOILING

DOCTOR OF PHILOSOPHY (2002)   MCMASTER UNIVERSITY

(Mechanical Engineering)   Hamilton, Ontario, Canada.

TITLE: Bubble Growth Dynamics in Boiling

AUTHOR: Anthony James Robinson, M. Eng.

SUPERVISOR: Dr. R. L. Judd

NUMBER OF PAGES: xix, 256

ABSTRACT

This dissertation details a fundamental study of bubble growth dynamics for both spherical vapour bubbles in a uniform temperature field and hemispherical bubbles on a heated plane surface in a non-uniform temperature field in microgravity. The governing equations were solved numerically in order that accurate predictions of bubble growth could be generated for a wide range of system conditions for two fluids, water and R113.

One dimensional spherically symmetric bubble growth in an initially uniformly superheated liquid was investigated by first developing grid and time step independent solutions on a computational grid with uniform spacing between adjacent nodes. These solutions were utilized as benchmark solutions for subsequent bubble growth models. A clustered grid arrangement was then implemented to reduce the computational time with insignificant loss of accuracy. The numerical predictions of the uniform and clustered grid arrangements predict the available analytic theories and experimental data with sufficient accuracy.

The mechanisms which govern the growth of a spherical vapour bubble in an unbounded liquid were exposed by investigating the complex interaction between the heat transfer and the fluid flow surrounding a bubble as it grows from inception, through the various growth stages, to diffusion controlled growth. The influence of system pressure and liquid superheat were also investigated.

Utilizing similar physical arguments, the model developed for spherically symmetric growth was extended to simulate hemispherical growth at a heated plane surface in microgravity. The theory was able to accommodate both spatial and temporal variations in the temperature and velocity fields in the liquid surrounding the bubble as it grows. Utilizing the present theory, the complicated thermal and hydrodynamic interactions between the vapour, liquid and solid have been manifested for a single isolated bubble growing on a heated plane surface from inception.

ACKNOWLEDGEMENTS

TABLE OF CONTENTS

LIST OF FIGURES

LIST OF TABLES

NOMENCLATURE

SYMBOL	DESCRIPTION	UNITS
A	area	m^2
B	parameter to alter coarseness of time step	-
C_p	specific heat	J/kg K
b	area change coefficient	-
D_j	radial grid line	m
d	distance from vapour-liquid interface	m
g	earth gravity	m/s^2
g_∞	gravity in which experiments were performed	m/s^2
h	enthalpy	J/kg
h_{fg}	latent heat of evaporation	J/kg
J	Jacobian	m^2
Ja	Jakob Number	-
k	thermal conductivity	W/mK
K	number of time step iterations	-
Lc	characteristic length	m
M	grid parameter	-
$m^{//}$	mass flux	kg/m^2s
n	exponent for infinite grid approximation	-
N	grid parameter	-
P	pressure	Pa

SYMBOL	DESCRIPTION	UNITS
Q	energy required for bubble growth	J
q''	heat flux	W/m^2
r	radial direction	m
r_b	radial coordinate location of bubble interface	m
r_η	radial metric	m
r_ε	azimuthal metric	m
R	bubble radius	m
R_c	initial bubble radius	m
S_R	grid clustering coefficient	-
t	time	s
t^*	time to nucleation	s
t_c	characteristic time	s
t_{delay}	delay time	s
T	temperature	°C
u	radial velocity (spherical coordinates)	m/s
U	radial velocity (cylindrical coordinates)	m/s
U^c	contravarient velocity	m^2/s
V	axial velocity	m/s
V^c	contravarient velocity	m^2/s
z	axial direction	m
z_b	axial coordinate location of bubble interface	m

Symbol	DESCRIPTION	UNITS
z_η	radial metric	m
z_ϵ	azimuthal metric	m

Greek

α	thermal diffusivity	m^2/s
δ	thermal boundary layer thickness	m
γ	angle measured from z-axis	rad
η	transformed computational coordinate	m
ν	kinematic viscosity	m^2/s
ρ	density	kg/m^3
σ	surface tension	N/m
τ	transformed computational time	s
ϵ	transformed computational coordinate	m

Subscripts

HT	heat transfer
I	inertia
l	liquid
sat	saturation condition
v	vapour
w	wall
1D	one-dimensional
∞	far field

CHAPTER 1: INTRODUCTION

The increased rate of heat transfer during nucleate boiling is determined by the vapour bubbles which grow and depart from the heated surface. Energy is introduced into the liquid by conduction from the heated solid surface and is stored within a thin thermal boundary layer adjacent to the surface. During surface boiling, this energy is ultimately used to vaporize the liquid and cause bubbles to form and grow. Furthermore, fluid motions induced by bubble growth disrupt the thermal boundary layer, thus enhancing the local rate of heat transfer. Consequently, insight into the mechanisms which are responsible for transporting energy away from a heated surface can be gained by understanding the nature of bubble growth.

The progression towards an accurate prediction of the heat transfer during nucleate pool boiling is hampered by the seemingly insurmountable task of developing a physical model and solution technique which takes into account all of the factors which contribute significantly to bubble growth and departure. As a result, the state of the art has been advanced primarily through experimentation. On the other hand, over the past century, theoretical developments have progressed markedly and have provided considerable insight into nucleate boiling by exploring the fundamental nature of bubble growth.

Initial theoretical work focussed on the ideal case of spherically symmetric bubble expansion in a uniformly superheated infinite pool of liquid. With these simplifications, the

rate of bubble growth is determined by the surface tension, the liquid inertia and the difference in pressure between the vapour within the bubble and the ambient liquid. Analytic expressions which fully describe the growth of a bubble were unattainable because of the complicated thermal and hydrodynamic interaction of the vapour and liquid at the bubble wall. This was further complicated by coupling between the liquid momentum and energy equations through the non-linear convection term. To reduce the complexity of the problem, Rayleigh [1917], Fritz and Ende [1936], Plesset and Zwick [1954] and Forster and Zuber [1954] considered two limiting regions of bubble growth separately. Lord Rayleigh [1917] first solved the one-dimensional problem by considering the case in which growth or collapse is governed by momentum interaction between the bubble and ambient fluid. This later became known as the *inertia controlled* stage of bubble growth. Almost four decades later, Plesset and Zwick [1954] and Forster and Zuber [1954] independently determined that the later stage of bubble growth is controlled by the rate at which energy is transferred through the liquid to the vapour-liquid interface. This was termed the *diffusion* or *heat transfer controlled* growth stage. By assuming that a thin thermal boundary layer existed in the liquid surrounding the bubble, an approximate solution to the energy equation was obtained. The first order solutions were shown to agree very well with the experimental results provided by Dergarabedian [1953] for water with low superheats at atmospheric pressure. For the limiting case of moderate to high superheat, Scriven [1959] obtained an expression which was very similar to that of Plesset and Zwick [1954] without having to make the assumption of a thin thermal boundary layer. For low superheats, the theory took a much different form.

The results of these investigations suggested that the early stage of bubble growth

is limited primarily by momentum interactions between the liquid and the expanding bubble. As the bubble grows, the influence of thermal diffusion becomes progressively more important until it is the mechanism which regulates the rate of bubble expansion. For intermediate times, bubble growth should be characterised by a smooth transition between these two limiting stages.

Analytical treatment of spherically symmetric bubble growth in a superheated liquid which incorporates the effects of both liquid inertia and thermal diffusion are limited to simple interpolation formulas and are not valid for the early surface tension dominated growth stage. Perhaps the most well known is the formula suggested by Mikic, Rohsenow and Griffith [1970]. By assuming that the bubble growth rate was bounded by the analytic solutions of Rayleigh [1917] for small values of time and that of Plesset and Zwick [1954] as time approached infinity, a general interpolation formula was derived which could predict bubble growth during the stage in which both liquid inertia and thermal diffusion play a role. This theory was found to be in good agreement with the experimental data of Lien [1969] for water over a wide range of system pressures. However, since this formulation is not an exact solution to the equations governing bubble growth, its accuracy is not assured for times during which both inertia and diffusion are important. Furthermore, the use of the Clausius-Clapeyron relation to relate the variation of vapour pressure with vapour temperature reduces the accuracy of the predictions for moderate to high superheats (Carey [1992]). These shortcomings were first addressed by Theofanous and Patel [1976] and later by Prosperetti and Plesset [1978].

More accurate and complete descriptions of spherically symmetric bubble growth have been provided by Theophanous *et al* [1969], Judd [1969], Board and Duffy [1971],

Dalle Donne and Ferranti [1975], Lee [1993] and Lee and Merte [1996] by utilising numerical techniques to approximate the equations governing heat and fluid flow. In the first three works, approximate solutions to the energy equation were used, whereas in the latter two works, a more rigorous numerical solution of the entire energy equation, including the non-linear convective term, was obtained. The numerical predictions of bubble expansion provided new insight into the spherically symmetric phase growth problem since they included the influences of surface tension, liquid inertia and thermal diffusion. In this way, a more thorough description of the process of bubble growth was put forth. In particular, the recent work of Lee [1993] began to expose the underlying mechanisms which govern growth by considering how thermal and hydrodynamic interactions influence growth as the bubble progresses through the various growth stages. This was done for both uniform and non-uniform spherically symmetric temperature fields over a range of system conditions, including different fluids.

The mechanisms associated with vapour bubble growth at a plane heated surface are not understood nearly as well as unbounded growth in an infinite pool. Experimental investigations are inhibited by the fact that it is exceedingly difficult to control the temperature and flow field in the vicinity of growing bubbles due to natural convection and / or liquid motions induced by other bubbles. Due to the rapidly varying temperature and flow fields, large scatter is observed in the available bubble growth data during nucleate pool boiling. In the development of theoretical models, this makes comparison between experiment and theory very difficult because of the uncertainty involved in matching the initial and boundary conditions. Further complications arise because of the presence of the heated surface. With respect to theoretical modelling, the heated surface introduces spatial

and temporal variations in the solid phase, two-dimensional effects on the liquid velocity and temperature fields as well as the possible formation, growth and subsequent evaporation of a liquid microlayer at the base of the growing bubble. The enormity of the problem is such that there are a limited number of theoretical investigations which attempt to predict bubble growth on a heated surface. Analytical formulations include the works of Griffith [1958], Bankoff and Mikesell [1958], Zuber [1961], Han and Griffith [1965], Cole and Shulman [1966], van Stralen [1966], Mikic and Rohsenow [1969], Mikic, Rohsenow and Griffith [1970], and Kang et al [1993]. The more recent numerical investigations have been performed by Lee and Nydahl [1989], Gou and El-Genk [1996], Mei *et al* [1994], Buyevich and Webbon [1996], Welch [1998] and Son *et al* [1999]. The above investigations show considerable insight and ingenuity and have led to a better understanding of isolated bubble growth dynamics, as well as the mechanisms which are responsible for the increased rate of heat transfer during nucleate pool boiling. Even still, the complexity of the problem demands that the models incorporate idealizations which may or may not be physically realistic. This, coupled with the challenge of comparing predictions with the available experimental growth data, has led to uncertainty concerning fundamental issues such as, the prediction of the waiting time between successive bubbles, the mechanisms responsible for transporting heat away from the heated surface, the proportional contribution of the evaporating microlayer to bubble expansion and its influence on the thermal field in the solid, the shape of evolving bubbles, the effect of the thermal characteristics of the solid, the importance of viscosity, the contribution of surface tension, the forces which govern the radial and translational motion of growing bubbles, and the mechanisms responsible for bubble departure.

Recent data has been reported by Lee [1993], Merte *et al* [1995] and Lee and Merte

[1996] in which the shortcomings associated with conventional surface boiling experiments are partially overcome by heating a stagnant pool of liquid to the onset of boiling in microgravity. The absence of any significant natural convection, combined with the fact that during the early stages of growth, the thermal and flow fields are not influenced by previous or neighbouring bubbles, provide well defined initial and boundary conditions. Because of this, the bubble growth measurements of this investigation are more reliable for validating theoretical predictions as compared with past investigations. Furthermore, for some of the measurements the bubble remained nearly hemispherical for a significant portion of the growth period. The nature of the experimental investigation, coupled with the fixed bubble shape, reduces the complexity of the problem enough that theoretical modelling of bubble growth is simplified considerably, for the circumstances of the experiment.

In this dissertation, the fundamental nature of bubble growth is investigated for spherically symmetric growth in an unbounded liquid, and the early stage of hemispherical growth near a heated solid surface in microgravity. The purpose of this study is to confirm and clarify existing ideas concerning bubble dynamics and to advance the current understanding of boiling by developing theoretical models based on as few physical assumptions as possible. The resulting system of equations are solved using conventional numerical techniques.

Chapter 2 describes the development of two numerical schemes which simulate spherically symmetric bubble growth in a uniformly superheated liquid. Infinite grid solutions of bubble growth over a range of boiling conditions were approximated by solving the governing equations on a progressively finer computational grid with uniform spacing between adjacent grid nodes. The infinite grid approximations show satisfactory agreement

with analytical formulations and experimental data and are deemed sufficiently accurate to be utilized as benchmark solutions for the development of more complex numerical schemes. Since spatial variations in temperature and velocity are confined to a region very near the vapour-liquid interface, a grid clustering technique was employed which considerably reduced the computational time of the simulations with minimal loss of accuracy. Grid independence was assured by refining the computational grid until sufficient convergence with the benchmark solutions was obtained. The more efficient code facilitated rigorous testing of the predictive capabilities of the numerical simulations. Excellent agreement between the predicted growth curves and those determined experimentally was observed for a wide range of system conditions.

The nature of vapour bubble growth in unbounded, uniformly superheated water was explored in Chapter 3. Since many of the underlying mechanisms are the same, studying this type of growth is fundamental to the understanding of bubble growth on a heated surface. First, the growth of a single isolated bubble from inception to thermal diffusion controlled growth was examined in detail. As the bubble grew through the various growth stages, the relative contributions of surface tension, liquid inertia and thermal diffusion were investigated. Next, the influence of varying system pressure and liquid superheat on bubble growth dynamics was examined with focus on how the system condition affected the surface tension, inertia, and diffusion controlled growth stages.

Chapter 4 describes the development of a two-dimensional theoretical model which is capable of predicting both spherically symmetric vapour bubble growth in an infinite pool of liquid and hemispherical vapour bubble growth at a heated plane surface in microgravity. Since many of the complexities associated with earth gravity boiling are absent in

microgravity, the development of the physical model was based on realistic physical arguments and the resulting equations were solved with conventional numerical techniques. The accuracy of the predictions was affirmed by showing agreement with the benchmark solutions for spherically symmetric growth in a uniformly superheated liquid as well as agreement with the recent experimental measurements for hemispherical growth near a heated surface in microgravity. Finally, by considering a significant portion of the growth period of a single isolated bubble beginning from inception, the proportional contributions of the various mechanisms which govern growth were investigated utilising the analytical techniques developed for spherically symmetric bubble growth. In this way, the effects of the two-dimensional temperature distribution in the liquid near the heater surface have been discerned.

CHAPTER 2: HOMOGENEOUS BUBBLE GROWTH

LITERATURE SURVEY AND NUMERICAL SIMULATIONS

2.0 Introduction

In this chapter, the theoretical model which has been developed to predict spherically symmetric vapour bubble growth in an unbounded liquid with uniform initial superheat will be detailed. A brief review of past theoretical models will be given followed by a description of the present model and the associated solution procedure. Grid size and time-step independent solutions for four separate one-dimensional test cases will be offered as 'benchmark solutions' for the development of subsequent bubble growth models. To avoid numerical complexity when approximating the spatial derivatives, the benchmark solutions were obtained on a grid with uniform spacing between neighbouring grid nodes. The correctness of the theory as well as the validity of the computational procedure is demonstrated by comparing the simulated bubble growth curves with the analytic solutions and experimental data.

In order to decrease the computation time, a grid clustering technique was employed which clusters grid points near the vapour-liquid interface where gradients in velocity and temperature are high. The reduction in the number of grid points and subsequent computation time is appreciable with no significant loss in accuracy of the numerical prediction.

With the more efficient numerical solution, simulations of homogeneous bubble growth in an unbounded, uniformly superheated liquid were obtained and compared with available experimental data over a wide range of system pressures and initial superheats for both water and R113.

2.1 Theoretical Development

The case of spherically symmetric bubble expansion in a uniformly superheated infinite pool of liquid is illustrated in Fig. 2.1. Assumption of potential flow and integration of the one-dimensional momentum equation in the liquid provides an expression which describes the growth of the vapour bubble,

$$\frac{P_v(T_v)-P_\infty}{\rho_l} = R\frac{d^2R}{dt^2} + \frac{3}{2}\left(\frac{dR}{dt}\right)^2 + \frac{2\sigma}{\rho_l R} \tag{2.1}$$

Equation (2.1) is known as the extended or modified Rayleigh equation. It relates the pressure difference which drives growth to the inertial forces exerted by the liquid on the bubble and surface tension forces at the interface. The classical derivation of this relationship is given in Appendix A. The influence and relevance of each term in the above expression will be thoroughly discussed in subsequent chapters.

As a result of the pressure-temperature dependance of the vapour, at least one more equation is required to fully describe the bubble growth problem. This is complicated further by the fact that the internal energy of the growing bubble is constantly changing. By considering an energy balance at the vapour-liquid interface, the energy, Q, required to

evaporate the liquid at the interface and hence expand the bubble is supplied by diffusion across the thermal boundary layer which exists in the liquid surrounding the bubble. The rate of change in the energy content of the vapour bubble is such that,

$$\frac{dQ}{dt} = \int_{A_S} k_l \left(\frac{\partial T}{\partial r} \right)_{r=R(t)} dA \qquad (2.2)$$

Due to the coupling of the momentum and energy equations through the non-linear convection term, the primary obstacle in obtaining a solution of the two coupled ordinary differential equations is that of predicting the interfacial temperature gradient, $(\partial T/\partial r)_{r=R(t)}$, as well as the interfacial temperature.

2.1.1. Early Analytical Work

The early theoretical works of Rayleigh [1917], Plesset and Zwick [1954], Forster and Zuber [1954] and Scriven [1959] among others, yielded analytic solutions for the bubble growth rate by considering the two limiting regions; the *inertia* and *diffusion* controlled growth regions.

Inertia controlled growth is restricted to the initial stages of rapid growth during which the rate at which the bubble expands is primarily limited by its ability to accelerate or 'push back' the surrounding liquid. During this stage, the rate of heat transfer to the interface is assumed sufficiently high such that growth is not constrained by the resultant vapour generation into the bubble. If this were true, and the rate at which the bubble expands were regulated by its ability to force the liquid out radially, then bubble growth could be

predicted by the solution to equation (2.1) alone.

During this stage of growth, the vapour pressure is nearly constant and assumed to be near its maximum value of value of $P_v \approx P_{sat}(T_\infty)$. This solution is referred to as the Rayleigh solution. For bubbles large enough that the surface tension term is negligible, equation (2.1) can be solved for the interface velocity such that,

$$\dot{R}^2 = \frac{2}{3}\left(\frac{P_{sat}(T_\infty) - P_\infty}{\rho_l} \right) \tag{2.3}$$

Substitution of the linearized form of the Clapeyron equation to relate the vapour temperature to the saturation pressure, the Rayleigh solution for inertial controlled growth is obtained (Plesset and Zwick [1954], Mikic et al [1970]),

$$R(t) = \left(\frac{2}{3}\left[\frac{T_\infty - T_{sat}(P_\infty)}{T_{sat}(P_\infty)} \right]\frac{h_{fg}\rho_v}{\rho_l} \right)^{1/2} t \tag{2.4}$$

It is evident from equation (2.4) that inertial controlled growth is characterized by a linear relationship between radius and time. At the time of its development, the applicability of equation (2.4) was difficult to ascertain because the time interval over which bubble growth is inertia controlled becomes significant only for very low system pressures for which no experimental data existed.

Plesset and Zwick [1954], Forster and Zuber [1954] and Scriven [1959] among others, extended bubble growth predictions beyond the inertial controlled growth region by taking into account the fact that as the bubble grows, the latent heat requirement of evaporation depletes the energy stored within the superheated layer which has formed at the

surface of the bubble (Plesset and Zwick [1954]). As the bubble grows, its equilibrium vapour temperature decreases from T_∞ to its minimum value of $T_{sat}(P_\infty)$. As the interfacial temperature and corresponding pressure drop, bubble growth becomes limited by the relatively slower diffusion of heat to the vapour-liquid interface, causing the growth rate to continually decrease.

Plesset and Zwick [1954] obtained an analytic solution which predicts the instantaneous bubble radius for thermal diffusion controlled growth by supplying an approximate expression for the temperature of the liquid at the interface by assuming the thickness of the thermal boundary layer surrounding the bubble is much smaller than the radius of the bubble. The 'thin thermal boundary layer' assumption resulted in an expression for the liquid temperature at the moving interface of the form,

$$T(R,t) = T_\infty - \left(\frac{\alpha}{\pi}\right)^{1/2} \int_0^t \left[\frac{R^2}{\left(\int_0^t R^4(y)dy\right)^{1/2}} \right] \left(\frac{\partial T}{\partial r}\right)_{r=R(x)} dx \qquad (2.5)$$

As pointed out by Riznic *et al.* [1999], the term in the square brackets accounts for the effect of the changing interfacial area on the temperature at the interface. Assuming thermal equilibrium between the liquid at the interface and the vapour, equations (2.1) and (2.5) were combined with a linear equation relating vapour pressure and temperature to give a leading order approximation for the interfacial temperature gradient,

$$\left(\frac{\partial T}{\partial r}\right)_{r=R(t)} = \sqrt{3}\frac{\Delta T}{(\pi\alpha t)^{1/2}} \qquad (2.6)$$

where $\Delta T = T_\infty - T_{sat}$. By comparing this result with the solution for the temperature gradient at a stationary plane interface of a semi-infinite solid, namely,

$$\left(\frac{\partial T}{\partial r}\right)_{r=R(t)} = \frac{\Delta T}{(\pi \alpha t)^{1/2}} \qquad (2.7)$$

it becomes apparent that the coefficient of the order unity in equation (2.6) is attributed to the effects of increasing interfacial area (Riznic *et al* [1999]). Equation (2.6), combined with a simplified expression for the energy balance at the interface, relates the rate of heat transfer to the bubble to the vapour mass balance,

$$\rho_v h_{fg} \frac{dR}{dt} = k_l \left(\frac{\partial T}{\partial r}\right)_{r=R(t)} \qquad (2.8)$$

to give an approximate expression for thermal diffusion controlled bubble growth,

$$R(t) \approx 2\sqrt{3} Ja \left(\frac{\alpha t}{\pi}\right)^{1/2} \qquad (2.9)$$

Here, $Ja = \rho_l C_l (T_\infty - T_{sat})/\rho_v h_{fg}$ is the dimensionless superheat known as the Jakob number. Equation (2.9) predicts that the radius will increase asymptotically with time if growth is diffusion controlled and is valid only for times large enough that the growth velocity is much smaller than the inertia controlled velocity (Prosperetti and Plesset [1978]). The theory was shown to agree very well with the experimental data of Dergarabedian [1953] for bubble growth in water at atmospheric pressure and superheats not exceeding 5.1 °C.

A similar analysis was performed by Forster and Zuber [1954]. In their work, the

interface temperature was approximated by integrating Green's function over the domain of the 'thin thermal boundary layer' and the vapour pressure and temperature were related through the Clausius-Clapeyron relation to give the asymptotic expression,

$$R(t) \approx 2\left(\frac{\pi}{2}\right) Ja \left(\frac{\alpha t}{\pi}\right)^{\frac{1}{2}}$$

(2.10)

This expression differs from equation (2.9) only by the numerical constant, $\pi/2$, which is again slightly larger than unity and is attributed to the increasing interfacial area (Riznic *et al* [1999]).

Scriven [1959] considered thermal diffusion controlled growth without the assumption of a thin thermal boundary layer. By obtaining exact solutions of the equation of energy flow including radial convection, the asymptotic relation of the form,

$$R(t) \approx 2\beta (\alpha t)^{\frac{1}{2}}$$

(2.11)

was obtained. Here the constant β depends on the system pressure (physical properties) and the degree of superheat. In the limiting case of moderate to high superheats, or large Jakob numbers, equation (2.11) simplifies to,

$$R(t) \approx 2\sqrt{3}\left(\frac{1}{1+\gamma}\right) Ja \left(\frac{\alpha t}{\pi}\right)^{\frac{1}{2}}$$

(2.12)

where,

$$\gamma = \left(\frac{C_{pl} - C_{pv}}{h_{fg}} \right) \Delta T \qquad (2.13)$$

For commonly used fluids and system conditions of practical interest $\gamma \ll 1$ and equation (2.12) is in fact identical to the Plesset and Zwick solution given by equation (2.9). This implies that for large enough Jakob number, the thin thermal boundary layer assumption is valid. For low superheats, or small Jakob numbers, Scriven [1959] obtained the expression,

$$R(t) \approx \sqrt{2\pi} \left(\frac{1}{1+\gamma} \right) Ja^{\frac{1}{2}} \left(\frac{\alpha t}{\pi} \right)^{\frac{1}{2}} \qquad (2.14)$$

which for $\gamma \ll 1$ simplifies to,

$$R(t) \approx (2 \, Ja \, \alpha t)^{\frac{1}{2}} \qquad (2.15)$$

It is noticed that this expression has the same asymptotic dependence on time but a different dependence on the Jakob number as identified in equations (2.9), (2.10) and (2.12). As pointed out by Scriven [1959], this difference can cause considerable discrepancy between the growth constant predicted by equation (2.15) and those predicted by equations (2.9), (2.10) and (2.12). This implies that for small Jakob numbers, the thin thermal boundary layer assumption may no longer be valid. For thermal diffusion controlled growth, equations (2.12) and (2.15) suggest the following dependence on the dimensionless superheat, or Jakob number;

$$R \sim Ja \quad (large\ Ja)$$
$$R \sim Ja^{\frac{1}{2}} \quad (small\ Ja) \tag{2.16}$$

This dependence on the Jakob number was in fact confirmed by Riznic *et al.* [1999] who showed that the difference is attributed to the effect of curvature of the interface on the temperature gradient. The energy integral method was utilized to obtain an estimate of the temperature gradient at the interface of a growing sphere which was combined with the energy balance at the interface, equation (2.8), to give the following expression for the growth rate:

$$\frac{dR}{dt} = \alpha Ja \left[\frac{b}{(3\alpha t)^{\frac{1}{2}}} + \frac{1}{R(t)} \right] \tag{2.17}$$

In the above expression, the first term in the brackets accounts for the interfacial area change and the second term is attributed to the effect of the curvature of the interface. Upon integration of equation (2.17), two limiting solutions were obtained. It was determined that for large Jakob numbers, corresponding with Ja>2, the radius varies as,

$$R(t) \approx 2\sqrt{3} Ja \left(\frac{\alpha t}{3} \right)^{\frac{1}{2}} \tag{2.18}$$

This is in excellent agreement with the thin thermal boundary layer theories of Plesset and Zwick [1954] and the limiting case of Scriven [1959] for large Ja. Thus, for large enough Jakob numbers, the affect of interface curvature is negligible and the thin thermal boundary layer assumption is valid. For small Jakob numbers, corresponding with Ja<2, Riznic *et al*

[1999] found that the radius varies as

$$R(t) \approx (2 \, Ja \, \alpha t)^{\frac{1}{2}}$$ (2.19)

Although not noted explicitly by the authors, this expression is identical to the limiting case for small Jakob numbers obtained by Scriven [1959] (equation (2.15)). Consequently, for small Jakob number, the thin thermal boundary layer assumption is not valid and curvature of the interface plays an important role. The theory of Riznic *et al* [1999] showed reasonable agreement with the bubble collapse measurements of Florschuetz and Chao [1965] for water bubbles in the Jakob number range $15.1 \leq Ja \leq 39.3$, as well as with the bubble growth measurements of Thorncraft [1995] for forced convection boiling of FC-87 in the range $0.73 \leq Ja \leq 8.56$.

The discussion above postulates that the early stage of bubble growth is inertia controlled and the later stage is diffusion controlled. A complete description of the bubble growth process should be represented by a smooth transition between the two regimes. Mikic, Rohsenow and Griffith [1970] obtained an expression for the variation of bubble radius with time which spans both regions by interpolating between the limiting solutions for large and small times, equations (2.4) and (2.9) respectively. The expression is often referred to as the MRG solution and is given in the form,

$$R^+ = \frac{2}{3}[(t^+ + 1)^{3/2} - (t^+)^{3/2} - 1]$$ (2.20)

where the scaled variables are given by,

$$R^+ = \frac{RA}{B^2} \qquad t^+ = \frac{tA^2}{B^2}$$

$$B = \left(\frac{12\alpha_l}{\pi}\right)^{1/2} Ja$$

$$A^2 = \frac{2C_l\rho_v[T_\infty - T_{sat}(P_\infty)]}{3\rho_l T_{sat}(P_\infty)}$$

(2.21)

Because the exact conditions on both ends were built in during the derivation of equation (2.20), the expression approaches equation (2.4) at small times and is asymptotic to equation (2.9) as time approaches infinity. This theory was found to be in good agreement with the experimental data of Lien [1969] for water over a wide range of system pressures, including low pressure data with a significant inertia controlled region.

The use of the Plesset and Zwick [1954] solution in the interpolation formulation of Mikic *et al.* [1970] restricts the validity of the MRG solution to moderate to high Jakob numbers in which the thin thermal boundary layer assumption is valid. This was illustrated by Prosperetti and Plesset [1978] who showed excellent comparison between the predictions of those theories in which a thin thermal boundary layer is assumed and the more accurate numerical solution provided by Dalle Donne and Ferranti [1975] for superheated sodium and Jakob numbers in the range $2.979 \leq Ja \leq 565.7$. For the case in which $Ja=0.7331$, poor agreement was obtained because the assumption of the thin thermal layer is not valid. Prosperetti and Plesset [1978] extended the range of applicability of the MRG type interpolation formula by introducing scaling variables which describe growth over the entire range of superheats. By assuming a linear variation of vapour pressure with temperature, they obtained the expression,

$$R^+ = \left(\frac{2}{\pi^2}\right)\left(\frac{2}{3}\right)\left[\left(\frac{1}{2}\pi^2 t^+ + 1\right)^{3/2} - \left(\frac{1}{2}\pi^2 t^+\right)^{3/2} - 1\right]$$ (2.22)

where the scaled variables are expressed as,

$$R^+ = \mu^2 \frac{R}{R_c} \qquad t^+ = \beta\mu^2 t$$

$$\mu = \frac{1}{3}\left(\frac{2\sigma\alpha}{\pi}\right)^{1/2} \frac{\rho_v h_{fg}}{k(T_\infty - T_{sat})}(\rho_l[P_v(T_\infty) - P_\infty])^{-1/4}$$ (23)

$$\beta = \frac{[P_v(T_\infty) - P_\infty]^{3/2}}{2\sigma\rho_l^{1/2}}$$

This formulation over predicted growth at high superheats but not enough to be of importance for the range of boiling conditions of practical interest (Prosperetti and Plesset [1978]).

2.1.2. Computational Work

Numerical computations of vapour bubble growth in an infinite, uniformly superheated liquid have been performed by Theophanous *et al* [1969], Judd [1969], Board and Duffy [1971], Dalle Donne and Farranti [1975], Lee [1993] and Lee and Merte [1996]. In the earlier three works, the approach was to assume the shape of the temperature profile within the thermal boundary layer which exists around the growing bubble so that the temperature gradient at the vapour-liquid interface could be deduced. Perhaps the simplest numerical approach was proposed by Board and Duffy [1971] in which a linear temperature drop was assumed to exist across a thermal layer of variable thickness $\delta = ((\pi/3)\alpha_l t)^{1/2}$ such

that,

$$\left(\frac{\partial T}{\partial r}\right)_{r=R(t)} = \frac{T_v(t) - T_\infty}{\delta(t)} \qquad (2.24)$$

The assumed temperature profile was consistent with the leading term approximation of the Plesset and Zwick [1971] analysis for long times (equation (2.6)). Agreement with experimental data for water was found to be quite good for superheats up to $20.3\,^\circ$C. It was further shown that the numerical computations of Board and Duffy [1971], Theophanous *et al* [1969], Judd [1969] and the analytic method of Mikic *et al* [1970] were all in close agreement for bubbles in moderate to highly superheated sodium. This leant support to the notion that bubble growth is relatively insensitive to the assumed temperature profile shape (Board and Duffy [1971]).

Dalle Donne and Farranti [1975], Lee [1993] and Lee and Merte [1996] increased the flexibility of the analysis by numerically solving the one dimensional heat conduction equation in a moving medium,

$$\frac{\partial T}{\partial t} + u\frac{\partial T}{\partial r} = \alpha_l\left(\frac{\partial^2 T}{\partial r^2} + \frac{2}{r}\frac{\partial T}{\partial r}\right) \qquad (2.25)$$

In doing so, the temperature gradient in the liquid at the vapour-liquid interface was obtained from the computed temperature field. The work of Lee [1993] and Lee and Merte [1996] showed excellent agreement with the low pressure data of Bohrer [1973] for refrigerant R113, as well as the experimental data of Dergerabedian [1953] and Lien [1969] for water with system pressures within the range of 1.26 kPa-101.33 kPa, and initial liquid superheats

ranging between 0.8°C - 15.74°C. The predictions of Lee and Merte [1996] compared very well with the numerical work of Dalle Donne and Farranti [1975] for superheated sodium which confirmed the accuracy of each investigation.

2.2. Present One-Dimensional Theory

2.2.1 Equation Generation

Assuming that the liquid is inviscid and that the flow is irrotational, the equation of motion for the spherical bubble of radius, R, is approximated by the extended Rayleigh equation,

$$\frac{P_v(T_v) - P_\infty}{\rho_l} = R\frac{d^2R}{dt^2} + \frac{3}{2}\left(\frac{dR}{dt}\right)^2 + \frac{2\sigma}{\rho_l R} \qquad \textbf{(2.1, 2.26, A.10)}$$

The initial bubble radius is determined by assuming that the vapour is initially saturated with $T_v = T_\infty$ and that it exists in unstable equilibrium with the quiescent surroundings. The initial radius is predicted by the Young-Laplace equation ,

$$R_c = \frac{2\sigma}{P_{sat}(T_\infty) - P_\infty} \qquad \textbf{(2.27)}$$

Considering an energy balance at the vapour-liquid interface, the energy required to evaporate the liquid is supplied by thermal diffusion through the liquid. For a spherical bubble this gives,

$$\rho_v h_{fg} \frac{dR}{dt} + h_{fg} \frac{R}{3} \frac{d\rho_v}{dt} = \frac{1}{4\pi R^2} \int_{A_S} k_l \left(\frac{\partial T}{\partial n} \right)_R dA \qquad (2.28)$$

where $Q = \rho_v h_{fg} (^4/_3 \, \pi R^3)$ has been substituted into equation (2.2) and differentiated. The temperature gradient at the vapour-liquid interface is obtained by numerically solving the one-dimensional energy equation in spherical coordinates for the moving liquid,

$$\frac{\partial T}{\partial t} + u \frac{\partial T}{\partial r} = \alpha_l \left(\frac{\partial^2 T}{\partial r^2} + \frac{2}{r} \frac{\partial T}{\partial r} \right) \qquad (2.29)$$

with initial and boundary conditions given by,

$$\begin{aligned} T(r,0) &= T_\infty \\ T(R,t) &= T_v \\ T(R_\infty,t) &= T_\infty \end{aligned} \qquad (2.30)$$

The initial condition states that the entire temperature field in the liquid is constant. The first boundary condition is obtained by assuming that no temperature discontinuity exists across the vapour-liquid interface so that the temperature of the liquid at the interface is identical to the temperature of the vapour. The far field boundary condition is assumed to be constant and equal to the initial temperature. The radial velocity is determined as a function of the instantaneous bubble radius and interface velocity by assuming that the flow field can be determined by the solution for potential flow around the expanding sphere in an unbounded liquid. The local velocity is thus,

$$u(R,t) = \frac{dR}{dt}\left(\frac{R}{r}\right)^2$$

(2.31)

Finally, it is postulated that the vapour is saturated and remains in thermodynamic equilibrium throughout the growth period so that the pressure and density can be specified as functions of the saturated vapour temperature;

$$P_v(T_v) = a_1 T_v + a_2 T_v^2 + a_3 T_v^3 + a_4 T_v^4 + a_5 T_v^5$$
$$\rho_v(T_v) = c_1 T_v + c_2 T_v^2 + c_3 T_v^3 + c_4 T_v^4 + c_5 T_v^5$$

(2.32)

As in other works, such as Lee [1993], coefficients in these relationships, which represent the property variations with temperature, are obtained from best-fit correlations with available property data.

2.2.2. Solution Procedure

Specifying the vapour density and pressure as functions of the vapour temperature effectively reduces the problem to that of determining the instantaneous values of R, dR/dt and T_v. In order to do so, the following variables are defined,

$$\begin{aligned} y_1 &= T_v \\ y_2 &= R \\ y_3 &= \frac{dR}{dt} \end{aligned}$$

(2.33)

Equations (2.26) and (2.28) can now be rearranged such that a system of three simultaneous ordinary differential equations results,

$$\frac{dy_1}{dt} = \frac{dT_v}{dt} = f_1(t, y_1, y_2, y_3)$$

$$\frac{dy_2}{dt} = \frac{dR}{dt} = f_2(t, y_3) \qquad\qquad (2.34)$$

$$\frac{dy_3}{dt} = \frac{d^2R}{dt^2} = f_3(t, y_1, y_2, y_3)$$

Here, the function f_1 is determined by differentiating equation (2.32) for the density variation with vapour temperature, $d\rho_v/dt = (d\rho_v/dT_v)(dT_v/dt)$, and rearranging equation (2.28) to isolate dT_v/dt. The function f_2 is simply equal to the bubble interface velocity dR/dt, and the function f_3 is determined by rearranging equation (2.26) to isolate d^2R/dt^2. For a given time step Δt, the solution of the above system of equations requires that the values y_1, y_2 and y_3 be known at the beginning of the time interval. A fourth-order Runge Kutta scheme is then implemented to determine the updated values.

2.2.3 Initial Disturbance

In order to initiate bubble growth, the equilibrium radius R_c was perturbed by allowing it to increase by a very small amount over an infinitesimally small time interval. This is equivalent to a disturbance in temperature or pressure (Board and Duffy [1971]). A comprehensive discussion of the initial disturbance can be found in Lee [1993] and Lee and Merte [1996] which will be presented briefly later in this chapter. For this study, the initial time step was selected to be 10^{-9}s with a corresponding radius increase of 0.0005% of the initial radius. As will be discussed, the magnitude of the initial disturbance does not significantly influence the overall accuracy the computed growth curve.

2.3 Numerical Procedure

In this section, the methodology for obtaining the grid independent benchmark solutions for spherical bubble growth in an initially uniformly superheated, unbounded liquid will be detailed for four separate initial liquid states. For the benchmark solutions, the energy equation was solved on a progressively finer mesh with uniform spacing between adjacent nodes. However, steep gradients in temperature occur only in the immediate vicinity of the growing bubble. Because a grid independent solution on a uniform mesh is computationally expensive, a grid clustering technique was also employed which drastically reduced the number of grid points and the computation time without compromising the accuracy of the numerical predictions.

2.3.1 Grid Independent Solutions on a Uniform Grid

2.3.1.1 Solution of the Energy Equation

A grid independent solution requires that for a given set of initial and boundary conditions, the resulting bubble growth curve be insensitive to the number of grid points utilized in obtaining the solution of the energy equation. It was decided to keep the numerical approximation of the energy equation as simple as possible in order to avoid as many numerical complexities and pit-falls as possible. Hence, the numerical solution of the energy equation at each time step was initially performed on a grid with uniform grid spacing given by,

$$\Delta r = \frac{R - R_{inf}}{M - 1} \qquad (2.35)$$

where M is the number of grid points. The computational grid in the physical domain is illustrated in Fig. 2.2.

To accommodate the moving boundary resulting from the expanding vapour-liquid interface, a front-fixing method proposed by Crank [1984] was utilized. Here, the energy equation was transformed onto a coordinate system with uniform grid spacing which fixes the interface at the origin. The transformation is given by,

$$r = r(\eta, \tau)$$
$$t = \tau$$

(2.36)

where,

$$\eta = \frac{r - R}{\delta}$$
$$\delta = R_{inf} - R$$

(2.37)

The computational domain is illustrated in Fig. 2.2. Utilizing subscript notation to denote partial differentiation with respect to the subscript variable, the relevant derivatives in the physical and computational domain are related through the following;

$$T_r = \delta^{-1}(T_\eta)$$
$$T_{rr} = \delta^{-2}(T_{\eta\eta})$$
$$T_t = T_\tau - \delta^{-1}R_t(1 - \eta)T_\eta$$

(2.38)

In this way, the energy equation becomes,

$$T_\tau + aT_\eta + bT_{\eta\eta} = 0$$

(2.39)

where,

$$a = \frac{1}{\delta}\left(R_f \left(\frac{R}{\delta \eta + R} \right)^2 - R_f(1 - \eta) \right) - \frac{2\alpha}{\delta \eta + R}$$
$$b = -\frac{\alpha}{\delta^2}$$

(2.40)

Here it should be noted that equation (2.31) has been substituted for the radial velocity in the liquid.

Equation (2.39) was discretized using second order central difference representations of the spatial derivatives and a fully implicit first order representation of the time derivatives. At a given time step, the temperature field was determined by solving the resulting system of algebraic expressions with the Tri-Diagonal Matrix Algorithm (TDMA). The code was developed in FORTRAN 90 and is given in Appendix D.

2.3.1.2 Infinite Grid Solutions

Grid independent solutions for the four separate test cases given in Table 2.1 have been obtained. The test cases have been chosen to adequately represent a range of growth curves which have been encountered experimentally. The system conditions listed in the table result in growth curves which are characterized by slow diffusion controlled growth, as in Case A, to rapid predominantly inertial controlled growth, as in Case D. The intermediate Cases B and C are predominantly diffusion controlled but display some dependence on the inertia of the surrounding liquid. The fourth test case, for low system pressure highly superheated R113, was also chosen for its different fluid properties.

A grid independent solution is the converged solution which is obtained when the

number of grid points, M, in the computational domain is systematically increased. Ideally

an infinite number of grid points should be utilized which in numerical work is obviously

not realizable.

Table 2.1: Test Cases for Grid Independent Study				
Case	Fluid	System Pressure P_∞	Initial Superheat ΔT_{sup}	Characteristic Growth
A	Water	1.0 atm	3.1 °C	Diffusion
B	Water	0.372 atm	6.3 °C	Intermediate
C	Water	0.362 atm	17.0 °C	Intermediate
D	R113	0.0361 atm	48.21 °C	Inertial

Fig. 2.3a shows the computed growth curves for Test Case A for increasing values

of M. In this and the following cases, the far field boundary is held fixed at R_{inf}=5 cm and

it will later be shown that this more than sufficient to approximate a semi-infinite boundary

for the range of growth considered in this work. It is evident from the graph that the growth

curves converge as M is increased from 5000 to 40000 grid points. This is better illustrated

in Fig. 2.3b in which each curve is subtracted from the curve determined using M=40000.

This graph shows that the difference between the two curves diminishes to nearly zero as M

is increased.

With this set of curves, an infinite grid solution has been approximated by assuming

that the difference between the instantaneous magnitude of the computed radius, R(M), and

that which would result on an infinite mesh, $R(M_\infty)$, is proportional to the mesh spacing

raised to an arbitrary power. This gives the expression,

$$|R(M_\infty) - R(M)| = C_{\Delta}r^{\,n} \qquad\qquad (2.41)$$

Here, C is a proportionality constant and the exponent n represents the order of error of the solution which should coincide with the leading truncation error term which results from neglecting higher order terms in the Taylor Series expansions when approximating the spatial derivatives. For a given time t, three simultaneous equations are generated for the three unknowns $R(M_\infty)$, C and n by applying equation (2.25) to three separate curves generated using different values of M. In this way, the infinite grid solution is extrapolated from the three computed curves.

Figure 2.4a shows the comparison of the *grid independent solution* determined using the method outlined above with the computed growth curve for M=40000, which shall be considered the *converged solution*. The curves for M_1 =20000, M_2 = 30000 and M_3 = 40000 were utilized to extrapolate the grid independent radius values. Figure 4b shows that the order of error of the solution is approximately $(\Delta r)^{2.2}$ which coincides very well with leading truncation error term of $(\Delta r)^2$ which results from utilizing a central difference scheme in approximating the spatial derivatives.

The identical procedure to that outlined above was applied to Case B, C and D in Table 2.1. The results are shown in Figs. 2.5 through 2.10. Each case shows trends similar to those observed in Case A. First, the growth curves converge as the number of mesh points is increased from 5000 to 40000. Second, M=40000 appears to be sufficient to be defined as the **converged solution** for each test case seeing that there is no appreciable difference between the curves obtained with M=30000 mesh points and M=40000 mesh points. Finally, the order of error of the numerical approach as predicted by the exponent, n, in

equation (2.41) is close to the expected value of n=2 for the central difference approximation of the spatial derivatives in the discretized energy equation. For future reference, the benchmark radius versus time data is tabulated in Appendix B together with the data for the converged solutions.

2.3.1.3 Far Field Effect

The far field boundary is approximated as a semi-infinite medium by setting the position of the far field ,R_{inf}, far enough away from the growing bubble that gradients in temperature and velocity are not appreciable compared with those near the bubble interface. Because the choice R_{inf} affects the grid spacing as determined by equation (2.35), it is desirable to set this distance constant for the entire range of growth curves which will be encountered during this study so that grid independence is assured without having to repeat the procedure outlined in the previous section for each new far field placement. For this work, the far field has been set at R_{inf}=5 cm for all cases studied. This distance has been deemed sufficient to cover the wide range of conditions that will be encountered. In order to test this choice, the far field position was halved to R_{inf}=2.5 cm and converged solutions were obtained for each case listed in Table 2.1. It is evident from the comparison of the converged solutions with the benchmark solutions in Fig. 2.11 that halving the distance of the far field boundary has no significant influence on the accuracy of the computed solution for each test case.

2.3.1.4 Time Step Independence

As will be detailed in the subsequent chapters, the nature of bubble growth is such

that the growth rate varies significantly during its lifetime. Initially, when the bubble is near its equilibrium radius given by equation (2.27), the growth rate is slow. This is followed by an extremely rapid increase in the growth rate as the bubble enters and passes through the inertial growth stage, only to be followed by a continually decreasing growth rate during the asymptotic diffusion controlled growth stage. Consequently, the time step, Δt, selected when approximating the time derivative in equation (2.39) must be small enough to resolve the rapid transition to the inertial stage and not lead to numerical instabilities, while at the same time not being so small that it will result in unnecessary time consuming computations during the much slower asymptotic phase of growth.

In order to accommodate the need for the small time steps during the 'early' growth stage and the much coarser requirements during the 'later' growth stage, a simple exponential function has been chosen. The time step is given by,

$$\Delta t = t_o \exp\left(\frac{K-1}{B}\right) \qquad (2.42)$$

where K is the total number of time steps which have been performed since t=0, t_o is the magnitude of the first time step and B is a parameter which allows for the variation of the growth of Δt with time such that a smaller value of B coincides with a coarser distribution of the time step.

For the present work, time step independence is assured by selecting a fixed value of $t_o=1.0 \times 10^{-9}$ and systematically increasing B until adequate convergence is obtained for each test case in Table 2.1. Figs. 2.12 through 2.15 show the converging growth curves for Case A, B, C and D respectively. For each case, adequate convergence is obtained for

B=1500 with less than 1% difference between it and the curve obtained with B=1000.

2.3.1.5 Initial Disturbance Effect

The sensitivity of the three converged solutions to the magnitude of the initial disturbance is illustrated in Figs. 2.16 through 2.19. It is clear from the graphs that the delay time, which is the time interval between the disturbance and the time at which the bubble undergoes significant growth, varies depending on the magnitude of the disturbance. For each case, as the magnitude of the time and radius disturbance increase, the delay time decreases. However, for the four cases shown the differences are small enough to be of little practical interest as the curves converge quickly. For this study, the initial time step was selected to be 10^{-9}s with a corresponding radius increase of 0.0005% of the equilibrium radius, R_c. A comprehensive discussion on the effect of varying the disturbance parameters imposed to initiate bubble growth can be found in Lee [1993].

2.3.1.6 Comparison with Analytical Works

The analytic solutions of Rayleigh [1917], Plesset and Zwick [1954], and Mikic *et al.* [1970] are shown in Fig. 2.20. The Rayleigh solution corresponds with inertia controlled growth such that the non-dimensional radius and time are related by $R^+=t^+$. The Plesset and Zwick relation is valid for diffusion controlled growth and is predicted by the expression $R^+=(t^+)^{1/2}$. As illustrated, the Mikic *et al.* solution (MRG solution), given by equation (2.20), is asymptotic to the Rayleigh solution on the lower end and to the Plesset and Zwick solution on the upper end. In this way, it is expected that the MRG solution will predict the transition region between inertia and diffusion controlled growth stages. The inertia, intermediate and

diffusion controlled growth regions, as determined by Lee [1993], are also depicted in Fig.2.20. Clearly, there is very good agreement with the present work and the analytic solutions. Case D falls within the intermediate region slightly above the inertial region. Here the Plesset and Zwick relation grossly overestimates the predicted curves whereas the Rayleigh and MRG solutions appear to be in close agreement. This is shown more clearly in Fig. 2.21 where the computational and analytic solutions are shown on a Cartesian plot. It is evident that very good agreement exists between the present work and the MRG solution for Case D with a difference of 2% at t=10 ms. The discrepancy between the computed curve and the Rayleigh solution is accounted for by the fact that the influence of thermal diffusion is not negligible. For diffusion controlled growth, Figs. 2.20 and 2.21 show that the numerical predictions for Case A are in excellent agreement with both the Plesset and Zwick and MRG solutions, whereas the Rayleigh solution is largely in error. A discrepancy between the numerical and analytic solutions exists in the intermediate region where a 10% difference is observed between the numerical and MRG solution for Case C at t=10 ms. The corresponding difference with the Plesset and Zwick solution is 3%. These discrepancies are of little significance considering the fact that the MRG solution is not an exact analytic solution of the coupled momentum and energy equations in this region and that the numerical predictions lie within the two analytic curves. Case B shows good agreement with both the MRG and Plesset and Zwick solutions. Overall, the agreement with the present work and the analytic solutions is certainly acceptable.

2.3.1.7 Comparison with Experimental Data

Table 2.2 gives the experimental data which is available for comparison with the four

converged grid independent solutions. The experiments of Dergarabedian [1953], Board and

Duffy [1971] and Bohrer [1969] were chosen because of the wide range of experimental test

conditions offered as well as the experimental techniques which were utilized. In each study,

special care was taken to ensure that boiling took place in a uniformly superheated liquid far

enough away from the walls of the vessel. In the study of Dergarabedian [1953], the water

was heated slowly and uniformly by radiant heaters. In the other three experiments, slow

depressurization was utilized to yield the initial metastable state of the liquid. This technique

is desirable over rapid depressurization because it minimizes thermal gradients prior to

bubble nucleation.

Table 2.2: Experimental Test Cases						
Case	Fluid	Reference	Measured Superheat, ΔT_{sup}	Error in Superheat	Error in Time	Error in Radius
A	Water	Dergarabedian [1953]	3.1 °C	± 0.2°C	±1.0 ms	3%
B	Water	Board and Duffy [1971]	6.3 °C	± 0.4°C	±0.2 ms	5%
C	Water	Board and Duffy [1971]	17.0 °C	± 0.4 °C	±0.2 ms	5%
D	R113	Bohrer [1969]	48.21 °C	±0.96 °C	±0.1 ms	7.5%

Also listed in Table 2.2 are the experimental uncertainties in the measured values. For the

Dergarabedian [1953] experiments (Case A) the accuracy of the temperature measurements

was estimated at (±0.2 °C). For the Board and Duffy [1971] experiments (Case B and C),

the contribution of the temperature measurement and the estimated spatial variations within

the liquid (±0.2 °C) as well as the uncertainty in the measured pressure (±0.003 atm)

combine to give the overall uncertainty of ±0.4 °C. For Case D, Borher [1969] simply states the uncertainty at 2% of the measured superheat value. The error in time is due to the uncertainty in the time origin due to the framing rate of the camera. This is a result of the finite time delay between the frame in which the first visible bubble appears and the frame showing no bubble. In effect, this allows the time axis to be shifted for any bubble history to obtain the best fit. The uncertainty in radius primarily results from shape distortions of the growing bubbles. In Dergarabedian [1953] the bubble diameters were measured three times and the average value was taken. In both Board and Duffy [1971] and Bohrer [1969], the bubble radii were measured in two orthogonal directions and the arithmetic average was utilized.

Figs. 2.22, 2.23 ,2.24 and 2.25 show the comparison of the present converged solutions for Case A, B, C and D respectively with the experimental data. In each graph, there are three computed curves. The middle curve is computed using the measured superheat whereas the upper and lower curve are computed using the upper and lower superheat uncertainty limits respectively. The vertical error bars on the experimental data represent the error in the measured radius and the horizontal error bars characterize the uncertainty in time.

Figs.2.22 and 2.23 show that the present numerical simulations are within the uncertainty of the experimental data for Case A and B. For Case C, Fig. 2.24 shows that the numerical simulation over predicts the experimental data at larger times. However, the curve representing the lower superheat is within 4% of the upper limit on the radius data so that agreement between the experimental data and the numerical simulation is again very good. Finally, Fig. 2.25 shows that the numerical simulation is well within the uncertainty limits

for Case D.

In the above discussion, grid and time step independent solutions have been obtained for four different test conditions on a mesh with uniform grid spacing. Infinite mesh solutions have been approximated and will be used as the benchmark solutions for the remainder of this work. Finally, the efficacy of the present solution technique has been confirmed by showing very good agreement with analytic and experimental data over a sufficiently wide range of boiling conditions.

2.3.2 Clustered Grid Solutions

2.3.2.1 Solution of Energy Equation

As previously mentioned, numerical approximations of the energy equation on a uniform grid are computationally expensive because of the large number of grid points which are required to obtain a solution which is sufficiently close to the infinite grid benchmark solutions. However, it is possible to take advantage of the fact that steep gradients in temperature and velocity are confined to a narrow region adjacent to the vapour-liquid interface. This being the case, clustering grid points in the region where the gradients are high and allowing coarser grid spacing where gradients are expected to be much smaller will reduce the required number of grid points which translates into a reduction in the total computation time.

The energy equation was solved numerically on a grid which was constructed using a variant of the grid generation technique proposed by Chen *et al* [1995]. The grid variables in the physical domain are depicted in Fig. 2.26. Grid clustering near the vapour-liquid interface as well the moving boundary were facilitated by defining the grid in the physical

domain by the expression,

$$r_j = R + (R_\infty - R)\left(1 - S_R \tan^{-1}\left[\left(1 - \frac{j-1}{M-1}\right)\tan\left(\frac{1}{S_R}\right)\right]\right)$$

(2.43)

where the term S_R determines the percentage of grid points near the interface and has been chosen as 0.65 throughout this work.

In order that conventional finite difference techniques could be utilized, the energy equation was transformed into a stationary grid with uniform grid spacing. The computational domain is illustrated in Fig. 2.26. The coordinate transformation is given by,

$$r = r(\eta,\tau)$$
$$t = \tau$$

(2.44)

such that,

$$T_r = J^{-1} r_\eta T_\eta$$
$$T_t = T_\tau - T_r r_\tau$$

(2.45)

By defining the contravarient velocity as,

$$U^c = (u - r_\tau)r_\eta$$

(2.46)

the transformed energy equation becomes,

$$T_\tau + aT_\eta + bT_{\eta\eta} = 0$$

(2.47)

where J is the Jacobian and the coefficients a and b are related to the metric and its derivative through the following,

$$J = r_\eta^2$$
$$a = \frac{U^c}{J} + \frac{\alpha r_\eta r_{\eta\eta}}{J^2} - \frac{2\alpha r_\eta}{Jr}$$
$$b = -\frac{\alpha r_\eta^2}{J^2}$$

(2.48)

As with the uniform mesh solution, equation (2.47) was discretized using second order central difference representations of the spatial derivatives and a fully implicit first order representation of the time derivatives. At a given time step, the temperature field was determined by solving the resulting system of algebraic expressions with the Tri-Diagonal Matrix Algorithm (TDMA). The code was developed in FORTRAN 90 and is given in Appendix E.

2.3.2.2 Converged Solutions on a Clustered Grid

As the number of mesh points increases, the growth curves for the clustered grid arrangement should approach the converged solution on a uniform grid. For the clustered grid case, the number of grid points was systematically increased from 150 to 800 and the computed growth curves were compared with the converged solution on a uniform mesh. Figure 2.27 shows the percent relative difference between the clustered (M=800) and uniform mesh (M=40000) solutions for each Case A, B, C and D in Table 2.1. The maximum difference is less than 1.5 % for the range of growth curves considered. In this

way, M=800 is deemed sufficient to define the **converged solution** for the clustered grid arrangement. This is a fifty times reduction in the number of grid points as compared with the uniform grid solution without significant loss of accuracy. Fig. 2.28 shows excellent agreement between the converged solution on a clustered grid and the *benchmark* solutions.

2.4 Spherical Bubble Growth Data

With the more efficient clustered grid solution, it is now reasonable to compare the predictions of the computational technique with a wider variety of experimental data. There is a limited amount of data available in the literature. Even still, the experimental conditions cover a more than adequate range of boiling conditions for testing the computed predictions. Table 2.3 lists the range of system conditions for the water experiments of Dergerabedian [1953], Board and Duffy [1971], Abdelmessih [1969] and Lien [1969], as well as the Freon-113 experiments of Bohrer *et al* [1973]. Also listed is the available experimental error associated with each data set.

Table 2.3: Selected Experiments for Comparison with Homogeneous Bubble Growth.

Fluid	Experiment	P_∞ (atm)	ΔT_{sup} (°C)	ΔT_∞	Δt	ΔR
water	Dergarabedian [1953]	1	1.4→5.3	±0.2 (°C)	±1.0 ms	±10 %
water	Board & Duffy [1971]	.318-.395	4.3→20.3	±0.4 (°C)	±0.2 ms	±5 %
water	Lien [1969]	.012-.382	9.0→15.74	±N/A	±0.5 ms	N/A
water	Abdelmessih [1969]	1	6.83→38.8	±N/A	±0.08 ms	N/A
R113	Bohrer [1973]	.036-.083	11.34→48.21	±2 %	±0.1 ms	±7.5 mm

The atmospheric pressure, low superheat data of Dergerabedian is shown in Fig. 2.29 (a), (b), (c)and (d) together with the numerical predictions of the present work. The curves

are typical of slow asymptotic growth and the comparison is within experimental uncertainty except for the ΔT_{sup}=4.5 °C and ΔT_{sup}=5.3 °C cases where the prediction is outside of the uncertainty limits by at most 14%. The magnitude of this over prediction is consistent with other theories including the numerical work of Board and Duffy [1971] and Lee [1993] as well as the analytical prediction of Plesset and Zwick [1954] and has been attributed to air content in the water (Lee [1993]). Overall, the comparison with the low superheat, slow asymptotic growth curves is acceptable.

The experimental data of Board and Duffy [1971] presents a more rigorous test of the solution technique by providing measurements over a wider range of superheats for an almost constant system pressure. As would be expected, the measured values in Fig. 2.30 show a continual increase in the growth rate with increasing liquid superheat. Fig. 2.30 also shows very good agreement between the predictions of the present work with the experimental data for superheats in the range 4.3 °C - 20.3 °C. Only at the largest superheats are the predictions outside of the experimental uncertainty of the experimental curves. The largest discrepancy is within 5% of the upper experimental uncertainty limit which is acceptable.

The experiments of Lien [1969] cover a wide range of system pressures (0.0124atm - 0.382atm) over a less notable range of superheats (9.0 °C - 15.7 °C). The experimental and predicted curves are shown in Fig. 2.31. For the lowest pressure, the relationship is nearly linear, indicating that the growth is primarily inertial controlled. As the pressure increases the growth rates decrease as the growth becomes more influenced by thermal diffusion. Agreement with the predicted relationship is very good for each growth curve.

Fig. 2.32 shows the comparison of the present work with the experimental data of

Abdelmessih [1969] obtained with atmospheric pressure water for superheats in the range 6.83 °C - 38.77 °C. For a superheat of 6.83 °C the agreement is quite good. For the higher superheats the agreement gets progressively worse with over 50% difference between prediction and experiment for the highest superheat case. A possible explanation for the large discrepancy with the data of Abdelmessih [1969] is that the experimental procedure utilized rapid depressurization to invoke homogeneous bubble nucleation and subsequent growth (Theofanous et al [1969]). This is in contrast with the experimental procedures of the other four investigators in which either slow transient heating or slow depressurization techniques were employed so that the system pressures and effective superheats were essentially constant both temporally and spatially over the period of bubble growth. As noted by Theofanous et al [1969], long term bubble growth can be sensitive to the initial pressure transient in the liquid. This effect will become more pronounced at higher initial system pressures, which may account for the increased deviation between the Abdelmessih [1969] results and the computations with increasing initial superheat. Considering the agreement between theory and experiment for the other experiments mentioned, it is suggested that the high superheat data of Abdelmessih is not reliable for comparison with the predictive capabilities of homogeneous bubble growth theories for uniformly superheated liquids.

Finally, Fig. 2.33 shows that the present theory is not fluid specific, in as much as it shows excellent agreement with the experimental data of Bohrer [1973] for refrigerant R113.

43
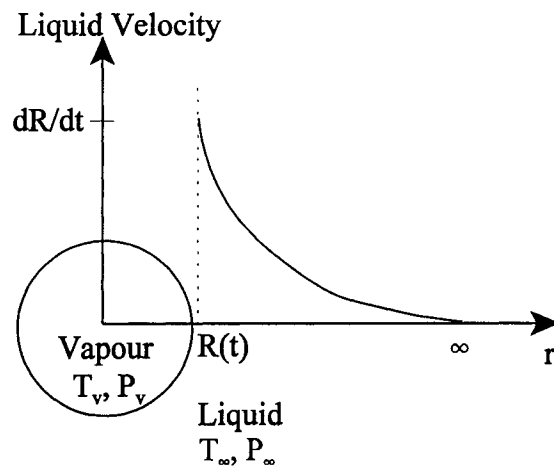
Figure 2.1: Growth of spherical bubble in an infinite liquid
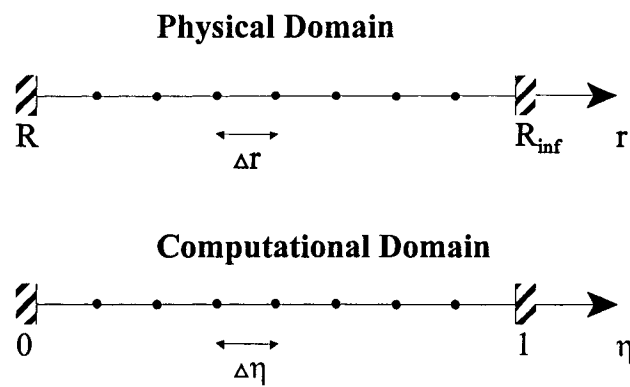
Figure 2.2: Physical and computational domains for the uniform grid solution technique.
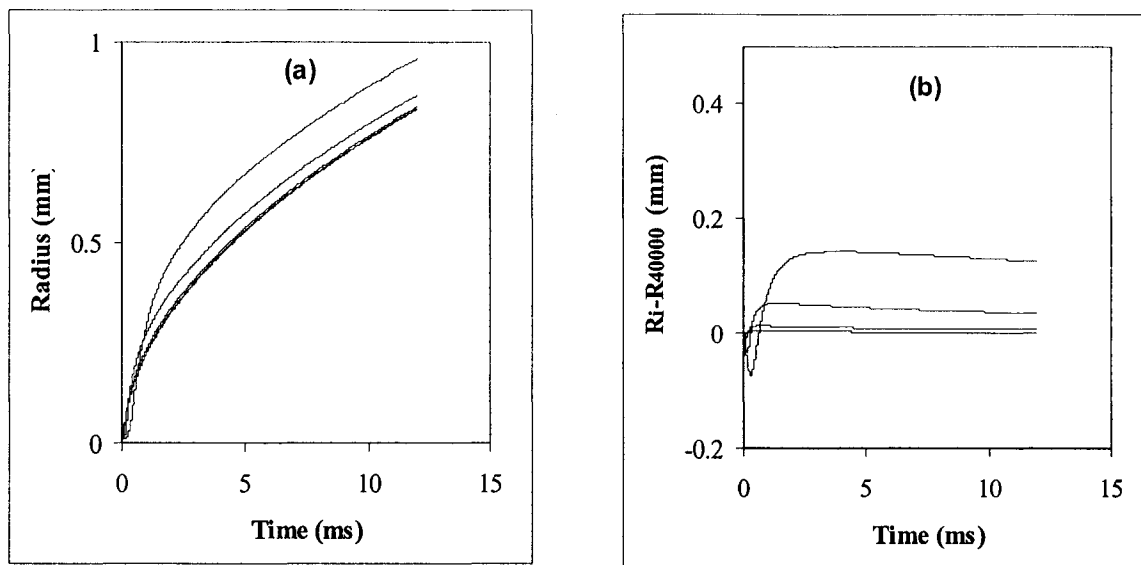
Figure 2.3: Case A; Water P=1.0 atm, ΔT_{sup}=3.1°C. Converging solution for grid points increasing from 5000 (top curves) to 40000 (bottom curves). a) Radius vs. time. b) Subtracted curves R_i-R_{40000}
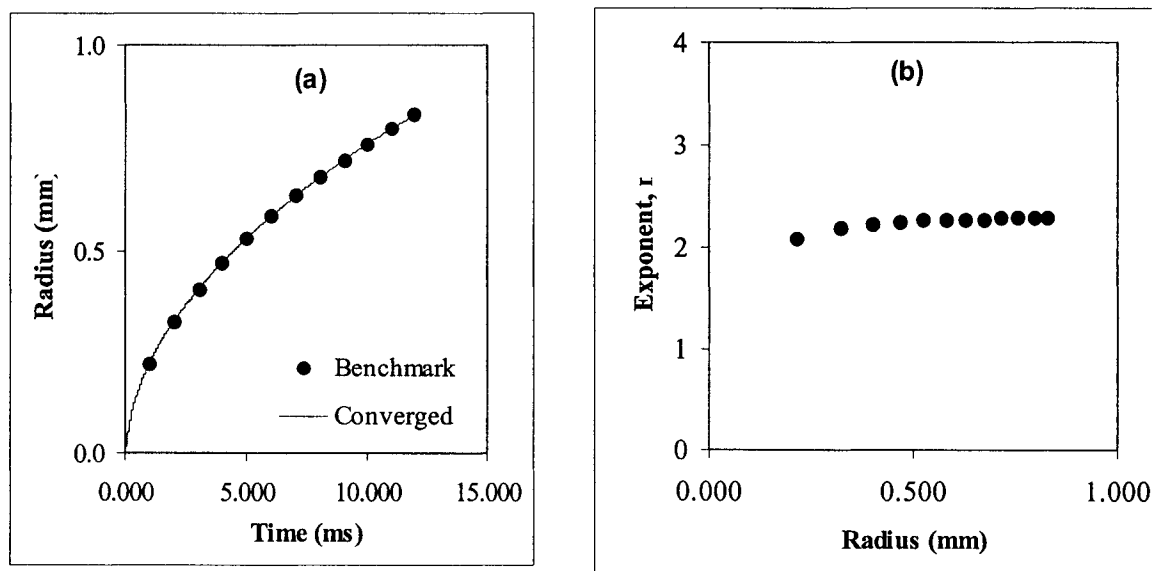
Figure 2.4: Case A; Water P=1.0 atm, ΔT_{sup}=3.1°C. a) Radius vs. time showing converged solution (M=40000) and the extrapolated benchmark solution. b) The exponent of Δr in equation (2.41).
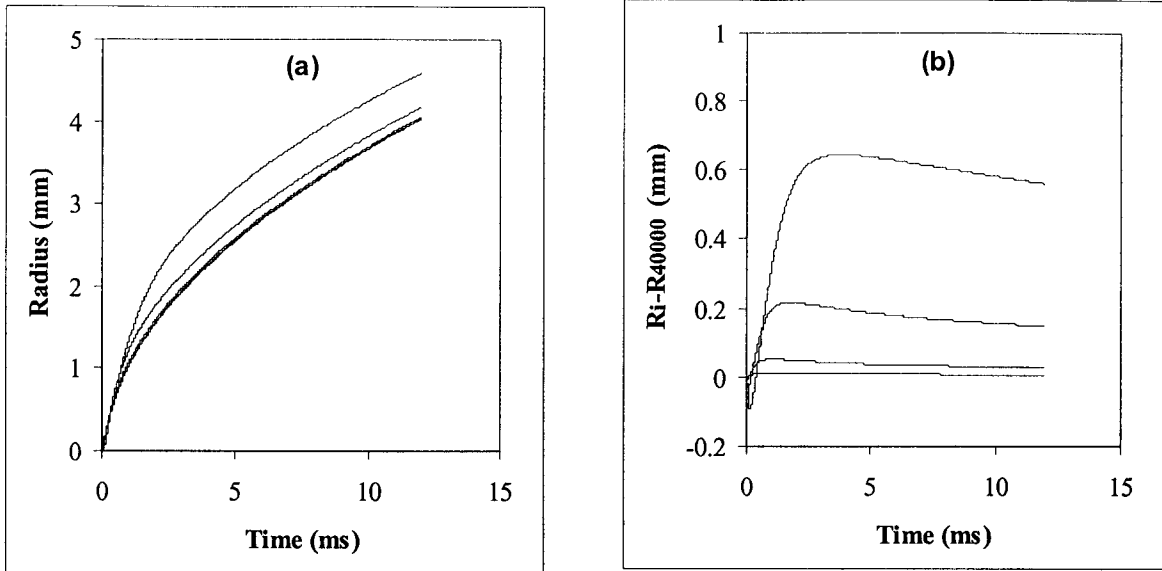
Figure 2.5: Case B; Water P=0.372 atm, ΔT_{sup}=6.3°C. Converging solution for grid points increasing from 5000 (top curves) to 40000 (bottom curves). a) Radius vs. time. b) Subtracted curves R_i-R_{40000}.
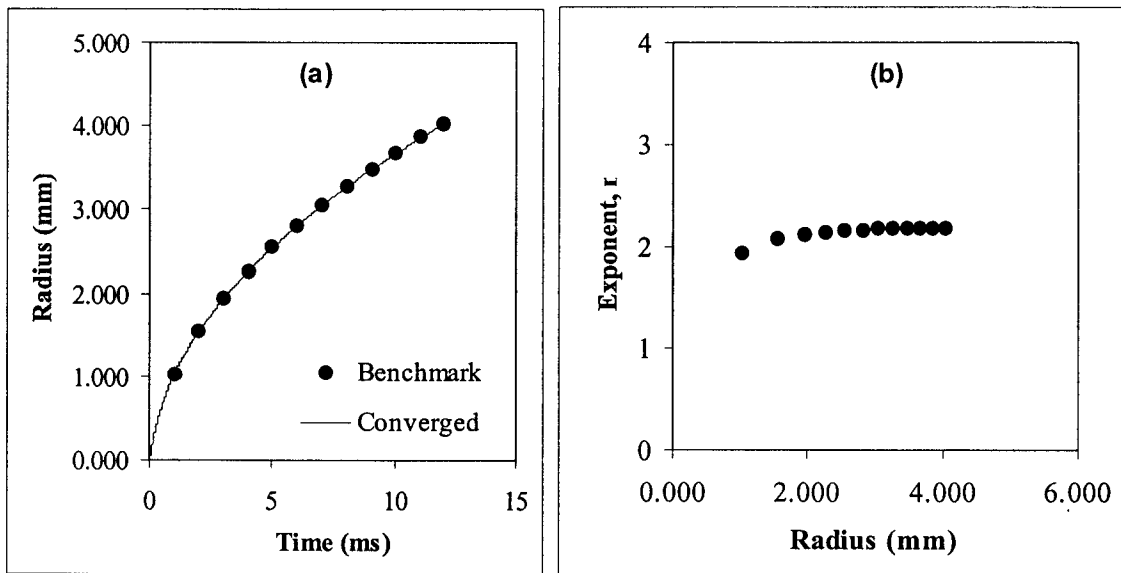
Figure 2.6: Case B; Water P=0.372 atm, ΔT_{sup}=6.3°C. a) Radius vs. time showing converged solution (M=40000) and the extrapolated benchmark solution. b) The exponent of Δr in equation (2.41).
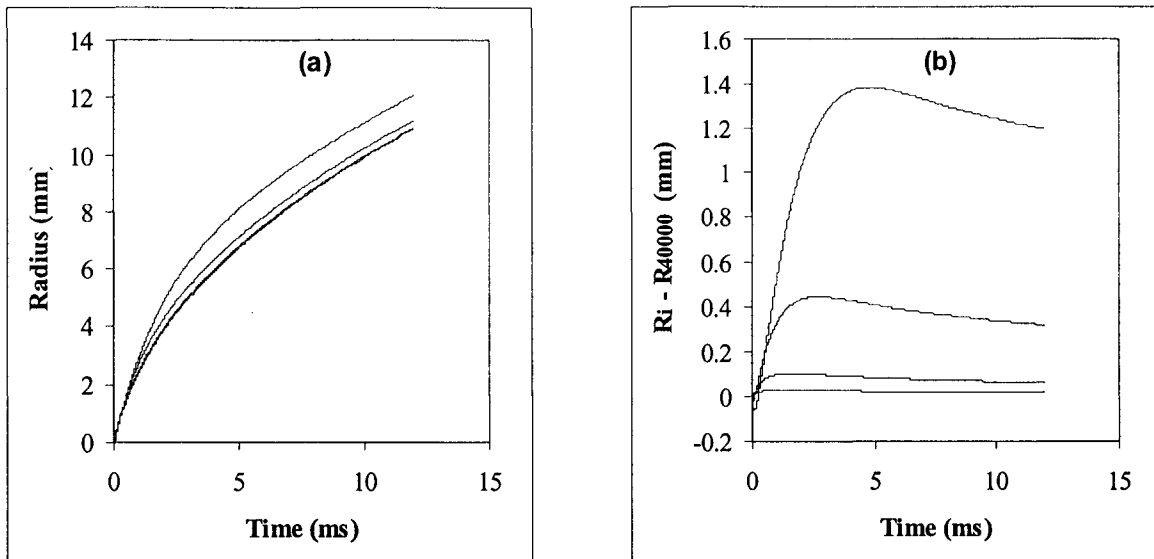
Figure 2.7: Case C; Water P=0.362 atm, ΔT_{sup}=17.0°C. Converging solution for grid points increasing from 5000 (top curves) to 40000 (bottom curves). a) Radius vs. time. b) Subtracted curves R_i-R_{40000}.
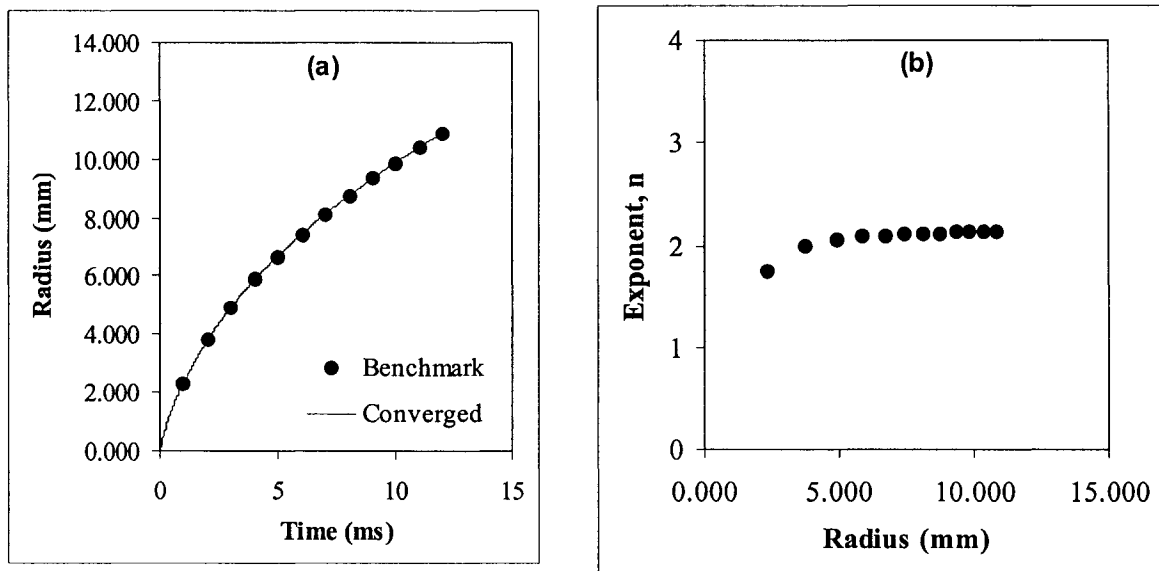
Figure 2.8: Case C; Water P=0.362 atm, ΔT_{sup}=17.0°C. a) Radius vs. time showing converged solution (M=40000) and the extrapolated benchmark solution. b) The exponent of Δr in equation (2.41).
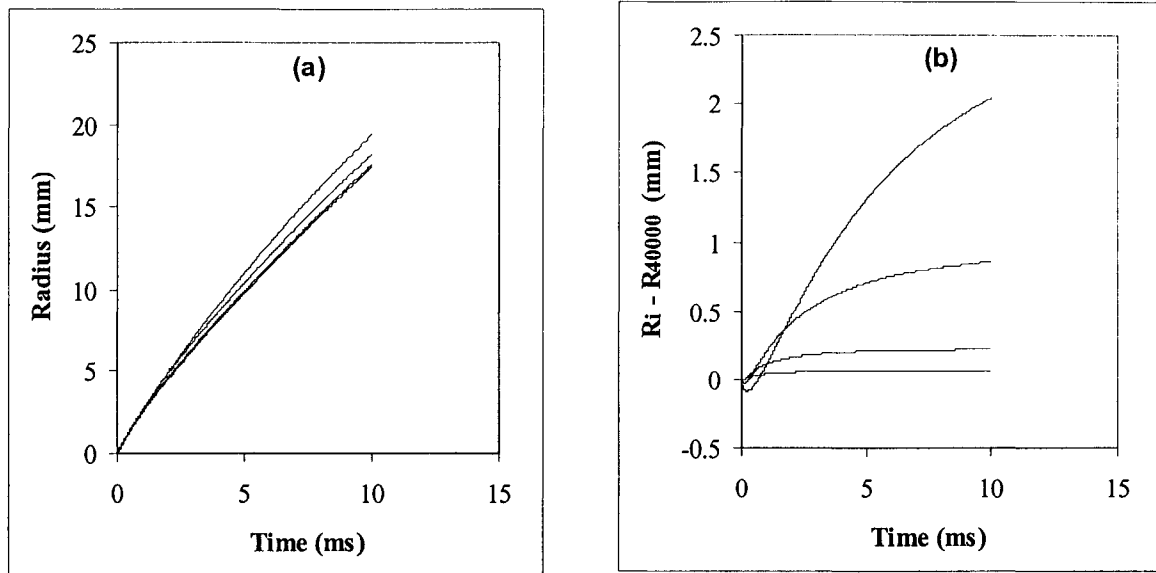
Figure 2.9: Case D; R113 P=0.0361 atm, ΔT_{sup}=48.1°C. Converging solution for grid points increasing from 5000 (top curves) to 40000 (bottom curves). a) Radius vs. time. b) Subtracted curves R_i-R_{40000}.
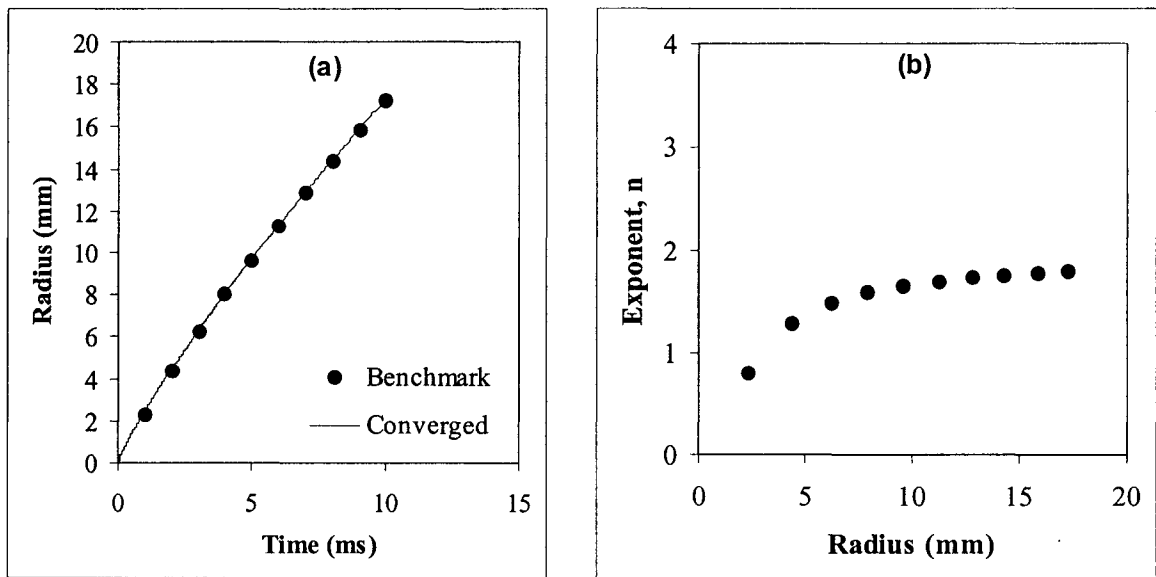
Figure 2.10: Case D; R113 P=0.0361 atm, ΔT_{sup}=48.1°C. a) Radius vs. time showing converged solution (M=40000) and the extrapolated benchmark solution. b) The exponent of Δr in equation (2.41).
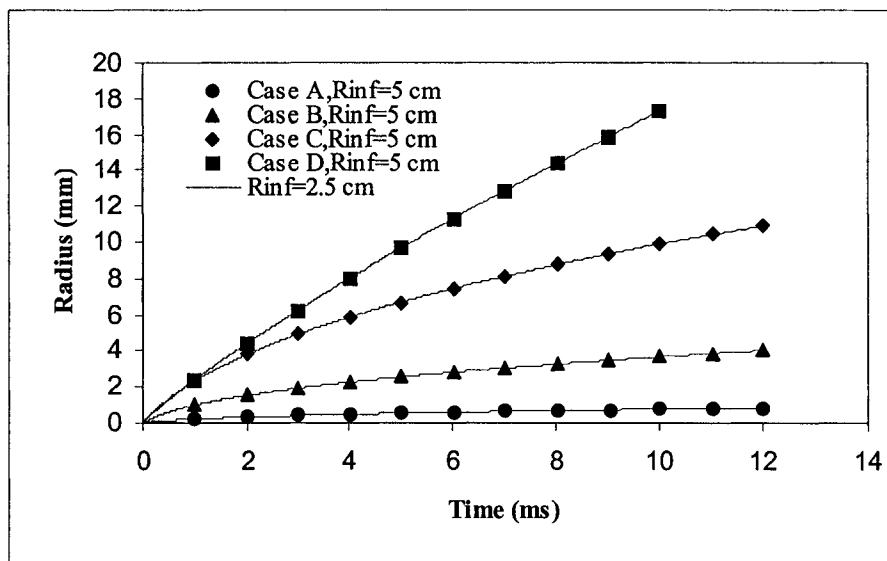
Figure 2.11: Converged growth curves (M=40000) for Case A, B, C and D showing that halving the magnitude of the far field boundary from R_{inf}=5 cm to R_{inf}=2.5 cm has no significant effect on the converged solution.
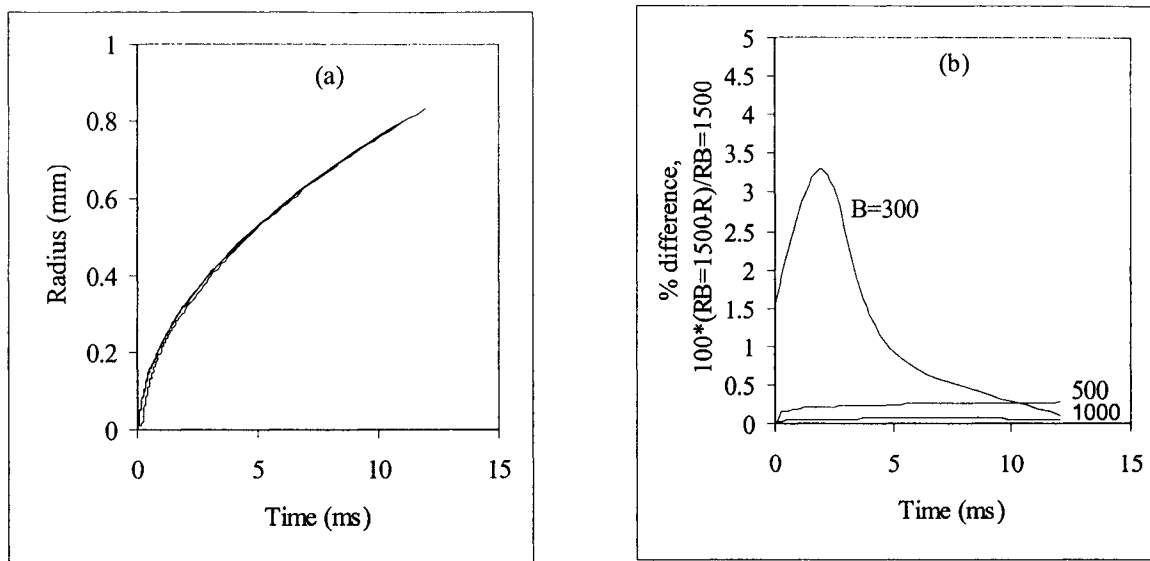
Figure 2.12: Case A; Water P=1.0 atm, ΔT_{sup}=3.1°C. Converging solution by refining the time step. a) Radius vs. time: From top to bottom, the curves correspond with B=300, 500, 1000, 1500 b) The percent difference between the computed curve and that obtained for B=1500
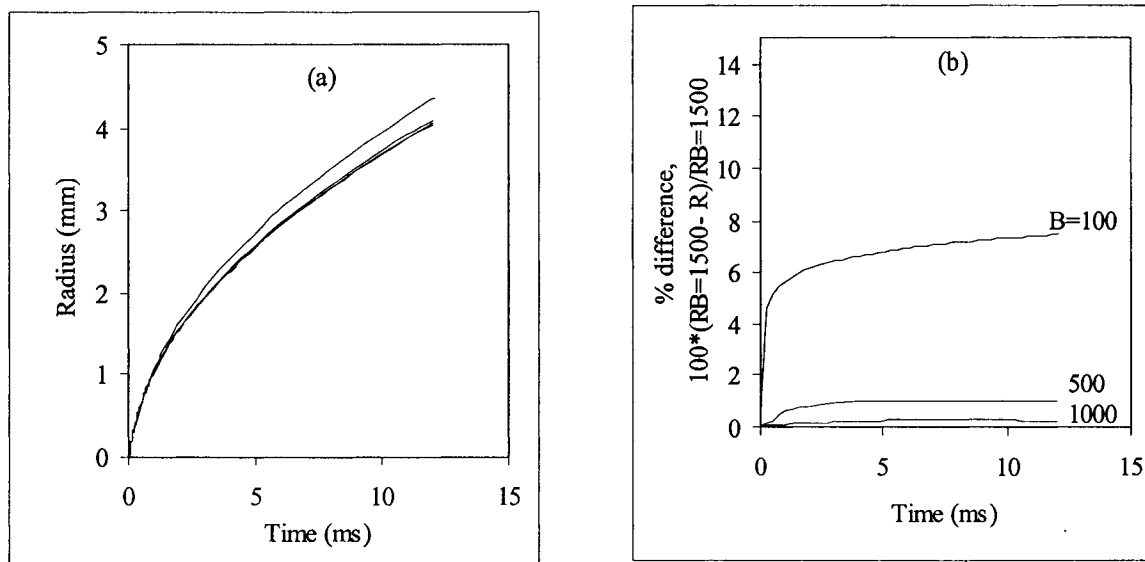
Figure 2.13: Case B; Water P=0.372 atm, ΔT_{sup}=6.3°C. Converging solution by refining the time step. a) Radius vs. time: From top to bottom, the curves correspond with B=100, 500, 1000, 1500 b) The percent difference between the computed curve and that obtained for B=1500
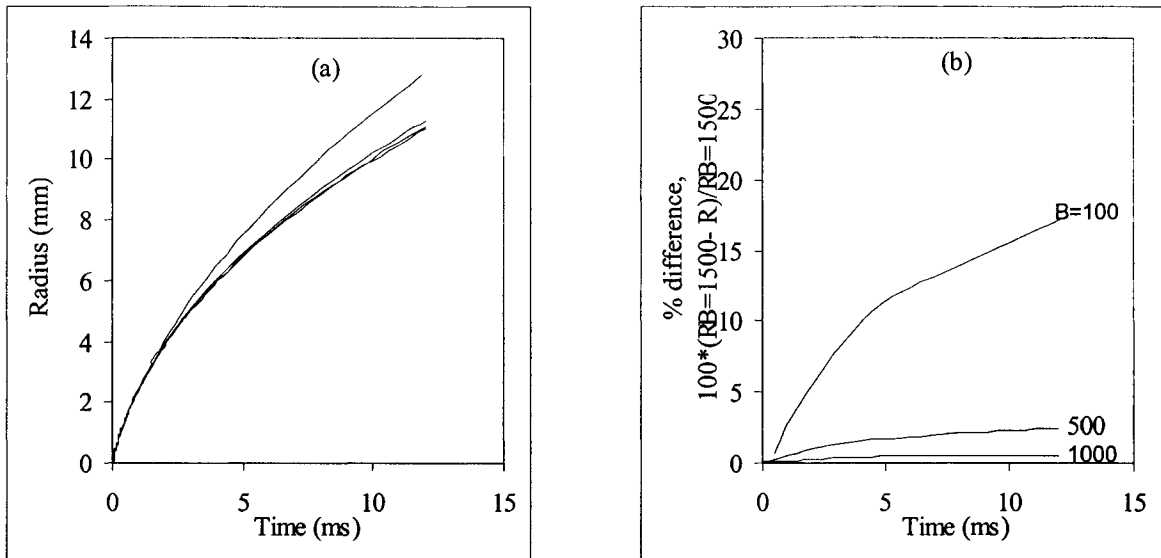
Figure 2.14: Case C; Water P=0.362 atm, ΔT_{sup}=17.0°C. Converging solution by refining the time step. a) Radius vs. time: From top to bottom, the curves correspond with B=100, 500, 1000, 1500 b) The percent difference between the computed curve and that obtained for B=1500
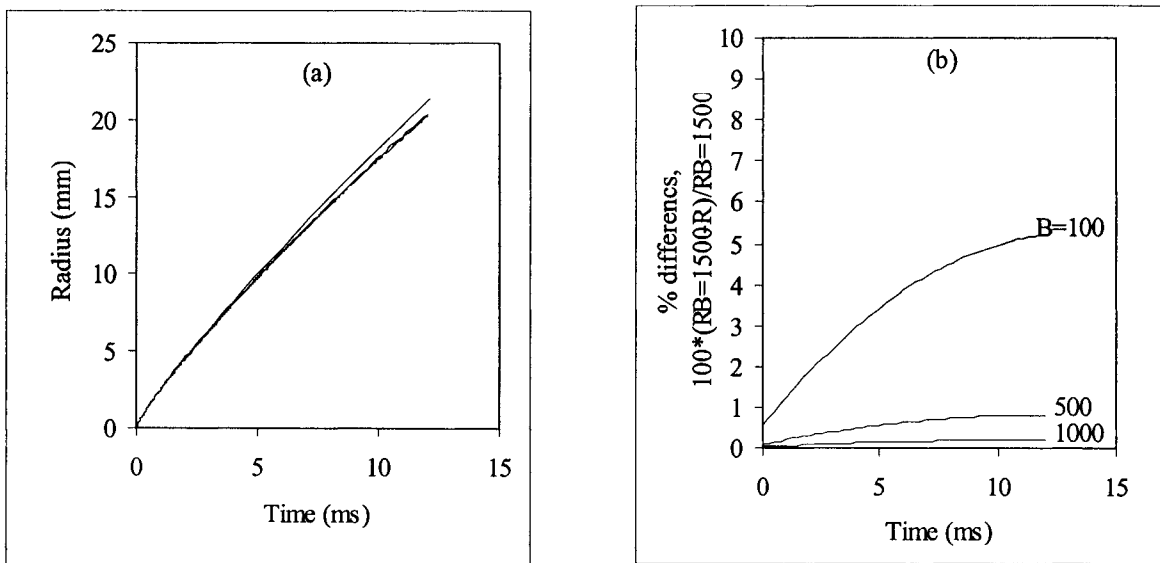
Figure 2.15: Case D; Water P=0.0361 atm, ΔT_{sup}=48.1°C. Converging solution by refining the time step. a) Radius vs. time: From top to bottom, the curves correspond with B=100, 500, 1000, 1500 b) The percent difference between the computed curve and that obtained for B=1500

51

1. $\Delta t = 1 \times 10^{-6}$s, $\Delta R = 5 \times 10^{-2}R_c$
2. $\Delta t = 1 \times 10^{-9}$s, $\Delta R = 5 \times 10^{-3}R_c$
3. $\Delta t = 1 \times 10^{-12}$, $\Delta R = 5 \times 10^{-6}R_c$

Radius (mm)

10

1

0.1

0.01

1

2

3

0.001   0.1   10   1000

Time (ms)
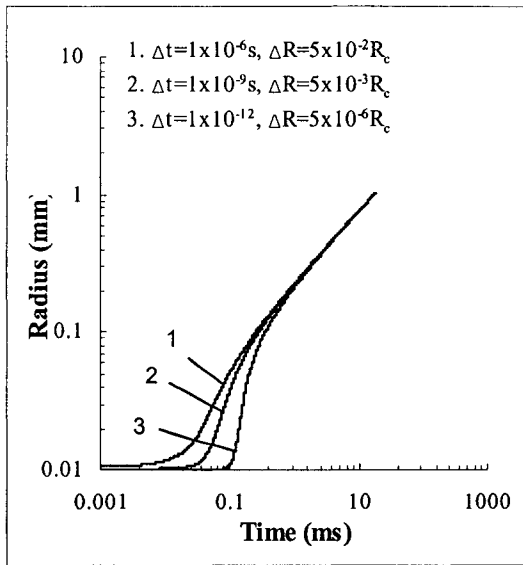
Figure 2.16: Case A: Effect of initial disturbance on growth curve.

Radius (mm)

10

1

0.1

0.01

1

2

3

1. $\Delta t = 1 \times 10^{-6}$s, $\Delta R = 5 \times 10^{-2}R_c$
2. $\Delta t = 1 \times 10^{-9}$s, $\Delta R = 5 \times 10^{-3}R_c$
3. $\Delta t = 1 \times 10^{-12}$, $\Delta R = 5 \times 10^{-6}R_c$

0.001   0.1   10   1000

Time (ms)
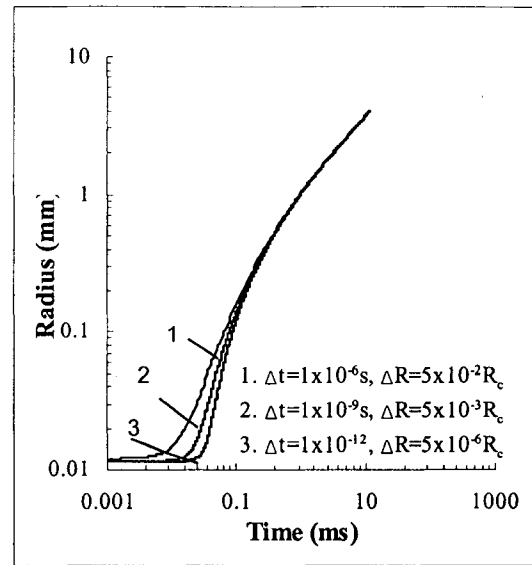
Figure 2.17: Case B: Effect of initial disturbance on growth curve

1. $\Delta t = 1 \times 10^{-6}$s, $\Delta R = 5 \times 10^{-2}R_c$
2. $\Delta t = 1 \times 10^{-9}$s, $\Delta R = 5 \times 10^{-3}R_c$
3. $\Delta t = 1 \times 10^{-12}$, $\Delta R = 5 \times 10^{-6}R_c$

Radius (mm)

100

10

1

0.1

0.01

0.001

1

2

3

0.0001   0.01   1   100

Time (ms)
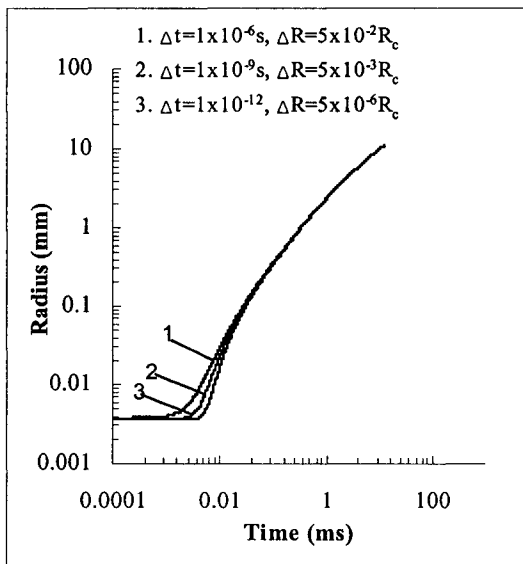
Figure 2.18: Case C: Effect of initial disturbance on growth curve

1. $\Delta t = 1 \times 10^{-6}$s, $\Delta R = 5 \times 10^{-2}R_c$
2. $\Delta t = 1 \times 10^{-9}$s, $\Delta R = 5 \times 10^{-3}R_c$
3. $\Delta t = 1 \times 10^{-12}$, $\Delta R = 5 \times 10^{-6}R_c$

Radius (mm)

100

10

1

0.1

0.01

0.001

1

2

3

0.00001   0.01   10   10000

Time (ms)
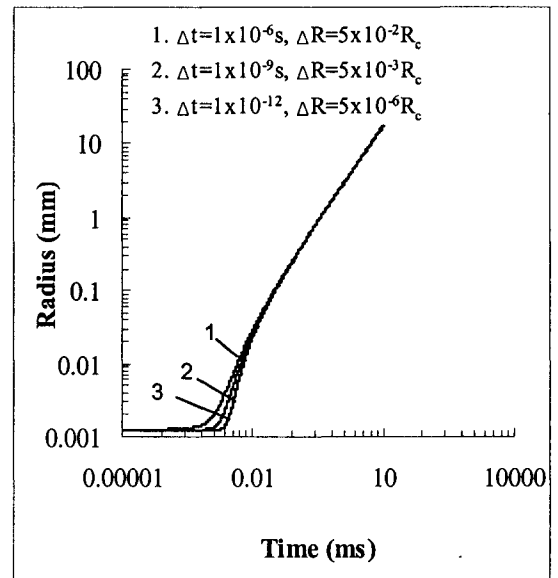
Figure 2.19: Case D: Effect of initial disturbance on growth curve
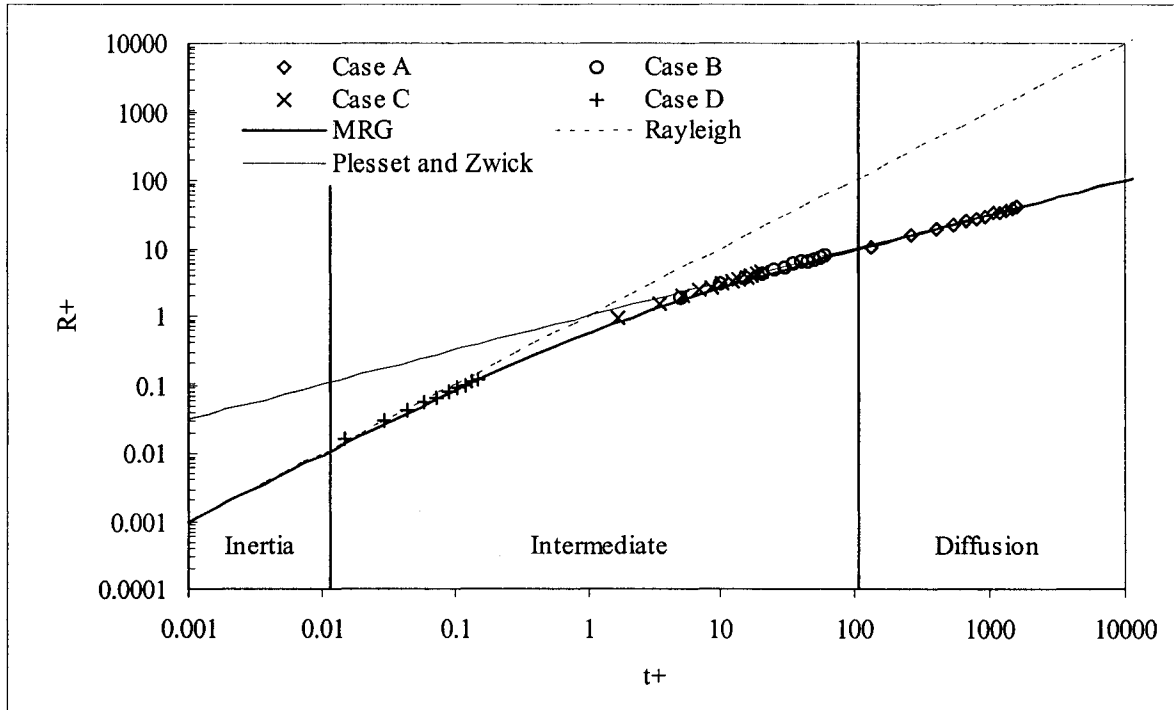
Figure 2.20: Comparison of the present work with the analytic works of Rayleigh [1917], Plesset and Zwick [1954] and Mikic *et al* [1970].
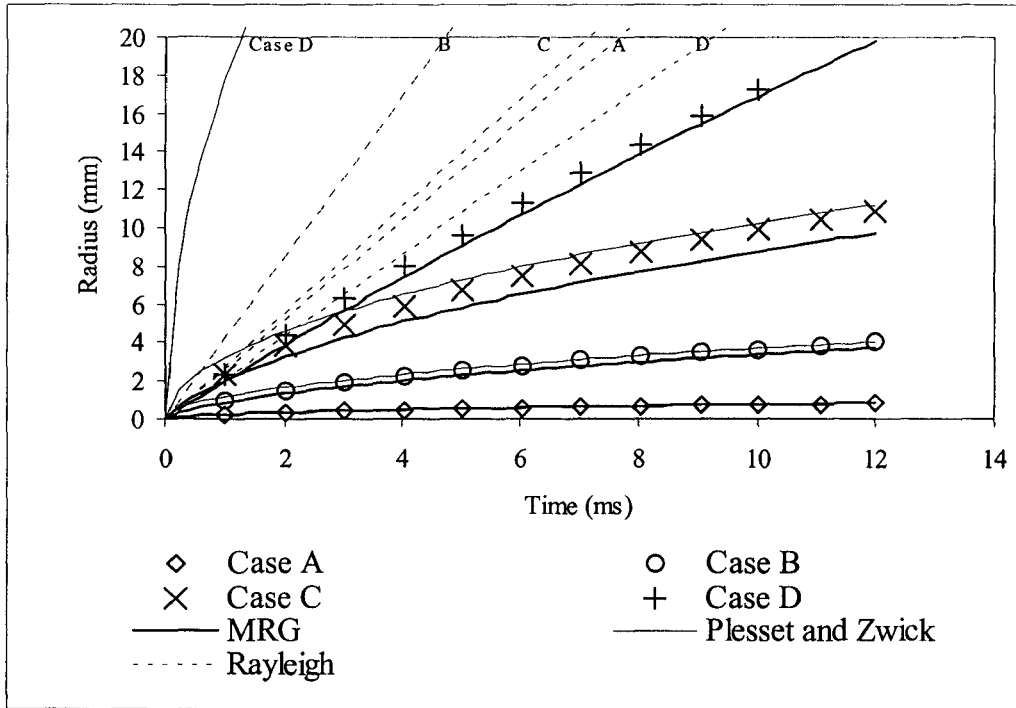
Figure 2.21: Comparison of the present work with the analytic works of Rayleigh [1917], Plesset and Zwick [1954] and Mikic *et al* [1970].
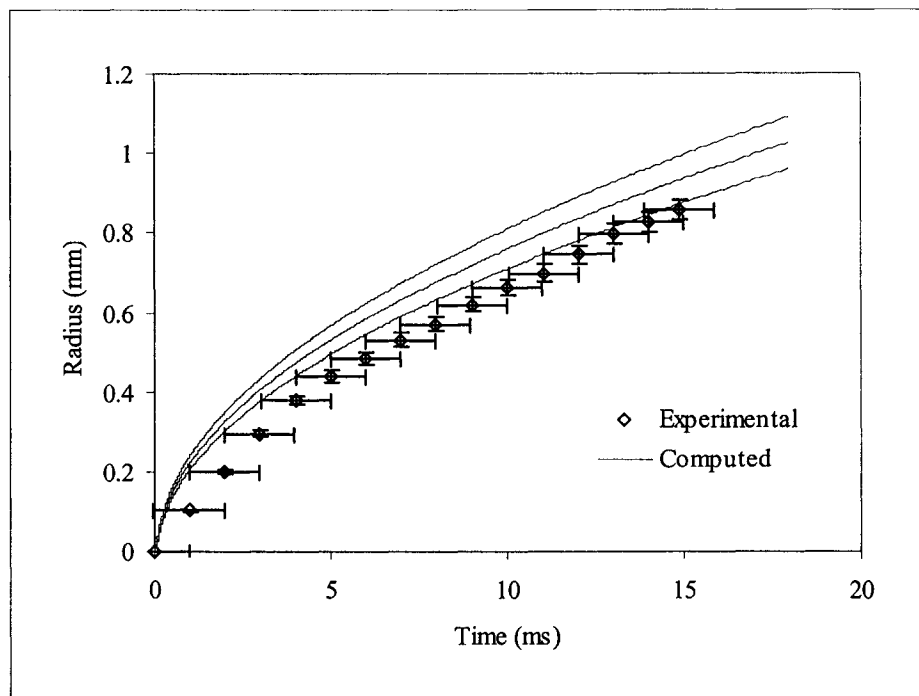
Figure 2.22: Comparison of converged solution with experiments of Dergarabedian [1953] for water at P=1.0 atm and ΔT_{sup}=3.1°C. The three computed curves depict the shift associated with an experimental error in superheat of ±0.2 °C.
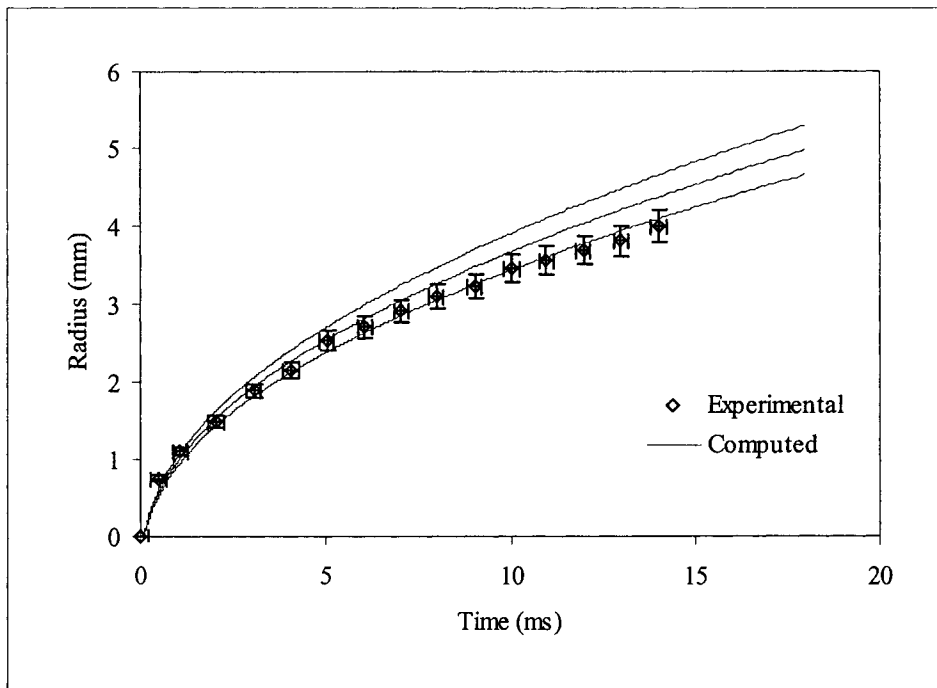
Figure 2.23: Comparison of converged solution with experiments of Board and Duffy [1971] for water at P=0.372 atm and ΔT_{sup}=6.3 °C. The three computed curves depict the shift associated with an experimental error in superheat of ±0.4 °C.
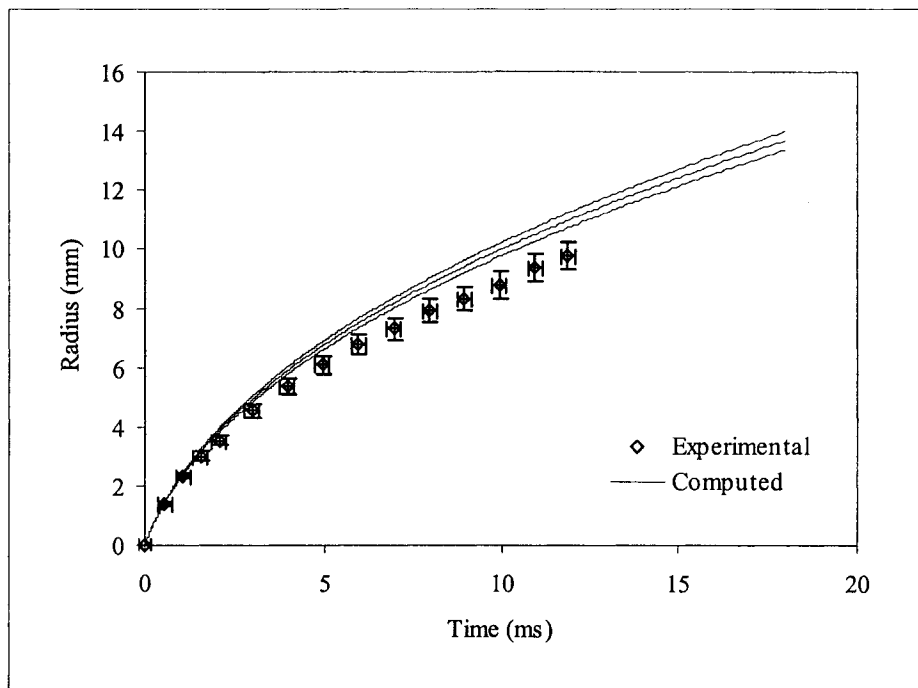
Figure 2.24: Comparison of converged solution with experiments of Board and Duffy [1971] for water at P=0.362 atm and ΔT_{sup}=17.0 °C. The three computed curves depict the shift associated with an experimental error in superheat of ±0.4 °C.
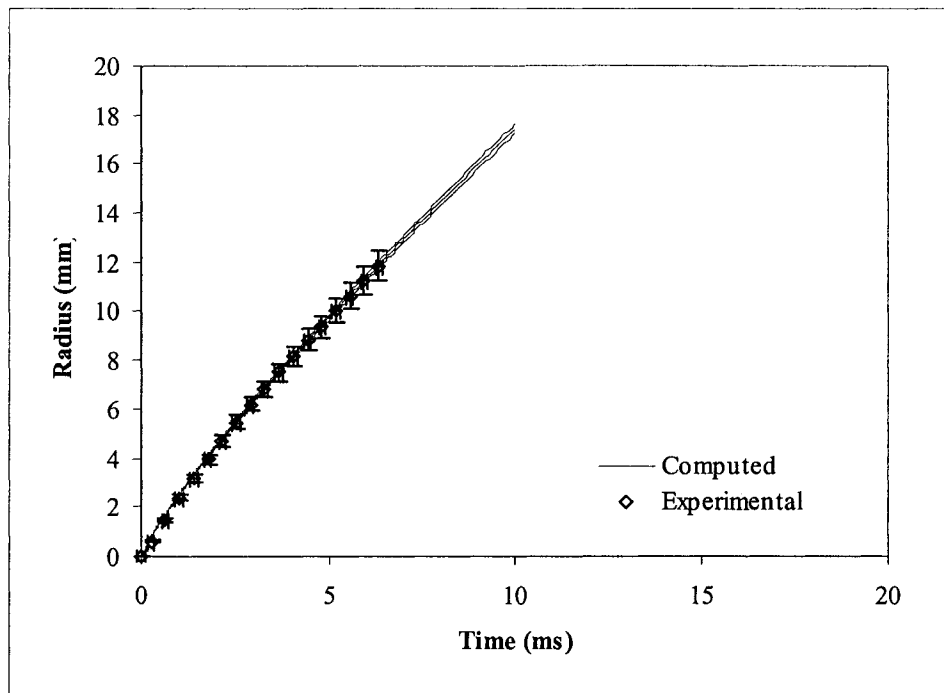
Figure 2.25: Comparison of converged solution with experiments of Bohrer *et al* [1973] for R113 at P=0.0361 atm and ΔT_{sup}=48.1 °C. The three computed curves depict the shift associated with an experimental error in superheat of ±0.96 °C.

Physical Domain

Computational Domain
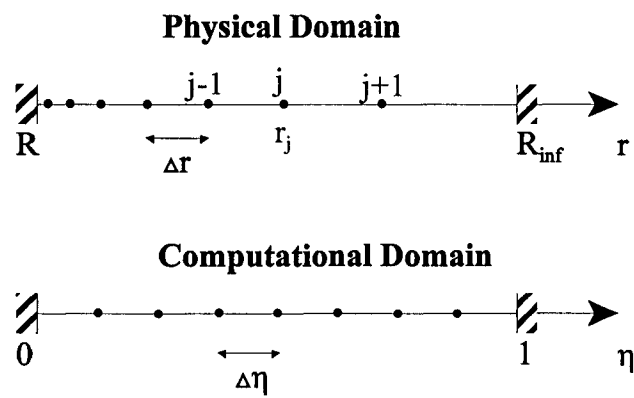
Figure 2.26: Physical and computational domain for the clustered grid solution.
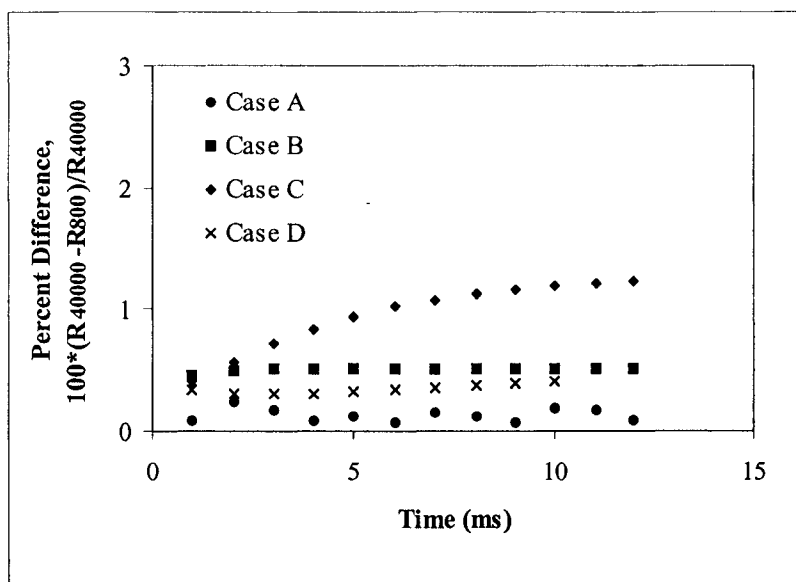
Figure 2.27: Relative difference between the converged solution obtained using the clustered grid arrangement with M=800 mesh points and the converged solution with uniform grid spacing and M=40000 mesh points.
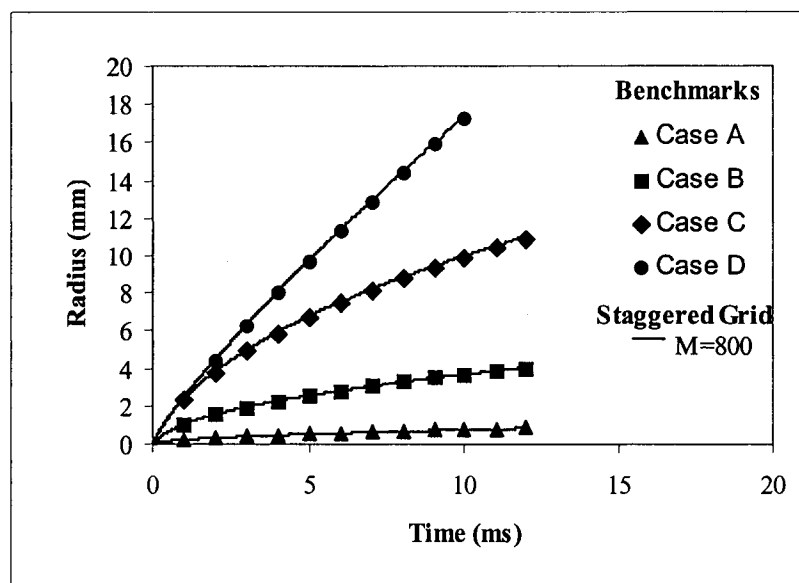
Figure 2.28: Comparison of the converged solutions obtained on a clustered grid and the benchmark solutions.
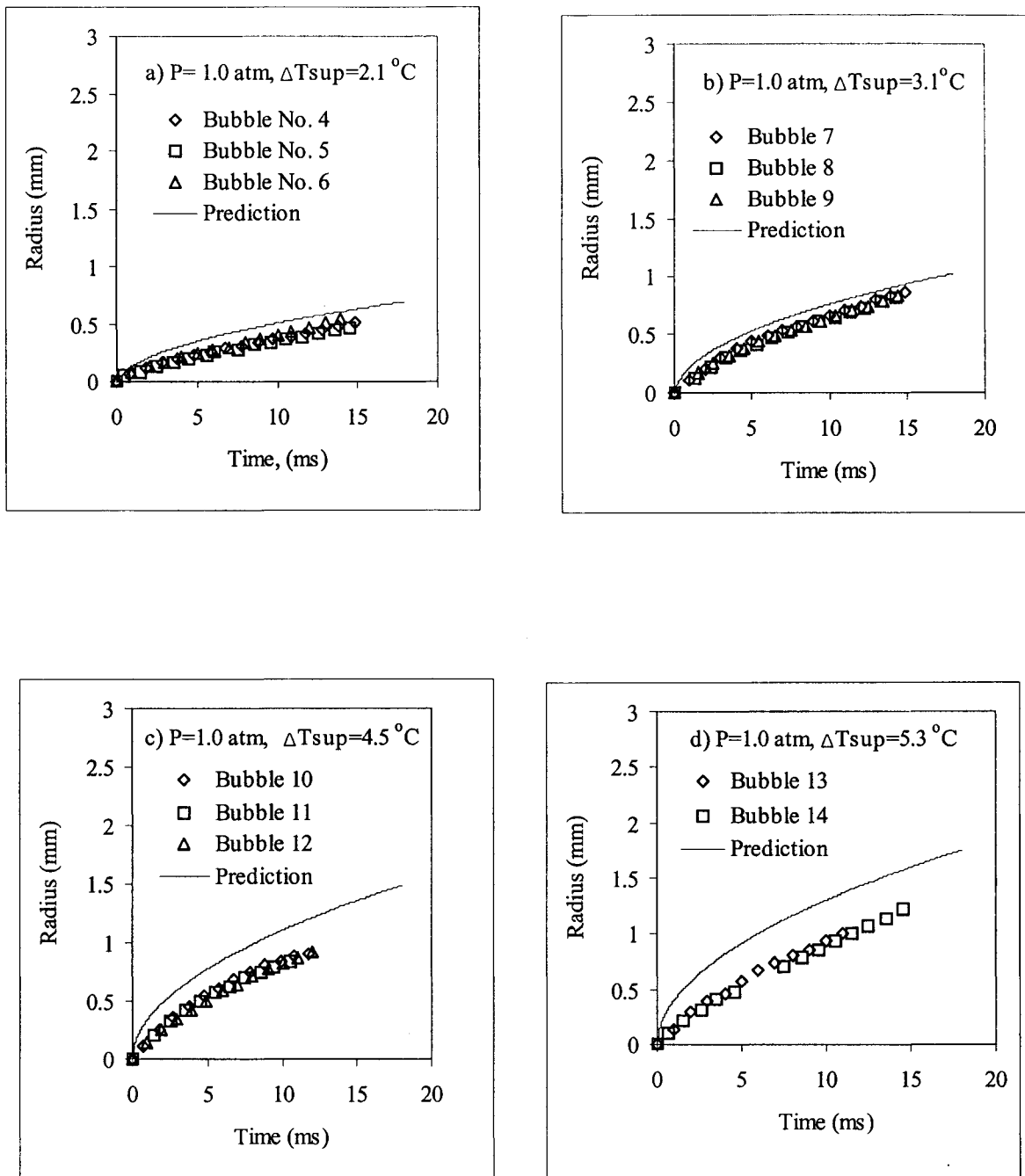
Figure 2.29: Comparison of present numerical calculations with measurements of Dergarabedian [1953] for water at atmospheric pressure at low superheats.
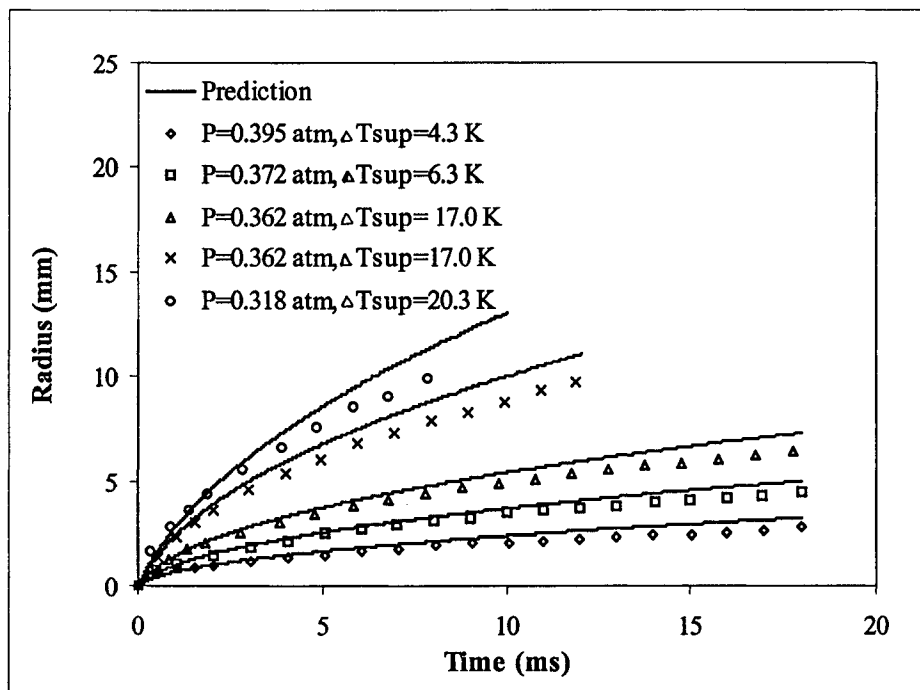
Figure 2.30:Comparison of present numerical calculations with measurements of Board and Duffy [1971] for water over a range of superheats.
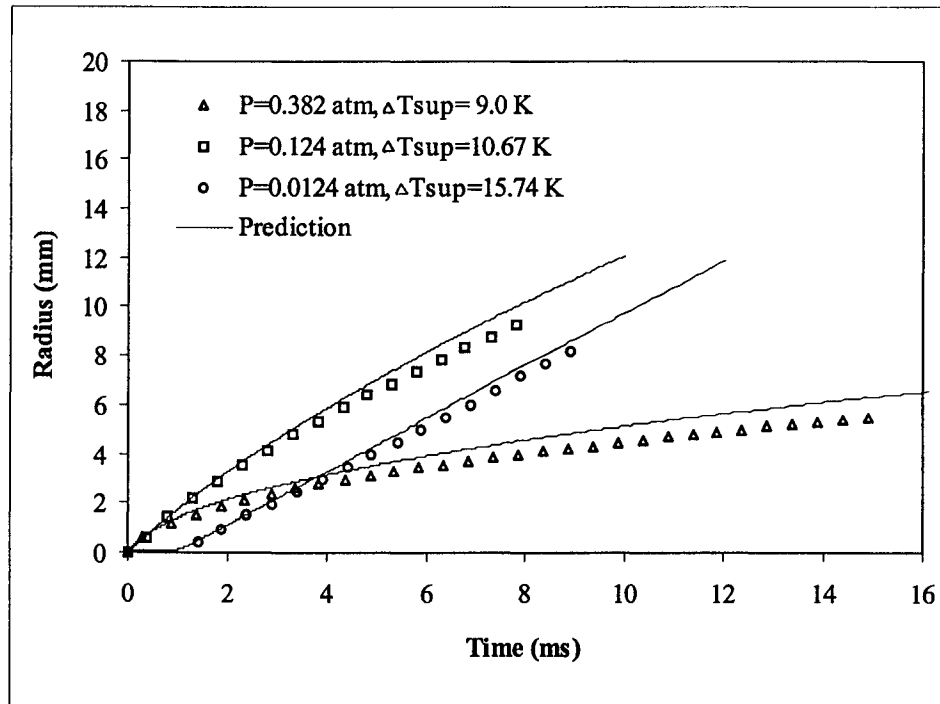
Figure 2.31: Comparison of present numerical calculations with measurements of Lien [1969] for water over a range of system pressures.
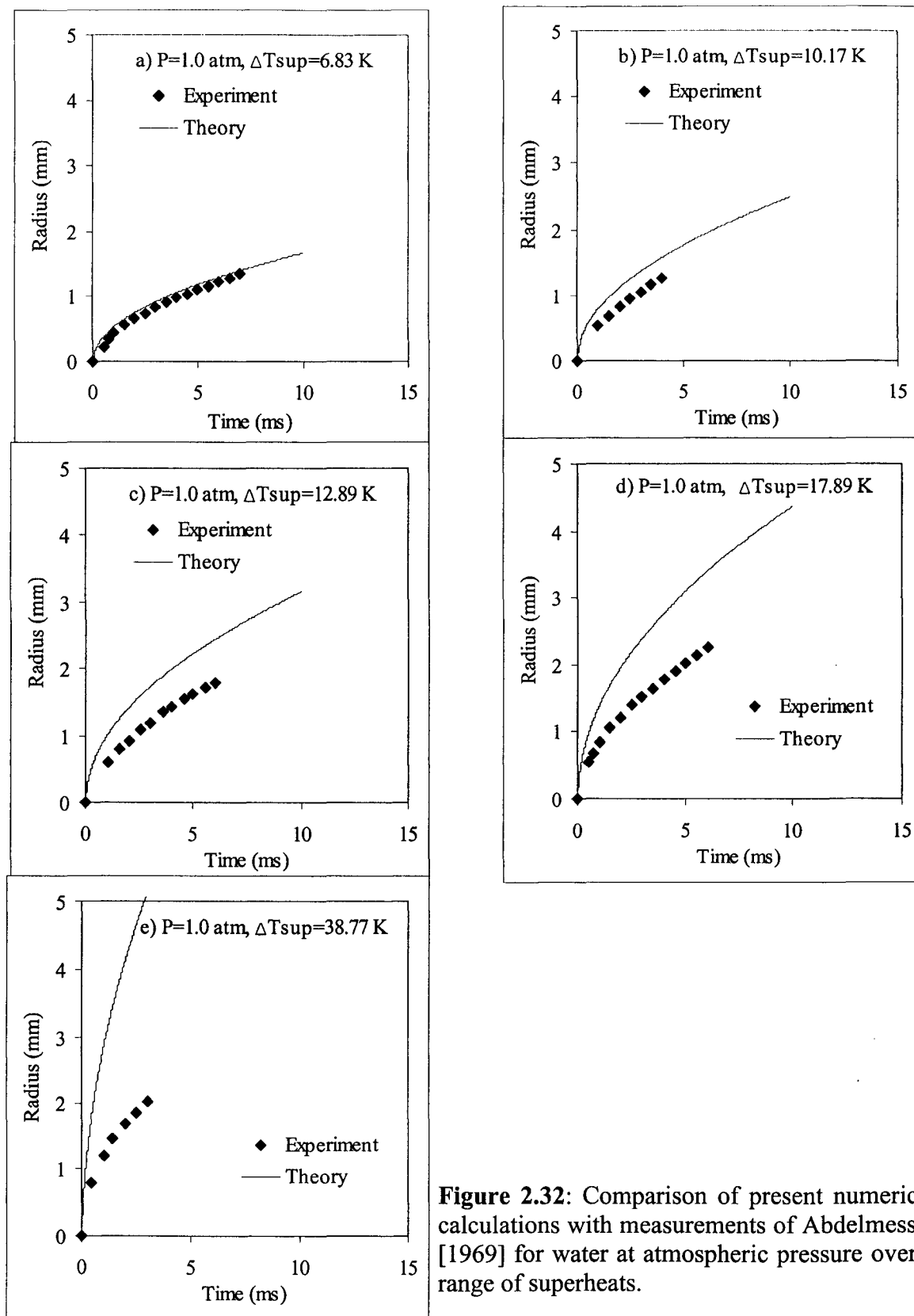
Figure 2.32: Comparison of present numerical calculations with measurements of Abdelmessih [1969] for water at atmospheric pressure over a range of superheats.
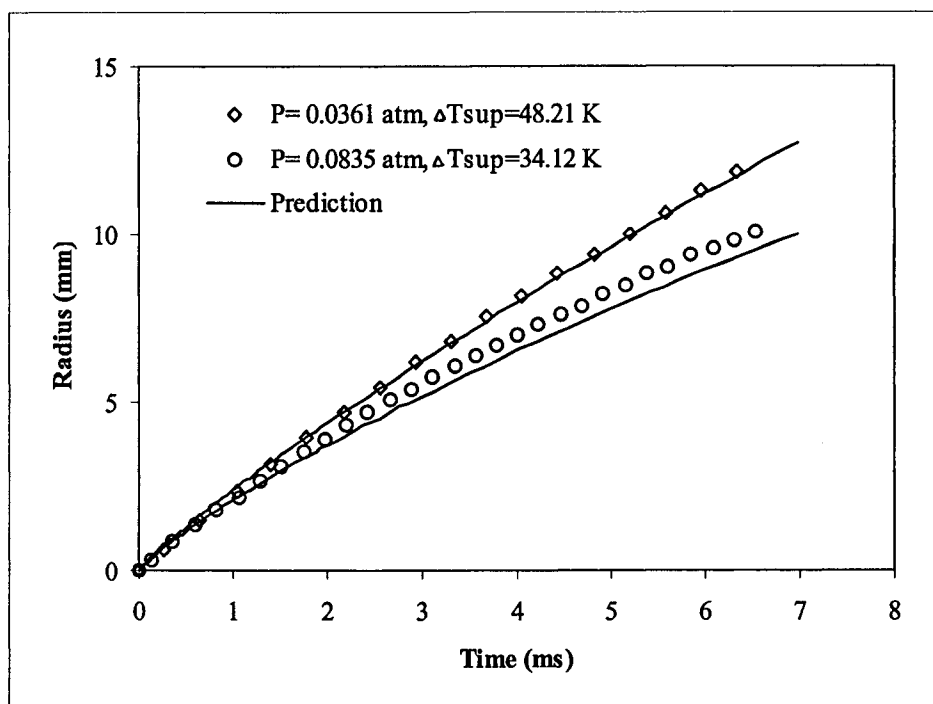
Figure 2.33: Comparison of present numerical calculations with measurements of Bohrer [1973] for R113 at low pressure and high superheat.

CHAPTER 3: HOMOGENEOUS BUBBLE GROWTH

BUBBLE GROWTH DYNAMICS

3.0 Introduction

In this chapter, spherical bubble growth in an initially uniformly superheated, unbounded liquid will be detailed. Because many of the fundamental mechanisms are the same, study of homogeneous bubble growth will offer insight into the mechanisms which are important in determining the growth characteristics of bubble growth near a heated surface.

Bubble growth dynamics will be discussed with focus on three separate but related topics. First, the characteristics of one bubble will be investigated in detail as it grows from a vapour nucleus through all the various growth stages until it is fully heat transfer limited. Utilizing the concepts developed for this single isolated bubble, the role that superheat plays during bubble growth will be considered by obtaining bubble data for a wide range of initial liquid superheats while keeping the ambient pressure constant. In a similar manner, the effect of varying the ambient pressure will be analysed by obtaining bubble growth data for a wide range of pressure while keeping the superheat constant.

3.1 Initial State

Bubble growth in a uniformly superheated unbounded liquid at constant pressure is

initiated by a phenomena called *homogeneous nucleation*. As described by Carey [1992], localized density fluctuations, often referred to as *heterophase fluctuations*, occur in the thermodynamically stable liquid. For a superheated liquid, a localized density fluctuation can become large enough to create a small region in which the density is reduced to almost that of the saturation vapour density. In this way, small vapour bubble 'embryos' are formed within the bulk liquid. Initially, the vapour embryo is in equilibrium with the surrounding liquid. The equilibrium state requires that both the temperature and chemical potentials of each phase be equal. Assuming a spherical vapour embryo, the initial state also requires that mechanical equilibrium be satisfied. This condition is provided by the well known Young-Laplace relation, which predicts an initial bubble radius given by,

$$R_c = \frac{2\sigma}{P_{ve} - P_\infty} \qquad (3.1)$$

where P_{ve} is the equilibrium vapour pressure and R_c is the critical vapour embryo radius. Utilizing the Second Law of Thermodynamics, Carey [1992] shows that the initial equilibrium state is unstable such that bubbles slightly larger than R_c will be subject to spontaneous growth.

The significance of the initial state of the vapour nucleus, with respect to theoretical modelling, is that it defines the minimum radius R_c, the maximum vapour temperature $T_{v,max}$, and the maximum vapour pressure, P_{ve}. Since the vapour and liquid are in thermal equilibrium, $T_{v,max}=T_\infty$. Furthermore, for cases of practical interest it is also reasonable to assume that the initial equilibrium vapour pressure is approximately equal to the saturation pressure corresponding to the liquid temperature $P_{ve}= P_{sat}(T_\infty)$. For example, water at

atmospheric pressure and 20°C superheat has an equilibrium vapour pressure of P_{ve}= 198.4 kPa and a saturation pressure of $P_{sat}(120°C)$=198.5 kPa (Carey [1992]). This slight difference becomes smaller at reduced system pressures.

3.2 Heat Transfer and Bubble Expansion

The initial thermal state of the vapour and liquid phase for a stationary critically sized vapour nucleus is depicted in Fig. 3.1. It is then assumed that the equilibrium condition is disturbed in such a way as to initiate bubble expansion opposed to bubble collapse. The disturbance can be a small fluctuation in pressure, density, temperature or radius (volume), the end effect of each being the same (Board and Duffy [1971]). If, for example, the radius is increased slightly, equation (3.1) states that the vapour pressure must decrease slightly as well. This will correspond with a decrease in the vapour temperature and thus the liquid temperature at the vapour-liquid interface. The thermal field for times after the initial disturbance is shown schematically in Fig. 3.2.

As a result of the decreased interfacial liquid temperature, a temperature gradient is established in the liquid which by Newton's Law of Cooling is responsible for a positive flux of energy, due to thermal diffusion, directed towards the interface,

$$q'' = -k_l \left(\frac{\partial T}{\partial r} \right)_{r=R(t)} \tag{3.2}$$

In the absence of significant compressibility effects, it is the perpetuation of the temperature gradient, and subsequent heat transfer to the interface, which sustains bubble expansion.

The interfacial energy balance equation can be developed by considering a control

volume with control surfaces immediately adjacent to the vapour-liquid interface. An energy balance gives,

$$\dot{m}_v'' h_v + \dot{m}_l'' h_l + q_{v,out}'' - q_{l,in}'' = 0 \tag{3.3}$$

where $\dot{m}_v''$ is the mass flux of vapour into the bubble, $\dot{m}_l''$ is the mass flux of liquid towards the bubble interface, h_v and h_l are the vapour and liquid enthalpies respectively, and q'' is the heat flux at the interface. The development of this expression, including all simplifying assumptions, can be found in Riznic *et al.* [1999]. Here it suffices to note that kinetic energy and viscous effects and the vapour motion and property variations are neglected. Continuity at the interface dictates that the mass flux of the vapour and liquid are related by,

$$\dot{m}_v'' + \dot{m}_l'' = 0 \tag{3.4}$$

This relationship, combined with the assumption of uniform vapour temperature such that $q_{out}'' = 0$ and that the heat transfer to the interface is by diffusion through the liquid results in the interfacial energy balance,

$$\dot{m}_v'' h_{fg} + k_l \left(\frac{\partial T}{\partial r} \right)_{r=R(t)} = 0 \tag{3.5}$$

Finally, the integral mass balance for the vapour bubble relates the mass flux into the bubble to the rate of change of mass within the volume through the equation,

$$\frac{dm_v}{dt} = -\int_A \dot{m}_v'' dA \tag{3.6}$$

Combination of equation (3.5) with equation (3.6) and rearrangement gives,

$$h_{fg}\frac{dm}{dt} = \int_A k_l \left(\frac{\partial T}{\partial r}\right)_{r=R(t)} dA \tag{3.7}$$

This equation explicitly states that the heat transfer by diffusion at the interface is directly responsible for the increase in the mass of the bubble. Assuming spherical symmetry and constant liquid properties, substitution of $m = \rho_v(^4/_3\pi R^3)$ results in the simplified expression for bubble expansion,

$$\frac{1}{3}h_{fg}R\frac{d\rho_v}{dt} + \rho_v h_{fg}\frac{dR}{dt} = k_l\left(\frac{\partial T}{\partial r}\right)_{r=R(t)} \tag{3.8}$$

Typically, compressibility effects are negligible such that,

$$\rho_v h_{fg}\frac{dR}{dt} \approx k_l\left(\frac{\partial T}{\partial r}\right)_{r=R(t)} \tag{3.9}$$

Therefore, the bubble expansion rate is proportional to the energy flux into the bubble by diffusion through the liquid. Because of this basic dependence, the growth of expanding bubbles will be discussed with particular focus on the how the dynamic coupling between the heat transfer and the flow dynamics determine the characteristics of growth as the bubble passes through the various growth regimes from inception to thermal diffusion controlled growth.

3.3 Bubble Dynamics

In the following sections, the growth characteristics of a single isolated spherical bubble expanding in a uniformly superheated unbounded liquid will be discussed. The liquid chosen is water and the boiling conditions selected are atmospheric pressure with an initial superheat of $\Delta T_{sup}=15\,^{\circ}C$. Fig. 3.3 shows the temporal variation of the predicted bubble radius and vapour temperature. In the figure, three regions of growth have been identified which will be discussed in turn. In Fig. 3.4, the energy equation for the vapour bubble, equation (3.8), has been decomposed to expose the time varying contributions of its constituent terms. From the figure, it is apparent that the term involving the rate of change of vapour density, $\frac{1}{3}h_{fg}R(d\rho_v/dt)$, is negligible compared with the interface velocity term, $\rho_v h_{fg}(dR/dt)$. Thus for discussion purposes, the growth rate can be considered proportional to the heat flux into the bubble throughout its growth,

$$\frac{dR}{dt} = \frac{k_l}{\rho_v h_{fg}} \left(\frac{\partial T}{\partial r} \right)_{r=R(t)} = \left(\frac{1}{\rho_v h_{fg}} \right) q'' \qquad (3.10)$$

As a result of the above relationship, it can be said that changes in the rate of heat transfer into the bubble are integrally connected to changes in bubble expansion. Furthermore, the interface acceleration is directly related to the time rate of change of the temperature gradient in the liquid at the interface. Assuming constant properties, the first derivative of equation (3.9) can be rearranged to give,

$$\frac{d^2R}{dt^2} \approx \frac{k_l}{\rho_v h_{fg}} \frac{d}{dt} \left(\frac{\partial T}{\partial r} \right)_{r=R(t)} \qquad (3.11)$$

In order to better conceptualize how changes in the interfacial temperature gradient affect bubble growth characteristics, the following simplification has been applied;

$$q'' \approx k_l \left(\frac{\Delta T(t)}{\delta(t)} \right) \qquad (3.12)$$

where $\Delta T(t) = T_\infty - T_v(t)$ is the effective temperature difference and $\delta(t)$ is the extrapolated thickness of the thermal boundary layer surrounding the bubble. The relevant details concerning the extrapolation technique for determining $\delta(t)$ are given in Appendix C. In this simplified view of heat transfer, the instantaneous heat flux into the bubble is determined by the driving temperature difference $\Delta T(t)$ and the thermal resistance to heat transfer $\delta(t)/k_l$. Each of these terms play a significant role with concern to bubble growth. For example, if $\Delta T(t)$ increases with time while $\delta(t)$ remains constant, then the bubble interface will accelerate ($d^2 R dt^2 > 0$). On the other hand, if $\delta(t)$ increases at a rate prescribed by the inequality,

$$\frac{d\delta}{dt} > \frac{\delta}{\Delta T} \frac{d}{dt}(\Delta T) \qquad (3.13)$$

then the interface will decelerate. Consequently, any mechanisms which act in such a way as to significantly influence the rate of change of $\Delta T(t)$ or $\delta(t)$ will have a bearing on the motion of the bubble interface.

In Fig. 3.5, the constituent components of the equation governing the motion of the interface, equations (2.1), are represented. In the figure, the driving pressure difference,

P_v-P_∞, is resisted by the stress in the interface through the surface tension term, $2\sigma/R$, and the hydrodynamic liquid pressure acting directly on the vapour-liquid interface, P_{hd}, defined as,

$$P_{hd} = \rho_l R \frac{d^2R}{dt^2} + \frac{3}{2}\rho_l\left(\frac{dR}{dt}\right)^2 \qquad (3.14)$$

The hydrodynamic pressure can be regarded as the excess pressure at the bubble interface that is a direct consequence of the bulk motion of the liquid. The total pressure in the liquid at the interface is related to the hydrostatic and hydrodynamic pressures through, $P_R = P_\infty + P_{hd}$.

3.3.1 Surface Tension Controlled Growth

The surface tension controlled domain exists in the region of time immediately after bubble growth is initiated. Generally, the surface tension controlled region is characterized by very slow changes in temperature, pressure and radius. These trends are illustrated in Fig. 3.3 and 3.5 where it is noticed that there is little change in the system variables during this region. Fig. 3.6 shows that the corresponding interface velocity and acceleration remain comparatively small for the early portion of the surface tension domain. Even still, energy is continuously being supplied to the bubble by diffusion through the liquid. This is evident from the positive value of q'' in Fig. 3.4b and the positive value of the temperature differential $\Delta T(t)$ shown in Fig. 3.7. However, the heat flux into the bubble, and thus the growth rate dR/dt, are small enough that the contribution of the hydrodynamic pressure in balancing the equation of motion is insignificant so that it essentially reduces to the static force balance, P_v-$P_\infty \approx 2\sigma/R$, as shown in Fig. 3.5a. Because P_∞ is constant, an increase in the

bubble radius must occur in conjunction with a decrease in P_v, which of course coincides with a proportional decrease in the vapour temperature, T_v. This is an important effect because, assuming thermal equilibrium, the decreasing vapour temperature represents a decreasing interface boundary temperature for the liquid. Because the liquid is essentially still, the decreasing interfacial liquid temperature acts to increase the interfacial temperature gradient, $(\partial T/\partial r)_{r=R(t)}$. Fig. 3.7 shows that the temperature difference driving the heat transfer to the interface, $\Delta T(t)$ is increasing with no significant change in the penetration depth of the thermal layer $\delta(t)$. This indicates that the observed increase in q'' is a result of the decreasing interfacial temperature and not due to thinning of the thermal layer. Thus it can be said that bubble growth in this domain is accelerated due to a positive thermal feedback effect in which bubble expansion (increasing R) is related to an increase in the driving temperature difference, $\Delta T(t)$. This causes an increase in the rate of diffusion to the vapour-liquid interface through the increase in the magnitude of the local temperature gradient, ($\sim \Delta T(t)/\delta(t)$),which feeds back by a proportional increase in the bubble growth rate, dR/dt.

In the earlier stage of the surface tension domain (t<0.002ms), the system is very near the initial equilibrium state provided that the initial disturbance is sufficiently small. Initially the temperature differential is of the order $O(\Delta T)\sim 10^{-6}$ °C which is still small enough that the expansion rate, and corresponding interface acceleration, are both small as compared with the maximum values shown in Fig. 3.6. Even still, minute changes in the bubble radius are sufficient to continually cause the temperature difference, $\Delta T(t)$, to increase as the surface tension stresses are relaxed causing P_v-P_∞ to decrease. Fig. 3.8 shows the curves for both $\Delta T(t)$ and $\delta(t)$ for the early stage of growth on a Cartesian plot. At approximately t=0.002 ms, the temperature difference begins to increase significantly. After

this point, d(ΔT)/dt increases dramatically as a direct consequence of the thermal feedback effect. In a relatively short time interval (0.002 ms$\leq$t$\leq$0.0036 ms), the driving temperature difference increases from nearly zero to almost 2 °C, which is significant. Fig. 3.6 shows that over the same time interval, the interface undergoes a drastic increase in acceleration. This is to be expected since for constant δ(t), the magnitude of the acceleration is proportional to the time rate of change of ΔT(t) through the expression,

$$\frac{d^2R}{dt^2} \propto \frac{1}{\delta}\frac{d(\Delta T)}{dt}$$

(3.15)

The peak value of the acceleration occurs at t=0.0036 ms and corresponds with the maximum rate of change of ΔT(t). As shown in Fig. 3.8, the slope ΔT(t) decreases after t=0.0036 ms. This is the point in time that the surface tension controlled growth domain is considered to end, referred to as the Onset of Significant Growth (OSG), and the bubble radius begins to increase considerably away from R_c as shown in Fig. 3.3. Once significant growth has begun, new mechanisms come into play which alter the dynamics of bubble growth.

3.3.2 Transition Domain

The transition domain occurs during the time interval beginning at the end of the surface tension controlled growth domain and ending when growth becomes limited by thermal diffusion. In this region, Fig. 3.5 shows that the pressure difference decreases from near its maximum value of $\Delta P \approx P_{sat}(T_\infty)-P_\infty$ to close to zero. Likewise the driving temperature difference ΔT(t) increases and approaches its maximum value corresponding with

$\Delta T = \Delta T_{sup} = 15\ ^\circ C$ as illustrated in Fig. 3.7. For the case selected, the transition region can be sectioned into two distinct subregions; the *intermediate region* where surface tension and inertial forces are both important and the *inertial region* where the hydrodynamic forces play a influential role in limiting bubble growth and surface tension forces do not.

3.3.2.1 Intermediate Region

As the bubble interface is accelerating radially outward, there comes a time when the effects of the bulk liquid motion outside the bubble are no longer insignificant. The intermediate domain is thus distinguished from the surface tension domain by the relative contributions of the surface tension term and the hydrodynamic pressure term in balancing the equation of motion. Fig. 3.5a shows that the excess pressure at the interface due to flow effects, P_{hd}, rises sharply at the beginning of this region and quickly becomes of the same order of magnitude as the surface tension term, $2\sigma/R$.

At the beginning of the intermediate region, the interface acceleration is near the maximum value of $d^2R/dt^2 \approx 3 \times 10^6\ m/s^2$, after which the magnitude of the acceleration begins to continually diminish and becomes zero at approximately $t=0.0068$ ms. This trend is shown in Fig. 3.6. Accordingly, q'' and dR/dt increase less rapidly and reach a maximum at $t=0.0068$ ms as shown in Figs. 3.4 and 3.6 respectively. The fact that the interface acceleration is decreasing signifies that there are mechanisms at work which tend to depress the thermal feedback effect. The most obvious is the fact that the expanding bubble now faces the additional resistance associated with forcing the bulk liquid out radially. The hydrodynamic pressure term rises sharply to become a significant term in the equation of motion and is responsible for a noticeable decrease in the rate at which the pressure

difference P_v-P_∞ is decreasing. The added importance of the fluid resistance is responsible

for large decrease in the slopes on both the P_v-P_∞ curves shown in Figs. 3.5 for t>0.004 ms.

Fig. 3.9 shows the influence of the hydrodynamic pressure more clearly. On this graph, the

actual pressure difference including the hydrodynamic term is plotted together with the

pressure difference which includes only surface tension. Initially the two curves are

essentially identical, such that relatively small increases in R(t) result in disproportionately

large increases in P_v-P_∞. However, at the onset of significant growth, the actual pressure

difference deviates markedly from the surface tension curve. Therefore, with the inclusion

of hydrodynamic forces, a much larger increase in radius is required to produce a like change

in P_v-P_∞ as compared with the case where hydrodynamic forces are not included. Because

changes in vapour pressure are analogous to changes in vapour temperature, the introduction

of hydrodynamic forces at the bubble interface will have a detrimental effect on the rate at

which the temperature difference $\Delta T(t)$ increases, thus depressing the thermal feedback

effect. This is the mechanism which is responsible for the observed decrease in the slope of

$\Delta T(t)$ in Figs. 3.7 and 3.8 for t>0.004ms. Furthermore, because $\delta(t)$ does not change

significantly and $d(\Delta T)/dt$ is decreasing, the magnitude of the acceleration must decrease

as predicted by equation (3.15) and shown in Fig. 3.6 for the time interval

0.0036 ms$\leq$t$\leq$ 0.0068 ms. Therefore, it can be said that the additional resistance of the fluid

plays an integral role in depressing the thermal feedback effect which causes the interface

acceleration to diminish.

3.3.2.2 Inertial Region

During the inertial growth stage, the pressure difference, P_v-P_∞, is primarily balanced

by the hydrodynamic pressure at the interface and surface tension forces are unimportant as shown in Fig. 3.5a and Fig. 3.9. The region is deemed inertial because the hydrodynamic forces play a role in determining the bubble growth characteristics and surface tension forces do not. It must be noted that this region is not necessarily 'inertia controlled' in the sense that the hydrodynamic forces are the limiting mechanism determining growth and the solution follows the Rayleigh solution given by equation 2.4. For realistic levels of superheat, truly inertial controlled growth only occurs at very low system pressures as will be discussed in Section 3.6.2.

As stated, the driving pressure difference is balanced by the hydrodynamic pressure acting at the bubble interface. The hydrodynamic pressure is comprised of two 'inertial' terms given in equation (3.14). These are the acceleration term, $\rho_l R(d^2 R/dt^2)$, and the velocity term, $^3/_2 \rho_l (dR/dt)^2$ which are plotted in Fig. 3.5b. The two terms have differing sign and thus tend to have an opposite influence on the total liquid pressure, and thus the force of the liquid on the bubble interface. The negative acceleration term accounts for the fact that the fluid body surrounding the bubble is decelerating causing outward force on the bubble surface. The velocity term is positive because the expanding bubble wall is effectively pushing the fluid outwardly. The reaction force of the liquid on the bubble wall is thus inwardly directed and must be of opposite sign. For t<0.1 ms, the magnitude of the velocity term is much larger than the acceleration term. However, for t>0.1 ms, the magnitudes of the two terms are comparable with the velocity term being slightly larger. In this way the overall influence of the hydrodynamic pressure is greatly reduced due to cancellation of the individual pressure terms.

The inertial growth domain is characterized by a decreasing heat flux and

decelerating interface as shown in Fig. 3.4 and 3.6 respectively. Inertial effects are regarded as being important because they influence the rate at which the vapour pressure and temperature drop by offering significant resistance to bubble expansion as compared with surface tension forces alone. Fig. 3.9 shows that with the added hydrodynamic pressure forces, the bubble must expand to a much larger radius in order for the pressure difference to diminish. In this respect, the momentum interactions of the bubble and the surrounding fluid have the effect of sustaining a significant pressure differential for a longer period of time. A consequence of this is that the rate at which the temperature difference increases, $d(\Delta T)/dt$,which tends to increase the rate of heat transfer, is slowed by the increased hydrodynamic pressure in the same way as described for the intermediate region discussed previously. Fig. 3.7 shows that the rate of change of $\Delta T(t)$ continually decreases approaching zero as it approaches the system superheat, $\Delta T_{sup}=15$ °C. However, this alone does not explain why the heat flux is decreasing in magnitude causing bubble expansion to decelerate considerably. The heat flux, q'', is decreasing because the positive influence that increasing $\Delta T(t)$ tends to have on the heat flux is not sufficient to compensate for the rate at which advection and conduction serve to decrease the temperature gradient at the interface by thickening the thermal boundary layer surrounding the bubble. Because there is significant fluid motion directed radially outward from the expanding interface, the cooler liquid from within the thermal layer penetrates deeper into the bulk of the liquid by advection. This, coupled with a net loss of thermal energy by conduction heat transfer out of the liquid and into the vapour bubble causes the the maximum temperature within the boundary layer to move further out from the bubble interface. Figs. 3.7 and 3.10 show that this portion of the transition region is identified by considerable growth of the thermal layer. Before this time,

the thermal layer thickness remained more or less constant at $\delta(t) \approx 3 \times 10^{-7}$ m. During this stage, however, the boundary layer has grown by nearly two orders of magnitude, $\delta(t=0.2 \text{ ms}) \approx 8.0 \times 10^{-6}$ m. The increasing thermal layer thickness is also depicted in Fig. 3.10 where the liquid temperature profiles are shown for various times during growth. The illustration shows that the maximum liquid temperature (≈ 115 °C) is moving further away from the vapour-liquid interface signifying thermal layer growth.

In summary, bubble expansion is decelerating considerably (decreasing q'') because the thickness of the thermal boundary layer is increasing much faster than the driving temperature difference is increasing. Because the rate at which $\Delta T(t)$ increases is significantly altered by the increased resistance of the fluid at the interface, this subregion of the transition domain is termed inertial. As will be discussed in succeeding sections, the relative importance of the liquid inertia depends on the superheat and system pressure.

3.3.3 Heat Transfer Controlled Growth

Heat transfer controlled growth refers to the interval of bubble growth in which the rate of bubble expansion is limited by the rate at which liquid is evaporated into the bubble, dictated by the rate of heat transfer through the liquid to the interface.

The heat transfer controlled growth domain is characterized by a decreasing heat flux and decelerating interface as shown in Fig. 3.4 and 3.6 respectively. In this domain, the pressure difference P_v-P_∞ has reduced to nearly zero (Fig. 3.5a and Fig. 3.9). As a result, liquid inertia and surface tension have a negligible influence on bubble growth because the rate at which P_v-P_∞ decreases no longer has a significant bearing on the rate at which the driving temperature difference $\Delta T(t)$ increases since it is approximately constant at 15 °C

according to Fig. 3.7. Consequently, the growth characteristics of this domain are determined solely by the thickening of the thermal boundary layer as a result the depletion of energy in the layer by conduction and the 'stretching' of the thermal layer by advection. The thickening of the thermal boundary layer with constant $\Delta T(t)$ is clearly illustrated in Fig. 3.10 where the liquid temperature profiles show that the interface temperature is approximately constant at $T_v=T_{sat}=100$ °C and the maximum liquid temperature is continually moving further out from the vapour-liquid interface. Likewise, Fig. 3.7 shows that the extrapolated thermal boundary layer thickness increases steadily with no significant change in $\Delta T(t)$. Also shown in the figure is the analytic expression for the thermal boundary layer thickness determined by Plesset and Zwick [1954] for a thin thermal boundary layer assumption, $\delta(t)=(^1/_3\pi\alpha t)^{1/2}$. The close agreement confirms the accuracy of the present solution as well as the applicability of using the extrapolated thermal boundary layer thickness, $\delta(t)$, for discussion purposes.

The choice for the time at which the heat transfer domain begins is somewhat arbitrary but must coincide roughly with $d(\Delta T)/dt \approx 0$. For this study it has been selected as the time at which $d(\Delta T)/dt \approx 0.5$ °C/ms. For the case shown, fully diffusion controlled growth begins at approximately $t \approx 0.4$ ms. Here $\Delta T(t)$ is within 2% of the maximum value prescribed by the system superheat ΔT_{sup}.

3.4 Effect of Superheat and System Pressure on Bubble Growth Dynamics

In the following sections, the effects of varying the level of superheat on bubble growth dynamics will be investigated by generating growth data for water at atmospheric pressure for the range of superheats 3°C $\leq \Delta T_{sup} \leq 30$ °C. The change in superheat

corresponds with a Jakob number range of $9.0 \leq Ja \leq 90$. Likewise, the effect of varying the system pressure will be detailed by considering growth data for water at a fixed superheat of $\Delta T_{sup} = 15\ ^\circ C$ and a system pressure range of $0.01\ atm \leq P_\infty \leq 5\ atm$. The range of system pressure corresponds with a Jakob number range of $10 \leq Ja \leq 3167$. The system conditions selected have been carefully chosen to represent the range of experimental bubble growth data available in the literature.

3.4.1 Surface Tension Domain

3.4.1.1 Effect of Increasing Superheat on Surface Tension Domain

Fig. 3.11 shows the growth curves for three levels of superheat, low ($\Delta T_{sup} = 3\ ^\circ C$), intermediate ($\Delta T_{sup} = 15\ ^\circ C$) and high ($\Delta T_{sup} = 30\ ^\circ C$). Concerning the surface tension growth domain, two trends are immediately apparent. First, the critical radius increases with decreasing superheat. Decreasing the system temperature results in a decrease in the initial vapour pressure $P_v = P_{sat}(T_\infty)$ causing R_c to decrease as predicted by equation (3.1) for constant P_∞. Fig. 3.12 shows a plot of the pressure difference versus radius for a stationary vapour bubble at equilibrium with the surrounding liquid. The relationship is obtained by rearranging equation (3.1) such that,

$$P_v - P_\infty = \frac{2\sigma}{R} \tag{3.16}$$

The critical radii for various degrees of superheat are also shown in the figure. Second, Fig. 3.11 indicates that the length of the *delay time*, t_{delay}, which is the time from the initial

disturbance to the onset of significant growth, increases substantially with decreasing superheat. As discussed in Section 2.3.1.5, the length of the delay time depends on the magnitude of the initial disturbance. However, as shown in Figs. 2.16 through 2.19, the order of magnitude of the delay time is not sensitive to the initial disturbance. As will be discussed, the order of magnitude of the delay time is related to the magnitude of the initial critical radius.

Considering the highest superheat case, $\Delta T_{sup}=30$ °C, the initial radius is small enough that it is located on the very steep downward sloping region of the curve in Fig. 3.12. Consequently, comparatively small increases in radius result in a disproportionately large increase in the vapour over- pressure, P_v-P_∞. A reduction in superheat causes R_c to increase and move to a region of the curve which becomes progressively less steep. This means that a larger increase in radius is now required to produce a like change in P_v-P_∞ and thus the driving temperature for heat transfer $\Delta T(t)$. This has an important bearing on the thermal feedback effect which is responsible for accelerating growth in this region. Recall that the thermal feedback effect denotes that an increase in $R(t)$ produces an increase in the temperature difference $\Delta T(t)$ due to a decrease in the vapour pressure. The response is an increase in the growth rate, dR/dt, because the elevated temperature difference increases the magnitude of the interfacial heat flux q''. For smaller initial bubble radii (higher superheat) the thermal feedback effect is intensified because a much smaller increase in radius is required to escalate $\Delta T(t)$. Consequently, the time that it takes for the temperature difference to increase substantially from zero is expected to be less for smaller initial radii. This is the mechanism which is likely responsible for the observed decrease in the delay time for decreasing system superheat.

Fig. 3.13 shows this effect clearly. In this figure, the temperature difference curves, $\Delta T(t)$, are shown for the range of superheat 5 °C$\leq\Delta T_{sup}\leq$30 °C. For ΔT_{sup}=5 °C, changes in $\Delta T(t)$ occur at a considerably slower rate as compared with the other three cases shown. As a result, the surface tension domain is prolonged because of the decreased thermal feedback. Increasing the superheat causes the $\Delta T(t)$ curves to become progressively more steep which amplifies the thermal feedback and reduces the delay time.

An order of magnitude approximation of the variation of the delay time with changing system superheat can be obtained by assuming that the time it takes for the thermal feedback effect to generate a significant driving temperature difference is related to the time it takes the system to react to a change in its thermal environment as characterized by the thermal time constant, t_c. With this assumption, the delay time can be scaled as $t_{delay} \sim t_c = L_c^2/\alpha$. The characteristic length scale for the system is defined by a sphere of radius R_c such that $L_c \sim \frac{1}{3}R_c$. These physical arguments result in an order of magnitude prediction of the delay time given by,

$$t_c = \frac{L_c^2}{\alpha} = \frac{1}{9\alpha}\left(\frac{2\sigma}{P_v - P_\infty}\right)^2 \tag{3.17}$$

where $L_c = \frac{1}{3}R_c$ and equation (3.1) has been substituted for R_c. Equation (3.17) is plotted in Fig. 3.14 and shows surprisingly good quantitative agreement with the predicted delay times of this work and those of Lee [1993]. In this simplified view, the delay time varies as the inverse square of the initial pressure differential, causing the delay time to diminish rapidly with increased superheat since $P_v = P_{sat}(T_\infty)$.

The end of the surface tension domain occurs at the onset of significant growth

which, as discussed earlier, corresponds with the maximum interface acceleration. Fig. 3.15 shows a plot of the interface acceleration for the various levels of superheat. It is evident that not only does the peak shift to larger values of time for decreasing superheat, but the magnitude of the peak acceleration decreases markedly. The increased magnitude of the peak acceleration with increasing superheat is also a direct consequence of the intensified thermal feedback, associated with the smaller initial bubble radii, which tends to drive the temperature difference $\Delta T(t)$ up at a greater rate for higher system superheat levels. For each superheat tested, the thermal layer thickness remained more or less constant during the respective surface tension controlled growth domain. Consequently, the magnitude of the interface acceleration is proportional to $d(\Delta T)/dt$ and inversely proportional to the thermal layer thickness $\delta(t)$ as predicted by equation (15). As shown in Fig. 3.13, the maximum rate of change of $\Delta T(t)$ decreases significantly for the superheat range shown. Between $\Delta T_{sup}=30°C$ and $\Delta T_{sup}=5°C$ there is a two order of magnitude decrease in $d(\Delta T)/dt|_{max}$, 1.56×10^4 °C/ms$\rightarrow1.88\times10^2$ °C/ms, respectively. This accounts for the two order of magnitude decrease in the peak acceleration shown in Fig. 3.15 for the same superheat range, $d^2R/dt^2|_{max}\approx1.8\times10^7m/s^2\rightarrow1.1\times10^5$ m/s^2, respectively.

3.4.1.2 Effect of Increasing Pressure on Surface Tension Domain

Fig. 3.16 shows the growth curves for a wide range of system pressures for a constant superheat of $\Delta T_{sup}=15$ °C. In the figure, it is evident that the initial critical radius decreases substantially with increasing system pressure as predicted by equation (3.1) given $P_v=P_{sat}(T_\infty)$. The initial critical radius influences the delay time in the same way as discussed

above where smaller critical radii are identified with smaller delay times as a result of intensified thermal feedback and an ability to react quickly to changes in its thermal environment. Fig. 3.17 shows acceptable agreement between the predictions of equation (3.17) and those of the numerical simulations for a wide range of system pressures, especially considering that the smaller values of t_{delay} are more sensitive to the magnitude of the initial disturbance.

Figure 3.18 shows that the magnitude of the peak acceleration decreases considerably with decreasing system pressure. Once again, this can be attributed to the intensified thermal feedback for smaller initial radii as discussed previously.

3.4.2 Transition Domain

The transition domain is the interval during bubble growth over which the vapour over-pressure, P_v-P_∞, drops from near its maximum equilibrium value to nearly zero. Likewise, the driving temperature difference for heat transfer, $\Delta T(t)$, increases to its maximum value of ΔT_{sup}. The rate at which the vapour pressure and temperature drop can be influenced by the momentum interactions of the liquid with the expanding interface through an increase in the hydrodynamic pressure acting at the interface. To better understand this, it is prudent to examine the two extreme cases, the case where hydrodynamic forces are small enough to have a negligible influence on the rate of expansion such that the limiting mechanism of growth is *heat transfer* and the case where hydrodynamic forces can be so large that expansion is limited by liquid inertia effects such that heat transfer plays a passive role, the so called *inertia controlled* growth domain.

Between these two extremes, bubble growth is governed by a combination of both liquid inertia and heat transfer.

3.4.2.1 Heat Transfer Limited Transition Domain (Low Superheats)

For low enough superheats, the inertial stage of growth is never truly reached. Here surface tension limited growth passes directly into a heat transfer limited growth phase.

The temporal variation of the interface velocity for Ja=9.0 (P_∞=1.0 atm, ΔT_{sup}=3.0°C) is shown in Fig. 3.19. For the low Jakob number case under consideration, the maximum velocity, which can be considered the characteristic velocity for the transition phase of growth, is approximately U_c=0.42m/s. This velocity is considerably less than the maximum velocity which would be characteristic of inertia limited growth as predicted by the Rayleigh solution,

$$U_{c,I} \sim \sqrt{\frac{2(P_{sat}(T_\infty)-P_\infty)}{3\rho_l}} \approx 3.0\,m/s \qquad (3.18)$$

The fact that $U_{c,I} \gg U_c$ indicates that liquid inertia is not the mechanism that is limiting the growth rate in this region

Fig. 3.20 shows the temporal variation of the vapour over-pressure, P_v-P_∞,whereas Fig. 3.21 shows the over-pressure variation with increasing bubble radius. In these figures it is clear that the inertial effects, as made manifest by the hydrodynamic pressure, P_{hd}, are so small that they have no significant influence on the rate at which the vapour pressure

drops during the transition domain. Here expansion is uninhibited by the surrounding liquid and the vapour and liquid remain in a quasi-steady equilibrium state prescribed by the mechanical balance of pressure and surface tension, P_v-P_∞≈$2\sigma/R$. The rate at which the pressure decreases depends on the rate at which the bubble expands through the inverse relationship with radius (Fig. 3.21). Since there are no other mechanisms present to promote or restrict growth, the rate at which the radius increases is governed solely by the rate at which energy is transported by diffusion through the liquid to the interface since dR/dt∝q''. Referring to Fig. 3.21, near the onset of significant growth, a significant pressure drop occurs in conjunction with a comparatively small increase in radius. From an order of magnitude analysis, it can be assumed that a pressure drop of the order ΔP~$2\sigma/R_c$ occurs without a significant change in the characteristic length L_c~$R_c/3$. The maximum velocity which characterizes diffusion limited growth can be predicted by,

$$U_{c,HT} \sim \frac{k}{\rho_v h_{fg}} \left(\frac{T_{sup}}{L_c} \right) \approx 0.49 \, m/s \qquad (3.19)$$

which is close to the actual maximum value of 0.42 m/s (see Fig. 3.20), confirming that the mechanism responsible for regulating the growth rate during the transition region is heat transfer.

3.4.2.2 Inertia Limited Transition Domain

For high enough superheats, the rate of bubble expansion becomes regulated by the ability of the interface to 'push back' the surrounding liquid.. Here the surface tension

limited growth region passes directly into an inertial limited growth region.

Fig. 3.22 shows the temporal variation of the vapour over-pressure, P_v-P_∞, and

Fig. 3.23 shows the over-pressure variation with increasing bubble radius for Ja=3166.8

(P_∞=0.01 atm, T_{sup}=15.0 °C). In the figures, it is clear that the surface tension forces diminish

rapidly and the hydrodynamic pressure, P_{hd}, increases to such an extent as to balance the

driving pressure, P_v-$P_\infty \approx P_{hd}$. In fact, P_{hd} becomes so large that the rate at which the vapour

pressure drops is dramatically reduced and remains very near the initial value for a

considerable time span. If inertial forces had not come into play and the growth rate were

governed by heat transfer to the interface, then posing the same arguments as discussed

earlier, the characteristic velocity would be of the order,

$$U_{c,HT} \sim \frac{k}{\rho_v h_{fg}} \left(\frac{T_{sup}}{L_c} \right) \approx 20 \, m/s \qquad (3.20)$$

which is an order of magnitude larger than the actual maximum velocity of U_c=0.98 m/s as

depicted in Fig 3.24. Since $U_{c,HT} \gg U_c$ heat transfer is not the mechanism which is limiting

the growth rate.

Bubble expansion is inhibited by the surrounding liquid and the quasi-steady

equilibrium state is now defined by a balance between the vapour pressure and the total

pressure acting at the interface $P_v \approx P_\infty + P_{hd}$. The rate at which the vapour pressure decreases

depends on the rate at which the hydrodynamic pressure drops. In this scenario, increases

in R(t) are subject to changes in P_{hd}. Fig 3.23 shows that the vapour over-pressure curve is

deflected away from the 2σ/R curve to such an extent that a small decrease in P_{hd} results in

a comparatively large rise in the bubble radius. Since the vapour over-pressure remains near the initial value of $P_v-P_\infty \approx P_{hd} \approx 2\sigma/R_c$, the characteristic velocity for inertial limited growth can be predicted by,

$$U_{c,I} \sim \sqrt{\frac{2(P_{sat}(T_\infty)-P_\infty)}{3\rho_l}} \approx 1.0\,m/s \qquad (3.21)$$

which is very close to the actual velocity of U_c=0.98 m/s. This confirms that the mechanism which is responsible for regulating the growth rate during the transition region is the momentum interaction between the bubble and the surrounding liquid.

3.4.2.3 Effect of Increasing Superheat on the Transition Domain

The level of superheat affects bubble growth during the transition domain in two critical ways. First and foremost, higher superheats result in higher growth rates. Second, the higher growth rates are responsible for an increase in the overall hydrodynamic pressure at the vapour-liquid interface, primarily through the increase in the $^3/_2\rho_l(dR/dt)^2$ term. If the superheat is high enough, the hydrodynamic pressure can increase to such an extent as to significantly alter the rate at which the vapour pressure and temperature decrease, thus influencing changes in the heat transfer rate to the bubble.

The growth rate, dR/dt, is larger for greater levels of system superheat. The larger growth rate with system superheat is illustrated in Fig. 3.25. In this figure the individual curves have been shifted to the left by an amount of time prescribed by the respective delay times so that comparisons can be made between bubbles which begin growing at the same

time. Since the growth rate is proportional to the heat flux according to equation (3.10), this indicates that the ratio of the driving temperature difference and the boundary layer thickness, $\Delta T(t)/\delta(t)$, is larger for the increased system superheat. Figs. 3.26 shows that the thermal boundary layer thickness curves converge very quickly subsequent to the onset of significant growth for each level of superheat. In approximately 0.045 ms, each curve follows very closely the analytic curve for a thin thermal boundary layer $\delta(t)=(^{1}/_{3}\pi\alpha t)^{\frac{1}{2}}$. Consequently, this mechanism is not responsible for the observed increase in the interface heat flux and subsequent growth rate. Fig. 3.13 shows that at the onset of significant growth, the driving temperature difference is greater for higher system superheat. More importantly, the rate at which $\Delta T(t)$ increases is substantially higher. This trend continues for the duration of the transition region, as illustrated in Fig. 3.27, and is responsible for the higher growth rates observed for larger superheats.

The influence that the momentum of the liquid has on the expanding vapour bubble tends to increase as the level of superheat is elevated. Fig. 3.28a shows that for the lowest superheat case tested, the hydrodynamic pressure term has a negligible effect on the decreasing vapour pressure. As discussed in Section 3.4.2.1, heat transfer is the limiting mechanism which governs the growth rate during this interval of growth. As the superheat level is raised, the hydrodynamic pressure term becomes progressively more significant. Figs. 3.28b and 3.28c show this clearly. For the highest superheat case, Fig 3.28c shows that the surface tension forces diminish quickly. The rate at which the vapour pressure drops becomes slowed considerably by changes in the liquid momentum surrounding the bubble. As a result, a substantial pressure differential is sustained over a longer time interval and the transition domain is prolonged. It should be noted that this is not truly *inertia controlled*

growth' in the traditional sense of the term where the vapour over-pressure remains near its maximum, the growth rate is constant, and the Rayleigh solution applies over a extended period of time. In the same manner as discussed in Section 3.3.2, changes in the heat transfer rate are integral in influencing changes in the growth rate. In this way there is a complex interaction between the heat transfer and liquid inertia which act together to govern the growth characteristics during the transition region.

The time interval over which liquid inertia influences the bubble growth during the transition domain increases from nearly zero as the level of system superheat is increased. This is illustrated in Fig. 3.29, where for comparison purposes, it has been assumed that the hydrodynamic pressure is 'important' if it comprises at least 20% of the total pressure difference, P_v-P_∞, during the transition domain. In the figure, the superheat has been made dimensionless and is expressed as the Jakob number. For the superheat range tested, the time interval for which liquid inertia effects are important rises at a relatively constant rate with the Jakob number and correlates roughly as $t_{inertia} \approx 10^{-2} Ja$.

3.4.2.4 Effect of Decreasing System Pressure on the Transition Region

Decreasing the system pressure for a constant superheat of $\Delta T_{sup} = 15\,^\circ C$ has two notable effects on the growth characteristics during the transition domain. First, as the system pressure is reduced, the influence of liquid inertia becomes progressively more dominant in limiting the growth rate. Secondly, decreasing the system pressure has the effect of reducing the characteristic velocity of the transition domain as represented by $dR/dt|_{max}$.

Figures 3.30a through 3.30d show the temporal variation of the vapour over-pressure

for a range of system pressures between 5 atm and 0.01 atm. The figures illustrate the fact that as the system pressure is reduced, the momentum interactions of the liquid with the expanding bubble becomes progressively more influential. The P_∞=5 atm case illustrates the extreme case by which the majority of the over-pressure has diminished by the time the hydrodynamic pressure has increased enough to be considered important. In this scenario, the limiting mechanism for growth is heat transfer in the same manner as discussed in Section 3.4.2.1. The P_∞=0.01 atm case illustrates the opposite extreme, as discussed in Section 3.4.1.2, whereby the hydrodynamic forces increase to such an extent as to maintain the vapour over-pressure near its maximum value for a considerable length of time.

As illustrated in Fig. 3.31, the maximum growth rate increases markedly when the system pressure is increased. This is a consequence of the interface acceleration being much higher for larger pressures (P_∞ =5 atm and 1 atm in Fig. 3.18) as a result of the intensified thermal feedback for smaller critical radii. However, the time interval over which these high growth rates can be sustained is smaller. This is in contrast to the trend observed earlier for increasing superheat in which the higher growth rates were sustained over a longer time interval. For the P_∞= 5 atm case, there are essentially no inertial forces present to restrict the vapour pressure and temperature from dropping. Because of this, the driving temperature increases to ΔT_{sup}=15°C very quickly so that the time interval of the transition region is comparatively short. This is illustrated in Fig. 3.32. The figure shows that as the system pressure is decreased, the increased level of the hydrodynamic pressure resists expansion to such an extent that the rate at which the driving temperature difference increases towards ΔT_{sup}=15°C is dramatically reduced as shown. This accounts for the comparatively slow changes in system variables associated with low pressures. However, lower pressures require

less energy and thus a smaller ΔT, to produce an equivalent volume of vapour because of the reduced vapour density. For example, at $t-t_{delay}=1.0$ ms the growth rate for the $P_\infty=0.01$ atm is 0.94 m/s and the driving temperature difference is only 0.65 °C. At the same time the growth rate for the $P_\infty=5$ atm case is only 0.13 m/s and the temperature difference is at its maximum value of 15 °C.

The time interval over which liquid inertia influences the bubble growth during the transition domain increases as the system pressure is reduced. Fig. 3.29 shows that for the pressure range tested the time interval for which liquid inertia effects are important rises at a relatively constant rate with the Jakob number and still correlates well with $t_{inertia} \approx 10^{-2} Ja$.

3.4.3 The Effect of Pressure and Superheat on Heat Transfer Controlled Growth

Up to this point, little mention has been made of the Jakob number,

$$Ja = \frac{\rho_l C_{pl}(T_\infty - T_{sat}(P_\infty))}{\rho_v h_{fg}}$$

(3.22)

This is an important parameter in boiling and represents non-dimensional superheat. For the surface tension and transition domains, this parameter in not as useful in characterizing bubble growth since the driving temperature difference $\Delta T(t)$ is less than the characteristic temperature, ΔT_{sup}, used in determining the Jakob number. Figs. 3.33 and 3.34 show the radius, growth rate and normalized temperature difference $\Delta T/\Delta T_{sup}$ for two bubbles with very different system conditions (ΔT_{sup} and P_∞) but nearly identical Jakob numbers ($Ja \approx 10$). Similarly, Figs. 3.35 and 3.36 show the same curves for a Jakob number $Ja \approx 90$. The figures

illustrate that during the surface tension and transition phases, the growth characteristics for nearly equal Jakob numbers are noticeably different. However, as each bubble enters its respective heat transfer controlled growth phase, indicated by $\Delta T/\Delta T_{sup} \approx 1$, the growth curves converge with surprising precision indicating that the Jakob number alone is sufficient to characterize bubble growth for this domain.

A more rigorous analysis reveals why this is the case. Fig. 3.37 shows the temporal variation of the thickness of the thermal boundary layer, $\delta(t)$ for each case shown in Figs. 3.33 and 3.35. The figure indicates that for early growth, the curves are very different but converge quickly. Initially, the characteristic length scale which dominates fluid flow and heat transfer is dictated by the initial radius of the bubble. This is confirmed by noting that the thermal layer thickness increases with initial bubble radius and is represented roughly by the characteristic length scale for a sphere $L_c \sim R_c/3$. However, each bubble expands at a rate which is much higher than the rate at which their respective thermal layer grows and a new length scale develops which is independent of the bubble radius since $\delta/R \ll 1$ for each bubble. This constitutes a thin thermal boundary layer which has been the subject of several studies, and has been discussed in Chapter 2. Growth of the thin thermal boundary layer in a semi-infinite medium is well understood and is predicted by,

$$\delta(t) = \sqrt{\frac{\pi \alpha t}{b}} \qquad (3.23)$$

The parameter b accounts for the effect of increasing area such that b=1 for a flat plate, whereas b≈3 for an expanding sphere (Riznic *et al* [1999]). Since the thermal diffusivity of water does not change considerably for water over the range of superheat and pressures

tested, the thermal layers grow at nearly the same rate regardless of the boiling conditions (Fig. 3.37).

Diffusion of energy to the bubble interface provides the latent heat of vaporization required to sustain bubble growth such that,

$$\frac{dR}{dt} \approx \frac{k_l}{\rho_v h_{fg}} \left(\frac{\Delta T(t)}{\delta(t)} \right) \qquad (3.24)$$

For the range of temperatures and pressures tested, most all of the liquid and vapour properties do not vary considerably except for the vapour density, $\rho_v = \rho_{v,sat}(P_\infty)$, which decreases considerably with pressure. Since $\delta(t)$ is nearly the same for all bubbles in the diffusion stage of growth, equation (3.24) shows that smaller superheats can produce identical growth rates for lower system pressures because the vapour density is lower. Allowing for some small variations in liquid properties, the ratio of the superheat and vapour density for the boiling conditions of Fig. 3.35 is close to unity;

$$\frac{(\Delta T_{sup}/\rho_v)_{1,atm,30°C}}{(\Delta T_{sup}/\rho_v)_{0.5atm,15°C}} = 1.04 \qquad (3.25)$$

The same ratio of $\Delta T_{sup}/\rho_v$ appears in the Jakob number and a quick manipulation of equation (3.24) gives,

$$\frac{dR}{dt} \approx \alpha \left(\frac{Ja}{\delta(t)} \right) \qquad (3.26)$$

which illustrates why the Jakob number alone is sufficient to characterize diffusion

controlled growth.

The effect of system pressure and liquid superheat on thermal diffusion controlled growth can be summarized as follows: i) The magnitude and growth rate of the thermal boundary layer is not sensitive to changes in pressure or superheat (Fig. 3.37). ii) For constant pressure, larger superheats produce higher growth rates, and thus larger bubbles, since $dR/dt \propto \Delta T_{sup}$ while all other variables in equation (3.24) are essentially the same (Fig. 3.11). iii) In order to produce the same growth rate, a lower system pressures requires less energy, and thus less superheat, to generate an equivalent volume of vapour because the vapour density is lower (Figs. 3.33 and 3.35).
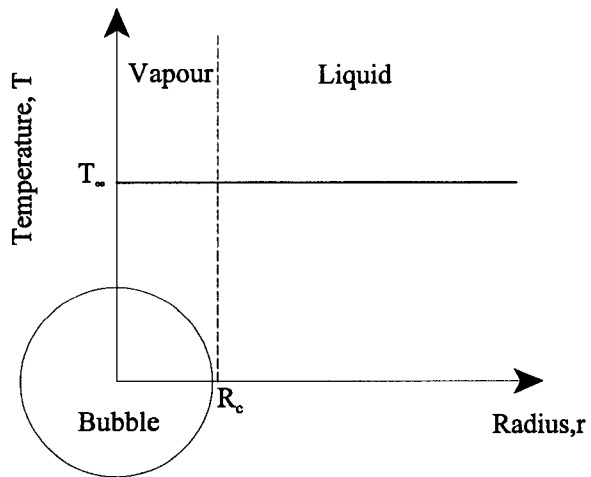
Figure 3.1: Thermal equilibrium of the vapour nucleus prior to initial disturbance.
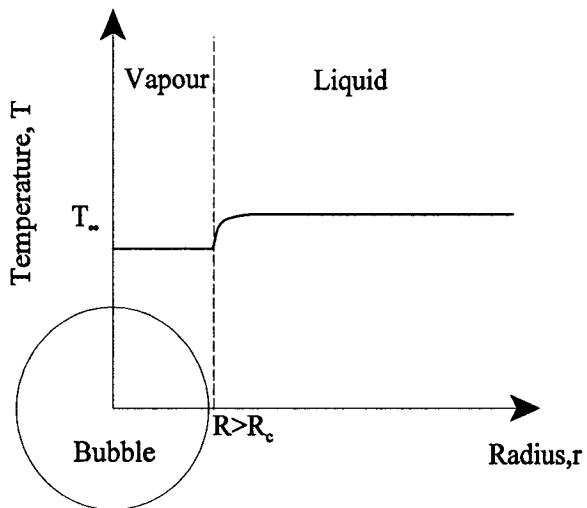
Figure 3.2: Schematic of the temperature distribution in the liquid and vapour during bubble growth.
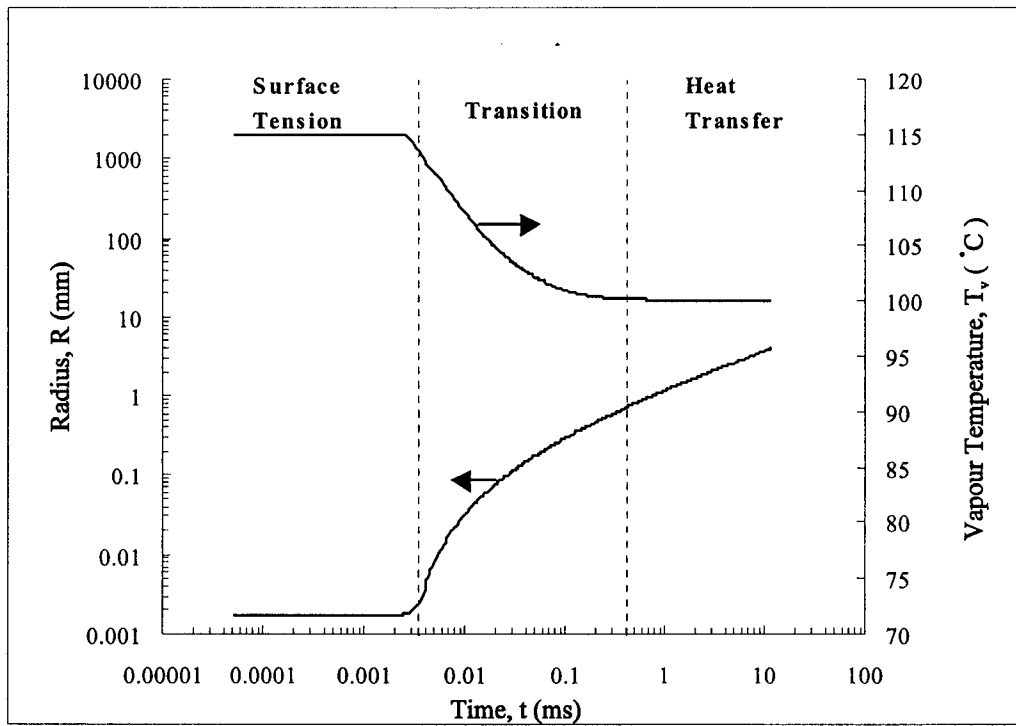
Figure 3.3: Temporal variation of bubble radius and vapour temperature
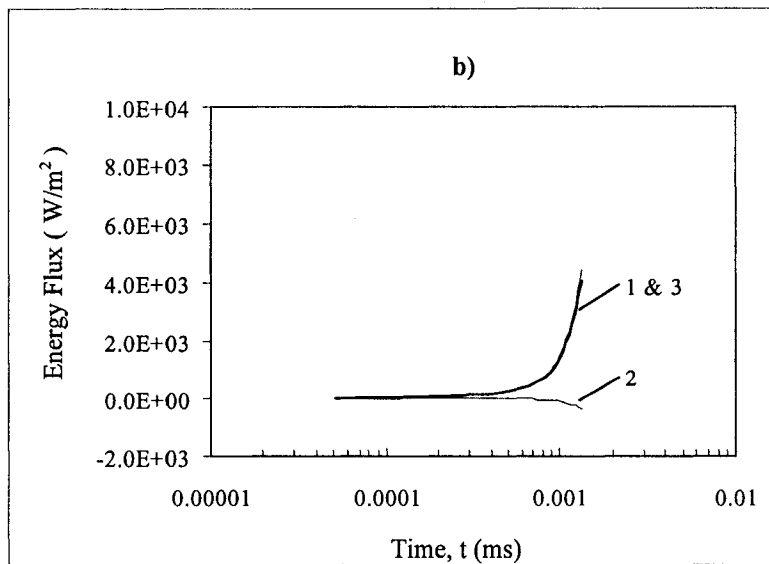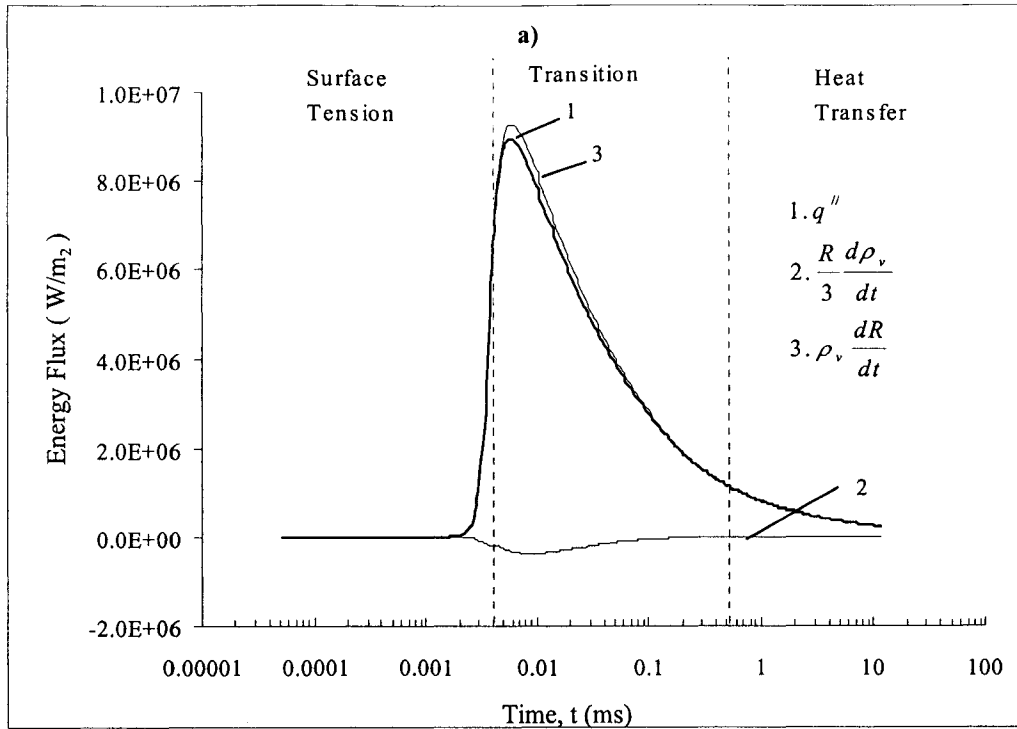
Figure 3.4: Decomposition of the energy balance equation, Eq. (3.8) a) entire growth interval studied b) early surface tension controlled growth.
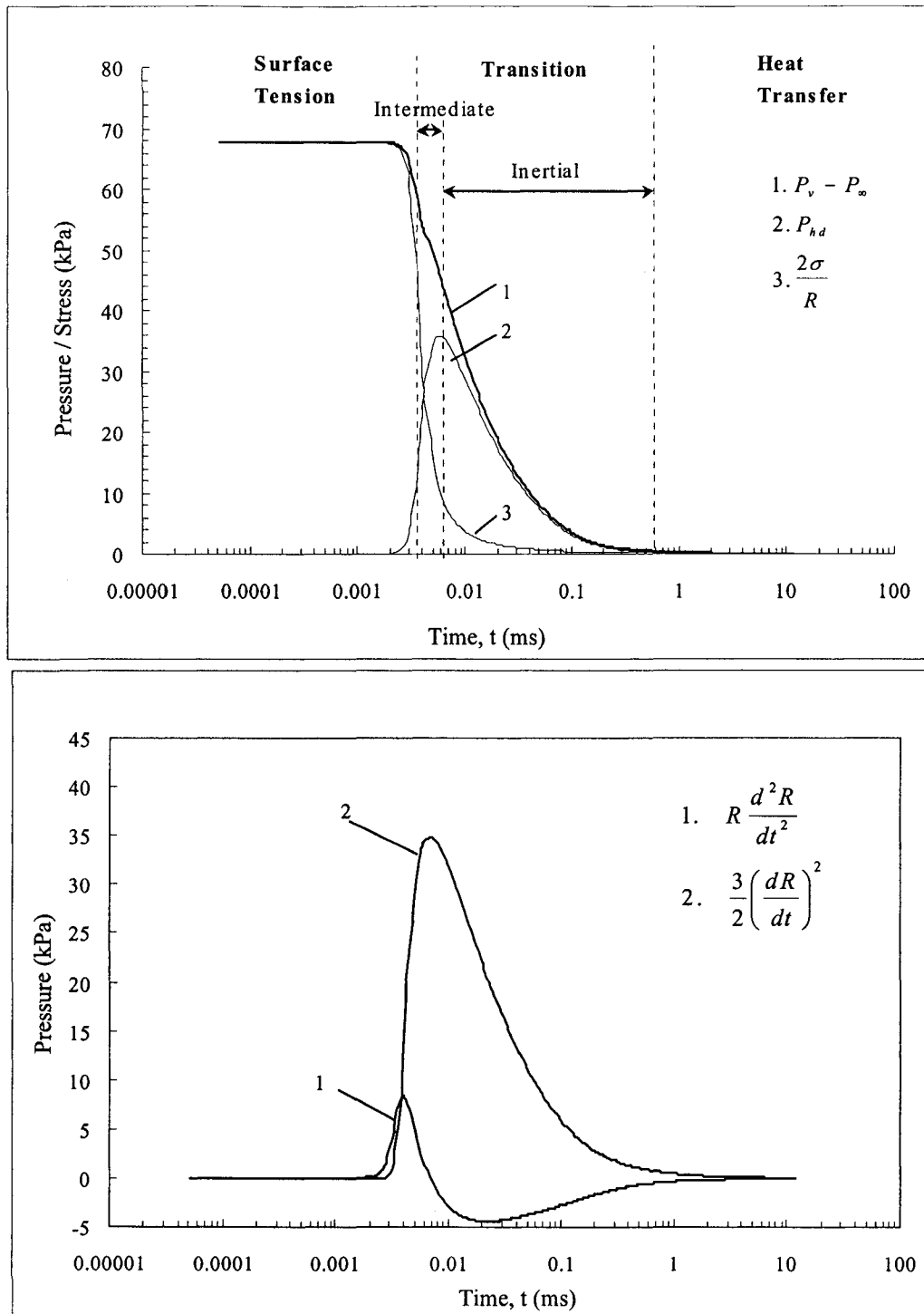
Figure 3.5: a) Decomposition of the equation of motion showing the individual growth domains. b) constituent terms of the hydrodynamic pressure given by equation (3.14).
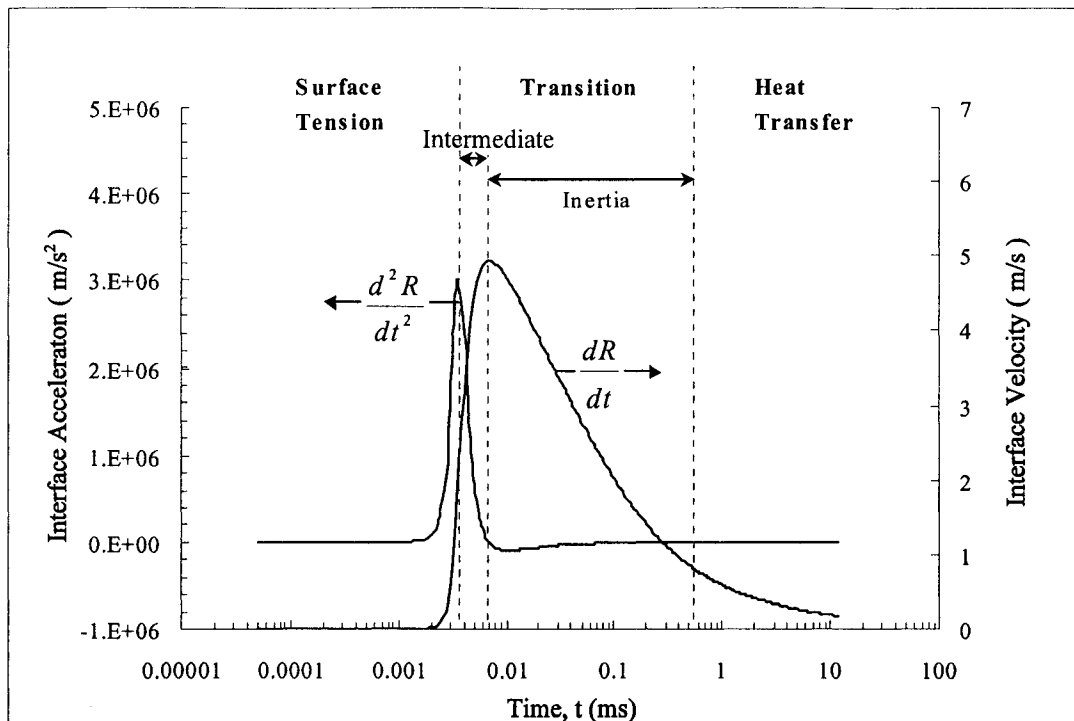
Figure 3.6: Interface velocity and acceleration curve variations.
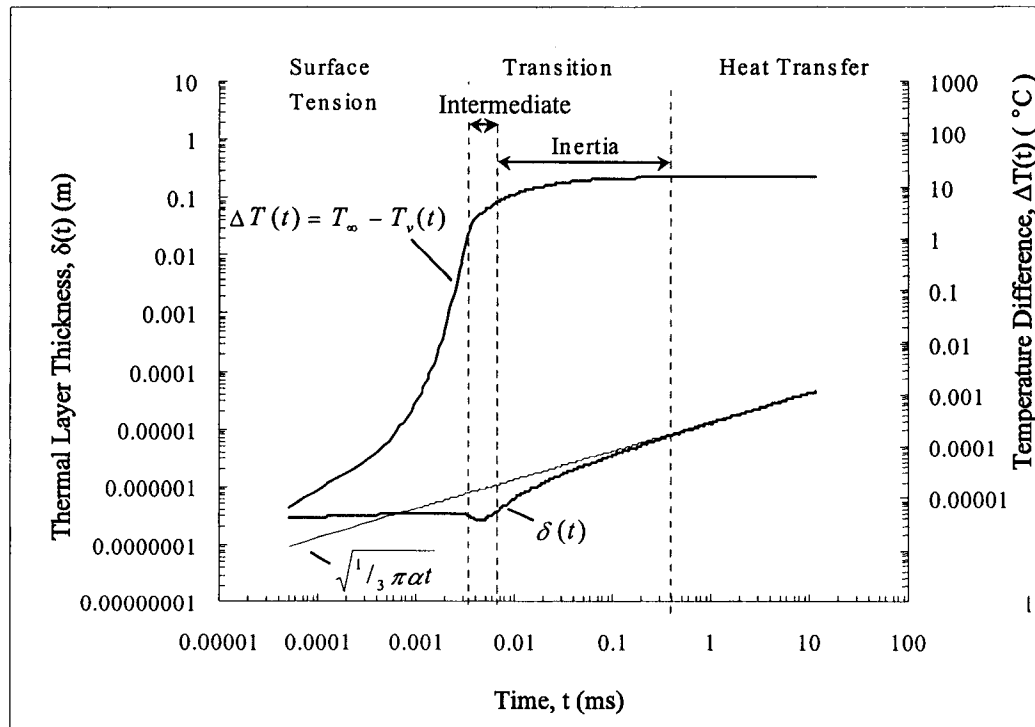
Figure 3.7: Driving temperature difference and thermal boundary layer thickness histories.
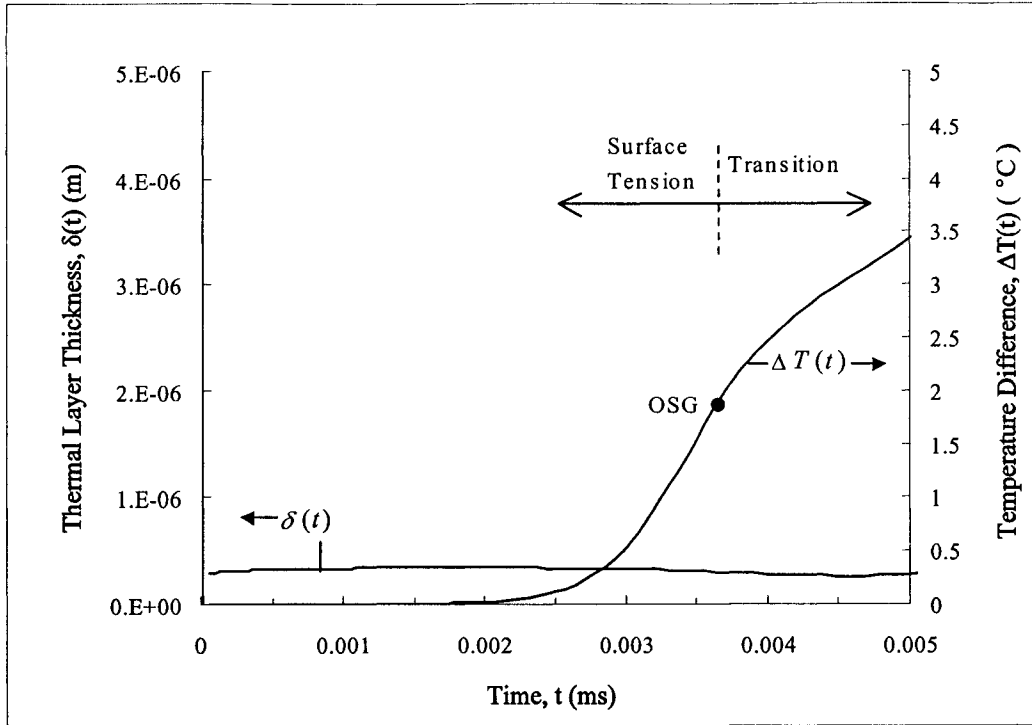
Figure 3.8: Driving temperature difference and thermal boundary layer thickness curves for early stage of growth.
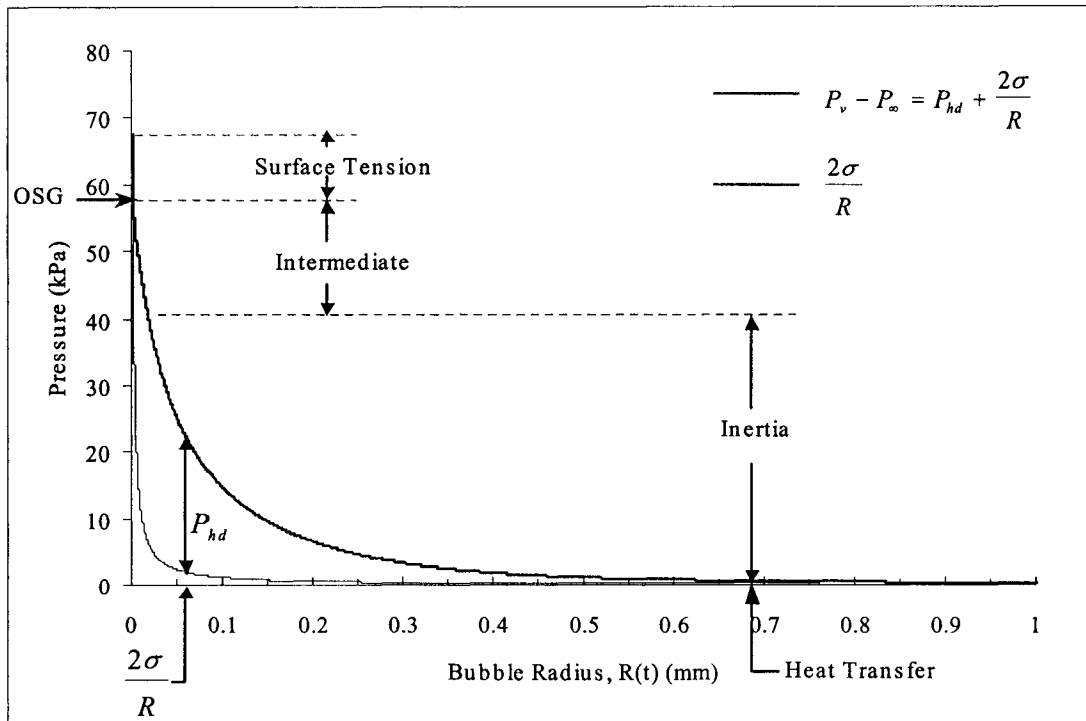
Figure 3.9: Pressure differential curves with and without the hydrodynamic pressure term.
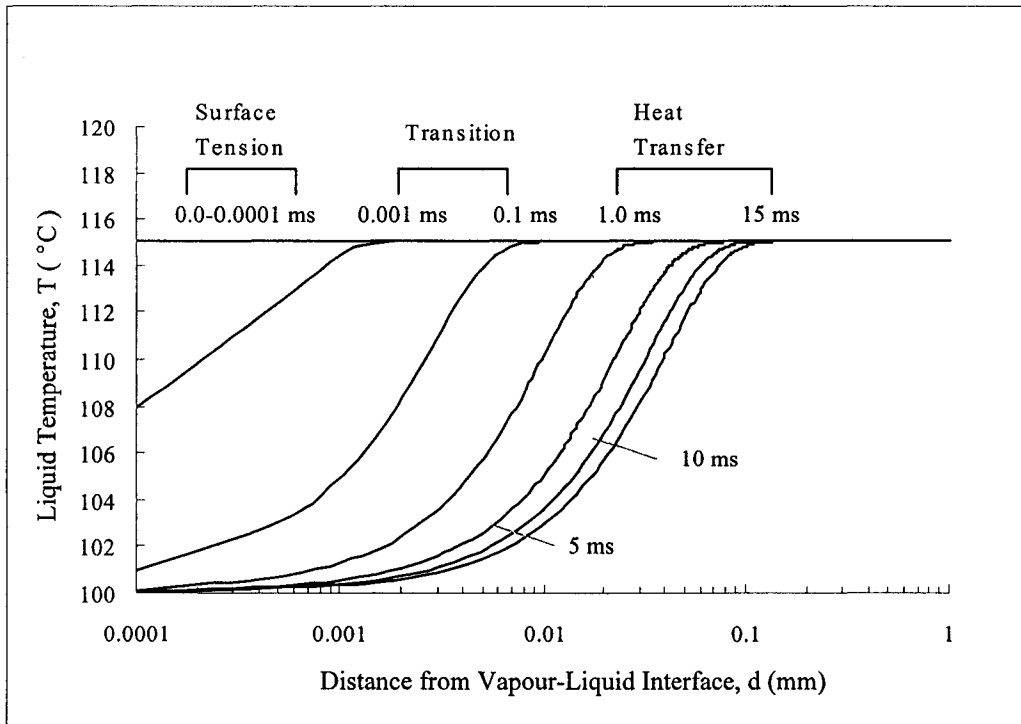
Figure 3.10: Liquid temperature profiles at various times during bubble growth.
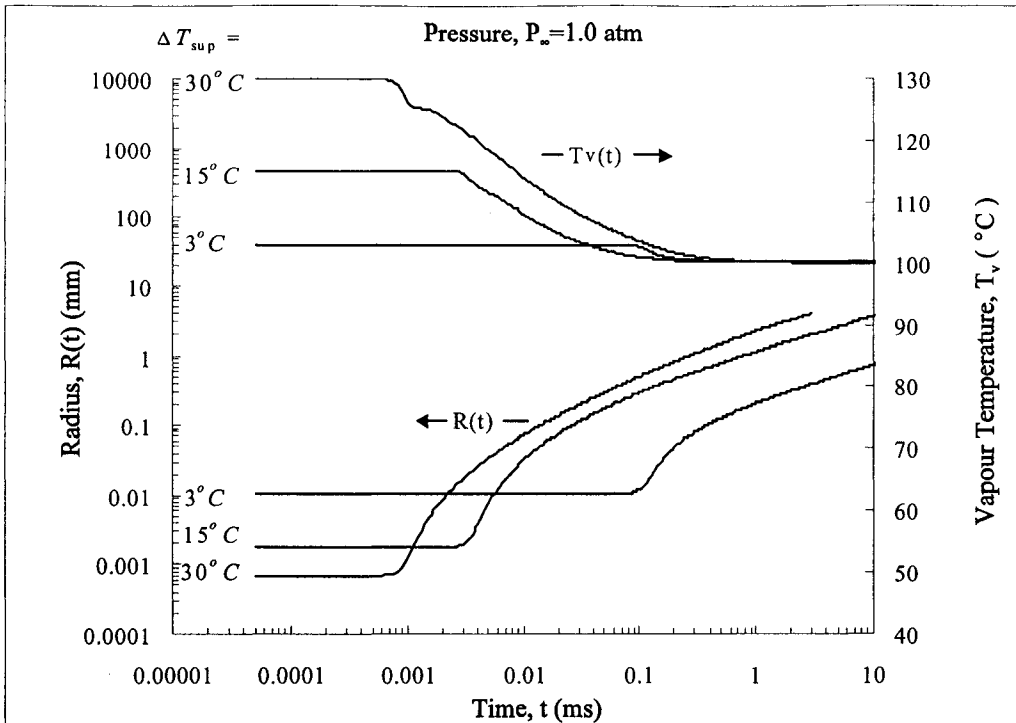
Figure 3.11: Vapour temperature and bubble radius curves for varying levels of superheat.
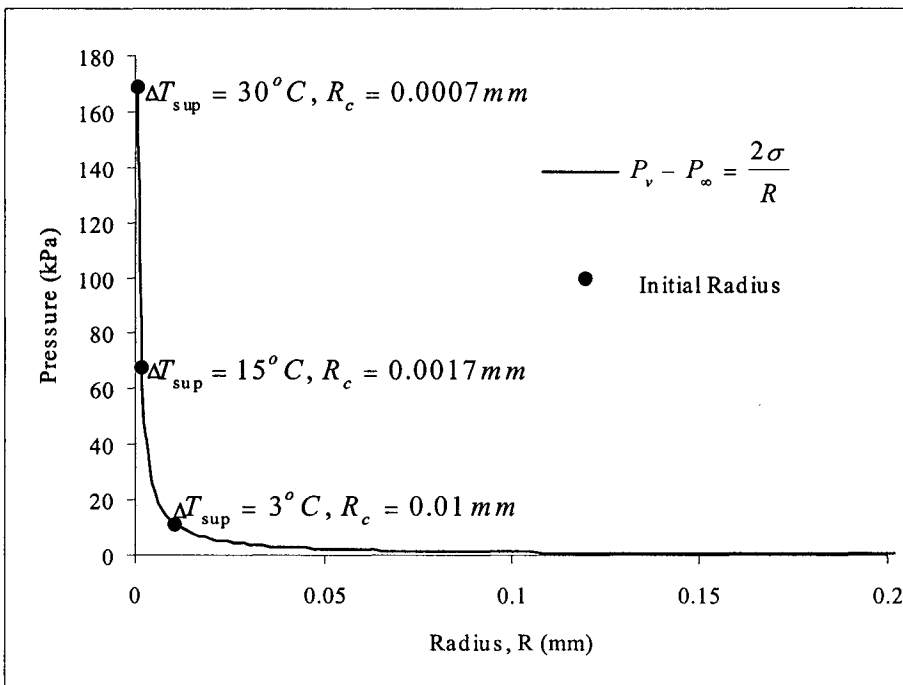
Figure 3.12: Pressure difference versus radius for stationary bubble.
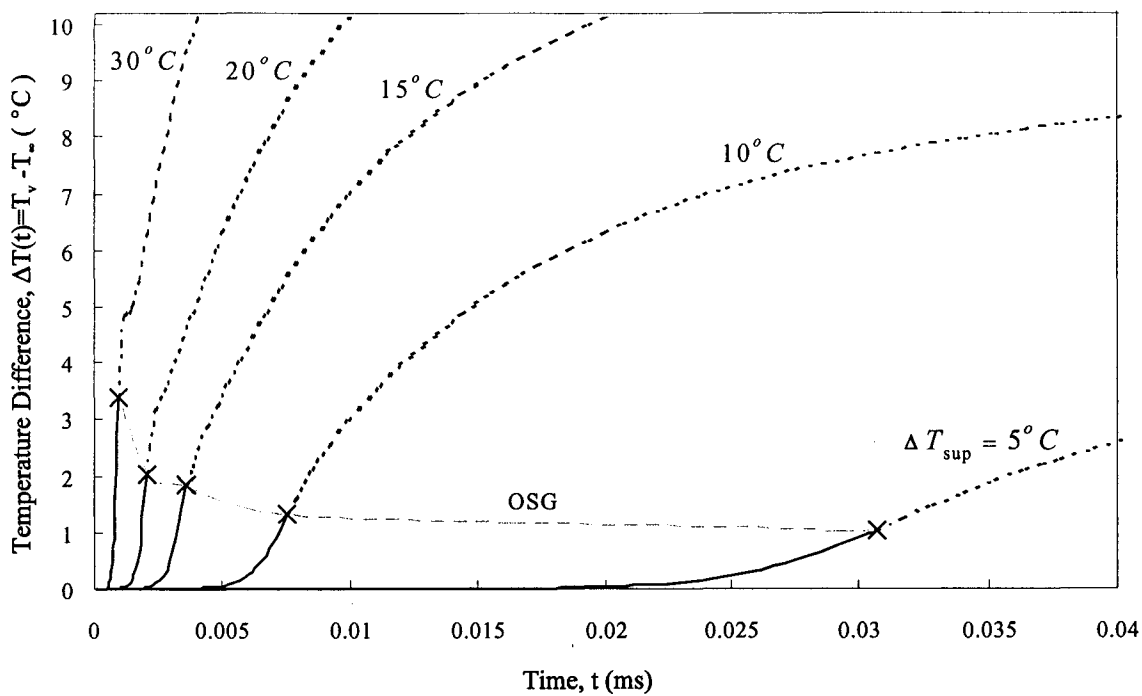
Figure 3.13: Temperature difference curves for surface tension domain and early transition domain.
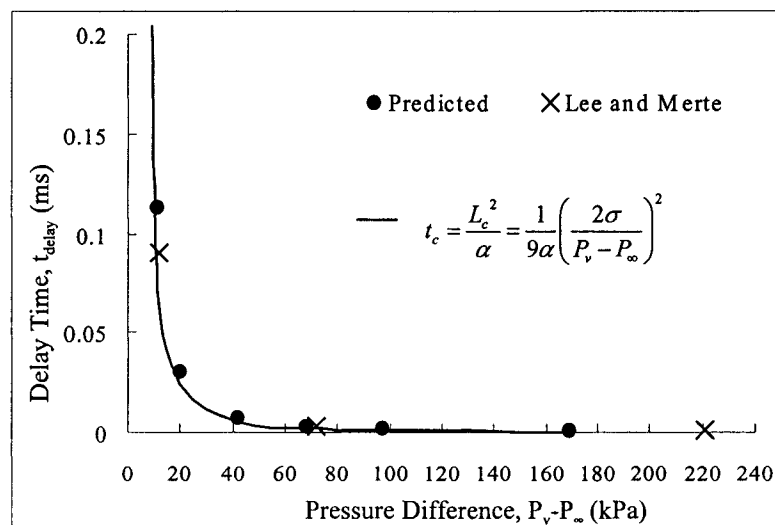
Figure 3.14: Delay time versus initial pressure difference for varying superheat.
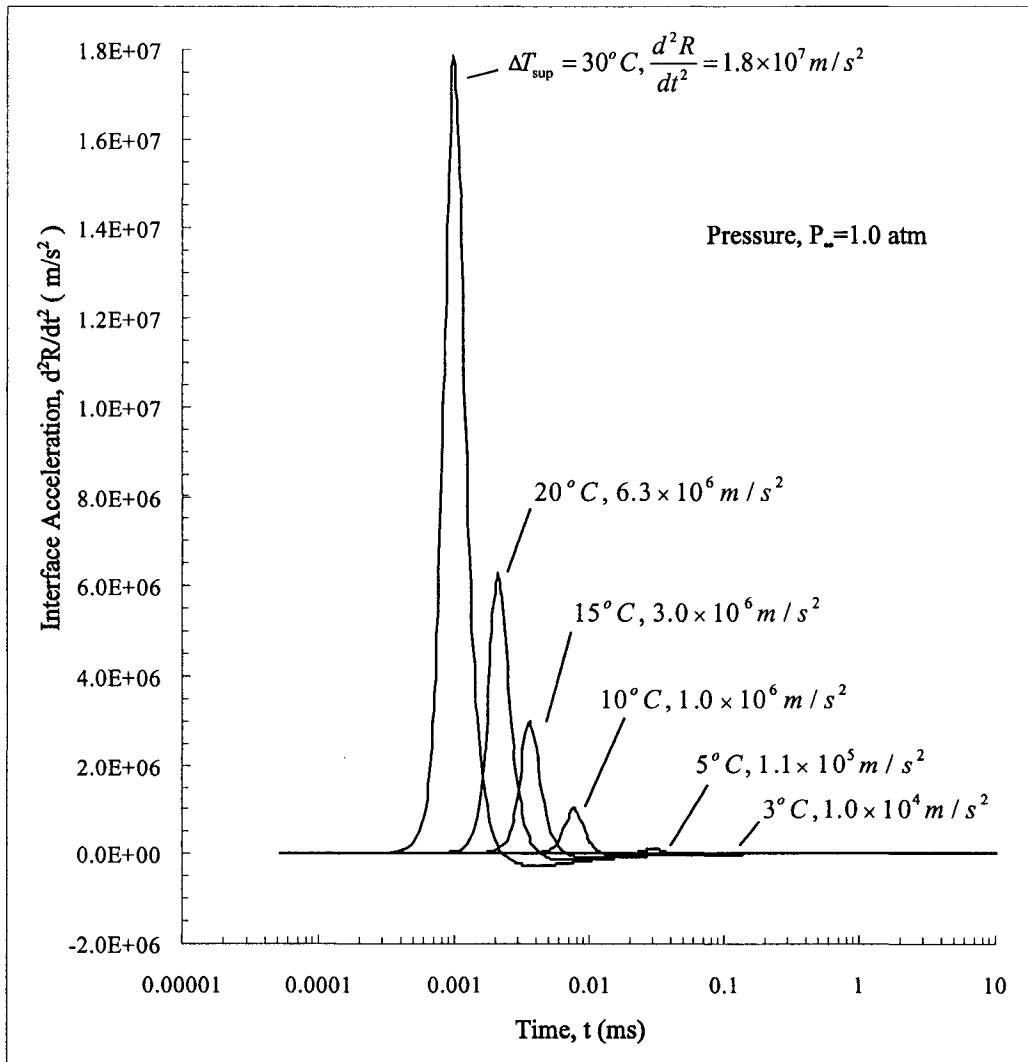
Figure 3.15: Interface acceleration curves for various system superheats.
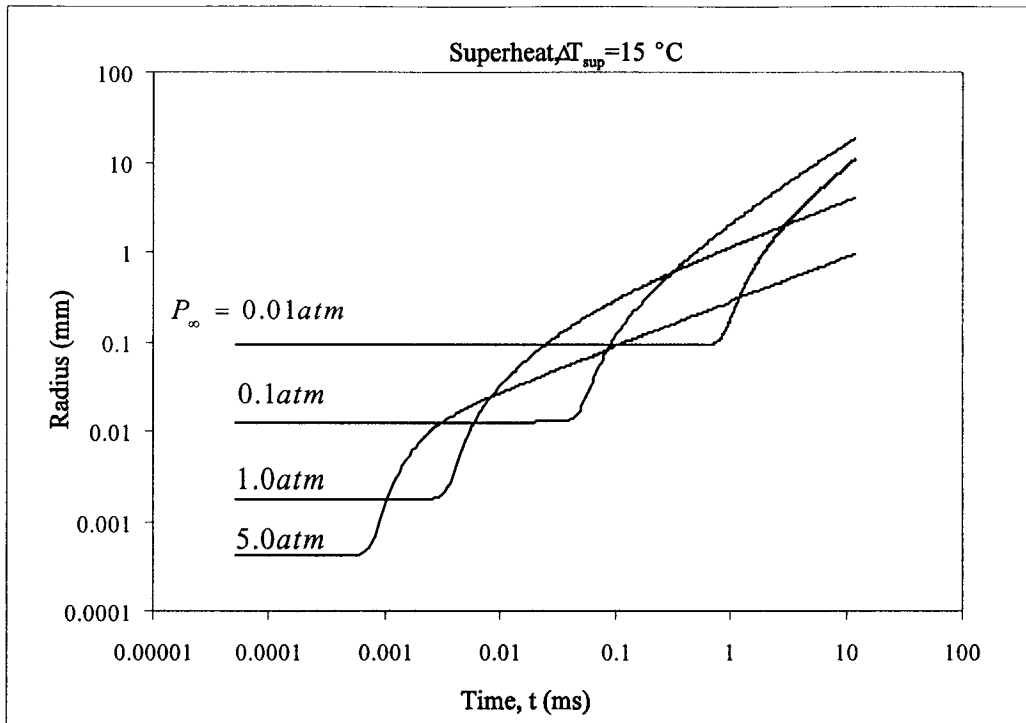
Figure 3.16: Vapour temperature and bubble radius curves for varying levels of system pressure.
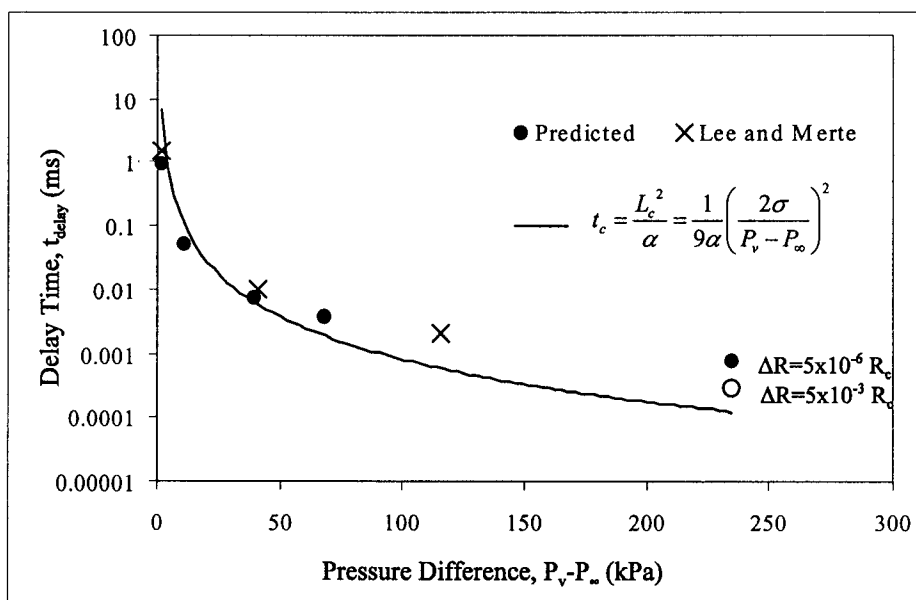
Figure 3.17: Delay time versus initial pressure difference for varying system pressure.
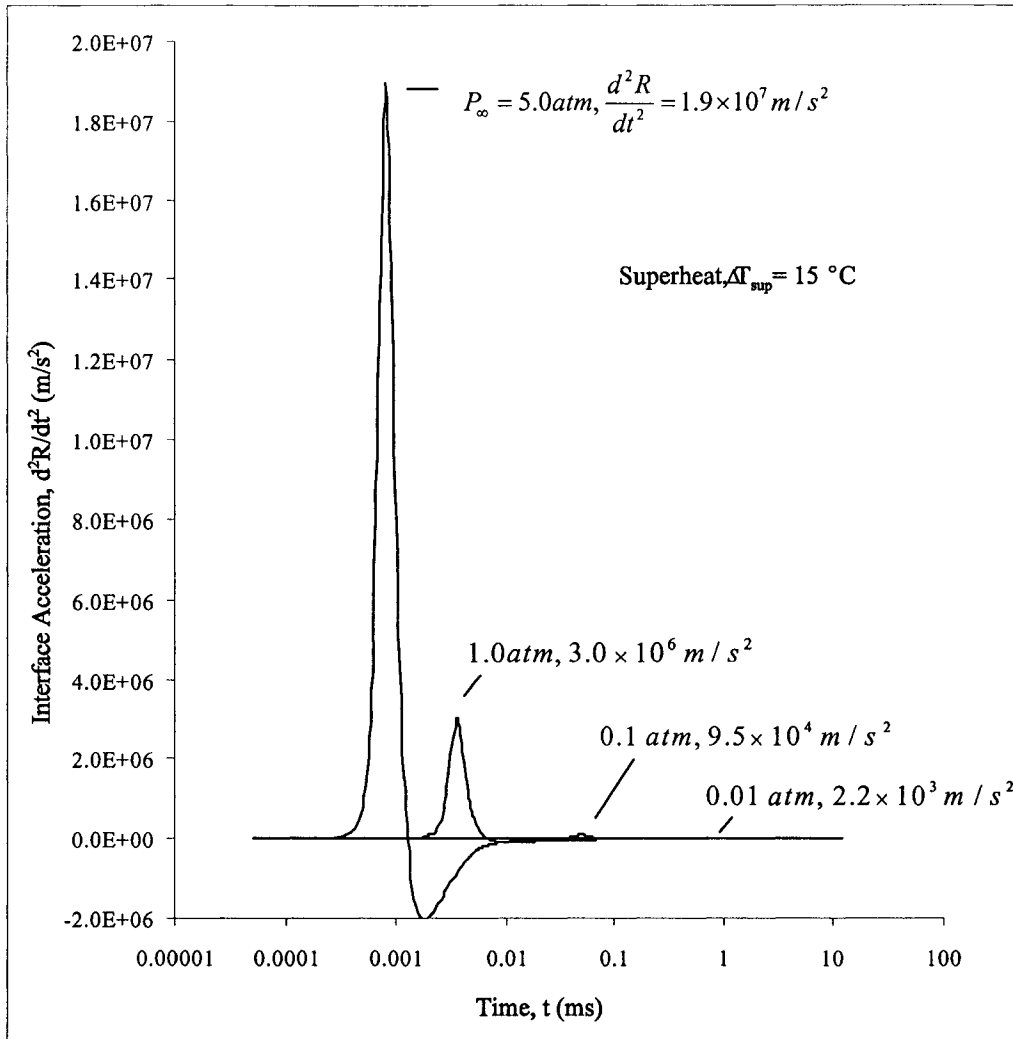
Figure 3.18: Interface acceleration curves for various system pressures.
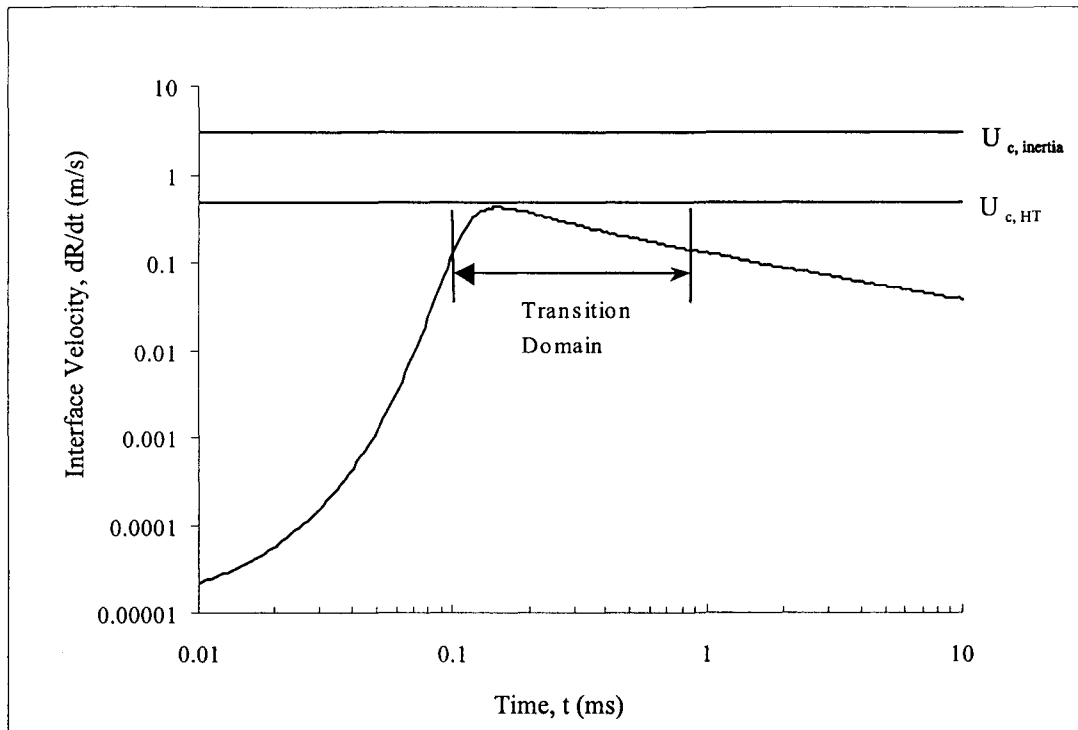
Figure 3.19: Temporal variation of the interface velocity for the transition domain (Ja=9.0, P_∞=1.0 atm, ΔT_{sup}=3.0 °C)
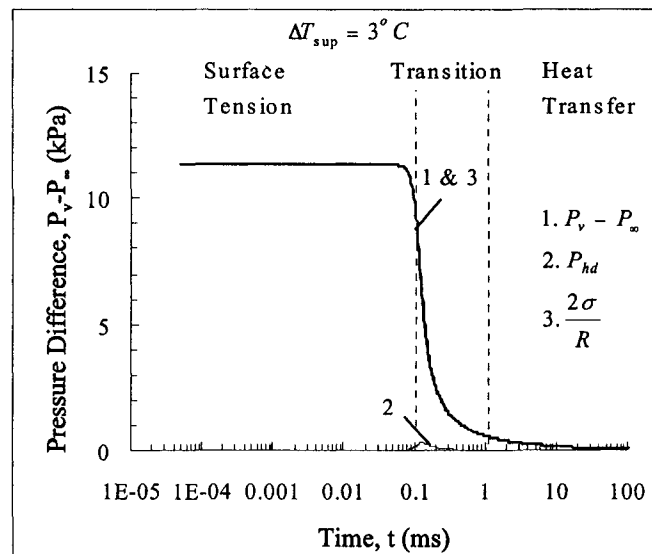
Figure 3.20: Temporal variation of vapour over-pressure, hydrodynamic pressure and surface tension stresses for P_∞=1.0 atm, Ja=9.0.
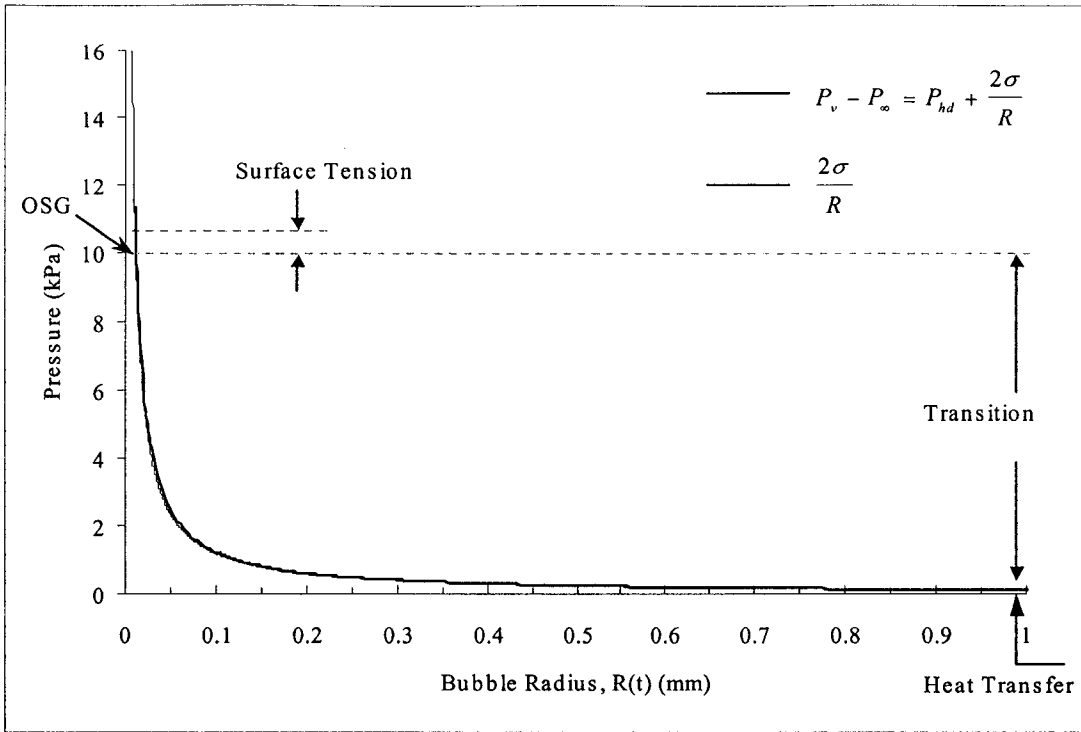
Figure 3.21: Vapour over-pressure versus bubble radius for $P_\infty=1.0$ atm, Ja=9.0.
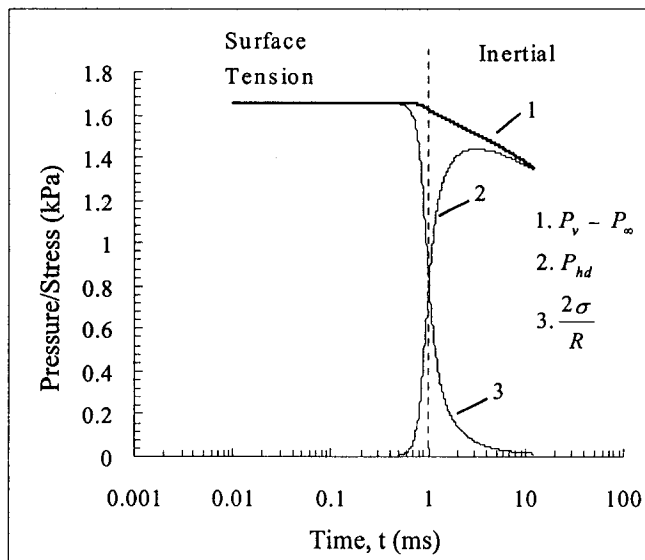
Figure 3.22: Temporal variation of vapour over-pressure, hydrodynamic pressure and surface tension stresses for $P_\infty=0.01$ atm, Ja=3166.8.
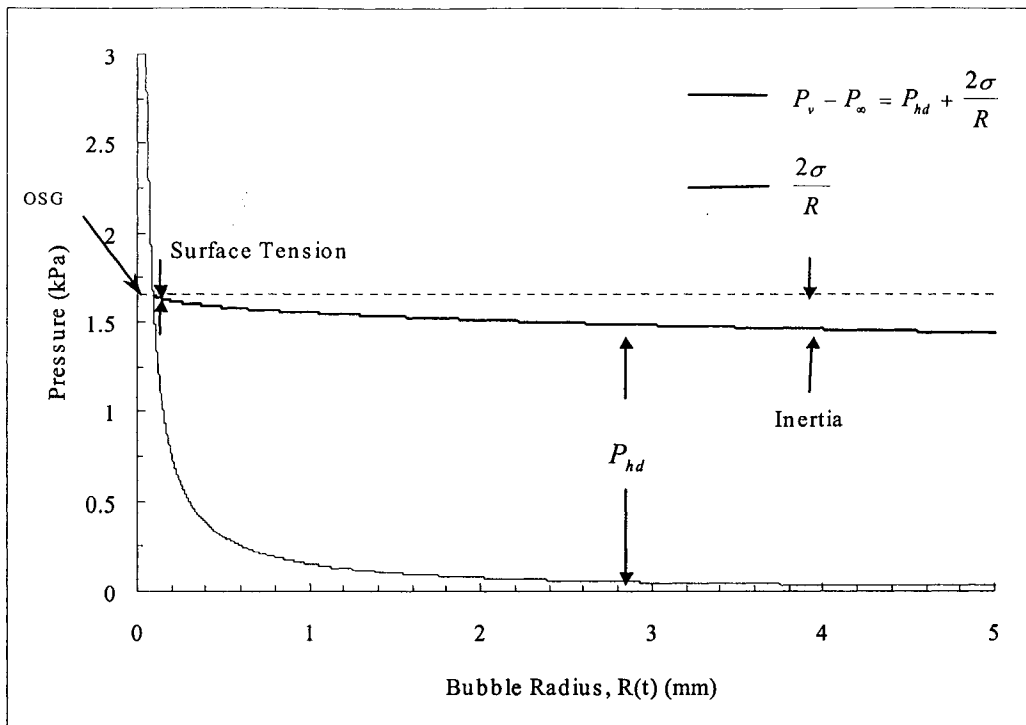
Figure 3.23: Vapour over-pressure versus bubble radius for P_∞=0.01 atm, Ja=3166.8.
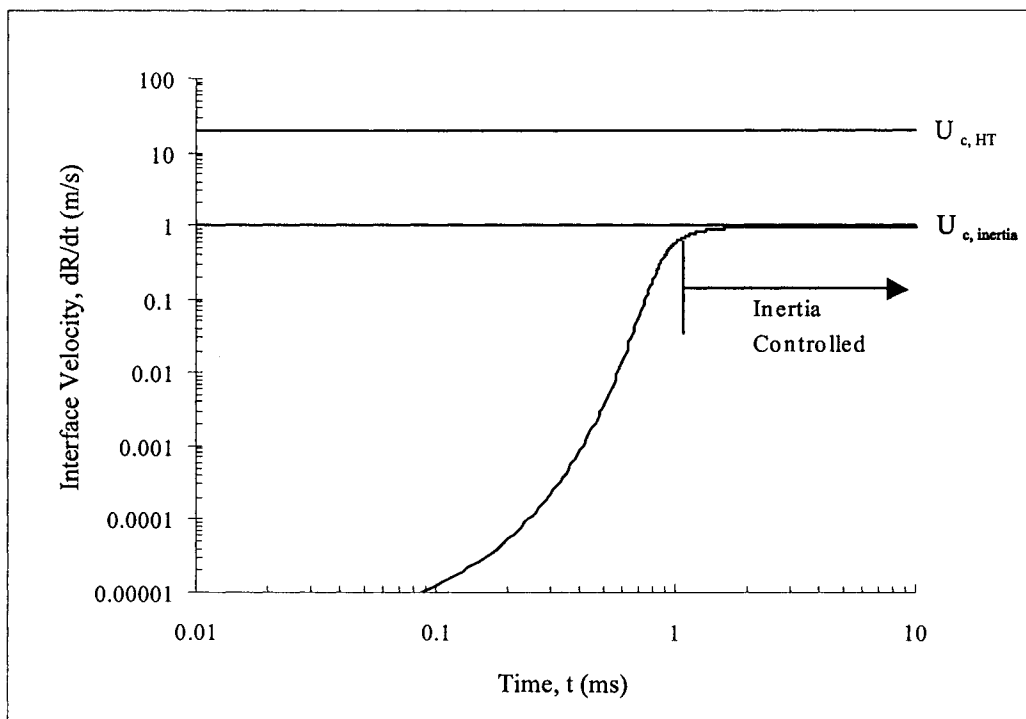
Figure 3.24: Temporal variation of the interface velocity for the transition domain (Ja=3166.8, P_∞=0.01 atm, ΔT_{sup}=15.0 °C)
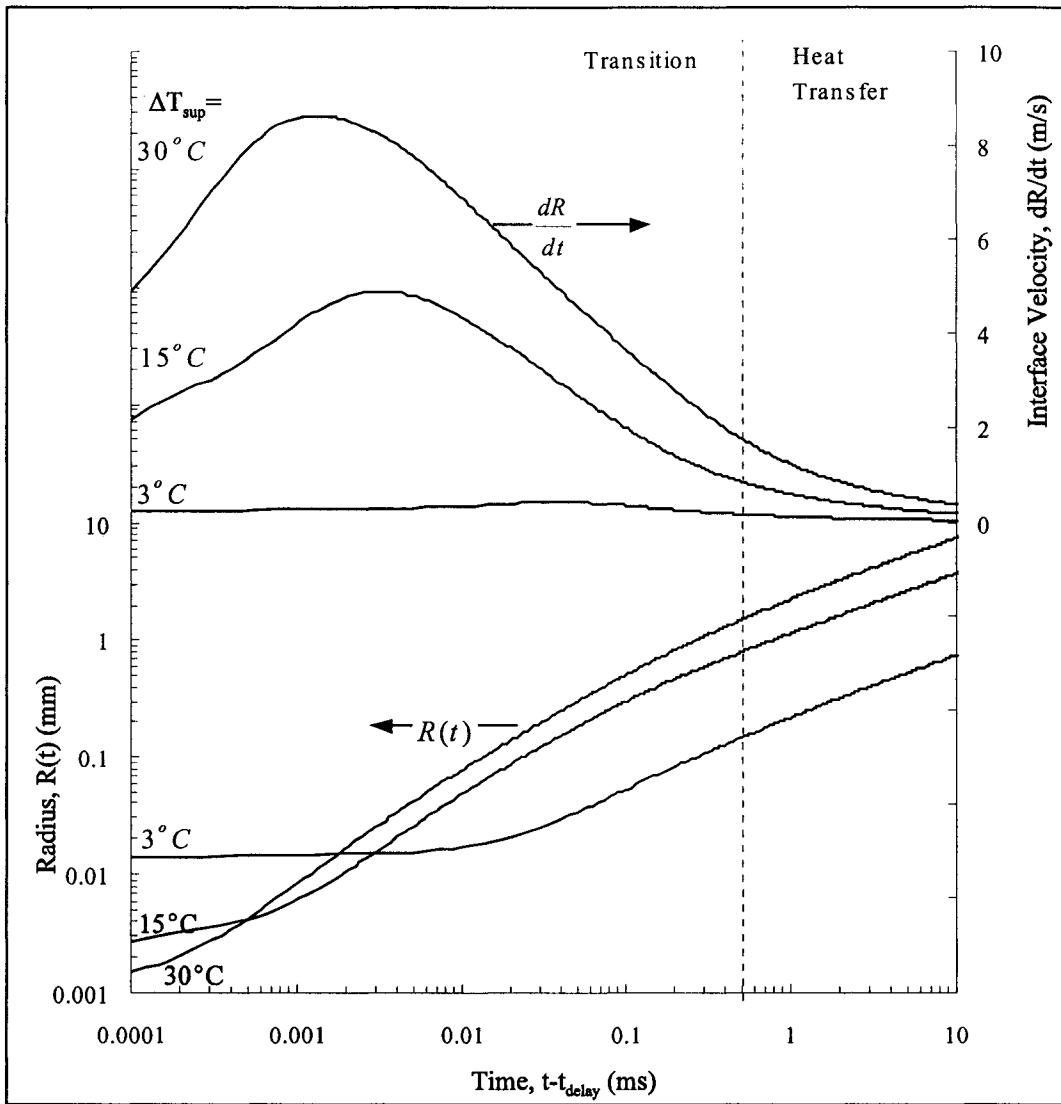
Figure 3.25: Temporal variation of the interface velocity during the transition domain for varying superheat at constant pressure.
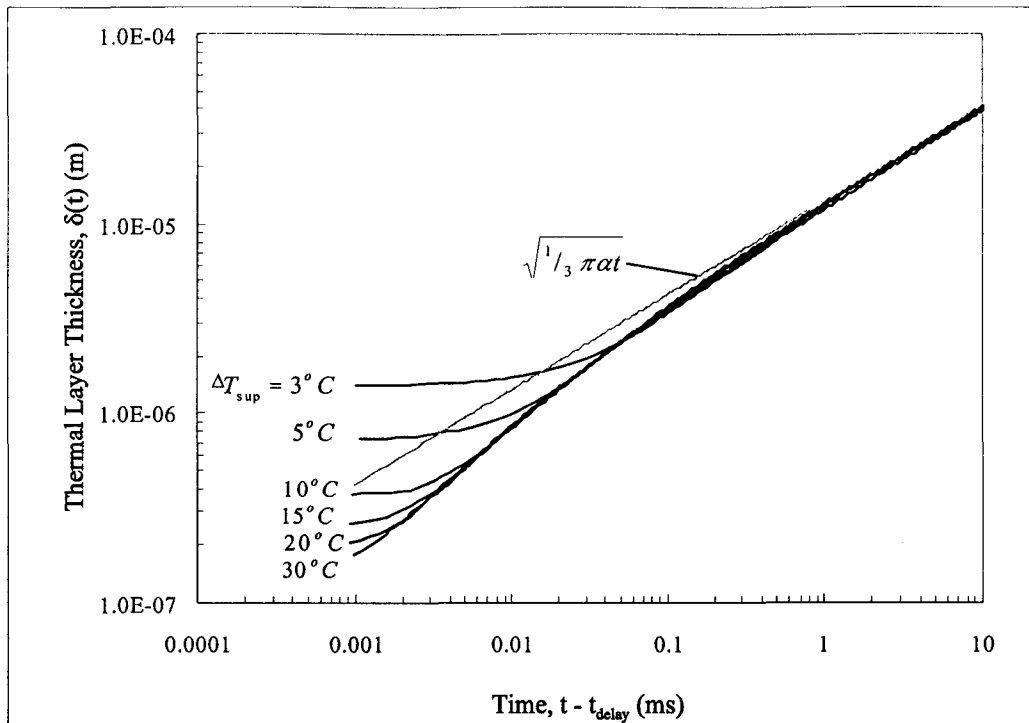
Figure 3.26: Temporal variation of the thermal layer thickness for varying superheat.
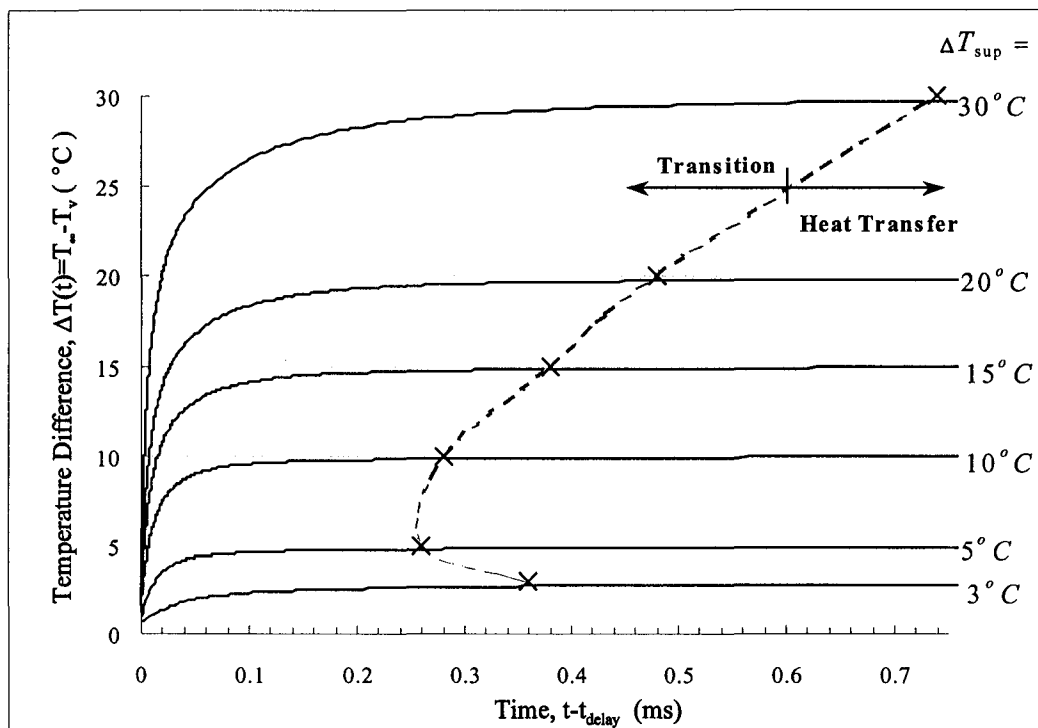
Figure 3.27: Temporal variation of driving temperature difference during transition domain for varying superheat and constant pressure.

a) $\Delta T_{sup} = 3^{\circ}C$

Surface Tension   Transition   Heat Transfer

Pressure / Stress (kPa)

15
10
5
0

1 & 3

2

1. $P_v - P_{\infty}$

2. P_{hd}

3. $\dfrac{2\sigma}{R}$

1E-05 1E-04 0.001 0.01 0.1 1 10 100

Time, t (ms)

b) $\Delta T_{sup} = 15^{\circ}C$

Surface Tension   Transition   Heat Transfer

Pressure / Stress (kPa)

80
70
60
50
40
30
20
10
0

1
2
3

1. $P_v - P_{\infty}$

2. P_{hd}

3. $\dfrac{2\sigma}{R}$

1E-05 1E-04 0.001 0.01 0.1 1 10 100

Time, t (ms)

c) $\Delta T_{sup} = 30^{\circ}C$

Surface Tension   Transition   Heat Transfer

Pressure / Stress (kPa)

200
180
160
140
120
100
80
60
40
20
0

1
2
3

1. $P_v - P_{\infty}$

2. P_{hd}

3. $\dfrac{2\sigma}{R}$

1E-05 1E-04 0.001 0.01 0.1 1 10 100

Time, t (ms)

Figure 3.28: Decomposition of the extended Rayleigh equation for varying superheat and constant pressure.
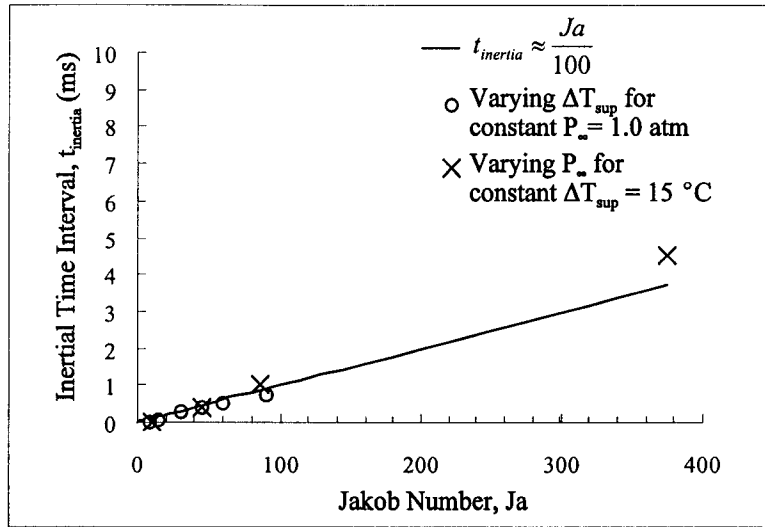
Figure 3.29: Variation of the time interval over which liquid inertia influences bubble growth for varying Jakob number.
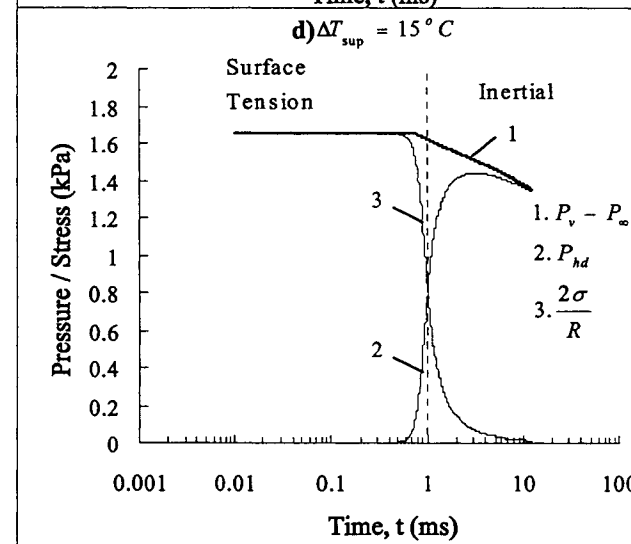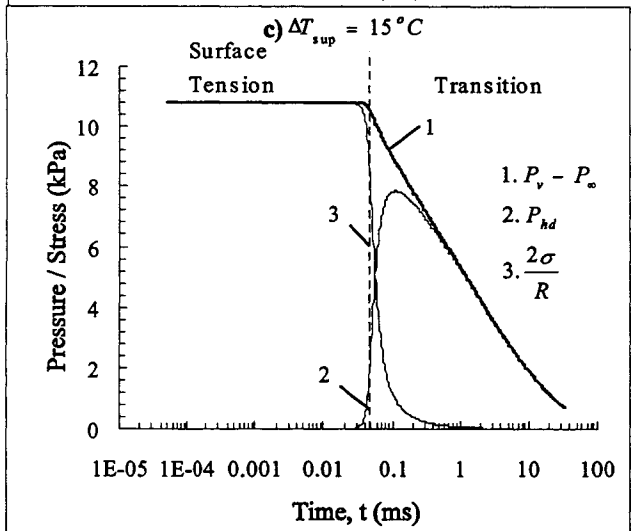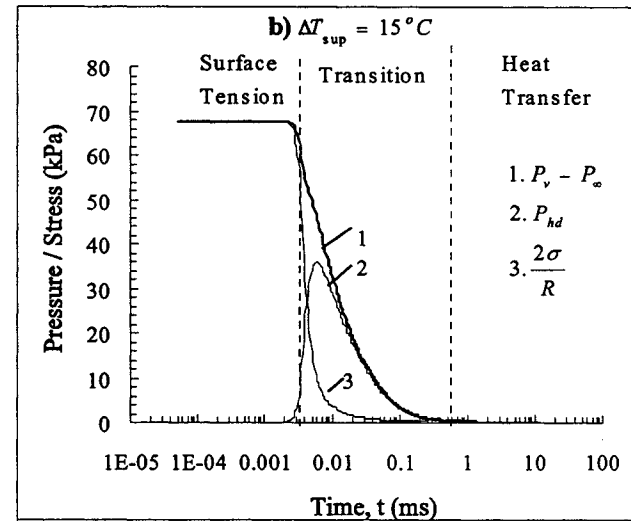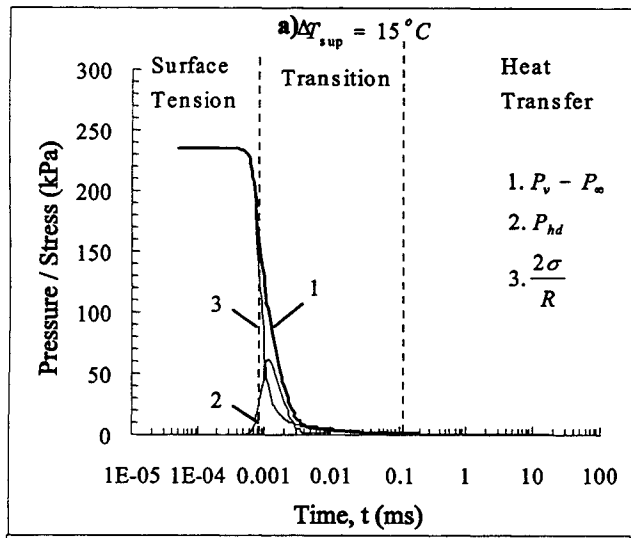
Figure 3.30: The extended Rayleigh equation decomposed a) P_∞=4.0 atm b) P_∞=1.0 atm c) P_∞=0.1 atm d)P_∞=0.01 atm.

$\Delta T_{sup} = 15° C$

5.0 atm

1.0 atm

0.5 atm

0.1 atm

$P_\infty = 0.01 atm$
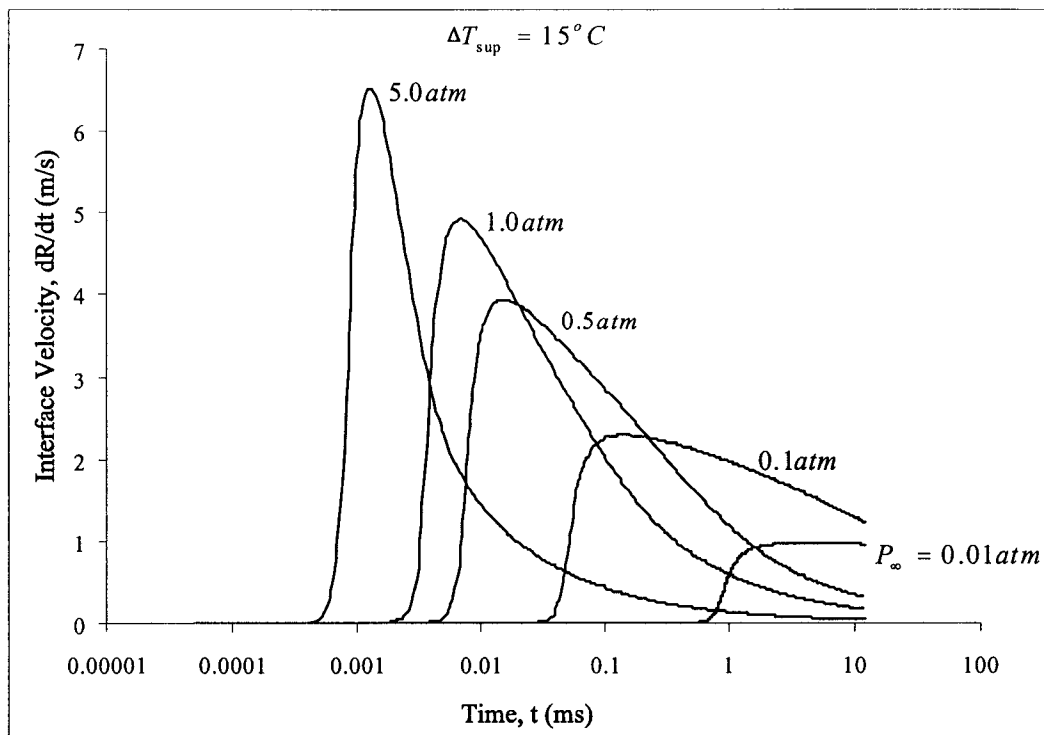
Figure 3.31: Temporal variation of the interface velocity for varying pressure at constant superheat.

$\Delta T_{sup} = 15° C$

5.0 atm

1.0 atm

0.1 atm

$P_\infty = 0.01 atm$
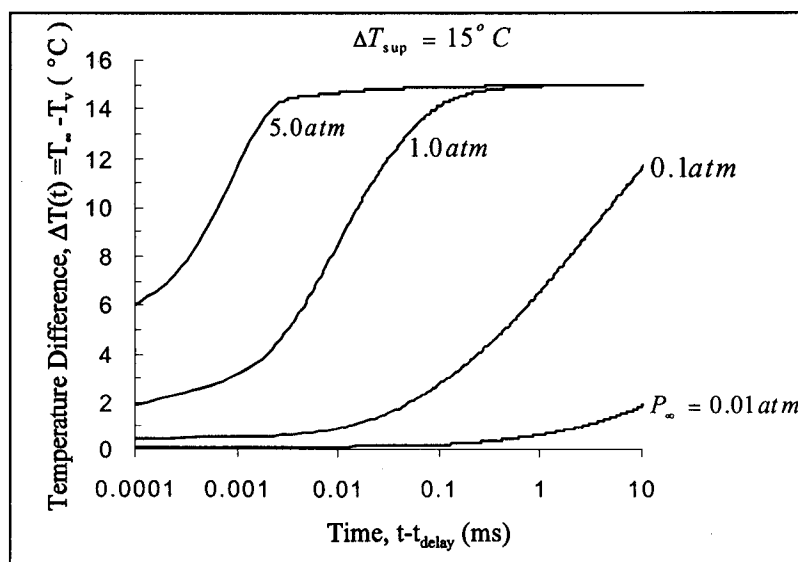
Figure 3.32: Temporal variation of the driving temperature difference during the transition domain for varying pressure at constant superheat.
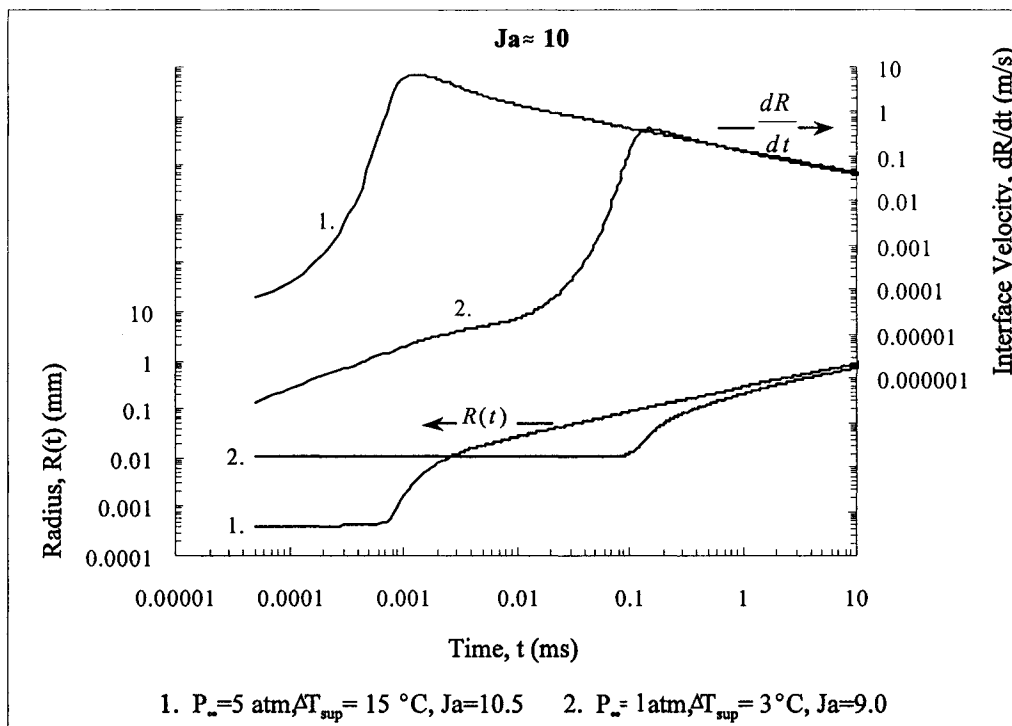
Figure 3.33: Radius and interface velocity curves for Ja≈10.
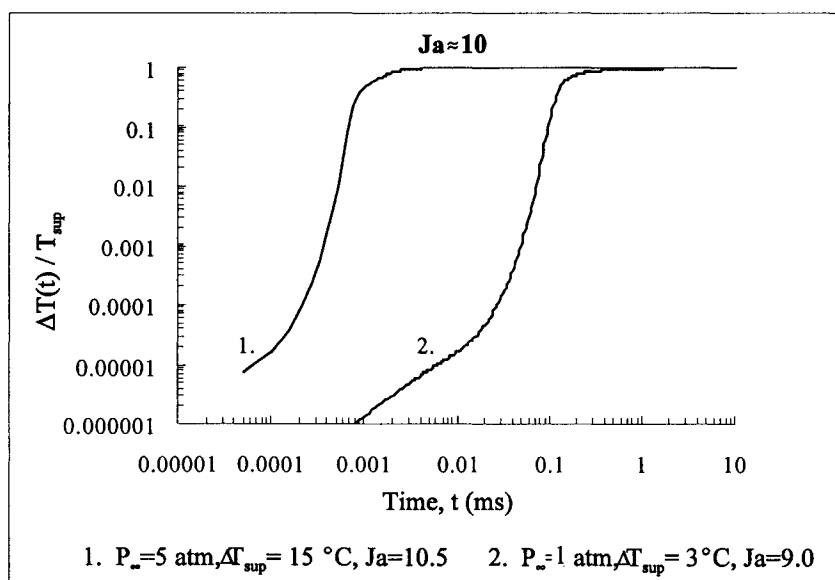
Figure 3.34: Normalized temperature difference curves for Ja≈10.

Ja≈90

$\dfrac{dR}{dt}$

10
1
0.1
0.01
0.001
0.0001
0.00001

Interface Velocity, dR/dt (m/s)

Radius, R(t) (mm)

10
1
0.1
0.01
0.001
0.0001

2.
1.
1.
2.

$R(t)$

0.00001   0.0001   0.001   0.01   0.1   1   10

Time, t (ms)

1. P_∞=0.5 atm,ΔT_{sup}= 15 °C, Ja=86   2. P_∞=1.0 atm, ΔT_{sup}= 30°C, Ja=90.
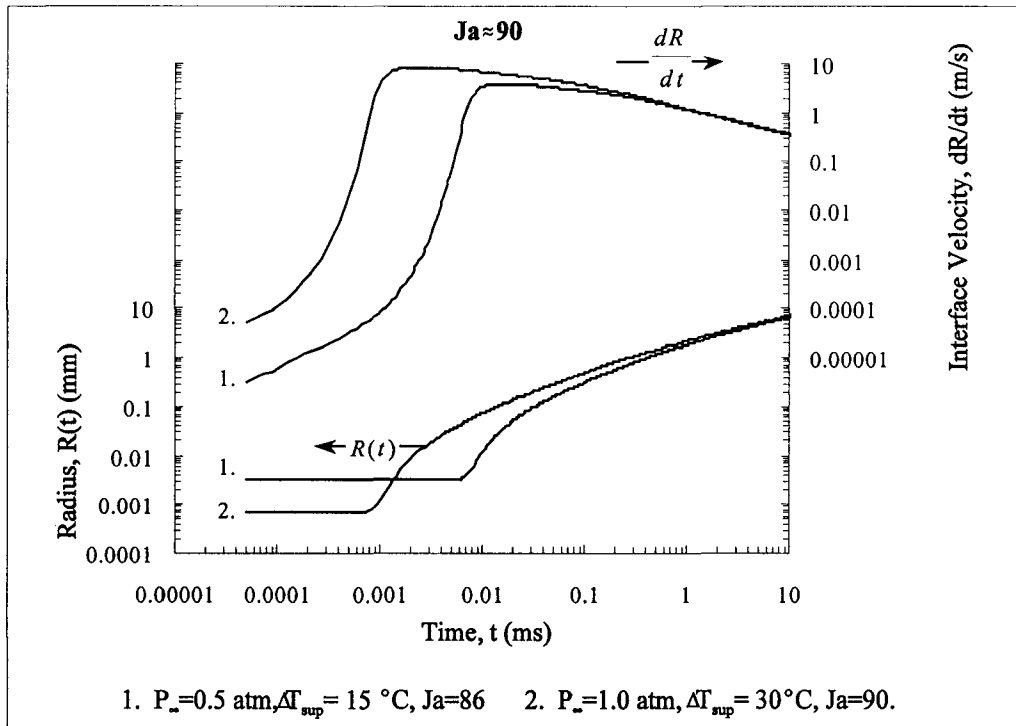
Figure 3.35: Radius and interface velocity curves for Ja≈90.

Ja≈90

1
0.1
0.01
0.001
0.0001
0.00001
0.000001

$\Delta T / T_{sup}$

2.
1.

0.00001   0.0001   0.001   0.01   0.1   1   10

Time, t (ms)

1. P_∞=0.5 atm,ΔT_{sup}= 15 °C, Ja=86   2. P_∞=1.0 atm, ΔT_{sup}= 30°C, Ja=90.
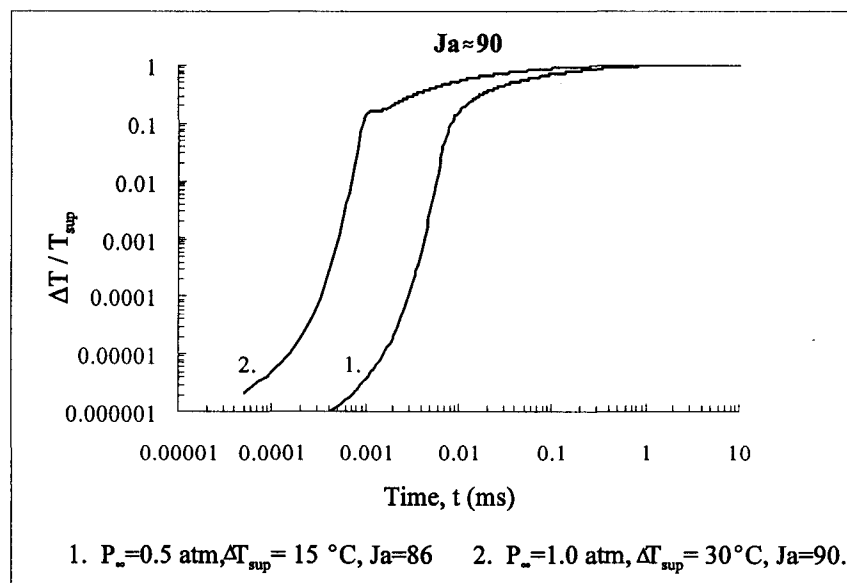
Figure 3.36: Normalized temperature difference curves for Ja≈90.
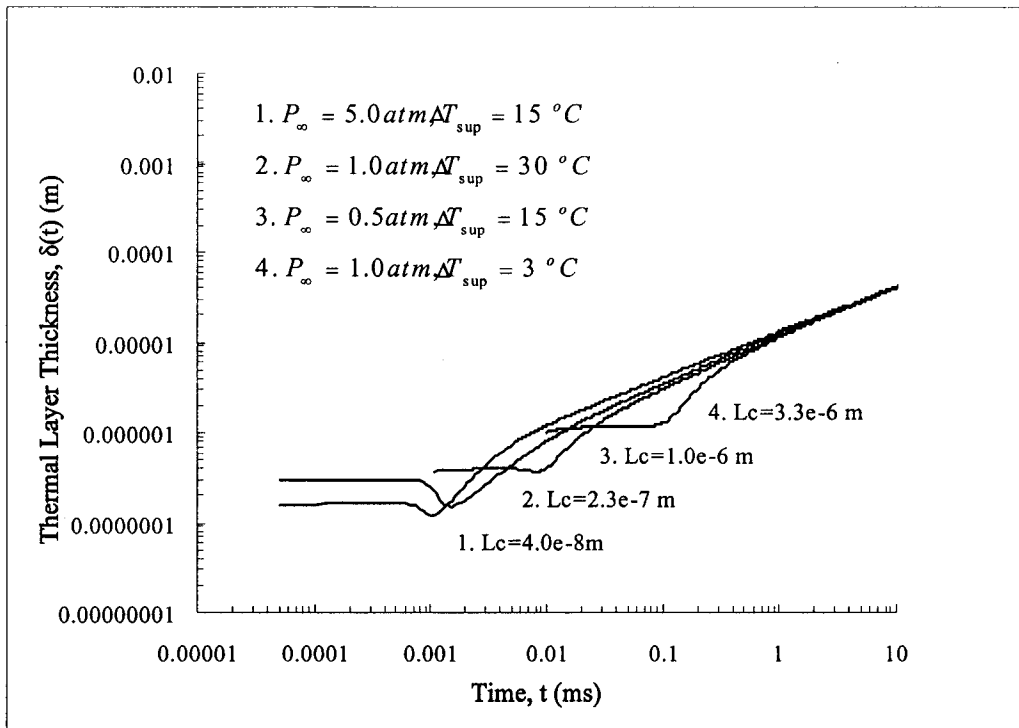
Figure 3.37: Growth of the thermal boundary layer for Ja≈10 and Ja≈90.

CHAPTER 4: HEMISPHERICAL BUBBLE GROWTH ON A HEATED

SURFACE IN MICROGRAVITY[1]

4.1 Introduction

The mechanisms associated with vapour bubble growth at a plane heated surface are not understood nearly as well as unbounded growth in an infinite pool. The large number of variables which influence heterogeneous bubble growth, combined with the difficult task of controlling and subsequently defining the temperature and flow fields in the vicinity of growing bubbles during experimental investigations, makes comparison of theoretical predictions with experimental measurements uncertain.

However, recent data has been reported by Lee [1993], Lee and Merte [1996], and Merte *et al* [1995], in which the shortcomings associated with earth gravity surface boiling experiments are partially overcome by heating a stagnant pool of liquid to the onset of boiling in microgravity. The absence of any significant natural convection, combined with the fact that during the early stages of growth, the thermal and flow fields are not influenced by previous or neighbouring bubbles, provide well defined initial and boundary conditions. Even still, the temperature distribution in the solid and liquid were not measured directly so that approximations are required for determining the initial liquid temperature field and the

---

[1]A significant portion of this chapter has been abstracted from Robinson, A. J. and Judd, R.L., 2001, "Bubble Growth in a Uniform and Spatially Distributed Temperature Field," published in the *International Journal of Heat and Mass Transfer*. The publication has been included in appendix G for reference purposes.

boundary condition for the solid heater. A further simplification results from the fact that for some of the measurements, the bubble remained nearly hemispherical for a significant portion of the growth period. The fixed bubble shape adds considerable simplification with respect to the theoretical modelling and the accompanying solution procedure. In this manner, Lee and Merte [1996] and Merte *et al* [1995] were able to compare the experimental hemispherical bubble growth data, obtained with R113 boiling on a flat solid surface subject to transient heating, and the theoretical predictions by means of a combination of two one-dimensional spherical models. With respect to the first model, an initial uniform liquid temperature, equal to the highest surface temperature that occurs at nucleation, was assumed. This represented the upper bound on the bubble growth rate since the highest temperature was assumed to exist everywhere throughout the liquid. With respect to the second model, a spherically symmetric, non-uniform temperature field around the bubble was assumed. The temperature distribution, assumed to be identical to that occurring normal to the heated surface at nucleation, was regarded as the 'minimum temperature distribution' and represented the lower bound on the bubble growth rate. All of the measured growth curves fell between bounds defined by the uniform and non-uniform models.

This chapter describes the development of a two-dimensional theoretical model which is capable of predicting both spherically symmetric vapour bubble growth in an infinite pool of liquid as depicted in Fig. 4.1a, and hemispherical vapour bubble growth at a heated plane surface depicted in Fig. 4.1b. The theory is the logical progression of the work provided in Lee [1993] and Lee and Merte [1996] in that it can incorporate either a one-dimensional radially symmetric or a two-dimensional spatially distributed liquid temperature field. It must be carefully noted that the applicability of the present model is

limited to the special case in which the energy utilized by the bubble as it grows is supplied by the superheated liquid layer which surrounds the bubble cap. Any contribution of an evaporating microlayer at the base of the bubble to the net mass transfer rate into the bubble, or its influence on the thermal field in the solid during heterogeneous bubble growth, is wholly disregarded.

The purpose of this investigation is twofold. Ones is to advance a simplified physical model and solution procedure for heterogeneous hemispherical bubble growth. A study of this simplified type of growth was undertaken because it provides a starting point for more complex theoretical development. A second is to elucidate the factors which contribute to heterogeneous bubble growth. In order to do that a significant portion of the growth period of a single isolated bubble was investigated beginning from inception in order to discern the proportional contributions of the various mechanisms which govern growth.

4.2. Formulation of the Problem

In the physical modelling of this problem, some of the concepts, idealizations and equations are the same as those expressed in chapter 2 and 3. For completeness and continuity, they will be repeated here but without rigorous definition and justification.

Fig. 4.2 shows a sketch of a hemispherical vapour bubble growing at a heated plane surface. Although a viscous boundary layer is known to exist in the liquid above the heated surface, in most practical situations this layer is very thin compared with the size of the bubble so that its overall influence on the bubble as it grows can be neglected. The inviscid fluid approximation, coupled with the impermeable wall boundary condition, allows for liquid flow symmetry to be assumed about the r-axis. As a result, hemispherical bubble

growth can be modelled as a half segment of the spherical case. In doing so, the equation of motion for the radius, R, of the hemispherical vapour bubble is approximated by the equation for a growing sphere given by,

$$P_v(T_v) - P_\infty = \rho_l R \frac{d^2 R}{dt^2} + \frac{3}{2}\rho_l \left(\frac{dR}{dt}\right)^2 + \frac{2\sigma}{R} \qquad (4.1)$$

Equation (4.1) is the extended Rayleigh equation which represents a force-momentum balance between the bubble and surrounding liquid.

During heterogeneous boiling, a bubble nucleates from a vapour nucleus which has been trapped within a small pit, scratch or crevice existing in the surface. The radius of the mouth of the cavity is believed to be an important factor in determining the time it takes for the vapour nucleus to begin significant growth because it partially dictates the initial thermodynamic state of the bubble. This dimension is extremely difficult to measure and is rarely, if ever, given as a part of the measured variable set which corresponds with an experimental bubble growth curve. With no knowledge of the cavity size from which the bubbles nucleate, it is reasonable to approximate the initial nucleus radius using the method described in Chapters 2 and 3. The initial bubble radius is determined by assuming that the vapour is initially saturated with $T_v = T_\infty$ and that it exists in unstable equilibrium with the quiescent surroundings. The stationary hemispherical vapour nucleus with internal pressure $P_{sat}(T_v)$ is in equilibrium with the ambient liquid and extends from the mouth of a cavity with radius predicted by the Young-Laplace equation,

$$R_c = \frac{2\sigma}{P_{sat}(T_v) - P_\infty}$$
(4.2)

As a result of the dependence of vapour pressure on temperature, another equation is required to fully describe this type of bubble growth problem. This expression is obtained by considering an energy balance at the vapour-liquid interface. The energy, Q, required to expand the bubble is supplied by molecular diffusion across the thin thermal boundary layer that exists in the liquid around the bubble. The rate of change of energy contained in the vapour bubble is given by,

$$\frac{dQ}{dt} = \int_{A_S} k_l \left(\frac{\partial T}{\partial r} \right)_{r=R(t)} dA$$
(4.3)

where A_s is the surface area of the bubble and $(\partial T/\partial r)_{r=R(t)}$ is the temperature gradient normal to the interface. For commonly used fluids well below the critical pressure, the interfacial energy balance can once again be reduced to,

$$\rho_v h_{fg} \frac{dR}{dt} + h_{fg} \frac{R}{3} \frac{d\rho_v}{dt} = \frac{1}{2\pi R^2} \int_{A_S} k_l \left(\frac{\partial T}{\partial r} \right)_{r=R(t)} dA$$
(4.4)

Typically, during nucleate pool boiling, energy is continually supplied to the liquid by heat transfer normal to the plane heated surface throughout the entire growth interval of the bubble. Furthermore, an initial liquid temperature distribution which is spherically symmetric around the bubble is not common for most practical boiling applications. These two conditions introduce two-dimensional effects which need to be accounted for in order

to adequately describe this type of bubble growth. As a result, the temperature gradient at the bubble wall is obtained by numerically solving the two-dimensional energy equation in axisymmetric cylindrical coordinates for the moving liquid,

$$\frac{\partial T}{\partial t} + U\frac{\partial T}{\partial r} + V\frac{\partial T}{\partial z} = \alpha_l\left(\frac{\partial^2 T}{\partial r^2} + \frac{1}{r}\frac{\partial T}{\partial r} + \frac{\partial T}{\partial z}\right) \qquad (4.5)$$

with initial and boundary conditions given by,

$$T(r,z,0) = T_o(r,z) \qquad \frac{\partial T}{\partial r}(0,z,t) = 0$$

$$T(r_b,z_b,t) = T_v \qquad \frac{\partial T}{\partial z}(r,0,t) = -\frac{q_w''}{k_l} \qquad (4.6)$$

$$T(\infty,\infty,t) = T_{1D}(z,t)$$

The initial condition requires the entire temperature field in the liquid to be specified. A zero flux boundary condition is assumed at the symmetry boundary (z-axis) and a constant heat flux boundary condition is established at the plane heated surface (r-axis). Some discussion is warranted concerning the assumption of a constant and uniform heat flux at the solid-liquid interface. Admittedly, this assumption significantly reduces the complexity of the problem by eluding the solution of the energy equation in the solid. However, Guo and El Genk [1996] showed that a constant heat flux can be a reasonable approximation for the case in which energy is supplied to the liquid by resistance heating of a thin metallic coating deposited on a glass substrate, so long as the layer is thin enough to restrict the lateral flow of heat through the metal coating. For the experiments presented in Lee [1993], Lee and Merte [1996] and Merte *et al* [1995] a 400-1400 Å transparent gold film was deposited on

a polished glass substrate. The thinness of the metallic layer precludes any significant lateral heat flow so that a constant heat flux boundary condition is an adequate representation of the surface for comparison with this data. A third boundary condition is obtained by assuming that the vapour phase is lumped and that the temperature of the liquid at the interface is identical to the temperature of the vapour. Finally, the far field boundary condition is approximated from the analytic solution for one-dimensional axial conduction in a semi-infinite medium. The axial and radial velocities are determined as functions of the instantaneous bubble radius and interface velocity by assuming that the flow field can be determined by the solution for potential flow around an expanding sphere in an unbounded liquid. The velocity components are,

$$U = \frac{dR}{dt} \left(\frac{R}{(r^2 + z^2)^{\frac{1}{2}}} \right)^2 \sin(\gamma)$$
$$V = \frac{dR}{dt} \left(\frac{R}{(r^2 + z^2)^{\frac{1}{2}}} \right)^2 \cos(\gamma)$$

(4.7)

Finally, it is postulated that the vapour is saturated and remains so throughout the bubble growth interval. In this way, the vapour pressure and density can be specified as functions of the saturated vapour temperature,

$$P_v(T_v) = a_1 T_v + a_2 T_v^2 + a_3 T_v^3 + a_4 T_v^4 + a_5 T_v^5$$
$$\rho_v(T_v) = c_1 T_v + c_2 T_v^2 + c_3 T_v^3 + c_4 T_v^4 + c_5 T_v^5$$

(4.8)

As in Chapter 2, the property variations with temperature are obtained from a fifth order polynomial representation of the available property data. With these simplifications, only the rate of change of one state variable, in this case temperature, need be considered given

that,

$$\frac{dP_v}{dt} = \left(\frac{dP_v}{dT_v}\right)\frac{dT_v}{dt}$$

$$\frac{d\rho_v}{dt} = \left(\frac{d\rho_v}{dT_v}\right)\frac{dT_v}{dt}$$

(4.9)

4.3. Computational Technique for the Energy Equation

Utilizing subscript notation to denote partial differentiation with respect to the subscript variable, the energy equation in axisymmetric cylindrical coordinates can be expressed as,

$$T_t + UT_r + VT_z = \alpha_l\left(T_{rr} + r^{-1}T_r + T_z\right)$$

(4.10)

where U and V are the axial and radial components of the liquid velocity defined in equation (4.7).

The energy equation was solved numerically on a grid which was constructed using an algebraic grid generation technique proposed by Chen *et al* [1995]. The grid variables in the physical domain are depicted in Fig. 4.3. Grid clustering near the vapour-liquid interface as well the moving boundary were facilitated by defining the grid such that,

$$r_{ij} = D_j\sin(\gamma_{ij})$$

$$z_{ij} = D_j\cos(\gamma_{ij})$$

(4.11)

where

$$\gamma_{ij} = \frac{\pi}{2}\left(\frac{i-1}{N-1}\right)$$

$$D_j = R + (R_\infty - R)\left(1 - S_R \tan^{-1}\left[\left(1 - \frac{j-1}{M-1}\right)\tan\left(\frac{1}{S_R}\right)\right]\right)$$

(4.12)

and the term S_R which determines the percentage of grid points near the interface and has been kept constant at $S_R = 0.65$ throughout this work. An example of the computational grid is depicted in Fig. 4.4. In order that conventional finite difference techniques could be utilized, the energy equation was transformed to a stationary grid with uniform grid spacing. The transformation is given by,

$$r = r(\varepsilon,\eta,\tau)$$
$$z = z(\varepsilon,\eta,\tau)$$
$$t = \tau$$

(4.13)

such that,

$$T_r = J^{-1}(z_\eta T_\varepsilon - z_\varepsilon T_\eta)$$
$$T_z = J^{-1}(r_\varepsilon T_\eta - r_\eta T_\varepsilon)$$
$$T_t = T_\tau - T_r r_\tau - T_z z_\tau$$

(4.14)

By defining the contravarient velocities as,

$$U^c = (U - r_\tau)z_\eta - (V - z_\tau)r_\eta$$
$$V^c = (V - z_\tau)r_\varepsilon - (U - r_\tau)z_\varepsilon$$

(4.15)

the transformed energy equation becomes,

$$T_\tau + J^{-1}U^c T_\varepsilon + J^{-1}V^c T_\eta = J^{-2}\alpha_i\left(aT_{\varepsilon\varepsilon} - 2bT_{\varepsilon\eta} + cT_{\eta\eta} + dT_\varepsilon + eT_\eta\right) + (Jr)^{-1}\alpha_i\left(z_\eta T_\varepsilon - z_\eta T_\eta\right) \tag{4.16}$$

where J is the Jacobian and the coefficients a through e are related to the metrics and their derivatives through the following,

$$\begin{aligned}
J &= z_\eta r_\varepsilon - z_\varepsilon r_\eta \\
a &= z_\eta^2 + r_\eta^2 \\
b &= r_\varepsilon r_\eta + z_\varepsilon z_\eta \\
c &= z_\eta^2 + z_\eta^2 \\
d &= J^{-1}(r_\eta \beta_1 - z_\eta \beta_2) \\
e &= J^{-1}(z_\varepsilon \beta_2 - r_\varepsilon \beta_1) \\
\beta_1 &= az_{\varepsilon\varepsilon} - 2bz_{\eta\varepsilon} + cz_{\eta\eta} \\
\beta_2 &= ar_{\varepsilon\varepsilon} - 2br_{\eta\varepsilon} + cr_{\eta\eta}
\end{aligned} \tag{4.17}$$

Equation (4.16) was discretized using second order central difference representations of the spatial derivatives and a fully implicit first order representation of the time derivatives. At a given time step, the temperature field was determined using Successive Over-Relaxation (SOR) by lines. For each line the resulting system of algebraic expressions was solved utilizing the Tri-Diagonal Matrix Algorithm (TDMA). The code was developed in FORTRAN 90 and is given in Appendix F.

4.4. Solution Procedure

Equation (4.8) and (4.9) together with equations (4.1) and (4.4) form a set of simultaneous equations for the four unknowns T_v, P_v, ρ_v, and R which were solved numerically using a fourth-order Runge-Kutta method. In order to initiate bubble growth, the equilibrium radius R_c was perturbed by allowing it to increase by a very small amount

over an infinitesimally small time interval. A comprehensive discussion on the initial

disturbance can be found in Chapter 2.

4.5. Code Verification

4.5.1. Spherical Bubble Growth

Grid independent benchmark solutions for spherically symmetric bubble growth in

liquids with an initial uniform superheat have been obtained in Chapter 2 for a range of

boiling conditions involving two different fluids. Since many of the more complex features

of heterogeneous growth are absent during homogeneous growth, comparison with the

benchmark solutions provide an excellent test for the present theory and computational

procedure. To investigate spherically symmetric growth, the initial temperature distribution

is set to be spatially uniform and symmetry about the r-axis is approximated by setting $q''_w=0$

to establish a zero temperature gradient.

Figs. 4.5 shows the comparison of the predictions of the present theory with the

benchmark solutions. In the figure, the numerical simulations, obtained using the two-

dimensional axisymmetric representation of the energy equation, show agreement with the

benchmark solutions for homogeneous bubble growth for a range of system pressures and

initial liquid superheats for two different fluids.

4.5.2. Hemispherical Bubble Growth

Heterogeneous bubble growth depends strongly on the amount of energy stored in

the thermal boundary layer which forms adjacent to the heater surface. The sensible heat

stored in the liquid is converted to latent heat by evaporation which flows into the bubble

as it grows. As a result, any predictive model of bubble growth requires that the temperature profile in the liquid be known prior to bubble growth. By heating a quiescent, uniform temperature liquid in microgravity, Lee [1993] was able to show that the solution of the one-dimensional transient heat conduction equation for a constant heat flux boundary condition in a semi-infinite solid did a very good job at predicting the measured mean surface temperature. Consequently, the initial temperature distribution in the liquid could be predicted by the expression,

$$T(z,t^*) = T_\infty + \frac{2q_w''\sqrt{\alpha_l t^*/\pi}}{k_l}\exp\left(-\frac{z^2}{4\alpha_l t^*}\right) - \frac{q_w''z}{k_l}erfc\left(\frac{z}{\sqrt{4\alpha_l t^*}}\right) \qquad (4.18)$$

where t^* is the time to the onset of boiling. This expression, together with the assumption of a quiescent liquid, specifies the initial conditions required by the present theory.

Bubble growth predictions for three different test cases are shown in Fig. 4.6. The condition of nearly zero gravity was obtained by performing the experiments in space aboard the NASA Space Shuttle. For each experiment, the computational predictions of the two one-dimensional spherically symmetric models, which represent the upper and lower bounds of growth, are given together with the two-dimensional heterogeneous model. As expected, the fully two-dimensional model predicts growth curves which are positioned somewhere in between the upper and lower bounds as depicted in the figure. More importantly, satisfactory agreement is observed between the measured growth curves over a large portion of the respective growth intervals. This lends support to the physical modelling of the problem as well as the numerical techniques utilized in the computations. It can be noted that the agreement between the computed and experimental curves lends support to the

assumption that, for these specific test cases, microlayer evaporation did not play a significant role in bubble growth process.

Fig. 4.7 shows the comparison of the present numerical simulations with the microgravity pool boiling experiments which were conducted in the drop tower facility at the NASA Lewis Research Centre. For approximately 15 ms, the agreement is quite good after which time the experimental curves increase at a significantly higher rate than the simulated curves. As discussed by Lee [1993], the mechanism responsible for the divergence of the two curves is bubble surface roughening. For early growth, the measured bubble interface is smooth as assumed for the simulated case. However, due to instabilities, the surface of the experimental bubbles became considerably roughened after t=15 ms. Since the surface area of the experimental bubbles is larger than that of a smooth interface, the overall heat transfer to the bubble is larger and thus the bubble expands at a higher rate. A comprehensive discussion of the role of instabilities in pool boiling can be found in Lee [1993].

4.6. Bubble Dynamics

In the following section, the growth characteristics of a single isolated hemispherical bubble growing at a plane heated surface with negligible effect of an evaporating microlayer will be discussed. The boiling conditions are identical to those of Fig. 4.6b. Fig. 4.8 shows the time variation of the predicted bubble radius and vapour temperature. In the figure, the four distinct regions of growth have been demarcated. For comparison purposes, the predicted curves for spherical homogeneous growth in a uniformly heated liquid are also shown in the figure. The liquid temperature for the homogeneous case was chosen to be the

heater surface temperature corresponding with the end of the waiting time, $T_\infty=T_w(t^*)=83.2$ °C. In Fig. 4.9 the energy equation for the vapour bubble, equation (4.4), has been decomposed to expose the time varying contributions of its constituent terms. Once again, the term involving the rate of change of vapour density, $^1/_3 h_{fg}R(d\rho_v/dt)$, is negligible compared with the interface velocity term, $\rho_v h_{fg}(dR/dt)$. For discussion purposes, the growth rate can be considered proportional to the area averaged heat flux into the bubble throughout its growth,

$$\frac{dR}{dt} \propto \frac{1}{A_s}\int_{A_S} k_l\left(\frac{\partial T}{\partial n}\right)_R dA = q''_{ave} \qquad (4.19)$$

4.6.1. The Waiting Time

The interval between the time when the heater is turned on and the time when the bubble appears to grow is termed the waiting time. During steady nucleate pool boiling, the waiting time is the time interval between the departure of the previous bubble and growth of the next. The waiting time is of fundamental importance during heterogeneous bubble growth because it is the time over which energy is transferred by thermal diffusion into the bulk liquid. Due to transient conduction, a thermal layer develops in the liquid adjacent to the wall. For long enough times, the liquid temperature rises above the saturation temperature of the liquid. Within this superheated layer exists the sensible energy required for the latent heat of evaporation.

One fundamental difference which distinguishes homogeneous growth in a uniformly superheated liquid and heterogeneous growth near a heated surface lies in the spatial distribution of the liquid temperature. For growth times much less than the waiting time,

heterogeneous bubble growth may occur in a liquid environment where the energy stored within the thermal layer is more or less fixed. If this is the case, the bubble has a finite amount of sensible energy from which to sustain growth, and depending on the heat flux and waiting time, it is possible for the bubble to deplete this energy in a relatively short time span. This is opposed to homogeneous growth where theoretically there is an infinite amount of energy available for bubble expansion.

4.6.2. Surface Tension Domain

A detailed discussion of growth dynamics occurring in the surface tension domain can be found in Chapter 3. In summary, the vapour bubble is expanding, although very slowly because it is still near its initial equilibrium state and the driving temperature difference for heat transfer $\Delta T = T_\infty - T_v$, and thus the heat flux into the bubble, is small as depicted in Fig. 4.9. However, Fig. 4.10 indicates that the hydrodynamic forces are negligible such that the vapour over-pressure is balanced by surface tension forces alone, $P_v - P_\infty = 2\sigma/R$. As a result, a minute increase in radius, as a result of the positive flow of energy into the bubble, causes a slight drop in the vapour pressure with a corresponding drop in the vapour temperature. This drop in temperature increases the driving temperature difference which increases the rate of heat transfer which in turn raises the growth rate (equation (4.19)). In this way the bubble expansion accelerates due to positive thermal feedback whereby the growth of the bubble is responsible for escalating its own rate of growth.

Referring to Fig. 4.8, it is evident that the characteristics of heterogeneous growth near a heated surface is the same as that for homogeneous growth in a uniformly superheated liquid during the surface tension stage, even though there exists an axial

distribution of temperature within the liquid adjacent to the heated surface. In the thermal layer adjacent to the heater surface the bulk liquid temperature varies from $T_w(t^*)=83.2$ °C at z=0 mm to $T_\infty=48.8$ °C at z≈0.9 mm. However, the bubble only protrudes a distance of $R_c=0.000156$mm into the liquid. Over this distance the liquid temperature changes by only 0.03 °C. Hence the bubble is essentially surrounded by a uniformly superheated liquid with $\Delta T_{sup}=T_w(t^*)-T_\infty=31.2$ °C. This is illustrated in Fig. 4.12 where the liquid temperature profiles along the z-axis (tip of bubble) and r-axis (base of bubble). For t=0.0001 ms, the end of the surface tension domain, Fig. 4.12a illustrates that the liquid temperature just outside of the thermal boundary layer is nearly constant and temperature variations in the bulk liquid occur far away from the bubble. Fig. 4.12b shows that for t=0.0001ms, the temperature profile near the vapour-liquid interface at the base is the same as at the tip which indicates spherical symmetry with respect to the liquid temperature distribution around the bubble. Since spatial variations of temperature within the bulk liquid occur far away from the interface, they do not contribute to the thermal transients occurring immediately adjacent to vapour-liquid interface. The bubble grows as if it were surrounded by a uniformly superheated liquid, the superheat being determined by the wall temperature at the end of the waiting time.

4.6.3 Transition Domain

A comprehensive discussion on growth dynamics during the transition domain can be found in Chapter 3. In summary, the transition domain is the interval of bubble growth during which the bubble undergoes significant expansion. The vapour pressure and temperature drop from near their maximum values of $P_{sat}(T_\infty)$ and T_∞ to their minimum

values of P_∞ and $T_{sat}(P_\infty)$ as depicted in Figs. 4.8 and 4.10 respectively. During the intermediate stage, the acceleration and velocity of the bubble interface increase dramatically as a consequence of an escalation in the positive thermal feedback. However, this effect is in part countered by an increase in the hydrodynamic pressure at the interface of the bubble as shown in Fig. 4.10. The increase in the hydrodynamic forces causes a noticeable reduction in the rate at which the vapour pressure and temperature drop as indicated by the inflection on the P_v-P_∞ and T_v curves (Figs. 4.8 and 4.10). As the bubble enters the inertial stage, the hydrodynamic pressure has risen to such an extent that surface tension becomes negligible and the rate at which the vapour pressure and temperature decrease is influenced considerably by the hydrodynamic forces at the interface. As discussed in Chapter 3, this effect coupled with changes in the thermal boundary layer surrounding the bubble are responsible for the continually decreasing growth rate depicted in Fig. 4.9.

Referring to Fig. 4.8, heterogeneous growth near the heated surface still shows the same characteristics of growth as homogeneous growth in a uniformly superheated liquid. Although the bubble has undergone a three order of magnitude increase in radius, it is still fully contained within the superheated layer which was established adjacent to the heated surface during the waiting time.

Fig. 4.13 shows the isotherms surrounding the bubble for t=0.01 ms, which corresponds roughly with the middle of the transition domain. In Fig. 4.13a, it is apparent that the bubble is beginning to penetrate into the thermal layer as indicated by the deflection of the isotherms of the bulk of the liquid above the bubble. Fig. 4.13b demonstrates that there is still radial symmetry in the temperature profiles surrounding the bubble, which is

consistent with one-dimensional homogeneous growth, and the isotherms are clustered near the vapour-liquid interface due to the high evaporative heat flux. Although the effects of the two-dimensional spatial distribution in the liquid temperature have not yet had a noticeable influence on the growth characteristics of the bubble, they are beginning to show. Fig. 4.12 demonstrates that for $0.001ms \leq t \leq 0.1ms$, the developing temperature profiles at the tip of the bubble are beginning to change significantly. For t=0.001 ms the liquid temperature increases to nearly T_w=83.2 °C and spatial variations within the bulk liquid are still far enough away from the vapour-liquid interface that their effects are not yet felt. At this time the thermal gradients at the tip and base of the bubble are nearly equal, as shown in Fig. 4.11, which indicates a uniform distribution of the energy flux around the bubble. For t=0.01 ms and t=0.1 ms, the maximum liquid temperature above the bubble is noticeably smaller than T_w=83.2 °C which signifies that the sensible energy stored in the liquid is slowly being depleted by the growing bubble. From this time onward, the rate of heat diffusion near the bubble tip will be less than that near the base since the driving temperature difference is smaller. This is illustrated in Fig. 4.11 for t>0.01 ms.

4.6.4 Heat Transfer Domain

Heat transfer controlled growth refers to the interval of bubble growth in which the rate of bubble expansion is limited by the rate at which liquid is evaporated into the bubble, which in turn is dictated by the net rate of heat transfer by diffusion through the liquid. In this late stage of bubble growth, the vapour pressure and temperature have decreased to their minimum values corresponding with P_v=P_∞ and T_v=$T_{sat}(P_\infty)$ as illustrated in Fig. 4.8 and 4.10 respectively. Because the liquid temperature at the vapour-liquid interface is now constant,

the positive thermal feedback does not occur in this domain of growth. As a result, liquid inertia and surface tension have a negligible influence on bubble growth. Conversely, the 'shrinking' and 'stretching' of the thermal layer in the liquid due to conduction and advection are responsible for the continuous deceleration of the interface due to the diminishing interfacial temperature gradients. Fig. 4.11 shows that the temperature gradients in the liquid surrounding the bubble have reduced considerably. Furthermore, the thermal gradient at the tip of the bubble is substantially less than that of the base which indicate that two-dimensional spatial effects have now become a factor in determining the growth rate of the bubble. This is confirmed by the departure between the predicted bubble radius for the heterogeneous and homogeneous cases shown in Fig. 4.8.

Fig. 4.14 shows the isotherms for t=1.0 ms. Fig. 4.14a shows that the bubble has grown to such an extent that it now penetrates deep into the thermal layer which was established during the waiting time. Fig 4.15b shows a magnification for the same case. In this figure the two-dimensional spatial effects become apparent. In the upper region of the bubble (z>0.3 mm) the surrounding liquid is comparatively cool and the isotherms are not tightly clustered. Together these indicate that the superheat in this region is nearly depleted. In the lower region (z<0.3 mm) the bubble is surrounded by liquid which is still substantially superheated considering that the T=65 °C isotherm corresponds to a superheat of 13 °C. The maximum temperature in the liquid adjacent to the bubble interface increases as heater surface is approached. The figure also shows that the local heat flux into the bubble increases near the heater surface as the isotherms become more tightly clustered at the vapour-liquid interface. Fig. 4.15 shows the isotherms for t=100 ms. Here the two-dimensional spatial effects are even more noticeable since the bubble is now almost completely outside of the

thermal layer adjacent to the wall. Here, the majority of the bubble protrudes into the comparatively cool bulk liquid, some of it being subcooled. It is only in a small region near the triple interface that significant clustering of the isotherms occurs.

The two-dimensional spatial effects can be characterized by considering the tip and base of the bubble as the limiting cases. Fig.4.12a and 4.12b illustrate the 'shrinking' and 'stretching' of the thermal boundary layer at the tip and base of the bubble which is responsible for the reduction in the bubble growth rate during the heat transfer domain. At the tip of the bubble, Fig. 4.12a shows that for $t>0.1$ ms, the maximum temperature is considerably less than $T_w=83.2$ °C and is moving further out from the bubble. Together these act to reduce the local heat flux. At the other extreme, the liquid temperature profile at the base of the bubble, as depicted in Fig. 4.12b, shows the maximum temperature moving further out from the interface indicating an increase in the thermal layer thickness and a corresponding reduction in the local heat flux. The decrease in the growth rate is compounded by the fact that for $t>10$, ms the top portion of the bubble penetrates into a region of liquid which is subcooled. This point is illustrated in Fig. 4.11 with the negative value of the interface temperature gradient for the tip of the bubble. Hence from this time onward, the net energy transfer into the bubble is the difference between that which leaves by condensation and that which enters by evaporation.

During the growth of the bubble, energy is continually being transferred into the liquid by axial conduction from the heater surface. At any point along the heated surface outside of the bubble, there are three heat transfer mechanisms which act together to transport the imposed heat flux; radial conduction tangent to the heater surface, axial conduction normal to the heater surface, and convection due to the flow of liquid over the

surface. Referring to Fig. 4.12b, the lower temperatures in the immediate vicinity of the bubble indicate that the imposed heat flux is being transported away from the surface very efficiently. This region is characterized by a relatively high evaporative heat flux into the bubble together with the possibility of significant convective heat transfer because it is the region of highest liquid velocity. This is shown in Fig 4.15b where the isotherms are tightly packed around the bubble near the triple interface. Moving further away from the interface, the influence of evaporation becomes less and the contribution of convective heat transfer decreases due to the rapidly diminishing liquid velocity $(U(r,0,t) \propto 1/r^2)$. The surface temperature increases as the less efficient mode of axial conduction normal to the surface becomes the prominent mode of heat transfer. One might expect the surface temperature to increase asymptotically to the surface temperature in the undisturbed region at R_∞. However, liquid motions induced by the growing bubble have deflected the isotherms away from the heater surface causing the thermal layer thickness to be thicker in the vicinity of the bubble. This is depicted in Fig. 4.15b. Consequently, in order that axial conduction can accommodate the imposed surface heat flux, the surface temperature must be higher in the region of the thicker boundary layer nearer the interface. This is the likely mechanism responsible for the observed overshoot in the liquid temperature profile at the heated surface depicted in Fig. 4.12b.
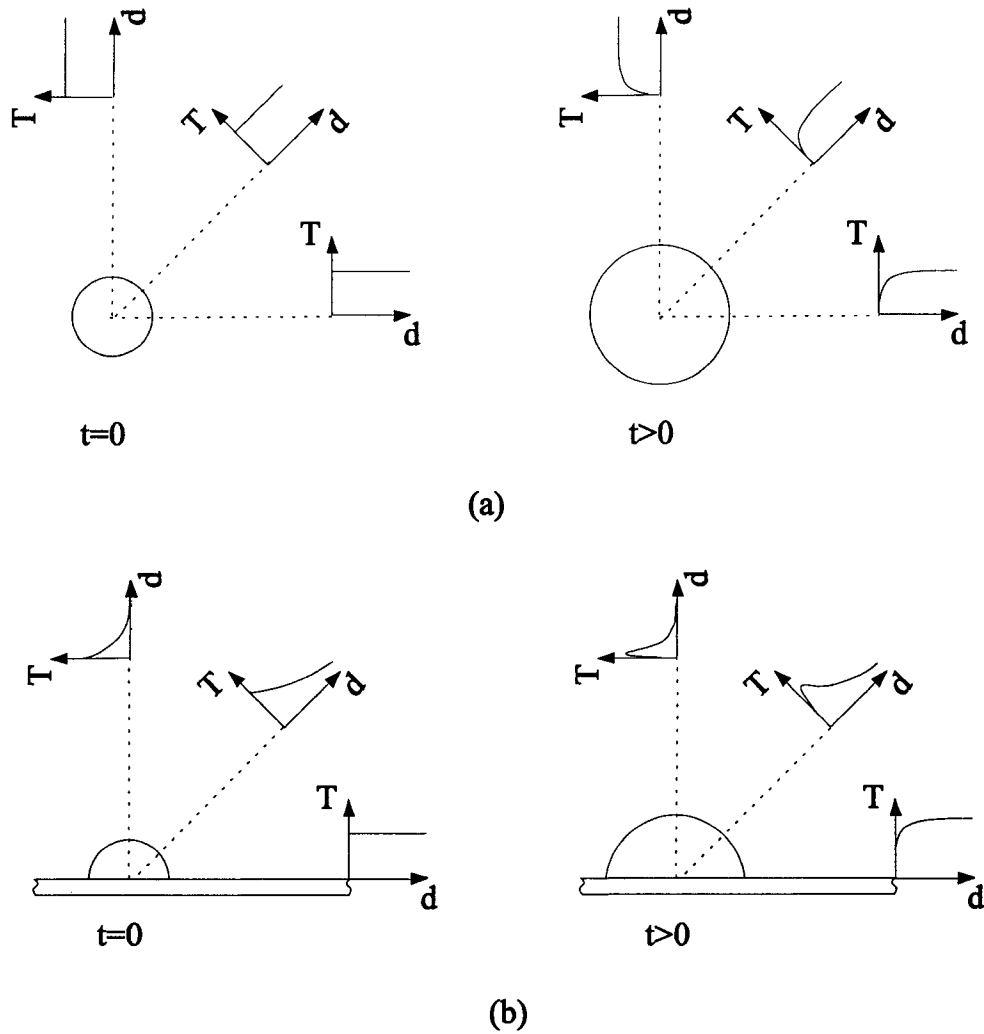
Figure 4.1:(a) Spherical vapour bubble growth in an unbounded liquid with a uniform temperature field at t=0 and a spherically symmetric temperature profile for t>0. (b) Hemispherical vapour bubble growth at a heated flat surface with a non-uniform temperature field at t=0 and a spherically non-symmetric temperature profile for t>0.
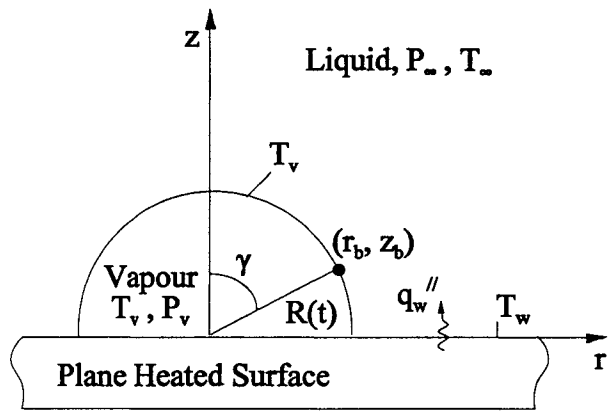
Figure 4.2: Hemispherical bubble growing on a plane heated surface.
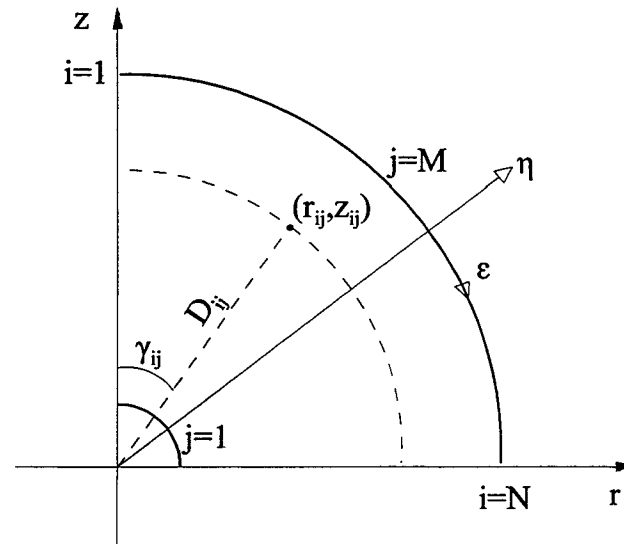
Figure 4.3: Grid parameters.
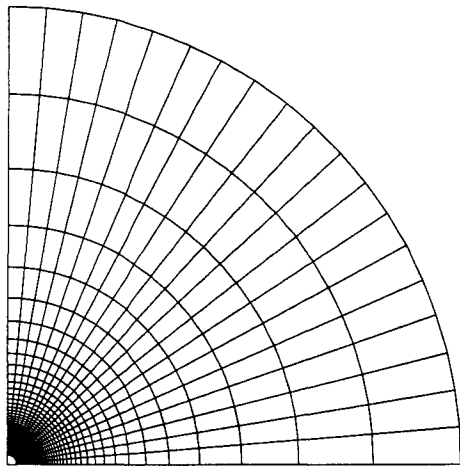
Figure 4.4: Computational grid.
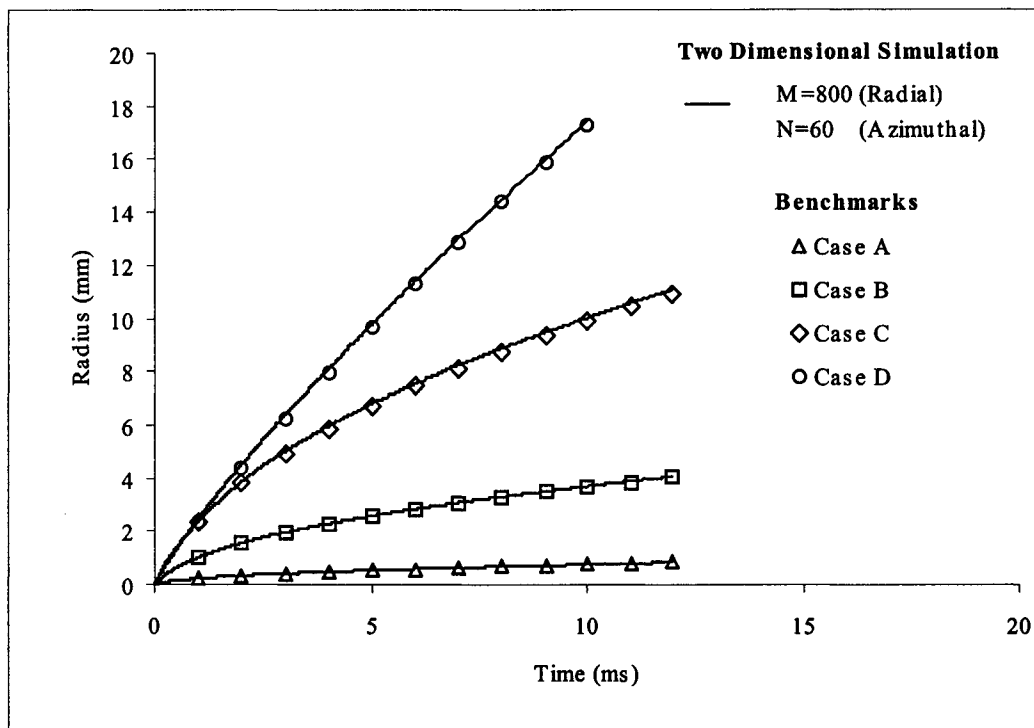
Figure 4.5: Comparison of prediction of two-dimensional simulations with benchmark solutions for spherically symmetric growth with uniform superheat. Case A: water, 1.0 atm, 3.1 °C. Case B: water, 0.372 atm, 6.3 °C. Case C: water, 0.362 atm, 17.0 °C. Case D: R113, 0.0361 atm, 48.1 °C.
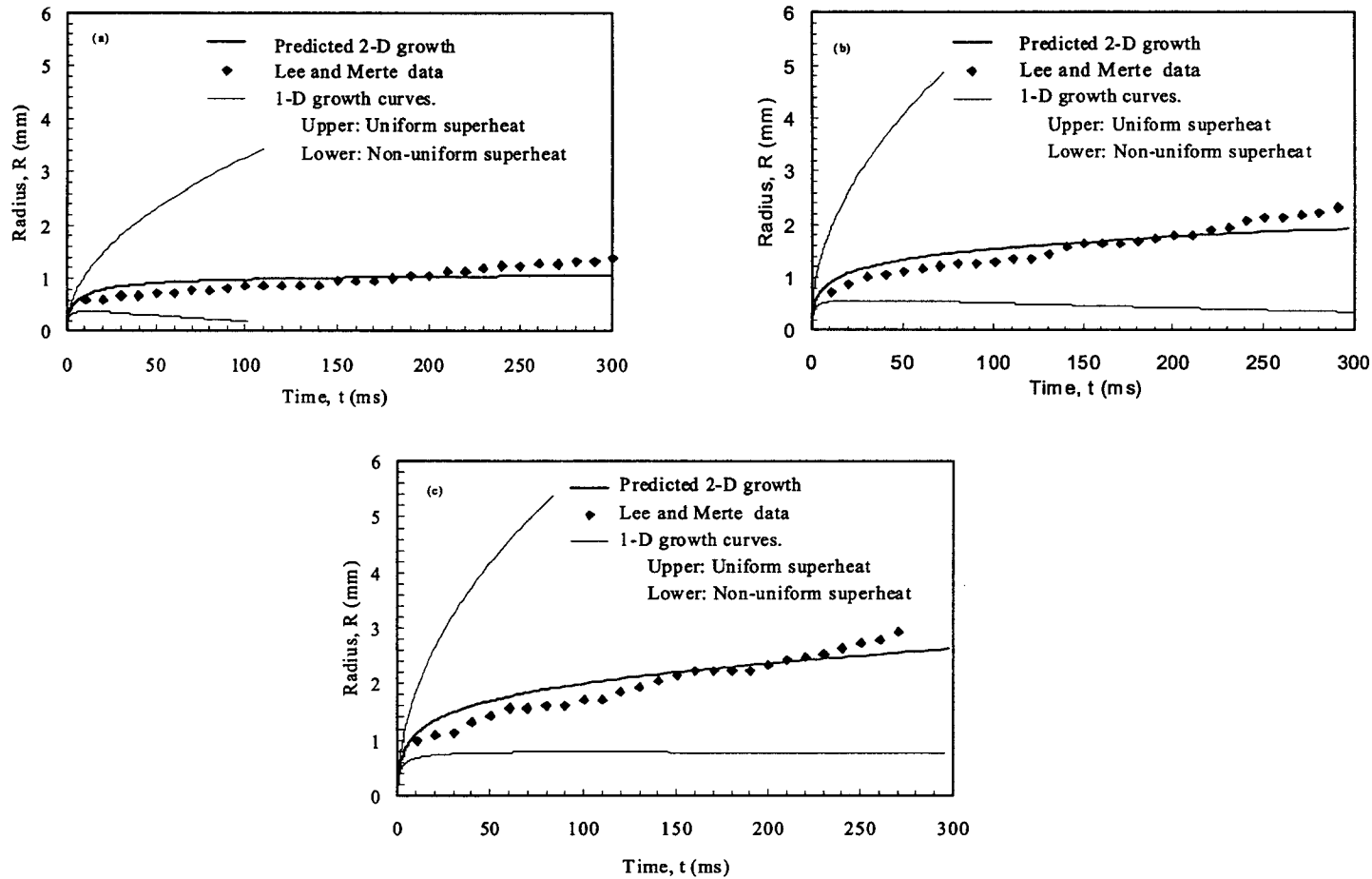
Figure 4.6: Comparison of computed results with experiments for hemispherical bubble growth of R113 on a heated plane surface in microgravity: Space data, $g_a/g=10^{-4}$ (a) $q''=7$ W/cm^2, $P_\infty=149.9$ kPa, $T_{sat}=59.8°$C, $T_\infty=48.3°$C, $t^*=0.91$, $T_w^*=85.8°$C, (b) $q''=6.5$ W/cm^2, $P_\infty=117.3$ kPa, $T_{sat}=52°$C, $T_\infty=48.8°$C, $t^*=0.74$s, $T_w^*=86.3°$C, (c) $q''=6.95$ W/cm^2, $P_\infty=106.8$ kPa, $T_{sat}=49.1°$C, $T_\infty=48.35°$C, $t^*=0.75$s, $T_w^*=84.1°$C.
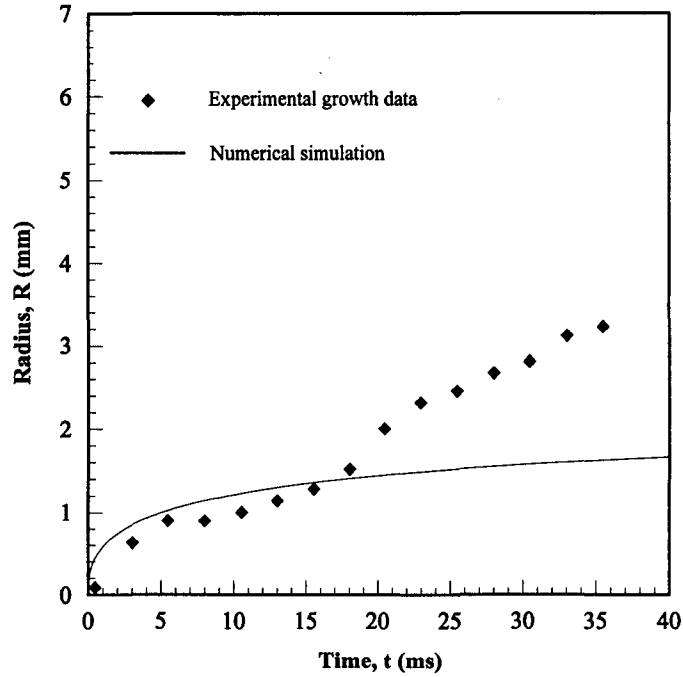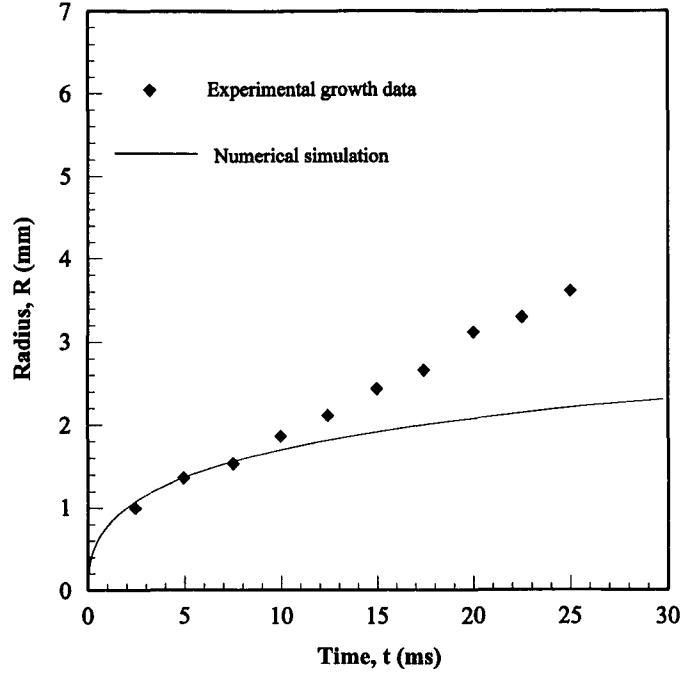
Figure 4.7: Comparison of computed results with experiments for hemispherical bubble growth of R113 on a heated plane surface in microgravity: Drop tower data, (a) $q''=7.87$ W/cm^2, $P_\infty=142.34$ kPa, $T_{sat}=58.19°C$, $T_\infty=47.06°C$, $t^*=1.55$ s, $T_w^*=110$ °C, (b) $q''=6.33$ W/cm^2, $P_\infty=103.32$ kPa, $T_{sat}=48.14$ °C, $T_\infty=47.33°C$, $t^*=1.55$ s, $T_w^*=100$ °C.
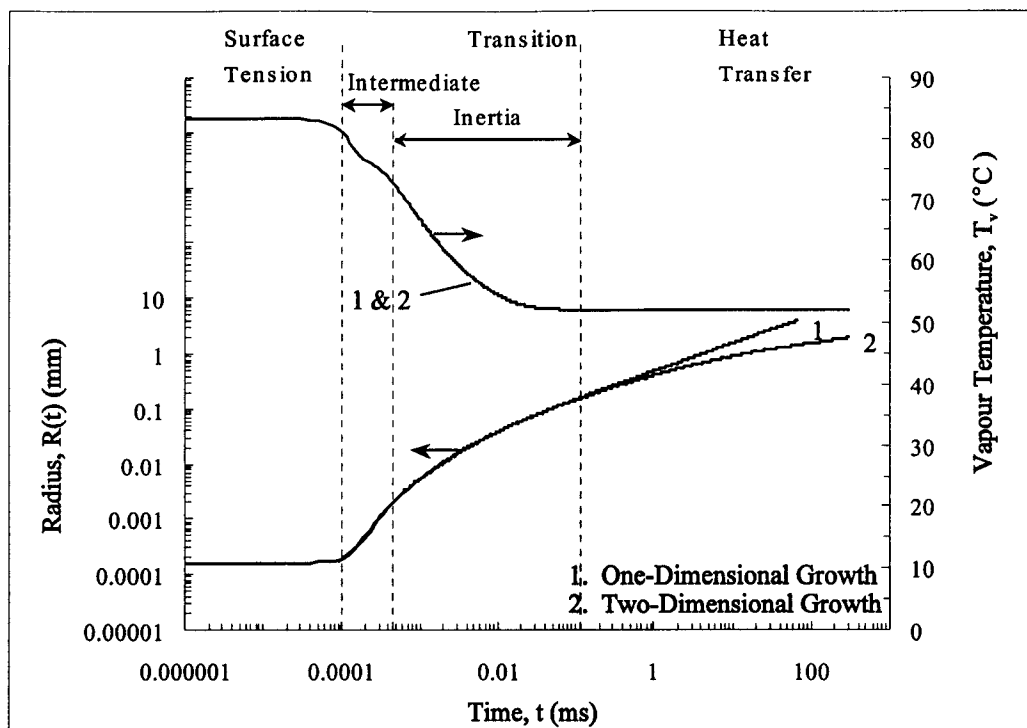
Figure 4.8: Bubble radius, R(t) and temperature, T_v, histories for hemispherical bubble growing atop a heated surface and spherical growth in a uniformly superheated liquid with $\Delta T_{sup}=31.2\ °C$.
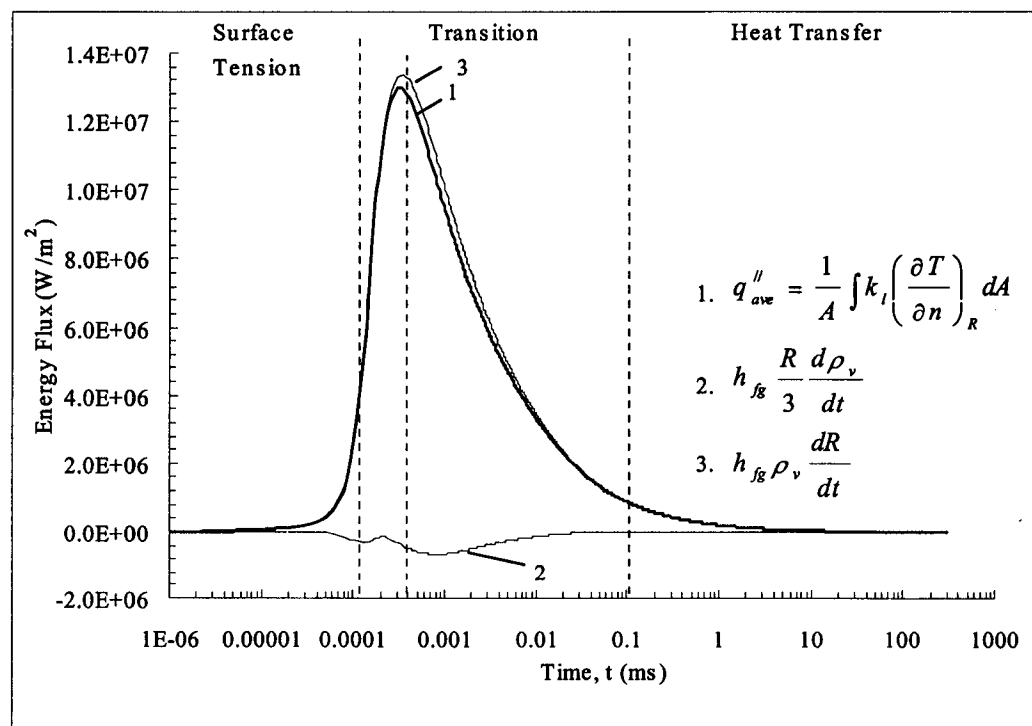
Figure 4.9: Decomposition of the energy equation, equation (4.4).

Figure 4.10: (a) Decomposition of the equation of motion, equation (4.1) (b) Constituent terms of the hydrodynamic pressure term
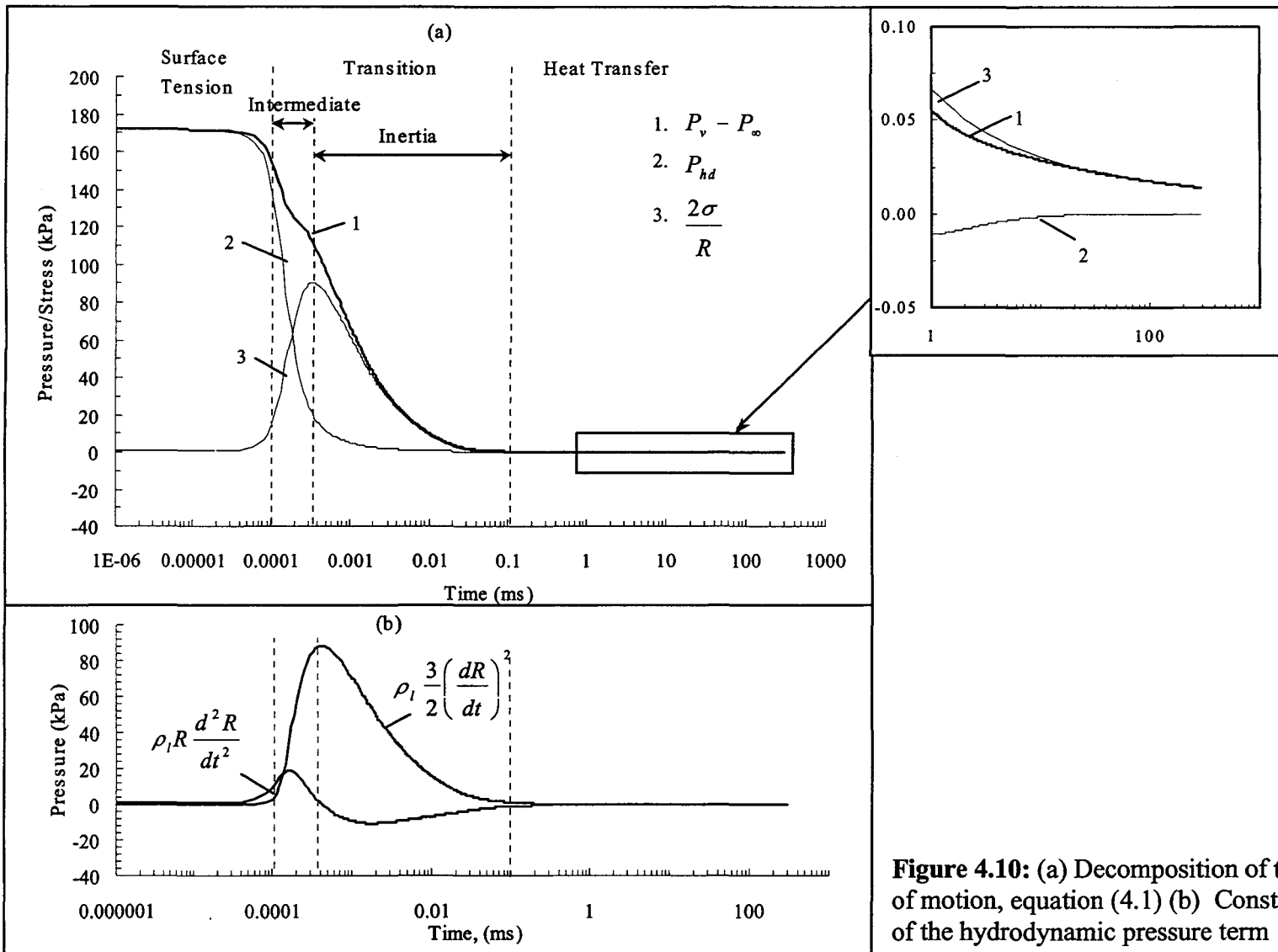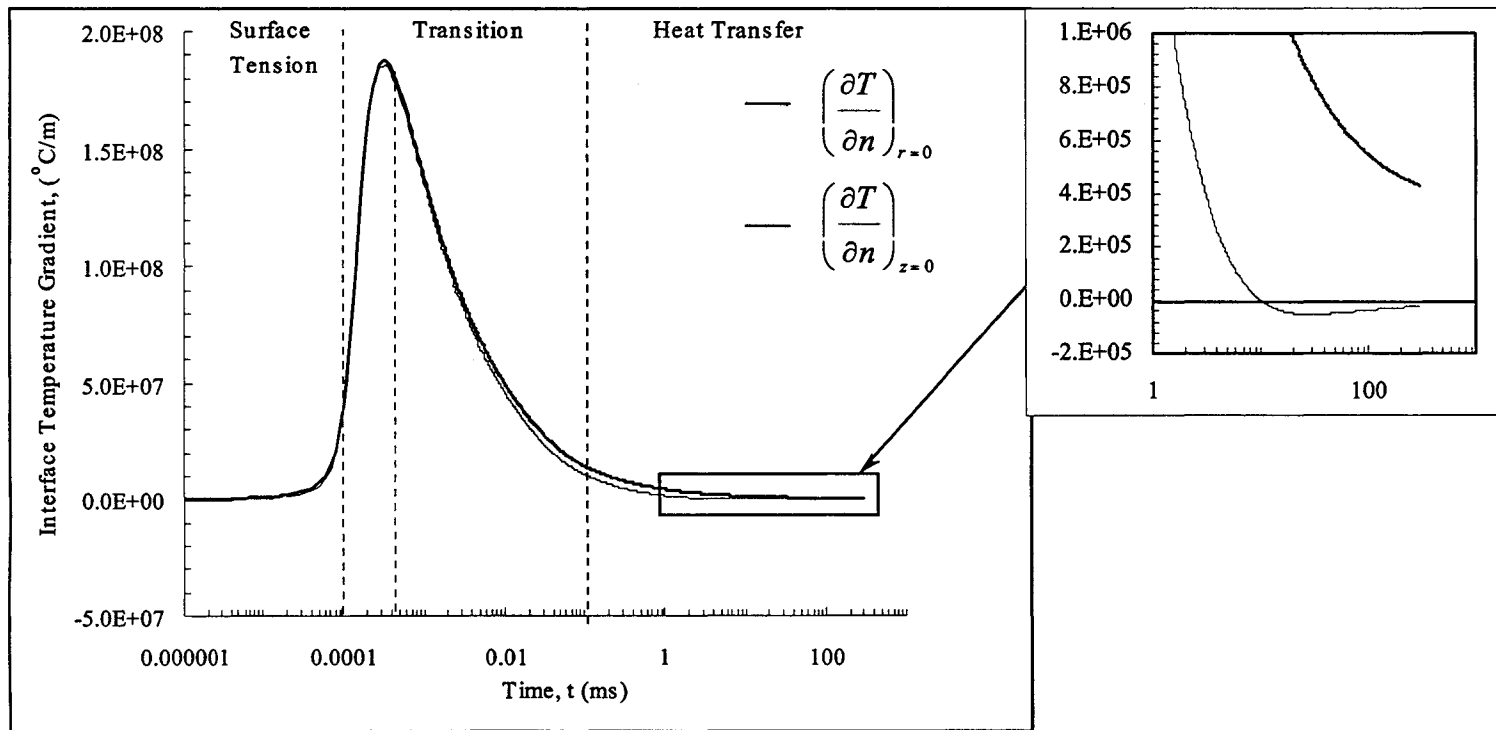
Figure 4.11: Interfacial liquid temperature gradient histories at the top of the hemispherical bubble (along z-axis), and the base of the hemispherical bubble (along r-axis).
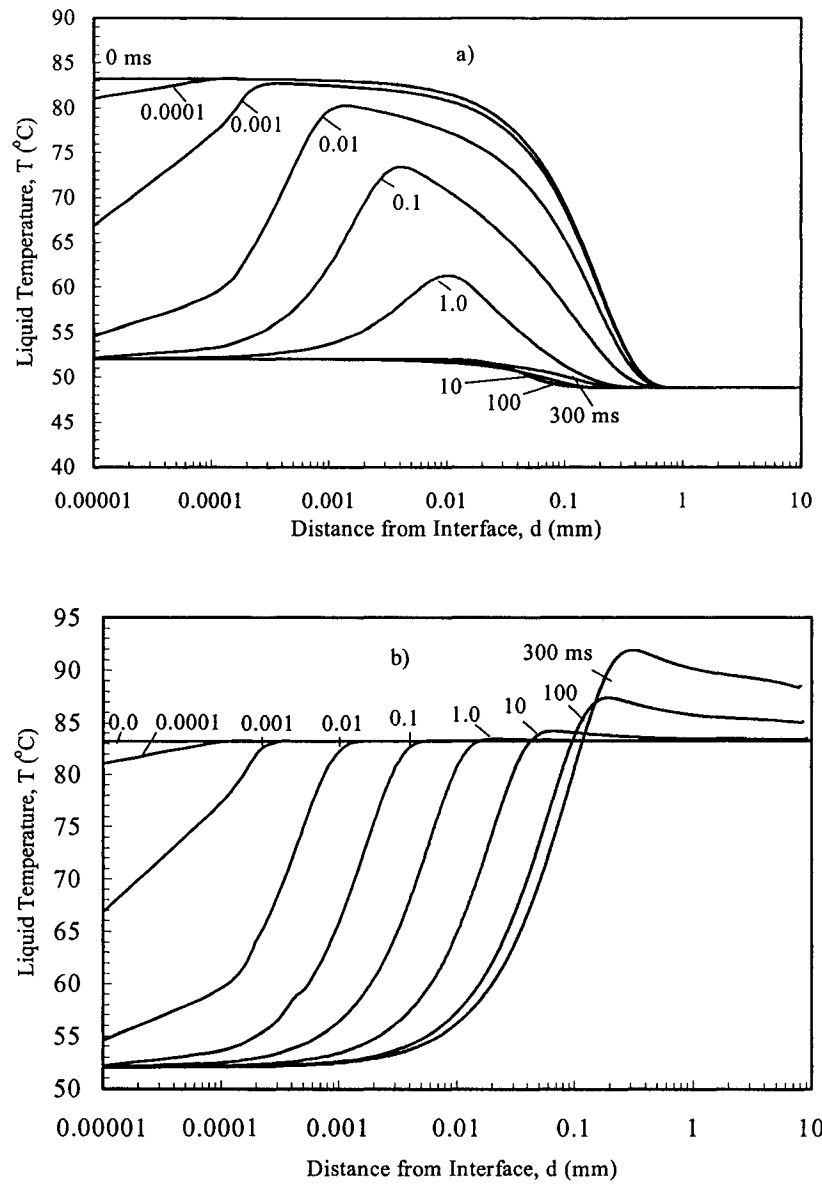
Figure 4.12: Computed liquid temperature distribution at (a) the top of the hemispherical bubble (along z-axis), and (b) the base of the hemispherical bubble (along r-axis) at various times.
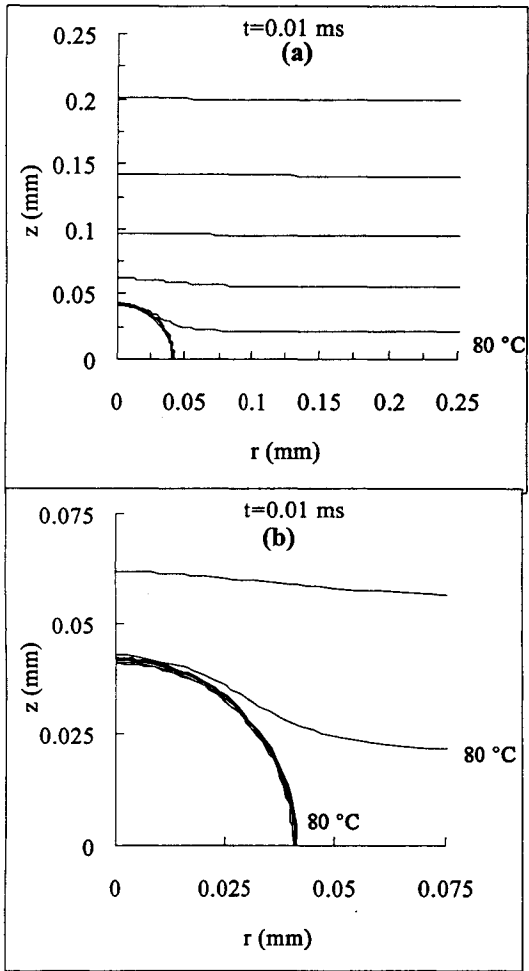
Figure 4.13: Isotherms surrounding the growing bubble at the end of the transition domain, t=0.01 ms. Isotherms are separated in 5 °C increments.
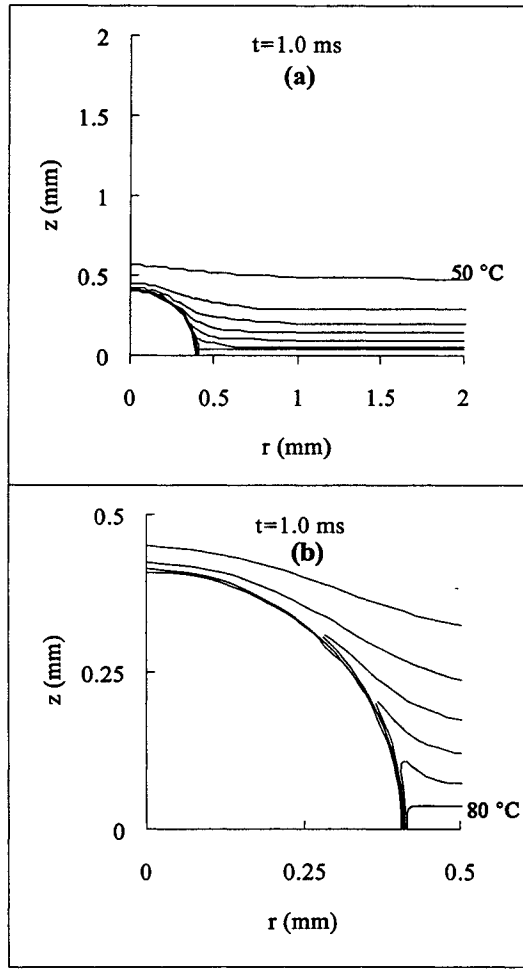
Figure 4.14: Isotherms surrounding the growing bubble at the end of the transition domain, t=1.0 ms. Isotherms are separated in 5 °C increments.
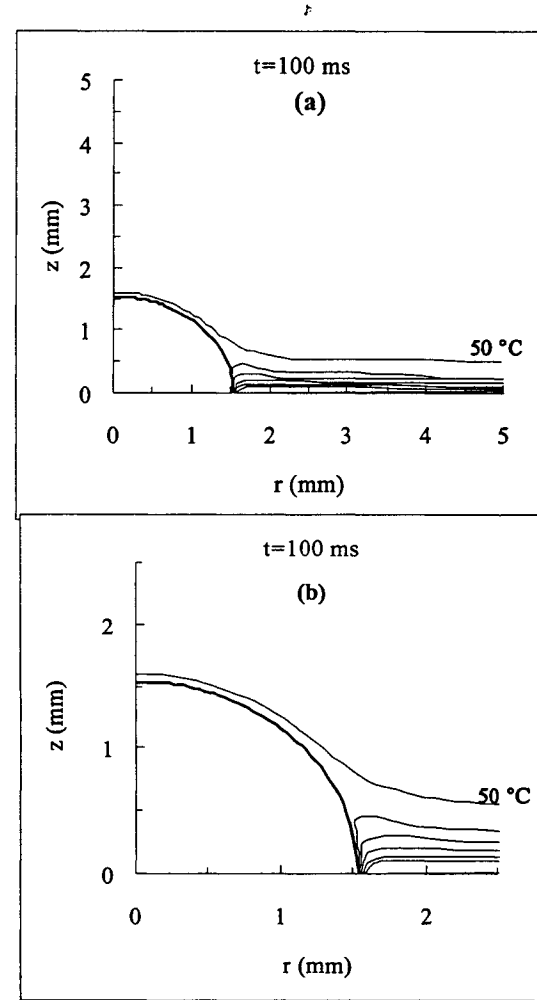
Figure 4.15: Isotherms surrounding the growing bubble at the end of the transition domain, t=100 ms. Isotherms are separated in 5 °C increments.

CHAPTER 5: SUMMARY AND RECOMMENDATIONS

FOR FUTURE WORK

5.1. Conclusions

In Chapter 2, a theoretical model and numerical procedure has been developed to predict spherically symmetric bubble growth in an unbounded liquid with initial uniform superheat. It was determined that 40000 grid points were sufficient to obtain a converged solution on a grid with uniform spacing between adjacent nodes. The converged solution was shown to be independent of time step, far field boundary placement and initial disturbance. Solutions on a uniform grid were also employed to approximate grid independent solutions on an infinite grid. The four infinite grid approximations for bubble growth cover a sufficient range of initial system conditions and are proposed as benchmark solutions for further theoretical development. Excellent agreement is observed between the prediction of the present work and the analytical solutions of Mikic *et al.* [1971] and Plesset and Zwick [1954] as well as the measured bubble growth data of Dergarabedian [1953], Board and Duffy [1971] and Bohrer [1973].

A grid clustering technique was implemented to reduce the total number of grid points required to obtain a converged solution. This resulted in a marked decrease in total computation time for a given growth curve without appreciable loss in accuracy. With the more efficient code, comparisons have been made between the predictions of the present work and the experimental data obtained from four independent experimental investigations

in which a variety of techniques had been used to initiate homogeneous boiling. The experimental data covered a wide range of initial liquid states for two different fluids. Close agreement was observed between the present work and those experiments which utilized slow transient heating or slow depressurization to obtain the initial metastable liquid state. Caution should be exercised when making comparisons with measurements obtained using rapid-depressurization techniques.

The close agreement between the analytic solutions, experimental data and the predictions of the present numerical work over such a wide range of boiling conditions instills confidence in the physical modelling of the problem as well as the numerical procedure which has been utilized to solve the relationship.

In Chapter 3 the complicated thermal and hydrodynamic interactions between the vapour and liquid have been manifested for a single isolated bubble growing in an unbounded liquid from inception to fully heat transfer limited growth. It has been shown that early bubble growth away from the initial radius is restricted by surface tension forces within the bubble wall. However, minuscule increases in radius result in an increase in the local interfacial temperature gradient which facilitates growth by increasing the heat flux into the bubble. Eventually, bubble growth becomes impeded by the fact that it now must force the surrounding liquid out radially. The heat flux increases to such an extent that this becomes a limiting factor to growth. Nevertheless, the growth rate must eventually decrease with increasing time as the thermal energy stored within the boundary layer which surrounds the bubble is consumed by the bubble as well as transported away from the bubble by advection into the bulk of the liquid. Eventually the growth rate slows enough that liquid inertia no longer plays an important role and the growth rate becomes limited by the rate at which

energy can be transported to the interface through the liquid.

Increasing the liquid superheat for a fixed ambient pressure has a significant effect on each individual growth domain. Higher superheats require smaller bubbles to initiate growth. The smaller bubbles define a length scale which allows them to react quickly to the changing thermal environment in such a way that the surface tension domain is shorter for higher superheats. These comparatively small bubbles grow rapidly enough that liquid inertia begins to play a role in limiting growth by slowing down the rate at which the vapour pressure and temperature decrease. Here the transition domain is prolonged due to liquid inertia. For low superheats, the bubbles grow much slower and the effects of the liquid inertia may not be felt at all. Here thermal diffusion is the only limiting factor for growth. During the thermal diffusion stage of growth, the thickness of the thermal boundary layer becomes independent of the liquid superheat and bubble size. The growth rate then becomes governed primarily by the magnitude of the liquid superheat since property variations are small for the range of temperatures tested. The higher superheats generate a higher growth rate which produces larger bubbles

Increasing the ambient liquid pressure at a fixed level of superheat has virtually the same effect on the surface tension domain as increasing superheat. Here the smaller bubbles grow quickly away from their initial equilibrium radius. In contrast, however, these rapidly growing bubbles are not able to sustain a high growth rate because the interface velocity is not large enough for liquid inertia to become a limiting factor. However, bubbles growing in a lower pressure environment are able to generate substantial hydrodynamic forces which regulate the rate at which the vapour pressure and temperature drop. This is accompanied by the fact that these bubbles require less energy to sustain growth due to a lower vapour

density. Similarly, for the same superheat, lower pressures produce larger bubbles once they enter the thermal diffusion stage of growth since the same amount of energy will produce a larger volume of vapour due to the reduced vapour density.

In recent years, theoretical developments in nucleate pool boiling have been focussed on isolated bubble growth upon a heated surface. It is hoped that understanding of the mechanisms which determine growth of the bubble will offer insight into and perhaps predictions of the increased heat transfer coefficient observed in nucleate pool boiling. However, advances in the state of the art are inhibited by the apparent stochastic nature of boiling due to the rapidly varying thermal and flow fields. As a result of the overwhelming complexities, sufficient testing of the physical modelling and computational procedures has not been afforded in the past.

In Chapter 4, a simple theory and numerical procedure have been developed which overcome this shortcoming in two ways. First, the theory is simple enough to facilitate comparison with data for homogeneous growth in an unbounded fluid. Second, the theory can accommodate the added complexities of a heated surface and time varying spatially distributed liquid temperature fields for hemispherical bubble growth in microgravity. Close agreement has been observed between the predictions of the present theory and the one-dimensional benchmark solutions, as well as with experimental data for hemispherical bubble growth on a heated surface. This has instilled confidence in the physical modelling of the problem as well as the computational procedure which has been utilized.

The complicated thermal and hydrodynamic interactions between the vapour, liquid and solid have been manifested for a single isolated bubble growing on a heated plane surface from inception with a negligible contribution of an evaporating microlayer. During

the surface tension controlled growth stage, the bubble protrudes only a very small distance into the liquid above the solid surface where the liquid temperature is almost uniform. As the bubble expands the vapour temperature decreases and a thin, spherically symmetric thermal boundary layer forms around the bubble. Axial variations in the liquid temperature normal to the solid surface occur far enough away from the bubble that they do not influence the thermal transients occurring at the vapour-liquid interface. Consequently, the bubble expands as if it were surrounded by a uniform temperature liquid which is heated to the temperature of the solid surface. During the transition domain, the bubble growth rate increases significantly. As a result, the hydrodynamic forces acting at the bubble wall increase to such an extent that they play an important role in determining the growth rate of the bubble. As the bubble grows significantly away from its initial critical radius, it begins to penetrate into the thermal layer of the bulk liquid. The spatial temperature distribution within the bulk liquid causes the thermal field surrounding the bubble to become progressively less symmetric around the bubble cap. In this way, a distribution in the heat flux into the bubble exists. The minimum heat flux occurs at the tip of the bubble where the sensible energy is being depleted, and the maximum heat flux occurs at the base of the bubble where there is an abundance of superheated liquid stored in the region close to the solid surface. During the diffusion controlled growth stage, the vapour pressure and temperature have decreased to near their minimum values. Because of this, surface tension and liquid inertia no longer play an important role and bubble growth is limited by the net rate of heat transfer into the bubble. The growth rate slows at a rate which is notably less than that which would be predicted for a uniformly superheated liquid because the bubble has consumed the superheat which was stored in the liquid around the bubble during the

waiting time. This is compounded by the fact that the bubble tip has penetrated through the thermal layer adjacent to the solid surface into a region of liquid which is subcooled.

5.2. Recommendations for Future Work

It is well known that the earliest stage of bubble growth is hemispherical. The length of the hemispherical growth stage depends on many factors including system pressure, the level of superheat near the heated surface, the formation of a microlayer, and the level of gravity in which boiling is taking place. Inevitably however, the centre of curvature of the bubble begins to rise above the horizontal surface. In this growth stage, the bubble is expanding radially as well as translating perpendicular to the surface. The translational motion of the bubble is of considerable importance because it is largely responsible for how long the bubble remains affixed to the surface. This in turn affects other parameters such as departure size, the overall rate of heat transfer and so on.

In the literature, the translational motion of the bubble is often oversimplified. In Lee and Nydahl [1989] and and Son, Dhir and Ramanujapu [1999], a constant contact angle was assumed which provided a relation between the centre of curvature and the radius. In Chen, Mei and Klausner [1995], an empirical function was developed which dictated when the centre of curvature would begin to rise and then how quickly. In these two cases, as well as others, closure of the governing equations is obtained at the expense of the physical mechanisms which determine translational growth. In the analysis of Buyevich and Webbon [1996], two coupled non-linear ordinary differential equations were developed, one for radial expansion and the other for vertical translation. Even still, solutions could only be obtained for the idealized cases of hemispherical and spherical growth near the heated surface.

It is the opinion of the author that future developments in bubble growth dynamics should focus on a simplified theory for isolated growth at a heated surface from inception to departure. Since the early stage of growth is known to be nearly hemispherical, the work outlined in this dissertation provides a logical starting point for the development of a more complete description of heterogeneous bubble growth. Next, the mechanisms which govern translational growth must be discerned. The idealized case in which the bubble remains a spherical segment throughout its growth time simplifies the geometry of the problem enough that the present numerical technique may require only minor modifications to incorporate the vertical motion of the bubble. The physical model must also incorporate the possibility of an evaporation microlayer at the base of the growing bubble.

The validity of the resulting predictions can be verified by comparison with the recent experimental measurements which have been obtained at McMaster University (Robinson [2001]). In this photographic study, bubble growth measurements were obtained in which the bubble remains nearly spherical throughout its growth time. Fig. 5.1 shows a sample of the results which have been obtained. Bubble interface measurements are given in Fig. 5.2 together with a regression best-fit of a spherical segment to the interface measurements for both sides of the bubble. In this way, both the bubble radius and height of the centre of curvature have been estimated for each frame of the sequence. Fig. 5.3 shows the temporal variation of both the radius and centre of curvature for the entire growth time of the bubble.

The fixed bubble shape, combined with the specification of both the instantaneous radius and centre of curvature of the growing bubble, makes this investigation unique and ideal for conducting a preliminary investigation of bubble translation during isolated bubble

growth in nucleate pool boiling.

5.2 Contribution to Knowledge

The complicated nature of isolated bubble growth during nucleate pool boiling has dictated the wide diversity of research which has been performed on the subject over the past century. Through careful and creative experimentation and thoughtful theoretical exploration, the scope of the problem seems to have been established. With the overall picture in view, theoretical investigations can now proceed in a more structured pragmatic manner. In this work, the first steps along this course have been taken. By providing accurate, properly tested numerical predictions of idealized bubble growth, a foundation has been established upon which more complicated numerical schemes may be constructed. Furthermore, the direction of theoretical development has been refocused by providing a more thorough understanding of the spherically symmetric phase growth problem in order to lend clarity to the effects of added complexities. Finally, the simple case of hemispherical growth at a heated surface in microgravity has been analysed. This defines the new starting point for theoretical development. By adding one layer of complexity at a time, the logical sequence of study will continue to progress towards an accurate and complete description of isolated bubble growth. This will in turn lead to reliable predictions of the heat transfer rate during nucleate pool boiling.
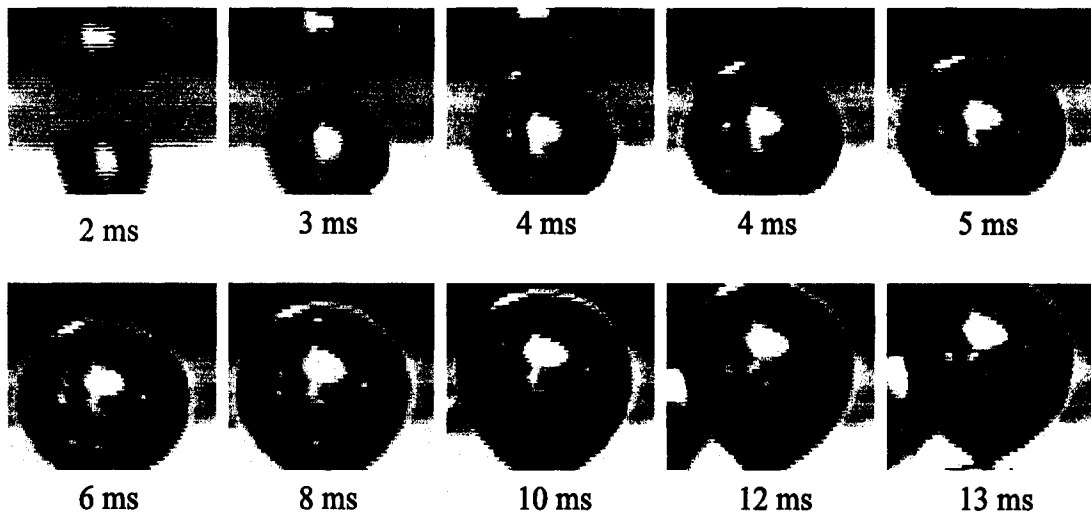
Figure 5.1: Photographs of bubble growth.
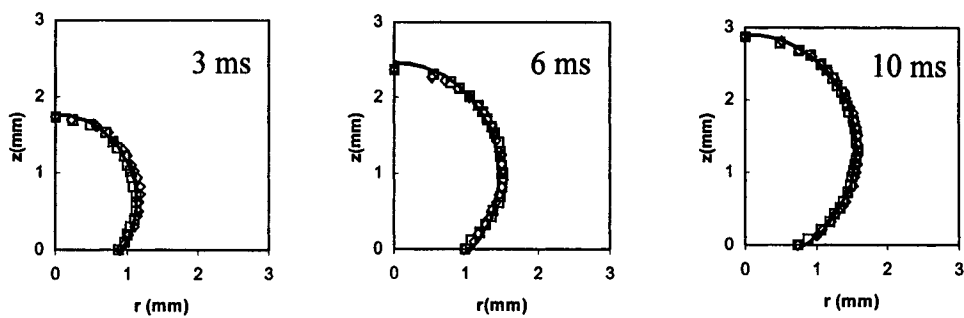
Figure 5.2: Bubble interface measurements and best fit spherical segment.
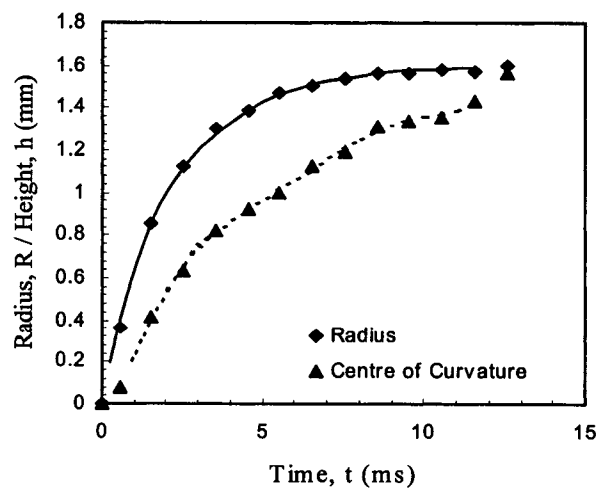
Figure 5.3: Growth curves for the radius and centre of curvature.

APPENDICES

APPENDIX A

Derivation of the Extended Rayleigh Equation

As a result of the spherical symmetry, the continuity and momentum equations in the liquid surrounding A growing spherical vapour bubble are given by,

$$\frac{\partial(r^2 u)}{\partial r} = 0 \qquad\qquad \text{A1}$$

$$\frac{\partial u}{\partial t} + u\frac{\partial u}{\partial r} = -\frac{1}{\rho}\frac{\partial P}{\partial r} + \frac{\mu}{\rho}\left(\frac{\partial^2 u}{\partial r^2} + \frac{2}{r}\frac{\partial u}{\partial r} - \frac{2u}{r^2}\right) \qquad\qquad \text{A2}$$

Simplification of equation (A1) gives,

$$\frac{\partial u}{\partial r} = -\frac{2u}{r} \qquad\qquad \text{A3}$$

Substitution of equation (A3) into equation (A2) results in the expression,

$$\frac{\partial u}{\partial t} - 2\frac{u^2}{r} = -\frac{1}{\rho}\frac{\partial P}{\partial r} \qquad\qquad \text{A4}$$

The instantaneous liquid velocity is determined by integration of equation (A3) with boundary conditions $u(0,t) = \dot{R}$ and $u(\infty,t) = 0$ such that,

162

$$u(r,t) = \dot{R}\frac{R^2}{r^2}$$
<div align="right">A5</div>

Differentiation with respect to time results in,

$$\frac{\partial u}{\partial t} = \frac{1}{r^2}(\ddot{R}R^2 + 2R\dot{R}^2)$$
<div align="right">A6</div>

Substitution of equations (A5) and (A6) into equation (A4) gives an expression for the pressure gradient in the liquid;

$$\frac{\partial P}{\partial r} = -\rho\left(\frac{1}{r^2}(\ddot{R} + 2R\dot{R}^2) - 2\dot{R}^2\frac{R^4}{r^5}\right)$$
<div align="right">A7</div>

Equation (A7) can be integrated between the limits P(R) and P_∞ to give,

$$\frac{P(R) - P_\infty}{\rho} = R\ddot{R} + \frac{3}{2}\dot{R}^2$$
<div align="right">A8</div>

where P(R) is the liquid pressure at the interface and P_∞ is the system pressure. The interface jump condition without the normal stress term is,

$$P_v - P(R) = \frac{2\sigma}{R}$$
<div align="right">A9</div>

Substitution for P(R) gives the extended Rayleigh equation,

$$\frac{P_v - P_\infty}{\rho} = R\ddot{R} + \frac{3}{2}\dot{R}^2 + \frac{2\sigma}{\rho R}$$

A10

APPENDIX B

Tabulated Bubble Growth Data

This appendix contains the tabulated bubble radius versus time predictions for homogeneous bubble growth in an uniformly superheated liquid for i) the converged solution on a uniform grid with M=40000 grid points ii) the extrapolated infinite grid benchmark solution.

Table C1: Case A: Water, P=1.0 atm, ΔT_{sup}=3.1 °C

Time (ms)	R(M=40000) (mm)	R(infinite) (mm)
1.002	0.222	0.218
2.006	0.326	0.323
3.013	0.405	0.402
4.014	0.472	0.469
5.002	0.529	0.527
6.028	0.584	0.581
7.027	0.632	0.630
8.030	0.677	0.675
9.054	0.720	0.719
10.006	0.759	0.757
11.059	0.799	0.797
11.980	0.832	0.831

Table C2: Case B: Water, P=0.372 atm, ΔT_{sup}=6.3 °C

Time (ms)	R(M=40000) (mm)	R(infinite) (mm)
1.002	1.017	1.030
2.006	1.542	1.555
3.013	1.938	1.949
4.014	2.265	2.275
5.002	2.549	2.558
6.028	2.814	2.822
7.027	3.050	3.058
8.030	3.270	3.278
9.054	3.481	3.489
10.006	3.666	3.674
11.059	3.861	3.868
11.980	4.024	4.031

Table C3: Case C: Water, P=0.362 atm, ΔT_{sup}=17.0°C

Time (ms)	R(M=40000) (mm)	R(infinite) (mm)
1.002	2.356	2.316
2.006	3.818	3.784
3.013	4.955	4.925
4.014	5.898	5.871
5.002	6.710	6.685
6.028	7.466	7.443
7.027	8.138	8.116
8.030	8.762	8.741
9.054	9.359	9.339
10.006	9.882	9.863
11.059	10.431	10.413
11.980	10.890	10.872

Table C4: Case D: R113, P=0.0361 atm, ΔT_{sup}=48.1°C

Time (ms)	R(M=40000) (mm)	R(infinite) (mm)
1.002	2.462	2.317
2.006	4.473	4.363
3.013	6.329	6.227
4.014	8.071	7.973
5.002	9.718	9.622
6.028	11.369	11.275
7.027	12.927	12.835
8.030	14.448	14.358
9.054	15.965	15.876
10.006	17.346	17.258

APPENDIX C

Thermal Boundary Layer Thickness

In this appendix, the calculation for the extrapolated thermal boundary layer thickness is outlined. Fig. C1 shows a schematic of the instantaneous temperature distribution in the liquid outside of the growing vapour bubble.
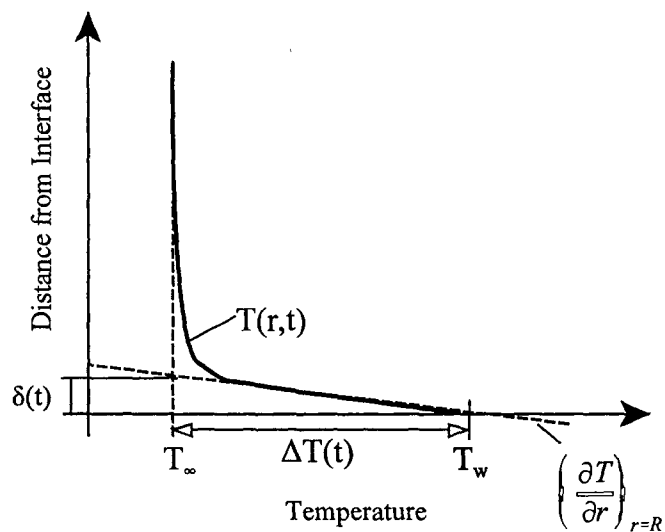
Figure C1: Extrapolated thermal layer thickness.

The heat flux into the bubble is determined by Newton's Law of Cooling which can be approximated by,

$$q'' = -k_l \left(\frac{\partial T}{\partial r} \right)_{r=R} \approx -k_l \frac{\Delta T(t)}{\delta(t)} \tag{C1}$$

such that the extrapolated thermal boundary layer thickness can be predicted by the expression,

$$\delta(t) = \frac{\Delta T(t)}{\left(\dfrac{\partial T}{\partial r} \right)_{r=R}} \tag{C2}$$

The interface temperature gradient in the denominator of equation C2 is determined from the numerical solution of the energy equation in the liquid.

APPENDIX D

FORTRAN 90 Code for Homogeneous Growth with a Uniform Grid Arrangement

This program solves the one dimensional, radially symmetric bubble growth problem in an initially superheated liquid from its thermodynamic critical size through the surface tension, inertial and heat transfer controlled stages of growth. Bubble growth away from the initial unstable equilibrium state of the vapor nucleus is instigated by a small increase in radius dRo over a small time step dto. A fourth order Runge-Kutta scheme is then utilized to solve the modified Rayleigh equation together with the Interfacial Energy balance equation for the variables Tv, R, dRdt from which Pv and dv can also be determined. The vapor phase is assumed to behave as a perfect gas and the saturated pressure and temperature are related from the integrated Clausius-Clapeyron equation. It was found that an accurate curve-fitted P-T rendered essentially the same result. The temperature gradient at the interface is determined from the energy equation including the convective term. The energy equation is solved using a finite difference scheme on a uniform grid. Excellent agreement with experimental results has been found and the number of grid points which result in a 'grid independent' solution has been found to be approximately 40000 for water and R113 with an infinity boundary set at 5 cm.

```
program onedimension
implicit none

INTEGER :: K, J
INTEGER, PARAMETER :: M=40000, N=2000000

DOUBLE PRECISION, DIMENSION(N) :: t_, R_, Tmp_, dRdt_,P_
DOUBLE PRECISION, DIMENSION(M) :: TEMP, TEMP_old
!Liquid
DOUBLE PRECISION :: Tsup
!Vapor
DOUBLE PRECISION :: Ro, R, Pv, Tv, dRdt
!Both
DOUBLE PRECISION :: hfg
!Runge Kutta
DOUBLE PRECISION :: xi, yli, y2i, y3i, F1, F2, F3, x, y1, y2, y3, x_1, yli_1, y2i_1, y3i_1, &
         k11, k21, k31, k41, k12, k22, k32, k42, k13, k23, k33, k43
!Miscillaneous
DOUBLE PRECISION :: t, dt, dist, Rinf, del_t, t_o, beta, P, del_r,tend


!Functions
DOUBLE PRECISION :: PRESS, LATENT, D_LATENT, TENSION, l_sp_heat, therm_cond, l_dens, T_sat,
PRESS2
LOGICAL :: IDEAL
!Common
DOUBLE PRECISION :: Cpl, kl, al, dl, sigma, G, hfgo, dhfgo, Tinf, Pinf, Tsat, pi
COMMON/bub_param/Cpl, kl, al, dl, sigma, G, hfgo, dhfgo, Tinf, Pinf, Tsat, pi, IDEAL

OPEN(UNIT=1, FILE='c:\output\check1.dat', STATUS='old')

IDEAL=.TRUE.

t_o=1.0D-9
beta=1500.0  !this term affects the rapid growth region. ie. for 'long' surface tension
             !growth, the time step may be too course to capture the rapid growth term
             !so it must be increased

K=1
Rinf=0.05D0 !m

!Constants
G=0.461504302*(1.0D3)  !J/kgK for water ie=Ru/M=3.314/18.015
pi=3.1415926535897931D0


IDEAL=.FALSE. ! If IDEAL=.TRUE. the vapour is treated as an ideal gas and the Clausius-Clapeyron
             ! equation is used to determine the vapour pressure.
tend=18.0D-3


!_____


!LIQUID initial conditions
Pinf=1.0*101.33D0    ! Set the system pressure kPa
```

```
Tsat=T_sat(Pinf)    !K this is the experimental value
Tsup=3.1D0      !K
Tinf=Tsat+Tsup   !K
Cpl=(1.0D3)*l_sp_heat(Tinf)  !J/kgK
kl=therm_cond(Tinf)  !W/mK
dl=l_dens(Pinf)
al=kl/(dl*Cpl)
sigma=TENSION(Tsat)*(1.0D-3)   !N/m

hfgo=(1.0D3)*LATENT(Tsat)  !J/kgK
dhfgo=(1.0D3)*D_LATENT(Tsat) !J/kgK

do J=1,M
TEMP_old(J)=Tinf
end do

!VAPOR initial condition
Tv=Tinf
hfg=(1.0D3)*LATENT(Tv)

IF(IDEAL)THEN
Pv=PRESS(Tv, hfg)
ELSE
Pv=PRESS2(TV)
ENDIF

Ro=(2.0*sigma)/((1.0D3)*(Pv-Pinf))

t_(K)=t*1.0D3
R_(K)=Ro*1.0D3
Tmp_(K)=Tv
dRdt_(K)=0.0
P_(K)=Pinf
!_____


!INITIAL DISTURBANCE
dt=1.0D-9
dist=5.0D-6
R=Ro+dist*Ro

20 K=K+1
!find kl's

del_t=0.0D0
xi=t
y1i=Tv
y2i=R
y3i=dRdt

CALL FF1(x, y1i, y2i, y3i, M, del_t, Rinf, TEMP_old, TEMP, F1)
F2=y3i
call FF3(t, y1i, y2i, y3i, F3)
```

```
k11=F1
k12=F2
k13=F3

del_t=0.5D0*dt
x=xi+del_t
y1=y1i+k11*0.5D0*dt
y2=y2i+k12*0.5D0*dt
y3=y3i+k13*0.5D0*dt

CALL FF1(x, y1, y2, y3, M, del_t, Rinf, TEMP_old, TEMP, F1)
F2=y3
call FF3(t, y1, y2, y3, F3)

k21=F1
k22=F2
k23=F3

del_t=0.5D0*dt
x=xi+del_t
y1=y1i+k21*0.5D0*dt
y2=y2i+k22*0.5D0*dt
y3=y3i+k23*0.5D0*dt

CALL FF1(x, y1, y2, y3, M, del_t, Rinf, TEMP_old, TEMP, F1)
F2=y3
call FF3(t, y1, y2, y3, F3)

k31=F1
k32=f2
k33=f3

del_t=dt
x=xi+del_t
y1=y1i+k31*dt
y2=y2i+k32*dt
y3=y3i+k33*dt

!call FF1(x, y1, y2, y3, F1)
CALL FF1(x, y1, y2, y3, M, del_t, Rinf, TEMP_old, TEMP, F1)
F2=y3
call FF3(t, y1, y2, y3, F3)

k41=F1
k42=f2
k43=f3


x_1=xi+dt
y1i_1=y1i+(dt/6.0)*(k11+2.0*k21+2.0*k31+k41)
y2i_1=y2i+(dt/6.0)*(k12+2.0*k22+2.0*k32+k42)
y3i_1=y3i+(dt/6.0)*(k13+2.0*k23+2.0*k33+k43)
```

```
del_t=dt
t=x_1
Tv=y1i_1
R=y2i_1
dRdt=y3i_1

t_(K)=t*1.0D3
Tmp_(K)=Tv
R_(K)=R*1.0D3
dRdt_(K)=dRdt
!_____

_____

if (t<tend) then

!Momentum equation check

IF(IDEAL)THEN
P=PRESS(Tv, hfg)
ELSE
P=PRESS2(TV)
ENDIF

P_(K)=P

 call temper(M, del_t, R, Rinf, dRdt, TEMP_old, al, Tv, Tinf, TEMP, del_r)

do J=1,M
TEMP_old(J)=TEMP(J)
end do

dt=t_o*EXP(REAL(K-2)/beta)

GOTO 20
end if

100 do J=1,K,10
   WRITE (1,25) t_(J), R_(J), dRdt_(J), Tmp_(J), P_(J)
   25 FORMAT(f11.7, 1X, f15.10, 1X, f15.10, 1X, f12.8,1X, f12.5)
   end do

stop
end program

!_____

_____
SUBROUTINE FF3(t, y1, y2, y3, A3)
DOUBLE PRECISION :: t, g_R, f4, P, y1, y2, y3, A3, PRESS, hfg, LATENT, PRESS2
DOUBLE PRECISION :: Cpl, kl, al, dl, sigma, G, hfgo, dhfgo, Tinf, Pinf, Tsat, pi
LOGICAL :: IDEAL

COMMON/bub_param/Cpl, kl, al, dl, sigma, G, hfgo, dhfgo, Tinf, Pinf, Tsat, pi, IDEAL
```

```
hfg=(1.0D3)*LATENT(y1)


IF(IDEAL)THEN
P=PRESS(y1, hfg)
ELSE
P=PRESS2(y1)
ENDIF

g_R=2.0D0*sigma/(dl*y2**2)

f4=(1.0D3)*(P-Pinf)/(dl*y2)

A3=f4-g_R-(3.0D0/2.0D0)*(y3**2)/y2


RETURN
END SUBROUTINE
!_____


_____


SUBROUTINE FF1(x, y1, y2, y3, M, del_t, Rinf, Told, T, A1)

INTEGER :: M
DOUBLE PRECISION, DIMENSION (M) :: Told, T
DOUBLE PRECISION :: x, P, hfg_, f1, f2, f3, hfg, dTdr, dv
DOUBLE PRECISION :: A1, y1, y2, y3
DOUBLE PRECISION :: Rinf, del_r, del_t, g_T
DOUBLE PRECISION :: LATENT, PRESS, v_sp_heat, PRESS2, v_dens, dvdT
DOUBLE PRECISION :: Cpl, kl, al, dl, sigma, G, hfgo, dhfgo, Tinf, Pinf, Tsat, pi
LOGICAL :: IDEAL

COMMON/bub_param/Cpl, kl, al, dl, sigma, G, hfgo, dhfgo, Tinf, Pinf, Tsat, pi, IDEAL

hfg=(1.0D3)*LATENT(y1)
Cpv=(1.0D3)*v_sp_heat(y1)

IF(del_t>0.0D0)then
 call temper(M, del_t, y2, Rinf, y3, Told, al, y1, Tinf, T, del_r)
 dTdr=(2.0D0*T(4)-9.0D0*T(3)+18.0D0*T(2)-11.0D0*T(1))/(6.0D0*del_r)
ELSE
 del_r=(Rinf-y2)/REAL(M-1)
 dTdr=(2.0D0*Told(4)-9.0D0*Told(3)+18.0D0*Told(2)-11.0D0*Told(1))/(6.0D0*del_r)
ENDIF

IF(IDEAL) THEN
P=PRESS(y1, hfg)  !kPa

hfg_=hfg+Cpl*(Tinf-y1)  !kJ/kg
dv=(1.0D3)*P/(G*y1)

f3=kl*dTdr
```

```
f2=hfg_*dv

f1=(1.0D0/3.0D0)*((hfg_*dv/y1)*(hfg/(G*y1)-1.0D0)+dv*Cpv)

A1=(1.0D0/(y2*f1))*(f3-f2*y3)

ELSE
P=PRESS2(Y1)

dv=v_dens(y1)
g_T=dvdT(y1)

f3=kl*dTdr
f2=hfg*dv
f1=(hfg/3.0)*g_T

A1=(1.0/(y2*f1))*(f3-f2*y3)
ENDIF

RETURN
END SUBROUTINE
!_____


_____


subroutine Temper(M, del_t, Rt, Rinf, dRdt, Told, al, Tv, Tinf, T, del_r)

DOUBLE PRECISION, DIMENSION (M) ::  e, c1, c2, T, Told, T_2, AA, BB, CC, DD
DOUBLE PRECISION, DIMENSION (M) :: a, b, c, d
DOUBLE PRECISION :: Rt, Rinf, dRdt, del, del_e, del_r, del_t

!properties
DOUBLE PRECISION ::  al, Tv, Tinf

del=Rinf-Rt
del_r=del/REAL(M-1)
del_e=1.0D0/REAL(M-1)

e(1)=0.0
do J=2,M
 e(J)=e(J-1)+del_e
end do

  do J=1,M
  c2(J)=-al/(del**2)
  c1(J)=(-2.0D0*al/(del*e(J)+Rt))*(1.0D0/del)+&
     (dRdt*((Rt/(del*e(J)+Rt))**2+(e(J)-1.0D0)))*(1.0D0/del)
  end do

do J=2,M-1
AA(J)=(1.0D0)-2.0D0*c2(J)*del_t/del_e**2
BB(J)=c1(J)*del_t/(2.0D0*del_e)+c2(J)*del_t/(del_e**2)
CC(J)=-c1(J)*del_t/(2.0D0*del_e)+c2(J)*del_t/(del_e**2)
DD(J)=Told(J)
```

```
end do

!Set up equations so that they are in the form (Patanker):
!
!    a(1)T(1)=b(1)T(2)+d(2)
!    a(2)T(2)=b(2)T(3)+c(2)T(1)+d(2)
!    .....
!    a(J)T(J)=b(J)T(J+1)+c(J)T(J-1)+d(J)
!    .....
!    a(M-1)T(M-1)=c(M-1)T(M-2)+d(M-1)
!
!**********************************************************
do J=1,M-2
a(J)=AA(J+1)
b(J)=-BB(J+1)
c(J)=-CC(J+1)

 IF(J==1)then
 d(J)=DD(J+1)-CC(J+1)*Tv
 ELSEIF(J==M-2)then
 d(J)=DD(J+1)-BB(J+1)*Tinf
 else
 d(J)=DD(J+1)
 endif

end do


call TDMA(M-2, a, b, c, d, T_2)

 do J=1,M
     IF(J==1)then
       T(J)=Tv
     ELSEIF(J==M)then
       T(J)=Tinf
     else
       T(J)=T_2(J-1)
     endif
   end do

return
END subroutine
!_____

_____

subroutine TDMA(M, a, b, c, d, U)

INTEGER :: M
DOUBLE PRECISION , DIMENSION(M) :: a, b, c, d, P, Q, U
DOUBLE PRECISION :: BET


if (a(1)==0.0) pause
```

```
BET=a(1)
Q(1)=d(1)/BET
P(1)=b(1)/BET

do J=2,M

BET=a(J)-c(J)*P(J-1)

if (BET==0.0) pause

P(J)=b(J)/BET
Q(J)=(d(J)+c(J)*Q(J-1))/BET

end do

U(M)=Q(M)

do J=M-1,1,-1
U(J)=P(J)*U(J+1)+Q(J)
end do

return
end subroutine
!_____
_____
!*******************Water   Properties *** ****************************************

FUNCTION PRESS(T, hfg)
DOUBLE PRECISION :: T, hfg, PRESS
DOUBLE PRECISION :: Cpl, kl, al, dl, sigma, G, hfgo, dhfgo, Tinf, Pinf, Tsat, pi
LOGICAL :: IDEAL

COMMON/bub_param/Cpl, kl, al, dl, sigma, G, hfgo, dhfgo, Tinf, Pinf, Tsat, pi, IDEAL

PRESS=Pinf*EXP((1.0/G)*(hfgo/Tsat-hfg/T))*(T/Tsat)**(dhfgo/G)
return
END

FUNCTION LATENT(T)
DOUBLE PRECISION :: a, b, c, d, T, LATENT
a=4535.5338
b=-14.40485
c=0.034749747
d=-3.3548106D-5
  LATENT=a+(b*T)+(c*T**2)+(d*T**3)  !kJ/kg,  T in K
return
END

FUNCTION D_LATENT(T)
DOUBLE PRECISION ::b, c, d, T, D_LATENT
b=-14.40485
c=0.034749747
```

```fortran
      d=-3.3548106D-5
       D_LATENT=b+(2.0*c*T)+(3.0*d*T**2)  !kJ/kgK, T in K
      return
      END


      FUNCTION TENSION(T)
      DOUBLE PRECISION :: T, TENSION
      TENSION=235.8D0*((1.0D0-(T)/(374.15D0+273.15D0))**1.256D0)*(1.0D0-(0.625D0)*(1.0D0-(T)/(37
      4.15D0+273.15D0)))  !mN/m
      return
      end


      FUNCTION l_sp_heat(T)
      DOUBLE PRECISION :: T, l_sp_heat, a, b, c, d, e
      a=78.582798
      b=-0.14625086
      c=0.00010960625
      d=-17026.454
      e=1472551.8
       l_sp_heat=a+(b*T)+(c*T**2)+(d/T)+(e/T**2)     !kJ/kgK
      END


      FUNCTION v_sp_heat(T)
      DOUBLE PRECISION :: T, v_sp_heat, a, b, c, d
      a=-0.15521575
      b=2.1455738D-2
      c=-7.842041D-5
      d=9.8101939D-8
       v_sp_heat=a+(b*T)+(c*T**2)+(d*T**3)     !kJ/kgK
      END


      FUNCTION T_sat(P)
      DOUBLE PRECISION :: P, T_sat, a, b, c, d, e, f, g, h
      a=280.14591
      b=14.578656
      c=0.81618388
      d=0.090358794
      e=-0.01233292
      f=0.0036827453
      g=-0.00036521131
      h=1.7727335D-5


      T_sat=a+b*(LOG(P))+c*(LOG(P))**2+d*(LOG(P))**3+e*(LOG(P))**4+f*(LOG(P))**5+g*(LOG(P))*
      *6+h*(LOG(P))**7
       END


      function therm_cond(T)
      DOUBLE PRECISION :: therm_cond, T
      therm_cond=0.56917061+0.0018981353*(T-273.15)-8.8322257*10**(-6.0)*(T-273.15)**2.0+7.2806061
      *10**(-9.0)*(T-273.15)**3.0 !W/mK
      return
      end
```

```fortran
function l_dens(P)
DOUBLE PRECISION :: l_dens, P
l_dens=1008.1433+(-7.3239274)*P**0.41233836        !kg/m3
return
end


FUNCTION PRESS2(T)
DOUBLE PRECISION :: T, PRESS2, a, b, c
a=15.38366
b=-2111.3788
c=-36815.655
PRESS2=EXP(a+b/T+c/T**1.5)
return
END


function v_dens(T)
DOUBLE PRECISION :: v_dens, T, a, b, c
a=94.90762D0
b=-0.023178676D0
c=-0.24376403D0
  v_dens=EXP((a+c*T)/(1.0D0+b*T))    !kg/m3
return
end


function dvdT(T)
DOUBLE PRECISION :: dvdT, T, b, c
a=94.90762D0
b=-0.023178676D0
c=-0.24376403D0
  dvdT=((c-a*b)/(1.0D0+b*T)**2)*EXP((a+c*T)/(1.0D0+b*T))
return
end




!_____

!*********************** R113  Properties *** *****************************************

FUNCTION PRESS(T, hfg)
DOUBLE PRECISION :: T, hfg, PRESS
DOUBLE PRECISION :: Cpl, kl, al, dl, sigma, G, hfgo, dhfgo, Tinf, Pinf, Tsat, pi
LOGICAL :: IDEAL
COMMON/bub_param/Cpl, kl, al, dl, sigma, G, hfgo, dhfgo, Tinf, Pinf, Tsat, pi, IDEAL

PRESS=Pinf*EXP((1.0/G)*(hfgo/Tsat-hfg/T))*(T/Tsat)**(dhfgo/G)
return
END


FUNCTION D_LATENT(T)
DOUBLE PRECISION ::b, c, d, T, D_LATENT
b=-14.40485
c=0.034749747
d=-3.3548106D-5
```

```fortran
    D_LATENT=b+(2.0*c*T)+(3.0*d*T**2)  !kJ/kgK,  T in K
return
END


FUNCTION v_sp_heat(T)
DOUBLE PRECISION :: T, v_sp_heat, a, b, c, d
a=-0.15521575
b=2.1455738D-2
c=-7.842041D-5
d=9.8101939D-8
  v_sp_heat=a+(b*T)+(c*T**2)+(d*T**3)    !kJ/kgK
END


FUNCTION PRESS2(T)
DOUBLE PRECISION :: T, PRESS2, a, b, c, d, e,f
a=2957.142318D0
b=-53.1787872D0
c=0.371694819D0
d=-0.001235475106D0
e=1.860059877D-06
f=-8.710006423D-10
PRESS2=a+b*T+c*T**2+d*T**3+e*T**4+f*T**5
return
END


FUNCTION LATENT(T)
DOUBLE PRECISION :: a, b, c, d, e, f, T, LATENT
a=2737.48849146611D0
b=-39.3003642747073D0
c=0.239810862940233D0
d=-0.000727033297258D0
e=1.089453393D-06
f=-6.47894D-10
LATENT=a+b*T+c*T**2+d*T**3+e*T**4+f*T**5  !kJ/kg,  T in K
return
END


FUNCTION TENSION(T)
DOUBLE PRECISION :: T, TENSION, a, b, c, d, e
a=100.66367D0
b=-0.26354029D0
c=0.00017492986D0
d=-8150.6195D0
e=535170.24D0
TENSION=a+b*T+c*T**2+d/T+e/T**2 !mN/m
return
end


FUNCTION l_sp_heat(T)
DOUBLE PRECISION :: T, l_sp_heat, a, b, c, d
a=-2687.2937711853D0
b=32.1760788219D0
c=-0.0967652227D0
```

```fortran
d=0.0001001237D0
  l_sp_heat=(a+(b*T)+(c*T**2)+(d*T**3))/1000.0D0     !kJ/kgK
END


FUNCTION T_sat(P)
DOUBLE PRECISION :: P, T_sat, a, b, c, d, e
a=227.62444D0
b=13.885934D0
c=0.69937307D0
d=0.15567729D0
e=-0.01232013D0
f=0.002049886D0
  T_sat=a+b*LOG(P)+c*LOG(P)**2+d*LOG(P)**3+e*LOG(P)**4+f*LOG(P)**5
  END


function therm_cond(T)
DOUBLE PRECISION :: therm_cond, T, a, b, c, d, e, f
a=572.672566562039D0
b=-7.22070352101712D0
c=0.044478466185909D0
d=-0.000139306769359D0
e=2.15863959D-07
f=-1.32549D-10
therm_cond=(a+b*T+c*T**2+d*T**3+e*T**4+f*T**5)*1.0D-3 !W/mK
return
end


function l_dens(Tin)
DOUBLE PRECISION :: l_dens, T, Tin, a, b, c, d, e, f
T=Tin-273.15D0
a=16.1767736505804D0
b=-0.021409787008367D0
c=3.666728067D-06
d=-1.210948367D-06
e=1.1848044D-08
f=-3.7748D-11
l_dens=(a+b*T+c*T**2+d*T**3+e*T**4+f*T**5)*100.0D0     !kg/m3
return
end


function v_dens(T)
DOUBLE PRECISION :: v_dens, T, a, b, c, d, e, f
a=-299.6373102D0
b=4.974715994D0
c=-0.03322820191D0
d=0.0001134072022D0
e=-2.031981824D-07
f=1.585972295D-10
v_dens=a+b*T+c*T**2+d*T**3+e*T**4+f*T**5      !kg/m3
return
end


function dvdT(T)
```

```
DOUBLE PRECISION :: dvdT, T, b, c, d, e, f

b=4.974715994D0
c=-0.03322820191D0
d=0.0001134072022D0
e=-2.031981824D-07
f=1.585972295D-10
  dvdT=b+2.0*c*T+3.0*d*T**2+4.0*e*T**3+5.0*f*T**4   !
return
end
```

APPENDIX E

FORTRAN 90 Code for Homogeneous Growth with a Staggered Grid Arrangement

This program solves the one dimensional, radially symmetric bubble growth problem in initially superheated water from its thermodynamic critical size through the surface tension, inertial and heat transfer controlled stages of growth. Bubble growth away from the initial unstable equilibrium state of the vapor nucleus is instigated by a small increase in radius over a small time step. A fourth order Runge-Kutta scheme is then utilized to solve the modified Rayleigh equation together with the Interfacial Energy balance equation for the variables Tv, R, dR/dt from which Pv and dv can also be determined. The vapor phase is assumed to be saturated and the properties are related through curve fits of the tabulated property data. The temperature gradient at the interface is determined from the energy equation including the convective term. A staggered grid arrangement is utilized to cluster the grid points at the interface where the gradients are the highest. A coordinate transformation is performed so that the energy equation is solved on a uniform grid in the computational domain. Excellent agreement with experimental results as well as with a uniform grid, grid independent solution has been found. With a constant Sr=0.65, 800 grid points are required to give a grid independent solution. This is a 50 times reduction as compared with the uniform grid solution.

```fortran
program stagger
implicit none

INTEGER :: K, J, NEXT, KK
INTEGER, PARAMETER :: M=800, N=2000000
DOUBLE PRECISION, DIMENSION(N) :: Elhs_,Etm1_,Etm2_,Mlhs_,Mtm1_,Mtm2_,Mtm3_,dTdr_,d2Rdt_
DOUBLE PRECISION, DIMENSION(N) :: t_, R_, Tmp_, DELTA, dRdt_, dTdt_!,kin_,inert_
DOUBLE PRECISION, DIMENSION(M) :: TEMP, TEMP_old, rold, rr, rn, rnn, Ja,a,d,BB,EE,HH
DOUBLE PRECISION, DIMENSION(M,3) :: T__o, T_6, T_5, T_4, T_3, T_2, T_1, T_0, T__1, T__2, T__e

!Liquid
DOUBLE PRECISION :: Tsup
!Vapor
DOUBLE PRECISION :: Ro, R, Pv, Tv, dRdt

!Runge Kutta
DOUBLE PRECISION :: xi, y1i, y2i, y3i, F1, F2, F3, x, y1, y2, y3, x_1, y1i_1, y2i_1, y3i_1, &
        k11, k21, k31, k41, k12, k22, k32, k42, k13, k23, k33, k43
!Miscillaneous
DOUBLE PRECISION :: t, dt, dist, del_t, t_o, beta, P,   &      ! dTdr,
        Mlhs, Mtm2, Mtm3, d2Rdt2, Elhs,Etm1,Etm2,dTdt,g_T,dTdr,tend

!Functions
DOUBLE PRECISION :: dvdt, v_dens, LATENT, PRESS2, TENSION, l_sp_heat, therm_cond, l_dens, T_sat,
hfg, dv
!Common
DOUBLE PRECISION :: Sr,Cpl, kl, al, dl, sigma, Tinf, Pinf, Tsat, pi, del_e, Rinf
COMMON/bub_param/Sr,Cpl, kl, al, dl, sigma, Tinf, Pinf, Tsat, pi, del_e, Rinf

OPEN(UNIT=1, FILE='c:\tony\data files\one_dim.dat', STATUS='old')
OPEN(UNIT=2, FILE='c:\tony\data files\grad_o.dat', STATUS='old')
OPEN(UNIT=3, FILE='c:\tony\data files\grad_6.dat', STATUS='old')
OPEN(UNIT=4, FILE='c:\tony\data files\grad_5.dat', STATUS='old')
OPEN(UNIT=5, FILE='c:\tony\data files\grad_4.dat', STATUS='old')
OPEN(UNIT=6, FILE='c:\tony\data files\grad_3.dat', STATUS='old')
OPEN(UNIT=7, FILE='c:\tony\data files\grad_2.dat', STATUS='old')
OPEN(UNIT=8, FILE='c:\tony\data files\grad_1.dat', STATUS='old')
OPEN(UNIT=9, FILE='c:\tony\data files\grad_0.dat', STATUS='old')
OPEN(UNIT=10, FILE='c:\tony\data files\grad__1.dat', STATUS='old')
OPEN(UNIT=11, FILE='c:\tony\data files\grad__2.dat', STATUS='old')
OPEN(UNIT=12, FILE='c:\tony\data files\grad__e.dat', STATUS='old')
OPEN(UNIT=13, FILE='c:\tony\data files\onedim.dat', STATUS='old')
OPEN(UNIT=14, FILE='c:\tony\data files\property.dat', STATUS='old')


Sr=0.65D0
t_o=1.0D-9
beta=1500.0  !this term affects the rapid growth region. ie. for 'long' surface tension
        !growth, the time step may be too course to capture the rapid growth term
        !so it must be increased
del_e=1.0D0/(REAL(M-1))

K=1
```

```
Rinf=0.05D0 !m

!Constants
pi=3.1415926535897931D0

tend=12.0D-3
!_____
  ___
!LIQUID initial conditions
Pinf=(1.0D0D0)*101.33D0     !set the system pressure (kPa)
Tsat=T_sat(Pinf)     ! calculate the corresponding saturation temperature (K)
Tsup=(15.0D0 +0.0D0)       ! set the system superheat (K)
Tinf=Tsat+Tsup    !K
Cpl=(1.0D3)*l_sp_heat(Tinf)   !J/kgK
kl=therm_cond(Tinf)   !W/mK
dl=l_dens(Pinf)
al=kl/(dl*Cpl)
sigma=TENSION(Tsat)*(1.0D-3)   !N/m
hfg=(1.0D3)*LATENT(Tsat)
dv=v_dens(Tsat)

do J=1,M
TEMP_old(J)=Tinf
end do

!VAPOR initial condition
Tv=Tinf
Pv=PRESS2(TV)

WRITE(14,2) Tsat,Tsup,Tinf,dv,dl,hfg,Cpl,al,Pinf,Pv
2 format (f15.5,1x,f15.5,1x,f15.5,1x,f15.10,1x,f15.5,1x,E15.10,1x,E15.10,1x,E15.10,1x,E15.10,1x,E15.10)

Ro=(2.0*sigma)/((1.0D3)*(Pv-Pinf))
call radius(Ro, M, rold)    !sets initial radius

t_(K)=t*1.0D3
R_(K)=Ro*1.0D3
Tmp_(K)=Tv
dRdt_(K)=0.0
!_____         OUTPUT MATRICES_____
                            DO J=1,M
                            T__o(J,1)=t*1.0D3
                            T__o(J,2)=rold(J)*1.0D3  !mm   this is the same as z(1,J)
                            T__o(J,3)=TEMP_old(J)-273.15D0  !degrees Celcius
                            END DO
                            NEXT=1

!_____
  ___
!INITIAL DISTURBANCE
dt=1.0D-9
dist=5.0D-6
R=Ro+dist*Ro
```

```
20 K=K+1
!find k1's

del_t=0.0D0
xi=t
y1i=Tv
y2i=R
y3i=dRdt



CALL FF1(xi, y1i, y2i, y3i, M, del_t, TEMP_old, rold, TEMP, F1)
F2=y3i
call FF3(xi, y1i, y2i, y3i, F3)

k11=F1
k12=F2
k13=F3

del_t=0.5D0*dt
x=xi+del_t
y1=y1i+k11*0.5D0*dt
y2=y2i+k12*0.5D0*dt
y3=y3i+k13*0.5D0*dt

CALL FF1(x, y1, y2, y3, M, del_t, TEMP_old, rold, TEMP, F1)
F2=y3
call FF3(x, y1, y2, y3, F3)

k21=F1
k22=F2
k23=F3

del_t=0.5D0*dt
x=xi+del_t
y1=y1i+k21*0.5D0*dt
y2=y2i+k22*0.5D0*dt
y3=y3i+k23*0.5D0*dt

CALL FF1(x, y1, y2, y3, M, del_t, TEMP_old, rold, TEMP, F1)
F2=y3
call FF3(x, y1, y2, y3, F3)

k31=F1
k32=f2
k33=f3

del_t=dt
x=xi+del_t
y1=y1i+k31*dt
y2=y2i+k32*dt
y3=y3i+k33*dt
```

```
CALL FF1(x, y1, y2, y3, M, del_t, TEMP_old, rold, TEMP, F1)
F2=y3
call FF3(x, y1, y2, y3, F3)


k41=F1
k42=f2
k43=f3




x_1=xi+dt
y1i_1=y1i+(dt/6.0)*(k11+2.0*k21+2.0*k31+k41)
y2i_1=y2i+(dt/6.0)*(k12+2.0*k22+2.0*k32+k42)
y3i_1=y3i+(dt/6.0)*(k13+2.0*k23+2.0*k33+k43)


del_t=dt
t=x_1
Tv=y1i_1
R=y2i_1
dRdt=y3i_1

t_(K)=t*1.0D3
Tmp_(K)=Tv
R_(K)=R*1.0D3
dRdt_(K)=dRdt
!_____

_____

if (t<tend.and.R<40.00D-3) then

P=PRESS2(Tv)

call radius(R, M, rr)
call metrics(M, rr, rn, rnn)
call trans_coef(M, rn, rnn, Ja, a, d)
call temp_coef(M, del_t, rr, rold, rn, Ja, R, dRdt, a, d, Tv, BB, EE, HH)
call temp_matrix(M, del_t, BB, EE, HH, Tv, TEMP_old, TEMP)
dTdr=(2.0*(TEMP(4))-9.0*(TEMP(3))+18.0*(TEMP(2))-11.0*(TEMP(1)))/(6.0*del_e*rn(1))
dTdr_(K)=dTdr
DELTA(K)=(TEMP(M)-TEMP(1))/dTdr
!_____OUTPUT MATRICES_____

!THESE ARE THE TERMS IN THE EQUATION OF MOTION
Mlhs=(1.0D3)*(P-Pinf)/(dl*R)
Mtm2=(3.0D0/2.0D0)*(dRdt**2)/R
Mtm3=2.0D0*sigma/(dl*R**2)


d2Rdt2=Mlhs-Mtm2-Mtm3
d2Rdt_(K)=d2Rdt2
                          Mlhs_(K)=Mlhs*R*dl/1000.0
                          Mtm1_(K)=dl*R*d2Rdt2/1000.0
                          Mtm2_(K)=Mtm2*R*dl/1000.0
```

Mtm3_(K)=Mtm3*R*dl/1000.0

!THESE ARE THE TERMS IN THE INTERFACIAL ENERGY BALANCE EQUATION
dv=v_dens(Tv)
g_T=dvdT(Tv)

Elhs=kl*dTdr
Etm1=hfg*dv
Etm2=(hfg/3.0)*g_T

dTdt=(1.0/(R*Etm2))*(Elhs-Etm1*dRdt)

Elhs_(K)=Elhs
Etm1_(K)=Etm1*dRdt
Etm2_(K)=Etm2*R*dTdt
dTdt_(K)=dTdt

!in this section the temperature gradient matricies are filled
IF(t>=1.0D-9.and.NEXT==1)then
DO J=1,M
T_6(1,1)=t*1.0D3
T_6(J,2)=rr(J)*1.0D3 !mm   this is the same as z(1,J)
T_6(J,3)=TEMP(J)-273.15D0   !degrees Celcius
END DO
NEXT=NEXT+1
ELSEIF(t>=1.0D-8.and.NEXT==2)then
DO J=1,M
T_5(1,1)=t*1.0D3
T_5(J,2)=rr(J)*1.0D3 !mm   this is the same as z(1,J)
T_5(J,3)=TEMP(J)-273.15D0   !degrees Celcius
END DO
NEXT=NEXT+1
ELSEIF(t>=1.0D-7.and.NEXT==3)then
DO J=1,M
T_4(1,1)=t*1.0D3
T_4(J,2)=rr(J)*1.0D3 !mm   this is the same as z(1,J)
T_4(J,3)=TEMP(J)-273.15D0   !degrees Celcius
END DO
NEXT=NEXT+1
ELSEIF(t>=1.0D-6.and.NEXT==4)then
DO J=1,M
T_3(1,1)=t*1.0D3
T_3(J,2)=rr(J)*1.0D3 !mm   this is the same as z(1,J)
T_3(J,3)=TEMP(J)-273.15D0   !degrees Celcius
END DO
NEXT=NEXT+1
ELSEIF(t>=1.0D-5.and.NEXT==5)then
DO J=1,M
T_2(1,1)=t*1.0D3
T_2(J,2)=rr(J)*1.0D3 !mm   this is the same as z(1,J)
T_2(J,3)=TEMP(J)-273.15D0   !degrees Celcius
END DO
NEXT=NEXT+1

```
                    ELSEIF(t>=1.0D-4.and.NEXT==6)then
                    DO J=1,M
                    T_1(1,1)=t*1.0D3
                    T_1(J,2)=rr(J)*1.0D3  !mm   this is the same as z(1,J)
                    T_1(J,3)=TEMP(J)-273.15D0   !degrees Celcius
                    END DO
                    NEXT=NEXT+1
                    ELSEIF(t>=1.0D-3.and.NEXT==7)then
                    DO J=1,M
                    T_0(1,1)=t*1.0D3
                    T_0(J,2)=rr(J)*1.0D3  !mm   this is the same as z(1,J)
                    T_0(J,3)=TEMP(J)-273.15D0   !degrees Celcius
                    END DO
                    NEXT=NEXT+1
                    ELSEIF(t>=5.0D-3.and.NEXT==8)then
                    DO J=1,M
                    T__1(1,1)=t*1.0D3
                    T__1(J,2)=rr(J)*1.0D3  !mm   this is the same as z(1,J)
                    T__1(J,3)=TEMP(J)-273.15D0   !degrees Celcius
                    END DO
                    NEXT=NEXT+1
                    ELSEIF(t>=10.0D-3.and.NEXT==9)then
                    DO J=1,M
                    T__2(1,1)=t*1.0D3
                    T__2(J,2)=rr(J)*1.0D3  !mm   this is the same as z(1,J)
                    T__2(J,3)=TEMP(J)-273.15D0   !degrees Celcius
                    END DO
                    NEXT=NEXT+1
                    ELSEIF(t>=15.0D-3.and.NEXT==10)then
                    DO J=1,M
                    T__e(1,1)=t*1.0D3
                    T__e(J,2)=rr(J)*1.0D3  !mm   this is the same as z(1,J)
                    T__e(J,3)=TEMP(J)-273.15D0   !degrees Celcius
                    END DO
                    NEXT=NEXT+1
                    endif

call radius(R, M, rold)

do J=1,M
TEMP_old(J)=TEMP(J)
end do

dt=t_o*EXP(REAL(K-2)/beta)

GOTO 20
end if

100 do J=1,K,50
            WRITE  (1,25)  t_(J),  R_(J),  dRdt_(J),  d2Rdt_(J),  Tmp_(J)-273.15,
dTdr_(J),Tinf-Tmp_(J),(Tinf-Tmp_(J))/dTdr_(J),dTdt_(J)
    25 FORMAT(f11.7, 1X, f15.10, 1X, f15.10, 1x, E12.5, 1X, f12.8,1X, E12.5,1X, E12.5,1X, E12.5,1X,
E12.5)
```

```
      end do

do J=1,K,50
 WRITE (13,26) t_(J),Mlhs_(J), Mtm1_(J), Mtm2_(J),Mtm1_(J)+Mtm2_(J), Mtm3_(J), Elhs_(J), Etm1_(J),
Etm2_(J)
 26 FORMAT(f11.7,1X,1X,E12.5,1X,E12.5,1x,E12.5,1x,E12.5,1x,E12.5,1x,E12.5,1x,E12.5,1x,E12.5)
 end do


!***************************************************************************************

                              write (2,*) T__o(1,1)
                              do J=1,M
                              write (2,30) T__o(J,2), T__o(J,3), T__o(J,4)
                              30 format (f15.10, 1X, F10.5, 1X, F10.5)
                              end do

                              write (3,*) T_6(1,1)
                              do J=1,M
                               write (3,35) T_6(J,2), T_6(J,3), T_6(J,4)
                              35 format (f15.10, 1X, F10.5, 1X, F10.5)
                              end do

                              write (4,*) T_5(1,1)
                              do J=1,M
                              write (4,40) T_5(J,2), T_5(J,3), T_5(J,4)
                              40 format (f15.10, 1X, F10.5, 1X, F10.5)
                              end do

                              write (5,*) T_4(1,1)
                              do J=1,M
                               write (5,45) T_4(J,2), T_4(J,3), T_4(J,4)
                               45 format (f15.10, 1X, F10.5, 1X, F10.5)
                              end do

                              write (6,*) T_3(1,1)
                              do J=1,M
                              write (6,50) T_3(J,2), T_3(J,3), T_3(J,4)
                              50 format (f15.10, 1X, F10.5, 1X, F10.5)
                              end do

                              write (7,*) T_2(1,1)
                              do J=1,M
                               write (7,55) T_2(J,2), T_2(J,3), T_2(J,4)
                               55 format (f15.10, 1X, F10.5, 1X, F10.5)
                              end do

                              write (8,*) T_1(1,1)
                              do J=1,M
                               write (8,60) T_1(J,2), T_1(J,3), T_1(J,4)
                               60 format (f15.10, 1X, F10.5, 1X, F10.5)
                              end do

                              write (9,*) T_0(1,1)
```

```
      do J=1,M
      write (9,65) T_0(J,2), T_0(J,3), T_0(J,4)
      65 format (f15.10, 1X, F10.5, 1X, F10.5)
      end do

      write (10,*) T__1(1,1)
      do J=1,M
      write (10,70) T__1(J,2), T__1(J,3), T__1(J,4)
      70 format (f15.10, 1X, F10.5, 1X, F10.5)
      end do

      write (11,*) T__2(1,1)
      do J=1,M
      write (11,75) T__2(J,2), T__2(J,3), T__2(J,4)
       75 format (f15.10, 1X, F10.5, 1X, F10.5)
      end do

      write (12,*) T__e(1,1)
      do J=1,M
      write (12,80) T__e(J,2), T__e(J,3), T__e(J,4)
      80 format (f15.10, 1X, F10.5, 1X, F10.5)
      end do


stop
end program

!_____


SUBROUTINE FF3(t, y1, y2, y3, A3)
DOUBLE PRECISION :: t, g_R, f4, P, y1, y2, y3, A3, PRESS2!, ratio
DOUBLE PRECISION :: Sr,Cpl, kl, al, dl, sigma, Tinf, Pinf, Tsat, pi, del_e, Rinf
COMMON/bub_param/Sr,Cpl, kl, al, dl, sigma, Tinf, Pinf, Tsat, pi, del_e, Rinf
P=PRESS2(Y1)

!this assumes that R/Rinf=0
g_R=2.0D0*sigma/(dl*y2**2)

f4=(1.0D3)*(P-Pinf)/(dl*y2)

A3=f4-g_R-(3.0D0/2.0D0)*(y3**2)/y2

RETURN
END SUBROUTINE
!_____


SUBROUTINE FF1(x, y1, y2, y3, M, del_t, Told, r_old, T, A1)


INTEGER :: M
DOUBLE PRECISION, DIMENSION (M) :: Told, T, r, r_old, rn, rnn, Ja, a, d, BB, EE, HH
```

```
DOUBLE PRECISION :: x, f1, f2, f3, hfg, dTdr, dv
DOUBLE PRECISION :: A1, y1, y2, y3
DOUBLE PRECISION :: del_t
DOUBLE PRECISION :: LATENT, v_dens, dvdT, g_T
DOUBLE PRECISION :: Sr,Cpl, kl, al, dl, sigma, Tinf, Pinf, Tsat, pi, del_e, Rinf
COMMON/bub_param/Sr,Cpl, kl, al, dl, sigma, Tinf, Pinf, Tsat, pi, del_e, Rinf
hfg=(1.0D3)*LATENT(y1)

IF(del_t>0.0D0)then

call radius(y2, M, r)
call metrics(M, r, rn, rnn)
call trans_coef(M, rn, rnn, Ja, a, d)
call temp_coef(M, del_t, r, r_old, rn, Ja, y2, y3, a, d, y1, BB, EE, HH)
call temp_matrix(M, del_t, BB, EE, HH, y1, Told, T)

dTdr=(2.0D0*T(4)-9.0D0*T(3)+18.0D0*T(2)-11.0D0*T(1))/(6.0D0*del_e*rn(1))

ELSE

call radius(y2, M, r)
call metrics(M, r, rn, rnn)
dTdr=(2.0D0*Told(4)-9.0D0*Told(3)+18.0D0*Told(2)-11.0D0*Told(1))/(6.0D0*del_e*rn(1))

ENDIF

dv=v_dens(y1)
g_T=dvdT(y1)


f3=kl*dTdr
f2=hfg*dv
f1=(hfg/3.0D0)*g_T

A1=(1.0D0/(y2*f1))*(f3-f2*y3)

RETURN
END SUBROUTINE

!_____


!******************************************************************************
*****

subroutine radius(Rt, M, r)

INTEGER :: M
DOUBLE PRECISION, DIMENSION(M) :: r, Dj
DOUBLE PRECISION :: Rt
DOUBLE PRECISION :: Sr,Cpl, kl, al, dl, sigma, Tinf, Pinf, Tsat, pi, del_e, Rinf
COMMON/bub_param/Sr,Cpl, kl, al, dl, sigma, Tinf, Pinf, Tsat, pi, del_e, Rinf

do J=1,M
```

```fortran
! Set the radial grid lines in the physical domain
Dj(J)=Rt+(Rinf-Rt)*(1.0-Sr*ATAN((1.0-(REAL (J-1)/(M-1)))*TAN(1.0/Sr)))

r(J)=Dj(J)
end do

return
end subroutine


!_____


!**********************************************************************************
*****
subroutine metrics(M, r, rn, rnn)

INTEGER :: M
DOUBLE PRECISION, DIMENSION(M) :: r, rn, rnn
DOUBLE PRECISION :: Sr,Cpl, kl, al, dl, sigma, Tinf, Pinf, Tsat, pi, del_e, Rinf
COMMON/bub_param/Sr,Cpl, kl, al, dl, sigma, Tinf, Pinf, Tsat, pi, del_e, Rinf
do J=2,M-1

rn(J)=(r(J+1)-r(J-1))/(2*del_e)
rnn(J)=(r(J+1)-2*r(J)+r(J-1))/(del_e**2)

end do

rn(1)=(-3.0*r(1)+4.0*r(2)-r(3))/(2.0*del_e)
rnn(1)=(2.0*r(1)-5.0*r(2)+4.0*r(3)-r(4))/(del_e**2)


rn(M)=(3.0*r(M)-4.0*r(M-1)+r(M-2))/(2.0*del_e)
rnn(M)=(2.0*r(M)-5.0*r(M-1)+4.0*r(M-2)-r(M-3))/(del_e**2)

return
end subroutine


!_____


!**********************************************************************************
*****
subroutine trans_coef(M, rn, rnn, Ja, a, d)

INTEGER :: M, J
DOUBLE PRECISION, DIMENSION(M) :: rn, rnn, Ja, a, d

do J=1,M
  a(J)=rn(J)**2
  d(J)=-rn(J)*rnn(J)
  Ja(J)=1.0/(rn(J)**2)
end do

return
```

end subroutine

!_____

!***
*****

```fortran
subroutine temp_coef(M, del_t, r, rold, rn, Ja, Rt, dRdt, a, d, Tv, BB, EE, HH)
DOUBLE PRECISION, DIMENSION(M) :: r, rold, rn, Ja, a, d, BB, EE, HH, c1, c3, Uc
DOUBLE PRECISION :: del_t, Tv, Rt, dRdt
DOUBLE PRECISION :: Sr,Cpl, kl, al, dl, sigma, Tinf, Pinf, Tsat, pi, del_e, Rinf
COMMON/bub_param/Sr,Cpl, kl, al, dl, sigma, Tinf, Pinf, Tsat, pi, del_e, Rinf
do J=1,M
  Uc(J)=rn(J)*((dRdt*(Rt/r(J))**2)-(r(J)-rold(J))/del_t)
end do

do J=1,M
c1(J)=Ja(J)*Uc(J)/al-((Ja(J)**2)*d(J)+2.0*Ja(J)*rn(J)/r(J))
c3(J)=-(Ja(J)**2)*a(J)
end do


do J=1,M
BB(J)=(c1(J)/(2.0*del_e)+c3(J)/(del_e**2))
EE(J)=1.0/(al*del_t)-(2.0*c3(J)/(del_e**2))
HH(J)=(-c1(J)/(2.0*del_e)+c3(J)/(del_e**2))
end do
return
end subroutine
```

!_____

_____

```fortran
subroutine temp_matrix(M, del_t, BB, EE, HH, Tv, Told, T)
INTEGER :: M
DOUBLE PRECISION, DIMENSION(M) :: BB, EE, HH, a, b, c, d, Told, T, T_2
DOUBLE PRECISION :: del_t, Tv
DOUBLE PRECISION :: Sr,Cpl, kl, al, dl, sigma, Tinf, Pinf, Tsat, pi, del_e, Rinf
COMMON/bub_param/Sr,Cpl, kl, al, dl, sigma, Tinf, Pinf, Tsat, pi, del_e, Rinf
T(M)=Tinf

!Set up equations so that they are in the form (Patanker):
!
!     a(1)T(1)=b(1)T(2)+d(2)
!     a(2)T(2)=b(2)T(3)+c(2)T(1)+d(2)
!     .....
!     a(J)T(J)=b(J)T(J+1)+c(J)T(J-1)+d(J)
!     .....
!     a(M-1)T(M-1)=c(M-1)T(M-2)+d(M-1)
!
!***********************************************************

do J=2,M-1
  a(J)=EE(J)
```

```fortran
   if (J==2) then
     b(J)=-BB(J)
     c(J)=0.0
     d(J)=Told(J)/(al*del_t)-HH(J)*Tv
   ELSEIF(J==M-1)then
     c(J)=-HH(J)
     b(J)=0.0
     d(J)=Told(J)/(al*del_t)-BB(J)*Tinf
   else
     c(J)=-HH(J)
     b(J)=-BB(J)
     d(J)=Told(J)/(al*del_t)
   end if
end do

do J=1,M-2
a(J)=a(J+1)
b(J)=b(J+1)
c(J)=c(J+1)
d(J)=d(J+1)
end do
call TDMA(M-2, a, b, c, d, T_2)

 do J=1,M
     IF(J==1)then
       T(J)=Tv
     ELSEIF(J==M)then
       T(J)=Tinf
     else
       T(J)=T_2(J-1)
       endif
   end do
return
end subroutine


!_____

!*******************************************************************************
*****
subroutine TDMA(M, a, b, c, d, U)

INTEGER :: M
DOUBLE PRECISION , DIMENSION(M) :: a, b, c, d, P, Q, U
DOUBLE PRECISION :: BET

if (a(1)==0.0) pause

BET=a(1)
Q(1)=d(1)/BET
P(1)=b(1)/BET

do J=2,M
```

```
BET=a(J)-c(J)*P(J-1)

if (BET==0.0) pause

P(J)=b(J)/BET
Q(J)=(d(J)+c(J)*Q(J-1))/BET

end do

U(M)=Q(M)

do J=M-1,1,-1
U(J)=P(J)*U(J+1)+Q(J)
end do

return
end subroutine
!_____
_____

!*********************** Water  Properties *** **********************************

FUNCTION PRESS2(T)
DOUBLE PRECISION :: T, PRESS2, a, b, c
a=15.38366
b=-2111.3788
c=-36815.655
PRESS2=EXP(a+b/T+c/T**1.5)
return
END

FUNCTION LATENT(T)
DOUBLE PRECISION :: a, b, c, d, T, LATENT
a=4535.5338
b=-14.40485
c=0.034749747
d=-3.3548106D-5
  LATENT=a+(b*T)+(c*T**2)+(d*T**3) !kJ/kg,  T in K
return
END

FUNCTION TENSION(T)
DOUBLE PRECISION :: T, TENSION
TENSION=235.8D0*((1.0D0-(T)/(374.15D0+273.15D0))**1.256D0)*(1.0D0-(0.625D0)*(1.0D0-(T)/(37
4.15D0+273.15D0))) !mN/m
return
end

FUNCTION l_sp_heat(T)
DOUBLE PRECISION :: T, l_sp_heat, a, b, c, d, e
a=78.582798
b=-0.14625086
c=0.00010960625
d=-17026.454
```

```
e=1472551.8
  l_sp_heat=a+(b*T)+(c*T**2)+(d/T)+(e/T**2)    !kJ/kgK
END


FUNCTION T_sat(P)
DOUBLE PRECISION :: P, T_sat, a, b, c, d, e, f, g, h
a=280.14591
b=14.578656
c=0.81618388
d=0.090358794
e=-0.01233292
f=0.0036827453
g=-0.00036521131
h=1.7727335D-5



T_sat=a+b*(LOG(P))+c*(LOG(P))**2+d*(LOG(P))**3+e*(LOG(P))**4+f*(LOG(P))**5+g*(LOG(P))*
*6+h*(LOG(P))**7
 END


function therm_cond(T)
DOUBLE PRECISION :: therm_cond, T
therm_cond=0.56917061+0.0018981353*(T-273.15)-8.8322257*10**(-6.0)*(T-273.15)**2.0+7.2806061
*10**(-9.0)*(T-273.15)**3.0 !W/mK
return
end


function l_dens(P)
DOUBLE PRECISION :: l_dens, P
l_dens=1008.1433+(-7.3239274)*P**0.41233836          !kg/m3
return
end


function v_dens(T)
DOUBLE PRECISION :: v_dens, T, a, b, c
a=94.90762D0
b=-0.023178676D0
c=-0.24376403D0
  v_dens=EXP((a+c*T)/(1.0D0+b*T))    !kg/m3
return
end


function dvdT(T)
DOUBLE PRECISION :: dvdT, T, b, c
a=94.90762D0
b=-0.023178676D0
c=-0.24376403D0
  dvdT=((c-a*b)/(1.0D0+b*T)**2)*EXP((a+c*T)/(1.0D0+b*T))
return
end


!_____

  _____
```

!************************ R113 Properties *** ***

```fortran
FUNCTION PRESS2(T)
DOUBLE PRECISION :: T, PRESS2, a, b, c, d, e,f
a=2957.142318D0
b=-53.1787872D0
c=0.371694819D0
d=-0.001235475106D0
e=1.860059877D-06
f=-8.710006423D-10
PRESS2=a+b*T+c*T**2+d*T**3+e*T**4+f*T**5
return
END


FUNCTION LATENT(T)
DOUBLE PRECISION :: a, b, c, d, e, f, T, LATENT
a=2737.48849146611D0
b=-39.3003642747073D0
c=0.239810862940233D0
d=-0.000727033297258D0
e=1.089453393D-06
f=-6.47894D-10
LATENT=a+b*T+c*T**2+d*T**3+e*T**4+f*T**5  !kJ/kg, T in K
return
END




FUNCTION TENSION(T)
DOUBLE PRECISION :: T, TENSION, a, b, c, d, e
a=100.66367D0
b=-0.26354029D0
c=0.00017492986D0
d=-8150.6195D0
e=535170.24D0
TENSION=a+b*T+c*T**2+d/T+e/T**2 !mN/m
return
end

FUNCTION l_sp_heat(T)
DOUBLE PRECISION :: T, l_sp_heat, a, b, c, d
a=-2687.2937711853D0
b=32.1760788219D0
c=-0.0967652227D0
d=0.0001001237D0
  l_sp_heat=(a+(b*T)+(c*T**2)+(d*T**3))/1000.0D0     !kJ/kgK
END




FUNCTION T_sat(P)
DOUBLE PRECISION :: P, T_sat, a, b, c, d, e
a=227.62444D0
```

```
b=13.885934D0
c=0.69937307D0
d=0.15567729D0
e=-0.01232013D0
f=0.002049886D0
  T_sat=a+b*LOG(P)+c*LOG(P)**2+d*LOG(P)**3+e*LOG(P)**4+f*LOG(P)**5
END




function therm_cond(T)
DOUBLE PRECISION :: therm_cond, T, a, b, c, d, e, f
a=572.672566562039D0
b=-7.22070352101712D0
c=0.044478466185909D0
d=-0.000139306769359D0
e=2.15863959D-07
f=-1.32549D-10
therm_cond=(a+b*T+c*T**2+d*T**3+e*T**4+f*T**5)*1.0D-3 !W/mK
return
end


function l_dens(Tin)
DOUBLE PRECISION :: l_dens, T, Tin, a, b, c, d, e, f
T=Tin-273.15D0
a=16.1767736505804D0
b=-0.021409787008367D0
c=3.666728067D-06
d=-1.210948367D-06
e=1.1848044D-08
f=-3.7748D-11
l_dens=(a+b*T+c*T**2+d*T**3+e*T**4+f*T**5)*100.0D0      !kg/m3
return
end




function v_dens(T)
DOUBLE PRECISION :: v_dens, T, a, b, c, d, e, f
a=-299.6373102D0
b=4.974715994D0
c=-0.03322820191D0
d=0.0001134072022D0
e=-2.031981824D-07
f=1.585972295D-10
v_dens=a+b*T+c*T**2+d*T**3+e*T**4+f*T**5      !kg/m3
return
end

function dvdT(T)
DOUBLE PRECISION :: dvdT, T, b, c, d, e, f

b=4.974715994D0
c=-0.03322820191D0
```

```
d=0.0001134072022D0
e=-2.031981824D-07
f=1.585972295D-10
  dvdT=b+2.0*c*T+3.0*d*T**2+4.0*e*T**3+5.0*f*T**4   !
return
end
```

APPENDIX F

FORTRAN 90 Code for Heterogeneous Growth on a Heated Surface

This program solves the two-dimensional, spherical or hemispherical bubble growth problem in a radially symmetric or distributed liquid temperature field from its thermodynamic critical size through the surface tension, inertial and heat transfer controlled stages of growth. Bubble growth away from the initial unstable equilibrium state of the vapor nucleus is instigated by a small increase in radius dRo over a small time step dto. A fourth order Runge-Kutta scheme is then utilized to solve the modified Rayleigh equation together with the Interfacial Energy balance equation for the variables Tv, R, dRdt from which Pv and dv can also be determined. The vapor phase is assumed to be in thermodynamic equilibrium throughout its growth so that the vapour properties can be determined from curve fit functions of the available property data. The temperature gradient at the interface is determined from the Energy equation including the non-linear convective term. A staggered grid arrangement is utilized to cluster the grid points at the interface where the gradients are the highest. A coordinate transformation is performed so that the energy equation is solved on a uniform grid in the computational domain.

```fortran
program stagger
implicit none

INTEGER :: K, J, I, K_, NEXT,II
INTEGER, PARAMETER :: M=800, N=60, KK=20000

DOUBLE PRECISION, DIMENSION(KK) :: t_, R_, Tmp_, dRdt_, q1, q2, q3
DOUBLE PRECISION, DIMENSION(KK) :: Elhs_, Etm1_, Etm2_, Mlhs_, Mtm1_, Mtm2_, Mtm3_, dTdn_t,
dTdn_b
DOUBLE PRECISION, DIMENSION(N,M) :: TEMP, TEMP_old, r, z, rold, zold, GAM
DOUBLE PRECISION, DIMENSION(M) :: Dj
DOUBLE PRECISION, DIMENSION(N) :: dT_norm, Tff, Ai, qi
DOUBLE PRECISION, DIMENSION(M,4) :: T__o, T_6, T_5, T_4, T_3, T_2, T_1, T_0, T__1, T__2, T__e


!Liquid
DOUBLE PRECISION :: Tsup
!Vapor
DOUBLE PRECISION :: Ro, Rt, Pv, Tv, dRdt
!Runge Kutta
DOUBLE PRECISION :: xi, y1i, y2i, y3i, F1, F2, F3, x, y1, y2, y3, x_1, y1i_1, y2i_1, y3i_1, &
          k11, k21, k31, k41, k12, k22, k32, k42, k13, k23, k33, k43
!Miscillaneous
DOUBLE PRECISION :: t, dt, dist, del_t, t_o, beta, P
LOGICAL :: NONUNIF, SPHERE, INITSUP
DOUBLE PRECISION :: tw, ARG, erfc_x, sum_q, area, qevap, qcond
DOUBLE PRECISION :: Elhs, Etm1, Etm2, dTdt, g_T, dv, hfg
DOUBLE PRECISION :: Mlhs, Mtm2, Mtm3, d2Rdt2, TIME
DOUBLE PRECISION :: RAD,FIND
D O U B L E    P R E C I S I O N ,    D I M E N S I O N ( M , 3 )    : :
XY50,XY55,XY60,XY65,XY70,XY75,XY80,XY55_,XY60_,XY65_,XY70_,XY75_,XY80_


!Functions
DOUBLE PRECISION :: PRESS2, TENSION, l_sp_heat, therm_cond, l_dens, T_sat, DELTA, LATENT,&
                    v_dens, dvdT
!Common
DOUBLE PRECISION :: Cpl, kl, al, dl, sigma, Tinf, Pinf, Tsat, pi, Sr, Rinf, del_e, del_n, q
COMMON/bub_param/Cpl, kl, al, dl, sigma, Tinf, Pinf, Tsat, pi, Sr, Rinf, del_e, del_n, q

OPEN(UNIT=1, FILE='c:\tony\data files\one_dim.dat', STATUS='old')
OPEN(UNIT=2, FILE='c:\tony\data files\grad_o.dat', STATUS='old')
OPEN(UNIT=3, FILE='c:\tony\data files\grad_6.dat', STATUS='old')
OPEN(UNIT=4, FILE='c:\tony\data files\grad_5.dat', STATUS='old')
OPEN(UNIT=5, FILE='c:\tony\data files\grad_4.dat', STATUS='old')
OPEN(UNIT=6, FILE='c:\tony\data files\grad_3.dat', STATUS='old')
OPEN(UNIT=7, FILE='c:\tony\data files\grad_2.dat', STATUS='old')
OPEN(UNIT=8, FILE='c:\tony\data files\grad_1.dat', STATUS='old')
OPEN(UNIT=9, FILE='c:\tony\data files\grad_0.dat', STATUS='old')
OPEN(UNIT=10, FILE='c:\tony\data files\grad__1.dat', STATUS='old')
OPEN(UNIT=11, FILE='c:\tony\data files\grad__2.dat', STATUS='old')
OPEN(UNIT=12, FILE='c:\tony\data files\grad__e.dat', STATUS='old')
OPEN(UNIT=13, FILE='c:\tony\data files\onedim.dat', STATUS='old')
OPEN(UNIT=14, FILE='c:\tony\data files\rout.dat', STATUS='old')
OPEN(UNIT=15, FILE='c:\tony\data files\zout.dat', STATUS='old')
```

```
OPEN(UNIT=16, FILE='c:\tony\data files\Tout.dat', STATUS='old')
OPEN(UNIT=17, FILE='c:\tony\data files\T50.dat', STATUS='old')
OPEN(UNIT=18, FILE='c:\tony\data files\T70.dat', STATUS='old')
OPEN(UNIT=19, FILE='c:\tony\data files\T70_.dat', STATUS='old')
OPEN(UNIT=20, FILE='c:\tony\data files\T80.dat', STATUS='old')
OPEN(UNIT=21, FILE='c:\tony\data files\T80_.dat', STATUS='old')
OPEN(UNIT=22, FILE='c:\tony\data files\T60.dat', STATUS='old')
OPEN(UNIT=23, FILE='c:\tony\data files\T60_.dat', STATUS='old')
OPEN(UNIT=24, FILE='c:\tony\data files\T55.dat', STATUS='old')
OPEN(UNIT=25, FILE='c:\tony\data files\T55_.dat', STATUS='old')
OPEN(UNIT=26, FILE='c:\tony\data files\T65.dat', STATUS='old')
OPEN(UNIT=27, FILE='c:\tony\data files\T65_.dat', STATUS='old')
OPEN(UNIT=28, FILE='c:\tony\data files\T75.dat', STATUS='old')
OPEN(UNIT=29, FILE='c:\tony\data files\T75_.dat', STATUS='old')


!Constants NOT TO beta changed
NONUNIF=.true.
SPHERE=.false.
INITSUP=.true.
pi=3.1415926535897931D0
K_=1



!_____


!_____
!Specify the type of bubble growth. There three choices;
!1)Spherical growth in an initially uniform temperature field:: NONUNIF=.FALSE. SPHERE=.TRUE.
!2)Spherical growth in an initially non-uniform temperature field:: NONUNIF=.TRUE. SPHERE=.TRUE.
!3)Hemispherical growth in an initially non-uniform temperature field:: NONUNIF=.TRUE.
SPHERE=.FALSE.
NONUNIF=.TRUE.     !.......SPECIFIED
SPHERE=.FALSE.     !.......SPECIFIED


!Specify superheat for 1-D simulated spherical bubble growth. Two choices;
!1)specify the initial superheat and determine Tinf=Tsup+tsat:: INITSUP=.TRUE.
!2)let Tinf equal the surface temperature at tw (the waiting time):: INITSUP=.FALSE.
INITSUP=.FALSE.


!PHYSICAL DOMAIN
Sr=0.65D0    !controls the percentage of grid points clustered near the vapour/liquid interface
Rinf=0.05D0 !far field boundary in (m). Increasing this causes grid spacing to become larger so that it should
        !kept as small as possible but larger than the final bubble radius.


!Because of the initially high growth rate away from the Surface Tension controlled region and the relatively
!slower growth rate in the Heat Transfer controlled region, the time steps are initially small to resolve the
!high dRdt and becomes larger as dRdt decreases at larger times according to the function
dt=t_o*EXP((K-2)/beta).
!Increasing beta decreases the rate at which dt increases.
t_o=1.0D-8
beta=1500.0D0
K=1


!COMUTATIONAL DOMAIN
```

```
!in the two-dimensional computational domain the grid spacing is uniform and equal to,
del_e=DELTA(N)
del_n=DELTA(M)

!LIQUID INITIAL CONDITION
Pinf=117.3D0              !ambient pressure (kPa).......SPECIFIED
Tsat=T_sat(Pinf)          !saturation pressure in (K)
Cpl=(1.0D3)*l_sp_heat(Tsat)   !specific heat J/kgK
kl=therm_cond(Tsat)       !thermal conductivity in (W/mK)
dl=l_dens(Tsat)           !density in (kg/m3)
al=kl/(dl*Cpl)            !thermal diffusivity in (m2/s)
sigma=TENSION(Tsat)*(1.0D-3) !surface tension in (N/m)

!SYSTEM CONDITIONS
q=65000D0*0.175D0              !surface heat flux from Lee [1994] in (W/m2).......SPECIFIED
tw=0.5D0                  !time to nucleation in (s).......SPECIFIED
Tinf=48.8D0+273.15D0      !the initial liquid temperature in (K).......SPECIFIED
!_____
```
_____

```
!1)Spherical growth in an initially uniform temperature field:: NONUNIF=.FALSE. SPHERE=.TRUE.
if (.NOT.NONUNIF.AND.SPHERE) then

   if (INITSUP) then
      Tsup=3.0           !initial superheat (K).......SPECIFIED
      Tinf=Tsup+Tsat     !this overrides previous definition of Tinf
   else
      do I=1,N
      TEMP_old(I,1)=Tinf+(2.0D0*q*SQRT(al*tw/pi)/kl)
      end do
      Tinf=TEMP_old(1,1) !now Tinf is equal to the wall temperature at the waiting time
   end if

!Specify a zero heat flux at the wall to ensure axial symmetry
q=0.0D0

!VAPOR INITIAL CONDITION. Initially in thermal equilibrium with liquid
Tv=Tinf
Pv=PRESS2(Tv)

!LIQUID INITIAL CONDITION. Sets the uniform liquid temperature field to Tinf
do I=1,N
 do J=1,M
  TEMP_old(I,J)=Tinf
 end do
end do

!INITIAL BUBBLE RADIUS. Derived from mechanical equilibrium for a thin walled pressure vessel
(Young-Laplace eqn)
Ro=(2.0*sigma)/((1.0D3)*(Pv-Pinf))
call randz(Ro,N,M,rold,zold,GAM,Dj) !sets initial grid point distribution in the physical domain

ELSEIF(NONUNIF) THEN
```

```
!VAPOR INITIAL CONDITION. Initial temperature equal to the wall temperature at nucleation
Tv=Tinf+(2.0D0*q*SQRT(al*tw/pi)/kl)
Pv=PRESS2(Tv)

!Set the liquid temperature at the interface equal to the vapour temperature
do I=1,N
 TEMP_old(I,1)=Tv
end do

!INITIAL BUBBLE RADIUS. Derived from mechanical equilibrium for a thin walled presure vessel
(Young-Laplace eqn)
Ro=(2.0*sigma)/((1.0D3)*(Pv-Pinf))
call randz(Ro,N,M,rold,zold,GAM,Dj) !sets initial grid point distribution in the physical domain

!**************************************************************************************
******

    !2)Spherical growth in an initially non-uniform temperature field:: NONUNIF=.TRUE. SPHERE=.TRUE.
    IF(SPHERE) THEN
       !LIQUID INITIAL CONDITION. Sets the spherically symmetric non-uniform liquid temperature field
according to
       !that normal to wall at nucleation.

       DO I=1,N
       DO J=2,M
         ARG=(sqrt(rold(I,J)**2+zold(I,J)**2))/(2.0D0*SQRT(al*tw))
         call errorfnctn(ARG, pi, erfc_x)


TEMP_old(I,J)=Tinf+(2.0D0*q*SQRT(al*tw/pi)/kl)*EXP(-(rold(I,J)**2+zold(I,J)**2)/(4.0D0*al*tw))&
               -(q*(sqrt(rold(I,J)**2+zold(I,J)**2))/kl)*erfc_x
       END DO
       END DO

       !Specify a zero heat flux at the wall to ensure axial symmetry
       q=0.0D0

!**************************************************************************************
******
       !3)Hemispherical growth in an initially non-uniform temperature field:: NONUNIF=.TRUE.
SPHERE=.FALSE.
    ELSEIF(.NOT.SPHERE)THEN


       DO I=1,N
       DO J=2,M
         ARG=(zold(I,J))/(2.0D0*SQRT(al*tw))
         call errorfnctn(ARG, pi, erfc_x)

         TEMP_old(I,J)=Tinf+(2.0D0*q*SQRT(al*tw/pi)/kl)*EXP(-(zold(I,J)**2)/(4.0D0*al*tw))&
               -(q*(zold(I,J))/kl)*erfc_x

       END DO
       END DO
```

```
    END IF
ENDIF
!_____


!Set Initial Far Field boundary to constant temperature=T(r,z) @t=tw
do I=1,N
 Tff(I)=TEMP_old(I,M)
end do



!_____OUTPUT MATRICES_____
                           DO J=1,M
                           T__o(J,1)=t*1.0D3
                           T__o(J,2)=rold(N,J)*1.0D3  !mm   this is the same as z(1,J)
                           T__o(J,3)=TEMP_old(N,J)-273.15D0   !degrees Celsius
                           END DO
                           NEXT=1


                           t_(K)=t*1.0D3
                           R_(K)=Ro*1.0D3
                           Tmp_(K)=Tv-273.15D0
                           dRdt_(K)=0.0
                           q1(K)=0.0
                           q2(K)=0.0
                           q3(K)=0.0
!_____


!INITIAL DISTURBANCE
dt=1.0D-9
dist=5.0D-6
Rt=Ro+dist*Ro
!_____


20 K=K+1
   K_=K_+1

TIME=TIME+dt
!Update far field temperature field assuming it follows 1D steady state conduction
!This is only needed when transient heating is assumed.
DO I=1,N
ARG=(zold(I,M))/(2.0D0*SQRT(al*tw))
call errorfnctn(ARG, pi, erfc_x)

   Tff(I)=Tinf+(2.0D0*q*SQRT(al*(tw+TIME)/pi)/kl)*EXP(-(zold(I,M)**2)/(4.0D0*al*(tw+TIME)))&
          -(q*(zold(I,M))/kl)*erfc_x
END DO

_____FOURTH ORDER RUNGE-KUTTA_____

!Set initial values
```

```
del_t=0.0D0
xi=t
y1i=Tv
y2i=Rt
y3i=dRdt

!STEP #1
CALL FF1(xi, y1i, y2i, y3i, M, N, del_t, Tff,TEMP_old, rold, zold, TEMP, F1)
F2=y3i
call FF3(t, y1i, y2i, y3i, F3)

k11=F1
k12=F2
k13=F3

del_t=0.5D0*dt
x=xi+del_t
y1=y1i+k11*0.5D0*dt
y2=y2i+k12*0.5D0*dt
y3=y3i+k13*0.5D0*dt

!STEP #2
CALL FF1(x, y1, y2, y3, M, N, del_t, Tff,TEMP_old, rold, zold, TEMP, F1)
F2=y3
call FF3(t, y1, y2, y3, F3)

k21=F1
k22=F2
k23=F3

del_t=0.5D0*dt
x=xi+del_t
y1=y1i+k21*0.5D0*dt
y2=y2i+k22*0.5D0*dt
y3=y3i+k23*0.5D0*dt

!STEP#3
CALL FF1(x, y1, y2, y3, M, N, del_t, Tff,TEMP_old, rold, zold, TEMP, F1)
F2=y3
call FF3(t, y1, y2, y3, F3)

k31=F1
k32=f2
k33=f3

del_t=dt
x=xi+del_t
y1=y1i+k31*dt
y2=y2i+k32*dt
y3=y3i+k33*dt

!STEP#4
CALL FF1(x, y1, y2, y3, M, N, del_t, Tff,TEMP_old, rold, zold, TEMP, F1)
```

```
F2=y3
call FF3(t, y1, y2, y3, F3)

k41=F1
k42=f2
k43=f3

!STEP #4
!UPDATED VALUES OF t, R, and dRdt AT THE NEXT TIME STEP
x_1=xi+dt
y1i_1=y1i+(dt/6.0D0)*(k11+2.0D0*k21+2.0D0*k31+k41)
y2i_1=y2i+(dt/6.0D0)*(k12+2.0D0*k22+2.0D0*k32+k42)
y3i_1=y3i+(dt/6.0D0)*(k13+2.0D0*k23+2.0D0*k33+k43)

del_t=dt
t=x_1
Tv=y1i_1
Rt=y2i_1
dRdt=y3i_1
!_____OUTPUT MATRICES_____

                    t_(K)=t*1.0D3
                    Tmp_(K)=Tv-273.15D0
                    R_(K)=Rt*1.0D3
                    dRdt_(K)=dRdt

!_____


!CHECK TIME CONSTRAINT
if (t<=101.0D-3) then

!_____BUBBLE DYNAMICS_____
!this is identical to the subroutine to solve energy equation
hfg=(1.0D3)*LATENT(Tv)
!CALL FF1(dt, Tv, Rt, dRdt, M, N, dt, Tff,TEMP_old, rold, zold, TEMP, F1)
call new_Temp(M,N, Rt, Tv, dRdt, dt, TEMP_old, rold, zold, Tff, TEMP, dT_norm, GAM)

sum_q=0.0D0
area=0.0D0
qevap=0.0D0
qcond=0.0D0
do I=2,N
 Ai(I)=2.0D0*pi*(Rt**2)*(COS(GAM(I-1,1))-COS(GAM(I,1)))
 qi(I)=(0.5D0*k1*Ai(I)*(dT_norm(I-1)+dT_norm(I)))

 IF(qi(I)<0.0D0)then
 qcond=qcond+qi(I)
 ELSEIF(qi(I)>0.0)then
 qevap=qevap+qi(I)
 endif

 area=area+Ai(I)
 sum_q=sum_q+qi(I)
end do
```

```
!_____OUTPUT MATRICES_____

                        q1(K)=sum_q/2.0D0
                        q2(K)=qevap/2.0D0
                        q3(K)=qcond/2.0D0

                        dTdn_t(K)=dT_norm(1)
                        dTdn_b(K)=dT_norm(N)
!_____


_____
area=area
dv=v_dens(Tv)
g_T=dvdT(Tv)


!THESE ARE THE TERMS IN THE INTERFACIAL ENERGY BALANCE EQUATION

Elhs=sum_q/area
Etm1=hfg*dv
Etm2=(hfg/3.0)*g_T

dTdt=(1.0/(Rt*Etm2))*(Elhs-Etm1*dRdt)
!_____OUTPUT MATRICES_____

                        Elhs_(K)=Elhs
                        Etm1_(K)=Etm1*dRdt
                        Etm2_(K)=Etm2*Rt*dTdt
!_____


_____

!THESE ARE THE TERMS IN THE EQUATION OF MOTION
P=PRESS2(Tv)
Mlhs=(1.0D3)*(P-Pinf)/(dl*Rt)
Mtm2=(3.0D0/2.0D0)*(dRdt**2)/Rt
Mtm3=2.0D0*sigma/(dl*Rt**2)

d2Rdt2=Mlhs-Mtm2-Mtm3
!_____OUTPUT MATRICES_____
                        Mlhs_(K)=Mlhs*Rt
                        Mtm1_(K)=Rt*d2Rdt2
                        Mtm2_(K)=Mtm2*Rt
                        Mtm3_(K)=Mtm3*Rt
!_____


_____

PRINT 22, t_(K),R_(K), dTdn_t(K), dTdn_b(K), Tff(N), Tv
22 FORMAT(E12.5, 1x, E12.5, 1x, E12.5, 1x, E12.5, 1x, E12.5, 1X,E12.5)


!RESET THE "OLD" GRID POINT LOCATIONS AND TEMPERATURE FIELD FOR THE NEXT TIME
STEP
call randz(Rt,N,M,r,z,GAM,Dj)

DO I=1,N
```

```
DO J=1,M
 rold(I,J)=r(I,J)
 zold(I,J)=z(I,J)
 END DO
END DO

do I=1,N
 do J=1,M
  TEMP_old(I,J)=TEMP(I,J)
 end do
end do
```

```
!_____OUTPUT MATRICES_____
!in this section the temperature gradient matrices are filled
                              IF(t>=1.0D-9.and.NEXT==1)then
                              DO J=1,M
                              T_6(1,1)=t*1.0D3
                              T_6(J,2)=r(N,J)*1.0D3  !mm   this is the same as z(1,J)
                              T_6(J,3)=TEMP(1,J)-273.15D0  !degrees Celsius
                              T_6(J,4)=TEMP(N,J)-273.15D0
                              END DO
                              NEXT=NEXT+1
                              ELSEIF(t>=1.0D-8.and.NEXT==2)then
                              DO J=1,M
                              T_5(1,1)=t*1.0D3
                              T_5(J,2)=r(N,J)*1.0D3  !mm   this is the same as z(1,J)
                              T_5(J,3)=TEMP(1,J)-273.15D0  !degrees Celsius
                              T_5(J,4)=TEMP(N,J)-273.15D0
                              END DO
                              NEXT=NEXT+1
                              ELSEIF(t>=1.0D-7.and.NEXT==3)then
                              DO J=1,M
                              T_4(1,1)=t*1.0D3
                              T_4(J,2)=r(N,J)*1.0D3  !mm   this is the same as z(1,J)
                              T_4(J,3)=TEMP(1,J)-273.15D0  !degrees Celsius
                              T_4(J,4)=TEMP(N,J)-273.15D0
                              END DO
                              NEXT=NEXT+1
                              ELSEIF(t>=1.0D-6.and.NEXT==4)then
                              DO J=1,M
                              T_3(1,1)=t*1.0D3
                              T_3(J,2)=r(N,J)*1.0D3  !mm   this is the same as z(1,J)
                              T_3(J,3)=TEMP(1,J)-273.15D0  !degrees Celsius
                              T_3(J,4)=TEMP(N,J)-273.15D0
                              END DO
                              NEXT=NEXT+1
                              ELSEIF(t>=1.0D-5.and.NEXT==5)then
                              DO J=1,M
                              T_2(1,1)=t*1.0D3
                              T_2(J,2)=r(N,J)*1.0D3  !mm   this is the same as z(1,J)
                              T_2(J,3)=TEMP(1,J)-273.15D0  !degrees Celsius
                              T_2(J,4)=TEMP(N,J)-273.15D0
                              END DO
```

```
                        NEXT=NEXT+1
                        ELSEIF(t>=1.0D-4.and.NEXT==6)then
                        DO J=1,M
                        T_1(1,1)=t*1.0D3
                        T_1(J,2)=r(N,J)*1.0D3  !mm   this is the same as z(1,J)
                        T_1(J,3)=TEMP(1,J)-273.15D0  !degrees Celsius
                        T_1(J,4)=TEMP(N,J)-273.15D0
                        END DO
                        NEXT=NEXT+1
                        ELSEIF(t>=1.0D-3.and.NEXT==7)then
                        DO J=1,M
                        T_0(1,1)=t*1.0D3
                        T_0(J,2)=r(N,J)*1.0D3  !mm   this is the same as z(1,J)
            T_0(J,3)=TEMP(1,J)-273.15D0   !degrees Celsius
                        T_0(J,4)=TEMP(N,J)-273.15D0
                        END DO
                        NEXT=NEXT+1
                        ELSEIF(t>=1.0D-2.and.NEXT==8)then
                        DO J=1,M
                        T__1(1,1)=t*1.0D3
                        T__1(J,2)=r(N,J)*1.0D3  !mm   this is the same as z(1,J)
                        T__1(J,3)=TEMP(1,J)-273.15D0   !degrees Celsius
                        T__1(J,4)=TEMP(N,J)-273.15D0
                        END DO
                        NEXT=NEXT+1
                        ELSEIF(t>=1.0D-1.and.NEXT==9)then
                        DO J=1,M
                        T__2(1,1)=t*1.0D3
                        T__2(J,2)=r(N,J)*1.0D3  !mm   this is the same as z(1,J)
                        T__2(J,3)=TEMP(1,J)-273.15D0   !degrees Celsius
                        T__2(J,4)=TEMP(N,J)-273.15D0
                        END DO
                        NEXT=NEXT+1
                        ELSEIF(t>=2.960D-1.and.NEXT==10)then
                        DO J=1,M
                        T__e(1,1)=t*1.0D3
                        T__e(J,2)=r(N,J)*1.0D3  !mm   this is the same as z(1,J)
                        T__e(J,3)=TEMP(1,J)-273.15D0   !degrees Celsius
                        T__e(J,4)=TEMP(N,J)-273.15D0
                        END DO
                        NEXT=NEXT+1
                        endif


!_____
_____

!determine the next time step and repeat
dt=t_o*EXP(REAL(K-2)/beta)

GOTO 20
end if
```

```
!**************************************************************************
*******

do J=1,K,50
 WRITE (1,25) t_(J), R_(J), q1(J), q2(J), q3(J), dTdn_t(J), dTdn_b(J)
25 FORMAT(f11.7,1X,f15.10,1x,E12.5,1x,E12.5,1x,E12.5,1x,E12.5,1x,E12.5)
end do

do J=1,K,1
WRITE (13,29) tmp_(J), dRdt_(J), Mlhs_(J), Mtm1_(J), Mtm2_(J), Mtm3_(J), Elhs_(J), Etm1_(J), Etm2_(J)
29 FORMAT(f11.7,1X,f15.10,E12.5,1x,E12.5,1x,E12.5,1x,E12.5,1x,E12.5,1x,E12.5,1x,E12.5)
end do

                              write (2,*) T__o(1,1)
                              do J=1,M
                              write (2,30) T__o(J,2), T__o(J,3), T__o(J,4)
                              30 format (f15.10, 1X, F10.5, 1X, F10.5)
                              end do

                              write (3,*) T_6(1,1)
                              do J=1,M
                               write (3,35) T_6(J,2), T_6(J,3), T_6(J,4)
                              35 format (f15.10, 1X, F10.5, 1X, F10.5)
                              end do

                              write (4,*) T_5(1,1)
                              do J=1,M
                              write (4,40) T_5(J,2), T_5(J,3), T_5(J,4)
                              40 format (f15.10, 1X, F10.5, 1X, F10.5)
                              end do

                              write (5,*) T_4(1,1)
                              do J=1,M
                               write (5,45) T_4(J,2), T_4(J,3), T_4(J,4)
                               45 format (f15.10, 1X, F10.5, 1X, F10.5)
                              end do

                              write (6,*) T_3(1,1)
                              do J=1,M
                              write (6,50) T_3(J,2), T_3(J,3), T_3(J,4)
                              50 format (f15.10, 1X, F10.5, 1X, F10.5)
                              end do

                              write (7,*) T_2(1,1)
                              do J=1,M
                               write (7,55) T_2(J,2), T_2(J,3), T_2(J,4)
                               55 format (f15.10, 1X, F10.5, 1X, F10.5)
                              end do

                              write (8,*) T_1(1,1)
                              do J=1,M
                               write (8,60) T_1(J,2), T_1(J,3), T_1(J,4)
                               60 format (f15.10, 1X, F10.5, 1X, F10.5)
```

```
                 end do

                 write (9,*) T_0(1,1)
                 do J=1,M
                 write (9,65) T_0(J,2), T_0(J,3), T_0(J,4)
              65 format (f15.10, 1X, F10.5, 1X, F10.5)
                 end do

                 write (10,*) T__1(1,1)
                 do J=1,M
                 write (10,70) T__1(J,2), T__1(J,3), T__1(J,4)
              70 format (f15.10, 1X, F10.5, 1X, F10.5)
                 end do

                 write (11,*) T__2(1,1)
                 do J=1,M
                 write (11,75) T__2(J,2), T__2(J,3), T__2(J,4)
               75 format (f15.10, 1X, F10.5, 1X, F10.5)
                 end do

                 write (12,*) T__e(1,1)
                 do J=1,M
                 write (12,80) T__e(J,2), T__e(J,3), T__e(J,4)
              80 format (f15.10, 1X, F10.5, 1X, F10.5)
                 end do


!_____


!Generate Isotherms
II=1
FIND=50.0D0+273.15D0
XY50(1,3)=FIND-273.15
XY50(2,3)=z(1,1)*1000.0D0 !(mm)
XY50(3,3)=t*1000.0D0  !(ms)


do I=1,N
J=2
 800 CONTINUE
IF(TEMP(I,J)<FIND.AND.TEMP(I,J-1)>FIND) then

   Rad=Dj(J-1)+(FIND-TEMP(I,J-1))*(Dj(J)-Dj(J-1))/(TEMP(I,J)-TEMP(I,J-1))

   XY50(II,1)=RAD*SIN(GAM(I,J))*1000.0D0 !(mm)
   XY50(II,2)=RAD*COS(GAM(I,J))*1000.0D0 !(mm)
   II=II+1
else
  if (J<M) then
   J=J+1
   !PRINT *, I,J, TEMP(I,J), FIND
  else
   GOTO 801
```

```
        end if
     GOTO 800
     endif

801 CONTINUE
end do

  DO I=1,II
   WRITE(17,802) (XY50(I,J), J=1,3)
   802 format (3(1x,f10.5))
   END DO
!_____

_____

II=1
FIND=70.0D0+273.15D0
XY70(1,3)=FIND-273.15
XY70(2,3)=z(1,1)*1000.0D0 !(mm)
XY70(3,3)=t*1000.0D0  !(ms)


do I=1,N
J=2
 805 CONTINUE
IF(TEMP(I,J)>FIND.AND.TEMP(I,J-1)<FIND) then

   Rad=Dj(J-1)+(FIND-TEMP(I,J-1))*(Dj(J)-Dj(J-1))/(TEMP(I,J)-TEMP(I,J-1))

   XY70(II,1)=RAD*SIN(GAM(I,J))*1000.0D0 !(mm)
   XY70(II,2)=RAD*COS(GAM(I,J))*1000.0D0 !(mm)
   II=II+1
   else
    if (J<M) then
    J=J+1
    else
     GOTO 806
    end if
   GOTO 805
   endif

806 CONTINUE
end do

  DO I=1,II
   WRITE(18,807) (XY70(I,J), J=1,3)
   807 format (3(1x,f10.5))
   END DO
!_____

_____

II=1
FIND=70.0D0+273.15D0
XY70_(1,3)=FIND-273.15
```

```
XY70_(2,3)=z(1,1)*1000.0D0 !(mm)
XY70_(3,3)=t*1000.0D0  !(ms)


do I=1,N
J=M
 810 CONTINUE
IF(TEMP(I,J)>FIND.AND.TEMP(I,J+1)<FIND) then

  Rad=Dj(J-1)+(FIND-TEMP(I,J-1))*(Dj(J)-Dj(J-1))/(TEMP(I,J)-TEMP(I,J-1))

  XY70_(II,1)=RAD*SIN(GAM(I,J))*1000.0D0 !(mm)
  XY70_(II,2)=RAD*COS(GAM(I,J))*1000.0D0 !(mm)
 II=II+1
else
 if (J>1) then
  J=J-1
 else
  GOTO 811
 end if
GOTO 810
endif

811 CONTINUE
end do

 DO I=1,II
  WRITE(19,812) (XY70_(I,J), J=1,3)
  812 format (3(1x,f10.5))
  END DO

II=1
FIND=80.0D0+273.15D0
XY80(1,3)=FIND-273.15
XY80(2,3)=z(1,1)*1000.0D0 !(mm)
XY80(3,3)=t*1000.0D0  !(ms)


do I=1,N
J=2
 815 CONTINUE
IF(TEMP(I,J)>FIND.AND.TEMP(I,J-1)<FIND) then

  Rad=Dj(J-1)+(FIND-TEMP(I,J-1))*(Dj(J)-Dj(J-1))/(TEMP(I,J)-TEMP(I,J-1))

  XY80(II,1)=RAD*SIN(GAM(I,J))*1000.0D0 !(mm)
  XY80(II,2)=RAD*COS(GAM(I,J))*1000.0D0 !(mm)
 II=II+1
else
 if (J<M) then
  J=J+1
 else
  GOTO 816
```

```
      end if
    GOTO 815
    endif

816 CONTINUE
end do

  DO I=1,II
    WRITE(20,817) (XY80(I,J), J=1,3)
    817 format (3(1x,f10.5))
    END DO

II=1
FIND=80.0D0+273.15D0
XY80_(1,3)=FIND-273.15
XY80_(2,3)=z(1,1)*1000.0D0 !(mm)
XY80_(3,3)=t*1000.0D0  !(ms)


do I=1,N
J=M
 820 CONTINUE
IF(TEMP(I,J)>FIND.AND.TEMP(I,J+1)<FIND) then

  Rad=Dj(J-1)+(FIND-TEMP(I,J-1))*(Dj(J)-Dj(J-1))/(TEMP(I,J)-TEMP(I,J-1))

  XY80_(II,1)=RAD*SIN(GAM(I,J))*1000.0D0 !(mm)
  XY80_(II,2)=RAD*COS(GAM(I,J))*1000.0D0 !(mm)
  II=II+1
else
  if (J>1) then
   J=J-1
  else
   GOTO 821
  end if
 GOTO 820
endif

821 CONTINUE
end do

  DO I=1,II
    WRITE(21,822) (XY80_(I,J), J=1,3)
    822 format (3(1x,f10.5))
    END DO

II=1
FIND=60.0D0+273.15D0
XY60(1,3)=FIND-273.15
XY60(2,3)=z(1,1)*1000.0D0 !(mm)
XY60(3,3)=t*1000.0D0  !(ms)
```

```
do I=1,N
J=2
830 CONTINUE
IF(TEMP(I,J)>FIND.AND.TEMP(I,J-1)<FIND) then

   Rad=Dj(J-1)+(FIND-TEMP(I,J-1))*(Dj(J)-Dj(J-1))/(TEMP(I,J)-TEMP(I,J-1))

   XY60(II,1)=RAD*SIN(GAM(I,J))*1000.0D0 !(mm)
   XY60(II,2)=RAD*COS(GAM(I,J))*1000.0D0 !(mm)
   II=II+1
else
  if (J<M) then
  J=J+1
  else
   GOTO 831
  end if
GOTO 830
endif


831 CONTINUE
end do

  DO I=1,II
   WRITE(22,832) (XY60(I,J), J=1,3)
   832 format (3(1x,f10.5))
   END DO

II=1
FIND=60.0D0+273.15D0
XY60_(1,3)=FIND-273.15
XY60_(2,3)=z(1,1)*1000.0D0 !(mm)
XY60_(3,3)=t*1000.0D0  !(ms)


do I=1,N
J=M
835 CONTINUE
IF(TEMP(I,J)>FIND.AND.TEMP(I,J+1)<FIND) then

   Rad=Dj(J-1)+(FIND-TEMP(I,J-1))*(Dj(J)-Dj(J-1))/(TEMP(I,J)-TEMP(I,J-1))

   XY60_(II,1)=RAD*SIN(GAM(I,J))*1000.0D0 !(mm)
   XY60_(II,2)=RAD*COS(GAM(I,J))*1000.0D0 !(mm)
   II=II+1
else
  if (J>1) then
  J=J-1
  else
   GOTO 836
  end if
GOTO 835
endif
```

```
836 CONTINUE
end do

  DO I=1,II
   WRITE(23,837) (XY60_(I,J), J=1,3)
   837 format (3(1x,f10.5))
   END DO



II=1
FIND=55.0D0+273.15D0
XY55(1,3)=FIND-273.15
XY55(2,3)=z(1,1)*1000.0D0 !(mm)
XY55(3,3)=t*1000.0D0  !(ms)


do I=1,N
J=2
 840 CONTINUE
IF(TEMP(I,J)>FIND.AND.TEMP(I,J-1)<FIND) then

  Rad=Dj(J-1)+(FIND-TEMP(I,J-1))*(Dj(J)-Dj(J-1))/(TEMP(I,J)-TEMP(I,J-1))

  XY55(II,1)=RAD*SIN(GAM(I,J))*1000.0D0 !(mm)
  XY55(II,2)=RAD*COS(GAM(I,J))*1000.0D0 !(mm)
  II=II+1
 else
  if (J<M) then
   J=J+1
  else
   GOTO 841
  end if
GOTO 840
endif

841 CONTINUE
end do

  DO I=1,II
   WRITE(24,842) (XY55(I,J), J=1,3)
   842 format (3(1x,f10.5))
   END DO

II=1
FIND=55.0D0+273.15D0
XY55_(1,3)=FIND-273.15
XY55_(2,3)=z(1,1)*1000.0D0 !(mm)
XY55_(3,3)=t*1000.0D0  !(ms)


do I=1,N
J=M
```

```
845 CONTINUE
IF(TEMP(I,J)>FIND.AND.TEMP(I,J+1)<FIND) then

    Rad=Dj(J-1)+(FIND-TEMP(I,J-1))*(Dj(J)-Dj(J-1))/(TEMP(I,J)-TEMP(I,J-1))

    XY55_(II,1)=RAD*SIN(GAM(I,J))*1000.0D0 !(mm)
    XY55_(II,2)=RAD*COS(GAM(I,J))*1000.0D0 !(mm)
    II=II+1
else
  if (J>1) then
   J=J-1
  else
   GOTO 846
  end if
 GOTO 845
endif

846 CONTINUE
end do

 DO I=1,II
  WRITE(25,847) (XY55_(I,J), J=1,3)
  847 format (3(1x,f10.5))
  END DO




II=1
FIND=65.0D0+273.15D0
XY65(1,3)=FIND-273.15
XY65(2,3)=z(1,1)*1000.0D0 !(mm)
XY65(3,3)=t*1000.0D0  !(ms)


do I=1,N
J=2
 850 CONTINUE
IF(TEMP(I,J)>FIND.AND.TEMP(I,J-1)<FIND) then

    Rad=Dj(J-1)+(FIND-TEMP(I,J-1))*(Dj(J)-Dj(J-1))/(TEMP(I,J)-TEMP(I,J-1))

    XY65(II,1)=RAD*SIN(GAM(I,J))*1000.0D0 !(mm)
    XY65(II,2)=RAD*COS(GAM(I,J))*1000.0D0 !(mm)
    II=II+1
else
  if (J<M) then
   J=J+1
  else
   GOTO 851
  end if
 GOTO 850
```

```
endif

851 CONTINUE
end do

  DO I=1,II
  WRITE(26,852) (XY65(I,J), J=1,3)
  852 format (3(1x,f10.5))
  END DO

II=1
FIND=65.0D0+273.15D0
XY65_(1,3)=FIND-273.15
XY65_(2,3)=z(1,1)*1000.0D0 !(mm)
XY65_(3,3)=t*1000.0D0  !(ms)


do I=1,N
J=M
 855 CONTINUE
IF(TEMP(I,J)>FIND.AND.TEMP(I,J+1)<FIND) then

  Rad=Dj(J-1)+(FIND-TEMP(I,J-1))*(Dj(J)-Dj(J-1))/(TEMP(I,J)-TEMP(I,J-1))

  XY65_(II,1)=RAD*SIN(GAM(I,J))*1000.0D0 !(mm)
  XY65_(II,2)=RAD*COS(GAM(I,J))*1000.0D0 !(mm)
  II=II+1
  else
   if (J>1) then
    J=J-1
    else
     GOTO 856
    end if
  GOTO 855
  endif

856 CONTINUE
end do

  DO I=1,II
  WRITE(27,857) (XY65_(I,J), J=1,3)
  857 format (3(1x,f10.5))
  END DO


II=1
FIND=75.0D0+273.15D0
XY75(1,3)=FIND-273.15
XY75(2,3)=z(1,1)*1000.0D0 !(mm)
XY75(3,3)=t*1000.0D0  !(ms)


do I=1,N
```

```
J=2
860 CONTINUE
IF(TEMP(I,J)>FIND.AND.TEMP(I,J-1)<FIND) then

   Rad=Dj(J-1)+(FIND-TEMP(I,J-1))*(Dj(J)-Dj(J-1))/(TEMP(I,J)-TEMP(I,J-1))

   XY75(II,1)=RAD*SIN(GAM(I,J))*1000.0D0 !(mm)
   XY75(II,2)=RAD*COS(GAM(I,J))*1000.0D0 !(mm)
   II=II+1
else
  if (J<M) then
   J=J+1
  else
   GOTO 861
  end if
GOTO 860
endif

861 CONTINUE
end do

  DO I=1,II
   WRITE(28,862) (XY75(I,J), J=1,3)
   862 format (3(1x,f10.5))
   END DO

II=1
FIND=75.0D0+273.15D0
XY75_(1,3)=FIND-273.15
XY75_(2,3)=z(1,1)*1000.0D0 !(mm)
XY75_(3,3)=t*1000.0D0  !(ms)


do I=1,N
J=M
865 CONTINUE
IF(TEMP(I,J)>FIND.AND.TEMP(I,J+1)<FIND) then

   Rad=Dj(J-1)+(FIND-TEMP(I,J-1))*(Dj(J)-Dj(J-1))/(TEMP(I,J)-TEMP(I,J-1))

   XY75_(II,1)=RAD*SIN(GAM(I,J))*1000.0D0 !(mm)
   XY75_(II,2)=RAD*COS(GAM(I,J))*1000.0D0 !(mm)
   II=II+1
else
  if (J>1) then
   J=J-1
  else
   GOTO 866
  end if
GOTO 865
endif

866 CONTINUE
```

```
end do

 DO I=1,II
  WRITE(29,877) (XY75_(I,J), J=1,3)
  877 format (3(1x,f10.5))
  END DO
!_____


_____


 do I=1,N
  WRITE(14,1000) ((r(I,J)*1000.0D0), J=1,300)
  1000 FORMAT(1000(1x,f20.13))

  WRITE(15,1001) ((z(I,J)*1000.0D0), J=1,300)
  1001 FORMAT(1000(1x,f20.13))

  WRITE(16,1002) ((TEMP(I,J)-273.15), J=1,300)
  1002 FORMAT(1000(1x,f20.13))
  end do

 stop
 end program
!_____


_____


!In this subroutine, the interfacial energy balance equation is rearranged to solve for the rate of change of
!vapour temperature A1=dTdt.
!x=t
!y1=Tv
!y2=Rt
!y3=dRdt
 SUBROUTINE FF1(x, y1, y2, y3, M, N, del_t, Tff,Told, rold, zold, T, A1)
 INTEGER :: M, N
 DOUBLE PRECISION, DIMENSION (N,M) :: Told, T, rold, zold, GAM
 DOUBLE PRECISION , DIMENSION(N) :: qi, Ai, dT_norm, Tff
 DOUBLE PRECISION :: area, sum_q
 DOUBLE PRECISION :: x, f1, f2, f3, hfg, dv
 DOUBLE PRECISION :: A1, y1, y2, y3, g_T
 DOUBLE PRECISION :: del_t
 DOUBLE PRECISION :: LATENT, v_dens, dvdT
 DOUBLE PRECISION :: Cpl, kl, al, dl, sigma, Tinf, Pinf, Tsat, pi, Sr, Rinf, del_e, del_n, q
 COMMON/bub_param/Cpl, kl, al, dl, sigma, Tinf, Pinf, Tsat, pi, Sr, Rinf, del_e, del_n, q

 hfg=(1.0D3)*LATENT(y1)

 call new_Temp(M,N, Y2, Y1, Y3, del_t, Told, rold, zold, Tff,T, dT_norm, GAM)

! Now integrate the interface boundary around the bubble using Trapazoid Rule!  The area segment Ai is the
!surface area of a hemisphere segment derived from rotating a segment of a circle around the z-axis. This is
then !multiplied by the average temperature gradient (and kl) to get the average heat transfer rate into the area
segment.

 sum_q=0.0D0
```

```
area=0.0
do I=2,N
 Ai(I)=2.0D0*pi*(y2**2)*(COS(GAM(I-1,1))-COS(GAM(I,1)))
 qi(I)=(0.5D0*kl*Ai(I)*(dT_norm(I-1)+dT_norm(I)))

 area=area+Ai(I)    !total surface area
 sum_q=sum_q+qi(I)   !total heat transfer
end do

!These are the vapour density and the derivative of density with temperature so that ddv/dt=(ddv/dTv)*(dTv/dt)
dv=v_dens(y1)
g_T=dvdT(y1)

!This is the rearrangement of the interface energy balance to isolate A1=dTdt
f3=sum_q/area
f2=hfg*dv
f1=(hfg/3.0)*g_T
A1=(1.0/(y2*f1))*(f3-f2*y3)
RETURN
END SUBROUTINE
!_____


subroutine new_Temp(M,N,Rt,Tv,dRdt,del_t,Told,rold,zold,Tff,T,dT_norm, GAM)
implicit none

INTEGER :: I, J
INTEGER :: N, M

DOUBLE PRECISION, DIMENSION(N,M) :: GAM, r, rold, z, zold, rn, zn, rnn, znn, re, ze, ree, zee, ren, &
                  zen, Ja, a, b, c, d, e, AA, BB, DD, EE, FF, HH
DOUBLE PRECISION , DIMENSION(N,M) :: Ur, Uz
DOUBLE PRECISION , DIMENSION(N,M) :: T, Tn, Told
DOUBLE PRECISION , DIMENSION(N) :: dTde, dTdn, dTdr, dTdz, dT_norm, Tff
DOUBLE PRECISION , DIMENSION(M) :: Dj
DOUBLE PRECISION :: Rt, dRdt
DOUBLE PRECISION :: max_dif
DOUBLE PRECISION :: Tv, del_t
DOUBLE PRECISION :: Cpl, kl, al, dl, sigma, Tinf, Pinf, Tsat, pi, Sr, Rinf, del_e, del_n, q
COMMON/bub_param/Cpl, kl, al, dl, sigma, Tinf, Pinf, Tsat, pi, Sr, Rinf, del_e, del_n, q

call randz(Rt,N,M,r,z,GAM,Dj)
call metrics(N,M,r,z,rn,zn,rnn,znn,re,ze,ree,zee,ren,zen)
call trans_coef(N,M,re,ze,ree,zee,rn,zn,rnn,znn,ren,zen,Ja,a,b,c,d,e)

!Determine the velocity field in the liquid
do I=1,N
 do J=1,M
  Ur(I,J)=dRdt*((Rt/sqrt(r(I,J)**2+z(I,J)**2))**2)*SIN(GAM(I,J))
  Uz(I,J)=dRdt*((Rt/sqrt(r(I,J)**2+z(I,J)**2))**2)*COS(GAM(I,J))
 end do
end do
```

```
IF(del_t>0.0D0)then
!Here, the liquid temperature field is determined. Given the previous temperature field Told together with the
!new time step and the updated boundary conditions, the next approximation of the temperature field is
determined
!by lines, with J being a line and the sweep being done in the I direction. This temperature field is compared
!with the previous iteration and continues until the convergence criterion is achieved.
!
call Temp_coef(N,M,r,z,rn,re,zn,ze,rold,zold,a,b,c,d,e,Ja,del_t,Ur,Uz,Tv,AA,BB,DD,EE,FF,HH)
 1000 call Temp_matrix(N,M,del_t,AA,BB,DD,EE,FF,HH,Ja,rn,Tff,Tv,Told,Tn,T)
call maxdif(N,M,Tn,T,max_dif)

!Check for convergence of the nth iteration
 IF(max_dif>1.0D-9)then
   do I=1,N
   do J=1,M
     Tn(I,J)=T(I,J)
   end do
   end do

  GOTO 1000
  ENDIF

ELSE
 do I=1,N
 do J=1,M
 T(I,J)=Told(I,J)
 end do
end do

ENDIF

! Find the temperature gradient at the interface
do I=1,N
 dTde(I)=0.0D0  !because T(I,1)=Tv, then there is no gradient in e along the interface
 dTdn(I)=(2.0D0*T(I,4)-9.0D0*T(I,3)+18.0D0*T(I,2)-11.0D0*T(I,1))/(6.0D0*del_n)

 dTdr(I)=Ja(I,1)*(zn(I,1)*dTde(I)-ze(I,1)*dTdn(I))
 dTdz(I)=Ja(I,1)*(re(I,1)*dTdn(I)-rn(I,1)*dTde(I))

 dT_norm(I)=dTdr(I)*SIN(GAM(I,1))+dTdz(I)*COS(GAM(I,1))

end do

return
end subroutine
!_____


_____


!In this subroutine, the modified Rayleigh equation is rearranged to solve for the interfacial
!acceleration A3=dy3/dt=d2R/dt2.
!x=t
!y1=Tv
!y2=Rt
```

```fortran
!y3=dRdt
SUBROUTINE FF3(t, y1, y2, y3, A3)
DOUBLE PRECISION :: t, g_R, f4, P, y1, y2, y3, A3, PRESS2
DOUBLE PRECISION :: Cpl, kl, al, dl, sigma, Tinf, Pinf, Tsat, pi, Sr, Rinf, del_e, del_n, q
COMMON/bub_param/Cpl, kl, al, dl, sigma, Tinf, Pinf, Tsat, pi, Sr, Rinf, del_e, del_n, q


P=PRESS2(Y1)

g_R=2.0D0*sigma/(dl*y2**2)

f4=(1.0D3)*(P-Pinf)/(dl*y2)

A3=f4-g_R-(3.0D0/2.0D0)*(y3**2)/y2


RETURN
END SUBROUTINE
```

!_____

```fortran
! This subroutine solves for the grid point locations in the physical domain. Among other
! parameters which are held constant ie. Rinf, Sr, M, & N it requires both the instantaneous
! bubble radius Rt and the height zh.

subroutine randz(Rt,N,M,r,z,GAM,Dj)
IMPLICIT NONE

INTEGER :: N, M, I, J
DOUBLE PRECISION, DIMENSION(N, M) :: r, z, GAM
DOUBLE PRECISION, DIMENSION(M) :: Dj
DOUBLE PRECISION :: Rt, zh
DOUBLE PRECISION :: Cpl, kl, al, dl, sigma, Tinf, Pinf, Tsat, pi, Sr, Rinf, del_e, del_n, q
COMMON/bub_param/Cpl, kl, al, dl, sigma, Tinf, Pinf, Tsat, pi, Sr, Rinf, del_e, del_n, q

zh=0.0

do J=1,M

! Set the radial grid lines in the physical domain
Dj(J)=Rt+(Rinf-Rt)*(1.0D0-Sr*ATAN((1.0D0-(REAL (J-1)/(M-1)))*TAN(1.0D0/Sr)))


!set anglular grid spacing in the physical domain for each radial grid line
do I=1,N
  GAM(I,J)=(0.5D0*pi+ASIN(zh/Dj(J)))*(REAL(I-1)/(N-1))    !set angle gamma for I=1,N and J=1,M

!define (r,z) grid coordinates for the physical domain
r(I,J)=Dj(J)*SIN(GAM(I,J))
z(I,J)=Dj(J)*COS(GAM(I,J))+zh

end do
end do
return
end subroutine
```

```fortran
!
_____
_____

!This subroutine calculates the first and second order derivatives of the metrics using a second order
!finite difference representation of the derivatives
subroutine metrics(N,M,r,z,rn,zn,rnn,znn,re,ze,ree,zee,ren,zen)
implicit none

INTEGER :: I, J, N, M
DOUBLE PRECISION, DIMENSION(N,M) :: r, z, rn, zn, rnn, znn, re, ze, ree, zee, ren, zen
DOUBLE PRECISION :: Cpl, kl, al, dl, sigma, Tinf, Pinf, Tsat, pi, Sr, Rinf, del_e, del_n, q
COMMON/bub_param/Cpl, kl, al, dl, sigma, Tinf, Pinf, Tsat, pi, Sr, Rinf, del_e, del_n, q


!Calculate Metrics together with 1st, 2nd derivatives
do I=1,N
do J=1,M
IF(J==1)then   !forward difference
   rn(I,1)=(-3.0*r(I,1)+4.0*r(I,2)-r(I,3))/(2.0*del_n)
   zn(I,1)=(-3.0*z(I,1)+4.0*z(I,2)-z(I,3))/(2.0*del_n)
   rnn(I,1)=(2.0*r(I,1)-5.0*r(I,2)+4.0*r(I,3)-r(I,4))/(del_n**2)
   znn(I,1)=(2.0*z(I,1)-5.0*z(I,2)+4.0*z(I,3)-z(I,4))/(del_n**2)
ELSEIF(J==M)then !backward difference
   rn(I,M)=(3.0*r(I,M)-4.0*r(I,M-1)+r(I,M-2))/(2.0*del_n)
   zn(I,M)=(3.0*z(I,M)-4.0*z(I,M-1)+z(I,M-2))/(2.0*del_n)
   rnn(I,M)=(2.0*r(I,M)-5.0*r(I,M-1)+4.0*r(I,M-2)-r(I,M-3))/(del_n**2)
   znn(I,M)=(2.0*z(I,M)-5.0*z(I,M-1)+4.0*z(I,M-2)-z(I,M-3))/(del_n**2)
ELSE
   rn(I,J)=(r(I,J+1)-r(I,J-1))/(2D0*del_n)
   zn(I,J)=(z(I,J+1)-z(I,J-1))/(2D0*del_n)
   rnn(I,J)=(r(I,J+1)-2.0D0*r(I,J)+r(I,J-1))/(del_n**2)
   znn(I,J)=(z(I,J+1)-2.0D0*z(I,J)+z(I,J-1))/(del_n**2)
ENDIF


IF(I==1)then !forward difference
   re(1,J)=(-3.0*r(1,J)+4.0*r(2,J)-r(3,J))/(2.0*del_e)
   ze(1,J)=(-3.0*z(1,J)+4.0*z(2,J)-z(3,J))/(2.0*del_e)
   ree(1,J)=(2.0*r(1,J)-5.0*r(2,J)+4.0*r(3,J)-r(4,J))/(del_e**2)
   zee(1,J)=(2.0*z(1,J)-5.0*z(2,J)+4.0*z(3,J)-z(4,J))/(del_e**2)

ELSEIF(I==N)then !backward difference
   re(N,J)=(3.0*r(N,J)-4.0*r(N-1,J)+r(N-2,J))/(2.0*del_e)
   ze(N,J)=(3.0*z(N,J)-4.0*z(N-1,J)+z(N-2,J))/(2.0*del_e)
   ree(N,J)=(2.0*r(N,J)-5.0*r(N-1,J)+4.0*r(N-2,J)-r(N-3,J))/(del_e**2)
   zee(N,J)=(2.0*z(N,J)-5.0*z(N-1,J)+4.0*z(N-2,J)-z(N-3,J))/(del_e**2)

ELSE
   re(I,J)=(r(I+1,J)-r(I-1,J))/(2.0D0*del_e)
   ze(I,J)=(z(I+1,J)-z(I-1,J))/(2.0D0*del_e)
   ree(I,J)=(r(I+1,J)-2.0D0*r(I,J)+r(I-1,J))/(del_e**2)
   zee(I,J)=(z(I+1,J)-2.0D0*z(I,J)+z(I-1,J))/(del_e**2)
ENDIF
```

```fortran
end do
end do

!Cross derivatives
do I=1,N
do J=1,M
IF(J==1)then    !forward difference
   ren(I,1)=(-3.0*re(I,1)+4.0*re(I,2)-re(I,3))/(2.0*del_n)
   zen(I,1)=(-3.0*ze(I,1)+4.0*ze(I,2)-ze(I,3))/(2.0*del_n)

ELSEIF(J==M)then !backward difference
   ren(I,M)=(3.0*re(I,M)-4.0*re(I,M-1)+re(I,M-2))/(2.0*del_n)
   zen(I,M)=(3.0*ze(I,M)-4.0*ze(I,M-1)+ze(I,M-2))/(2.0*del_n)
ELSE
   ren(I,J)=(re(I,J+1)-re(I,J-1))/(2.0*del_n)
   zen(I,J)=(ze(I,J+1)-ze(I,J-1))/(2.0*del_n)
ENDIF

end do
end do

return
end subroutine metrics
!_____
```

_____

```fortran
!This subroutine calculates the coefficients for the transformed equation in the computational domain
subroutine trans_coef(N,M,re,ze,ree,zee,rn,zn,rnn,znn,ren,zen,Ja,a,b,c,d,e)
implicit none

INTEGER :: N, M, I, J
DOUBLE PRECISION, DIMENSION(N,M) :: rn, zn, rnn, znn, re, ze, ree, zee, ren, zen, Ja, a, b, c, d, e, beta_1, beta_2

!Calculate Transformation Coefficients
!The Jacobian (inverse)
do I=1,N
 do J=1,M
 Ja(I,J)=1.0D0/(zn(I,J)*re(I,J)-ze(I,J)*rn(I,J))
 end do
end do

! a, b, c, d, e
do I=1,N
do J=1,M
  IF(I==1)then
     a(I,J)=rn(I,J)**2+2.0D0*zn(I,J)**2
     b(I,J)=re(I,J)*rn(I,J)+2.0D0*ze(I,J)*zn(I,J)
     c(I,J)=re(I,J)**2+2.0D0*ze(I,J)**2

  else
     a(I,J)=rn(I,J)**2+zn(I,J)**2
     b(I,J)=re(I,J)*rn(I,J)+ze(I,J)*zn(I,J)
```

```
      c(I,J)=re(I,J)**2+ze(I,J)**2

   endif

beta_1(I,J)=zee(I,J)*a(I,J)-2.0D0*zen(I,J)*b(I,J)+znn(I,J)*c(I,J)
beta_2(I,J)=ree(I,J)*a(I,J)-2.0D0*ren(I,J)*b(I,J)+rnn(I,J)*c(I,J)

d(I,J)=Ja(I,J)*(rn(I,J)*beta_1(I,J)-zn(I,J)*beta_2(I,J))
e(I,J)=Ja(I,J)*(ze(I,J)*beta_2(I,J)-re(I,J)*beta_1(I,J))

end do
end do

return
end subroutine trans_coef


!_____


!Determine coefficients which put the energy equation in the form
!
![AAT(I+1,J+1)+BBT(I+1,J)-AAT(I+1,J-1)] + [DDT(I,J+1)+EET(I,J)+FFT(I-1,J-1)]
!                     + [AAT(I-1,J+1)+HHT(I-1,J)+-AAT(I-1,J-1)] = Told(I,J)

subroutine Temp_coef(N,M,r,z,rn,re,zn,ze,rold,zold,a,b,c,d,e,Ja,del_t,Ur,Uz,Tv,AA,BB,DD,EE,FF,HH)
implicit none

INTEGER :: N, M, I, J
DOUBLE PRECISION, DIMENSION(N,M) :: r, rold, z, zold, rn, re, zn, ze, a, b, c, d, e, Ja, &
                     Ur, Uz, AA, BB, DD, EE, FF, HH
DOUBLE PRECISION, DIMENSION(N,M) :: Uc, Vc, c1, c2, c3, c4, c5
DOUBLE PRECISION::Tv, del_t
DOUBLE PRECISION :: Cpl, kl, al, dl, sigma, Tinf, Pinf, Tsat, pi, Sr, Rinf, del_e, del_n, q
COMMON/bub_param/Cpl, kl, al, dl, sigma, Tinf, Pinf, Tsat, pi, Sr, Rinf, del_e, del_n, q


!Calculate the discritized equation coefficients
do I=1,N
do J=1,M
Uc(I,J)=((Ur(I,J)-(r(I,J)-rold(I,J))/del_t)*zn(I,J)-(Uz(I,J)-(z(I,J)-zold(I,J))/del_t)*rn(I,J))
Vc(I,J)=((Uz(I,J)-(z(I,J)-zold(I,J))/del_t)*re(I,J)-(Ur(I,J)-(r(I,J)-rold(I,J))/del_t)*ze(I,J))

  IF(I==1)then
   c1(I,J)=(Ja(I,J)*Uc(I,J)-al*(Ja(I,J)**2)*d(I,J))
   c2(I,J)=(Ja(I,J)*Vc(I,J)-al*(Ja(I,J)**2)*e(I,J))
  else
   c1(I,J)=(Ja(I,J)*Uc(I,J)-al*(Ja(I,J)**2)*d(I,J)-al*Ja(I,J)*zn(I,J)/r(I,J))
   c2(I,J)=(Ja(I,J)*Vc(I,J)-al*(Ja(I,J)**2)*e(I,J)+al*Ja(I,J)*ze(I,J)/r(I,J))
  endif

c3(I,J)=-(al*(Ja(I,J)**2)*a(I,J))
c4(I,J)=(2.0D0*al*(Ja(I,J)**2)*b(I,J))
c5(I,J)=-(al*(Ja(I,J)**2)*c(I,J))
```

```
end do
end do

do I=1,N
do J=1,M
  AA(I,J)=del_t*c4(I,J)/(4.0D0*del_n*del_e)
  BB(I,J)=del_t*c1(I,J)/(2.0D0*del_e)+del_t*c3(I,J)/(del_e**2)
  DD(I,J)=del_t*c2(I,J)/(2.0D0*del_n)+del_t*c5(I,J)/(del_n**2)
  EE(I,J)=1.0D0-(2.0D0*del_t*c3(I,J)/(del_e**2)+2.0D0*del_t*c5(I,J)/(del_n**2))
  FF(I,J)=-del_t*c2(I,J)/(2.0D0*del_n)+del_t*c5(I,J)/(del_n**2)
  HH(I,J)=-del_t*c1(I,J)/(2.0D0*del_e)+del_t*c3(I,J)/(del_e**2)
end do
end do


return
end subroutine


!_____


_____


!This subroutine sets up the tri-diagonal matrix of the form:
!
!     [a1 b1  0......................] [T1]    [d1]
!     [c2 a2 b2  0....................] [T2]    [d2]
!     [ 0 c3 a3 b3  0.................] [T3]    [d3]
!     [ . . . . .         . . .] [. ]  = [d4]
!     [ . . . . .         . . .] [. ]    [d5]
!     [ . . . . .         . . .] [. ]    [d6]
!     [ 0  0  0  0  0.........cK aK bK] [TK]    [d7]
!
!
!In the form of Patankar:
!
!     a(1)T(1)=b(1)T(2)+d(2)
!     a(2)T(2)=b(2)T(3)+c(2)T(1)+d(2)
!     .....
!     a(J)T(J)=b(J)T(J+1)+c(J)T(J-1)+d(J)
!     .....
!     a(K)T(K)=b(K)T(K+1)+c(M)T(K-1)+d(K)
!
!***********************************************************


subroutine Temp_matrix(N,M,del_t,AA,BB,DD,EE,FF,HH,Ja,rn,Tff,Tv,Told,Tn,T)
implicit none

INTEGER :: N, M, I, J
DOUBLE PRECISION , DIMENSION(N,M) :: AA, BB, DD, EE, FF, HH, Ja, rn
DOUBLE PRECISION , DIMENSION(N,M) :: T, Told, Tn
DOUBLE PRECISION , DIMENSION(M) :: a, b, c, d, U
DOUBLE PRECISION , DIMENSION(N) :: Tff
DOUBLE PRECISION :: Tv, del_t, Co
```

```
DOUBLE PRECISION :: Cpl, kl, al, dl, sigma, Tinf, Pinf, Tsat, pi, Sr, Rinf, del_e, del_n, q
COMMON/bub_param/Cpl, kl, al, dl, sigma, Tinf, Pinf, Tsat, pi, Sr, Rinf, del_e, del_n, q

!Main Loop. I represents 'lines' ie. a new "line" of potentials will be obtained for each I. These will
!be stored in the Ith row of T(I,J) and the next line is Tn
!
!x=using updated temperature from the current sweep
!u=the line at which temperature values are being solved for
!o=using the temperature values fro the previous sweep
!                              .   .   .
!                              .   .   .
!                              .   .   .
!                              .   .   .
!                              x   u   o  j+1
!
!                              x   u   o  j
!
!                              x   u   o  j-1
!                              .   .   .
!                              .   .   .
!                              .   .   .
!
!                              n+1 n+1 n   ---iteration number
!                              i-1 i   i+1

Co=-q/kl !This constant is the temperature gradient at the wall

do I=1,N

! set the values for the coefficient matrix
do J=2,M-1

  IF(I==1)then     !Symetry
    IF(J==2)then
      a(J)=EE(I,J)
      b(J)=-DD(I,J)
      d(J)=Told(I,J)-FF(I,J)*Tv-(BB(I,J)+HH(I,J))*Tn(I+1,J)
    ELSEIF(J==M-1)then
      a(J)=EE(I,J)
      c(J)=-FF(I,J)
      d(J)=Told(I,J)-DD(I,J)*Tff(I)-(BB(I,J)+HH(I,J))*Tn(I+1,J)
    ELSE
      a(J)=EE(I,J)
      c(J)=-FF(I,J)
      b(J)=-DD(I,J)
      d(J)=Told(I,J)-(BB(I,J)+HH(I,J))*Tn(I+1,J)

    ENDIF


  ELSEIF(I==N)then   ! Solid Surface
    IF(J==2)then
      a(J)=EE(I,J)
```

```
    b(J)=-DD(I,J)
    d(J)=Told(I,J)-FF(I,J)*Tv-(BB(I,J)+HH(I,J))*T(I-1,J)+(BB(I,J)*2.0D0*del_e*Co/(Ja(I,J)*rn(I,J)))
  ELSEIF(J==M-1)then
    a(J)=EE(I,J)
    c(J)=-FF(I,J)
    d(J)=Told(I,J)-DD(I,J)*Tff(I)-(BB(I,J)+HH(I,J))*T(I-1,J)+(BB(I,J)*2.0D0*del_e*Co/(Ja(I,J)*rn(I,J)))
  ELSE
    a(J)=EE(I,J)
    c(J)=-FF(I,J)
    b(J)=-DD(I,J)
    d(J)=Told(I,J)-(BB(I,J)+HH(I,J))*T(I-1,J)+(BB(I,J)*2.0D0*del_e*Co/(Ja(I,J)*rn(I,J)))
  ENDIF


ELSE             !Interior
  IF(J==2)then
    a(J)=EE(I,J)
    b(J)=-DD(I,J)
    d(J)=Told(I,J)-FF(I,J)*Tv-(AA(I,J)*Tn(I+1,J+1)+BB(I,J)*Tn(I+1,J))&
       -(-AA(I,J)*T(I-1,J+1)+HH(I,J)*T(I-1,J))

  ELSEIF(J==M-1)then
    a(J)=EE(I,J)
    c(J)=-FF(I,J)
    d(J)=Told(I,J)-DD(I,J)*Tff(I) &
       -(BB(I,J)*Tn(I+1,J)-AA(I,J)*Tn(I+1,J-1)) &
       -(HH(I,J)*T(I-1,J)+AA(I,J)*T(I-1,J-1))

  ELSE
    a(J)=EE(I,J)
    c(J)=-FF(I,J)
    b(J)=-DD(I,J)
    d(J)=Told(I,J)-(AA(I,J)*Tn(I+1,J+1)+BB(I,J)*Tn(I+1,J)-AA(I,J)*Tn(I+1,J-1))&
       -(-AA(I,J)*T(I-1,J+1)+HH(I,J)*T(I-1,J)+AA(I,J)*T(I-1,J-1))

  ENDIF

ENDIF

end do

DO J=1,M-2
a(J)=a(J+1)
b(J)=b(J+1)
c(J)=c(J+1)
d(J)=d(J+1)

END DO

call TDMA(M-2, N, I, a, b, c, d, U)

  do J=1,M
    IF(J==1)then
```

```
      T(I,J)=Tv
    ELSEIF(J==M)then
      T(I,J)=Tff(I)
    else
      T(I,J)=U(J-1)
    endif
  end do

end do

RETURN
end subroutine
!_____

_____

!This subroutine is Thomas Algorithm or TDMA which inverts a tri-diagonal matrix
subroutine TDMA(M, N, I, a, b, c, d, U)
implicit none

INTEGER :: M, N, I, J
DOUBLE PRECISION , DIMENSION(M) :: a, b, c, d, P, Q, U
DOUBLE PRECISION :: BET

if (a(1)==0.0) pause
 BET=a(1)
 Q(1)=d(1)/BET
 P(1)=b(1)/BET

do J=2,M
  BET=a(J)-c(J)*P(J-1)

 if (BET==0.0) pause
  P(J)=b(J)/BET
  Q(J)=(d(J)+c(J)*Q(J-1))/BET
end do

U(M)=Q(M)

 do J=M-1,1,-1
  U(J)=P(J)*U(J+1)+Q(J)
 end do

return
end subroutine
!_____

_____

!This subroutine determines the maximum of the absolute difference between two 2-D arrays
MAX(abs[X(I,J)-Y(I,J)])
subroutine maxdif(N, M, X, Y, max_dif)
implicit none

INTEGER :: N, M, I, J
```

```fortran
DOUBLE PRECISION , DIMENSION(N,M) :: X, Y, DIFF
DOUBLE PRECISION:: max_dif

do I=1,N
 do J=1,M
 DIFF(I,J)=100.0D0*ABS(Y(I,J)-X(I,J))/ABS(0.5D0*(X(I,J)+Y(I,J)))
 end do
end do

max_dif=MAXVAL(DIFF)


return
end subroutine
!_____
```

```fortran
!This subroutine solves for the complementary error function from its' power series representation. Given the
!argument x the subroutine returns erfc(x).
subroutine errorfnctn(x, pi, erfc_x)
INTEGER, PARAMETER :: INF=100
INTEGER :: I
DOUBLE PRECISION, DIMENSION(INF) :: DUM
DOUBLE PRECISION :: x, erf_x, erfc_x, pi, fact, ifact
erf_x=0.0D0
erfc_x=0.0D0
do I=1,inf
  fact=ifact(I-1)
  DUM(I)=REAL((-1)**(I-1))*(x**REAL(2*I-1))/(fact*REAL(2*I-1))
end do

erf_x=(2.0D0/SQRT(pi))*SUM(DUM)
 IF(x>4.0D0.or.erf_x>1.0D0)then
  erf_x=1.0D0
 endif

erfc_x=(1.0D0)-(erf_x)

return
end subroutine

!_____
```

```fortran
!This function determines the factorial of the integer KK
FUNCTION ifact(KK)
integer :: K, KK
DOUBLE PRECISION :: ifact
ifact=1.0D0
IF(KK==0)then
  ifact=1.0D0
else
 do K=1,KK
  ifact=ifact*REAL(K)
 end do
endif
```

```
return
end
```

!_____

!This function sets the grid spacing by dividing a unit length into X-1 segments

```
FUNCTION DELTA(X)
INTEGER :: X
DOUBLE PRECISION :: DELTA
DELTA=1.0D0/(REAL(X-1))
return
END
```

!*****************************PROPERTY DATA FOR R113***************************

```
FUNCTION PRESS2(T)
DOUBLE PRECISION :: T, PRESS2, a, b, c, d, e,f
a=2957.142318D0
b=-53.1787872D0
c=0.371694819D0
d=-0.001235475106D0
e=1.860059877D-06
f=-8.710006423D-10
PRESS2=a+b*T+c*T**2+d*T**3+e*T**4+f*T**5
return
END
```

```
FUNCTION LATENT(T)
DOUBLE PRECISION :: a, b, c, d, e, f, T, LATENT
a=2737.48849146611D0
b=-39.3003642747073D0
c=0.239810862940233D0
d=-0.000727033297258D0
e=1.089453393D-06
f=-6.47894D-10
LATENT=a+b*T+c*T**2+d*T**3+e*T**4+f*T**5  !kJ/kg,  T in K
return
END
```

```
FUNCTION TENSION(T)
DOUBLE PRECISION :: T, TENSION, a, b, c, d, e
a=100.66367D0
b=-0.26354029D0
c=0.00017492986D0
d=-8150.6195D0
e=535170.24D0
TENSION=a+b*T+c*T**2+d/T+e/T**2 !mN/m
return
end
```

```fortran
FUNCTION l_sp_heat(T)
DOUBLE PRECISION :: T, l_sp_heat, a, b, c, d
a=-2687.2937711853D0
b=32.1760788219D0
c=-0.0967652227D0
d=0.0001001237D0
 l_sp_heat=(a+(b*T)+(c*T**2)+(d*T**3))/1000.0D0    !kJ/kgK
END


FUNCTION v_sp_heat(T)
DOUBLE PRECISION :: T, v_sp_heat, a, b, c, d
a=0.0
b=0.0
c=0.0
d=0.0
 v_sp_heat=a+(b*T)+(c*T**2)+(d*T**3)    !kJ/kgK
END


FUNCTION T_sat(P)
DOUBLE PRECISION :: P, T_sat, a, b, c, d, e
a=227.62444D0
b=13.885934D0
c=0.69937307D0
d=0.15567729D0
e=-0.01232013D0
f=0.002049886D0
 T_sat=a+b*LOG(P)+c*LOG(P)**2+d*LOG(P)**3+e*LOG(P)**4+f*LOG(P)**5
 END


function therm_cond(T)
DOUBLE PRECISION :: therm_cond, T, a, b, c, d, e, f
a=572.672566562039D0
b=-7.22070352101712D0
c=0.044478466185909D0
d=-0.000139306769359D0
e=2.15863959D-07
f=-1.32549D-10
therm_cond=(a+b*T+c*T**2+d*T**3+e*T**4+f*T**5)*1.0D-3 !W/mK
return
end


function l_dens(Tin)
DOUBLE PRECISION :: l_dens, T, Tin, a, b, c, d, e, f
T=Tin-273.15D0
a=16.1767736505804D0
b=-0.021409787008367D0
c=3.666728067D-06
d=-1.210948367D-06
e=1.1848044D-08
f=-3.7748D-11
l_dens=(a+b*T+c*T**2+d*T**3+e*T**4+f*T**5)*100.0D0    !kg/m3
return
end
```

```fortran
function v_dens(T)
DOUBLE PRECISION :: v_dens, T, a, b, c, d, e, f
a=-299.6373102D0
b=4.974715994D0
c=-0.03322820191D0
d=0.0001134072022D0
e=-2.031981824D-07
f=1.585972295D-10
v_dens=a+b*T+c*T**2+d*T**3+e*T**4+f*T**5      !kg/m3
return
end


function dvdT(T)
DOUBLE PRECISION :: dvdT, T, b, c, d, e, f

b=4.974715994D0
c=-0.03322820191D0
d=0.0001134072022D0
e=-2.031981824D-07
f=1.585972295D-10
  dvdT=b+2.0*c*T+3.0*d*T**2+4.0*e*T**3+5.0*f*T**4   !
return
end



!***************************PROPERTY DATA FOR WATER************************

FUNCTION PRESS2(T)
DOUBLE PRECISION :: T, PRESS2, a, b, c
a=15.38366
b=-2111.3788
c=-36815.655
PRESS2=EXP(a+b/T+c/T**1.5)
return
END


FUNCTION LATENT(T)
DOUBLE PRECISION :: a, b, c, d, T, LATENT
a=4535.5338
b=-14.40485
c=0.034749747
d=-3.3548106D-5
  LATENT=a+(b*T)+(c*T**2)+(d*T**3)  !kJ/kg,  T in K
return
END


FUNCTION TENSION(T)
DOUBLE PRECISION :: T, TENSION
TENSION=235.8D0*((1.0D0-(T)/(374.15D0+273.15D0))**1.256D0)*(1.0D0-(0.625D0)*(1.0D0-(T)/(37
4.15D0+273.15D0)))  !mN/m
return
end
```

```fortran
FUNCTION l_sp_heat(T)
DOUBLE PRECISION :: T, l_sp_heat, a, b, c, d, e
a=78.582798
b=-0.14625086
c=0.00010960625
d=-17026.454
e=1472551.8
 l_sp_heat=a+(b*T)+(c*T**2)+(d/T)+(e/T**2)    !kJ/kgK
END


FUNCTION T_sat(P)
DOUBLE PRECISION :: P, T_sat, a, b, c, d, e, f, g, h
a=280.14591
b=14.578656
c=0.81618388
d=0.090358794
e=-0.01233292
f=0.0036827453
g=-0.00036521131
h=1.7727335D-5



T_sat=a+b*(LOG(P))+c*(LOG(P))**2+d*(LOG(P))**3+e*(LOG(P))**4+f*(LOG(P))**5+g*(LOG(P))*
*6+h*(LOG(P))**7
 END


function therm_cond(T)
DOUBLE PRECISION :: therm_cond, T
therm_cond=0.56917061+0.0018981353*(T-273.15)-8.8322257*10**(-6.0)*(T-273.15)**2.0+7.2806061
*10**(-9.0)*(T-273.15)**3.0 !W/mK
return
end


function l_dens(P)
DOUBLE PRECISION :: l_dens, P
l_dens=1008.1433+(-7.3239274)*P**0.41233836        !kg/m3
return
end


function v_dens(T)
DOUBLE PRECISION :: v_dens, T, a, b, c
a=94.90762D0
b=-0.023178676D0
c=-0.24376403D0
 v_dens=EXP((a+c*T)/(1.0D0+b*T))    !kg/m3
return
end


function dvdT(T)
DOUBLE PRECISION :: dvdT, T, b, c
a=94.90762D0
b=-0.023178676D0
c=-0.24376403D0
```

```
dvdT=((c-a*b)/(1.0D0+b*T)**2)*EXP((a+c*T)/(1.0D0+b*T))
return
end
```

APPENDIX G

**Publication of Robinson, A. J. and Judd, R. L. in the
International Journal of Heat and Mass Transfer, vol. 44, 2001.**

Bubble growth in a uniform and spatially distributed temperature field

A.J. Robinson, R.L. Judd *

Department of Mechanical Engineering, McMaster University, Hamilton, Ont. L8S 4L7, Canada

Received 29 February 2000; received in revised form 8 September 2000

Abstract

A theory has been developed which has been shown to predict experimental bubble growth data for both spherical growth in an unbounded liquid and hemispherical growth at a heated plane surface in microgravity. The theory is able to accommodate both spatial and temporal variations in the temperature and velocity fields in the liquid surrounding the bubble as it grows. Utilising the present theory, the complicated thermal and hydrodynamic interactions between the vapour, liquid and solid have been manifested for a single isolated bubble growing on a heated plane surface from inception. © 2001 Elsevier Science Ltd. All rights reserved.

1. Introduction

The increased rate of heat transfer during nucleate boiling is determined by the vapour bubbles which grow and depart from the heated surface. Energy is introduced into the liquid by conduction from the heated solid surface and is stored within a thin thermal boundary layer adjacent to the surface. During surface boiling, this energy is ultimately used to vaporise the liquid and cause bubbles to form and grow. Furthermore, fluid motions induced by bubble growth disrupt the thermal boundary layer, thus enhancing the local rate of heat transfer. Consequently, insight into the mechanisms which are responsible for transporting energy away from a heated surface can be gained by understanding the nature of bubble growth.

Early theoretical works focussed on the ideal case of spherically symmetric bubble expansion in a uniformly superheated infinite pool of liquid. With these simplifications, the rate of bubble growth is determined by the surface tension, the liquid inertia and the difference in pressure between the vapour within the bubble and the ambient liquid. Analytic expressions which fully describe the growth of a bubble were unattainable because of the complicated thermal and hydrodynamic interaction of the vapour and liquid at the bubble wall. This was further complicated by coupling between the liquid momentum and energy equations through the non-linear convection term. To reduce the complexity of the problem, Rayleigh [1], Plesset and Zwick [2] and Forster and Zuber [3] considered two limiting regions of bubble growth separately. Lord Rayleigh [1] solved the one-dimensional problem by considering the case in which growth or collapse is governed by momentum interaction between the bubble and ambient fluid. This later became known as the *inertia controlled* stage of bubble growth. Almost four decades later, Plesset and Zwick [2] and Forster and Zuber [3] independently determined that the later stage of bubble growth is controlled by the rate at which energy is transferred through the liquid to the vapour–liquid interface. This was termed the *diffusion* or *heat transfer controlled* growth stage. By approximating a solution to the energy equation, it was shown that their first-order solutions were in good agreement with the experimental results provided by Dergarabedian [4] for water with low superheats at atmospheric pressure. Including the effects of radial convection in the liquid, Scriven [5] obtained an expression for the bubble growth rate which is very similar to that of Plesset and Zwick [2] and Forster and Zuber [3].

Nomenclature

A	area	u	radial velocity (spherical coordinates)
D_j	radial grid line	U	radial velocity (cylindrical coordinates)
d	distance from vapour–liquid interface	U^c	contravarient velocity
g	earth gravity	V	axial velocity
g_x	gravity in which experiments were performed	V^c	contravarient velocity
h_{fg}	latent heat of evaporation	z	axial direction
J	Jacobian	z_b	axial coordinate location of bubble interface

Greek symbols

k	thermal conductivity	α	thermal diffusivity
M	grid parameter	γ	angle measured from z-axis
N	grid parameter	ε	transformed computational coordinate
P	pressure	η	transformed computational coordinate
Q	energy required for bubble growth	ν	kinematic viscosity
q''	heat flux	ρ	density
r	radial direction	τ	transformed computational time

r_b	radial coordinate location of bubble interface	*Subscripts*	
R	bubble radius	l	liquid
R_c	initial bubble radius	R	at bubble interface
S_R	grid clustering coefficient	v	vapour
t	time	w	wall
t^*	time to nucleation	1D	one-dimensional
T	temperature	∞	far field

By assuming that the bubble growth rate was bounded by the analytic solutions of Rayleigh [1] for small values of time and that of Plesset and Zwick [2] as time approached infinity, a general relationship was derived by Mikic et al. [6] for spherical bubble growth in a uniformly superheated liquid which involved both the inertia and heat transfer controlled growth stages. This theory was found to be in good agreement with the experimental data of Lien [7] for water over a wide range of system pressures.

Numerical computations of vapour bubble growth in an infinite, uniformly superheated liquid have been performed by Theofanous et al. [8], Judd [9], Board and Duffy [10], Dalle Donne and Ferranti [11], and Lee and Merte [12]. In the first three works, approximate solutions to the energy equation were used, whereas in the latter two works, a more rigorous numerical solution of the entire energy equation, including the non-linear convective term, was obtained.

The mechanisms associated with vapour bubble growth at a plane heated surface are not understood nearly as well as unbounded growth in an infinite pool. This is due to the fact that it is exceedingly difficult to control the temperature and flow field in the vicinity of growing bubbles during experimental investigations due to natural convection and liquid motions induced by other bubbles. Due to the rapidly varying temperature and flow fields, large scatter is observed in the available bubble growth data at earth gravity, which makes

comparison with theory very difficult because of the uncertainty involved in matching the initial and boundary conditions.

However, recent data have been reported by Lee [13], Lee and Merte [14], and Merte et al. [15], in which the shortcomings associated with earth gravity surface boiling experiments are partially overcome by heating a stagnant pool of liquid to the onset of boiling in microgravity. The absence of any significant natural convection, combined with the fact that, during the early stages of growth, the thermal and flow fields are not influenced by previous or neighbouring bubbles, provide well-defined initial and boundary conditions. Even still, the temperature distribution in the solid and liquid were not measured directly, so that approximations are required for determining the initial liquid temperature field and the boundary condition for the solid heater. A further simplification results from the fact that, for some of the measurements, the bubble remained nearly hemispherical for a significant portion of the growth period. The fixed bubble shape adds considerable simplification with respect to theoretical modelling and an accompanying solution procedure. In this manner, Lee and Merte [14] and Merte et al. [15] were able to compare the experimental hemispherical bubble growth data, obtained in R113 on a flat solid surface subject to transient heating, with the theoretical predictions of two one-dimensional spherical models. In the first, an initial uniform liquid temperature, equal to the highest surface

temperature which occurs at nucleation, was assumed. This represented the upper bound on the bubble growth rate, since the highest temperature was assumed to exist everywhere throughout the liquid. The second model assumed a spherically symmetric, non-uniform temperature field around the bubble. The temperature distribution was assumed to be identical to that occurring normal to the heated surface at nucleation. This was regarded as the 'minimum temperature distribution' and represented the lower bound on the bubble growth rate. All of the measured growth curves presented in [13–15] fell between bounds defined by the uniform and non-uniform models.

This paper describes the development of a two-dimensional theoretical model which is capable of predicting both spherically symmetric vapour bubble growth in an infinite pool of liquid as depicted in Fig. 1(a) and hemispherical vapour bubble growth at a heated plane surface as depicted in Fig. 1(b). The theory

is the logical progression from the work provided in [13–15] in that it can incorporate either a one-dimensional radially symmetric or a two-dimensional spatially distributed liquid temperature field. It must be carefully noted that the applicability of the present model is limited to the special case in which the energy utilised by the bubble as it grows is supplied by the superheated liquid layer which surrounds the bubble cap. Any contribution of an evaporating microlayer at the base of the bubble to the net mass transfer rate into the bubble, or its influence on the thermal field in the solid during heterogeneous bubble growth, is wholly disregarded. The purpose of this investigation is twofold. First, to advance a simplified physical model and solution procedure for heterogeneous bubble growth. Because many of the fundamental mechanisms are the same, study of this simplified type of growth provides a starting point for more complex theoretical development. Second, to elucidate the factors which contribute to bubble growth.
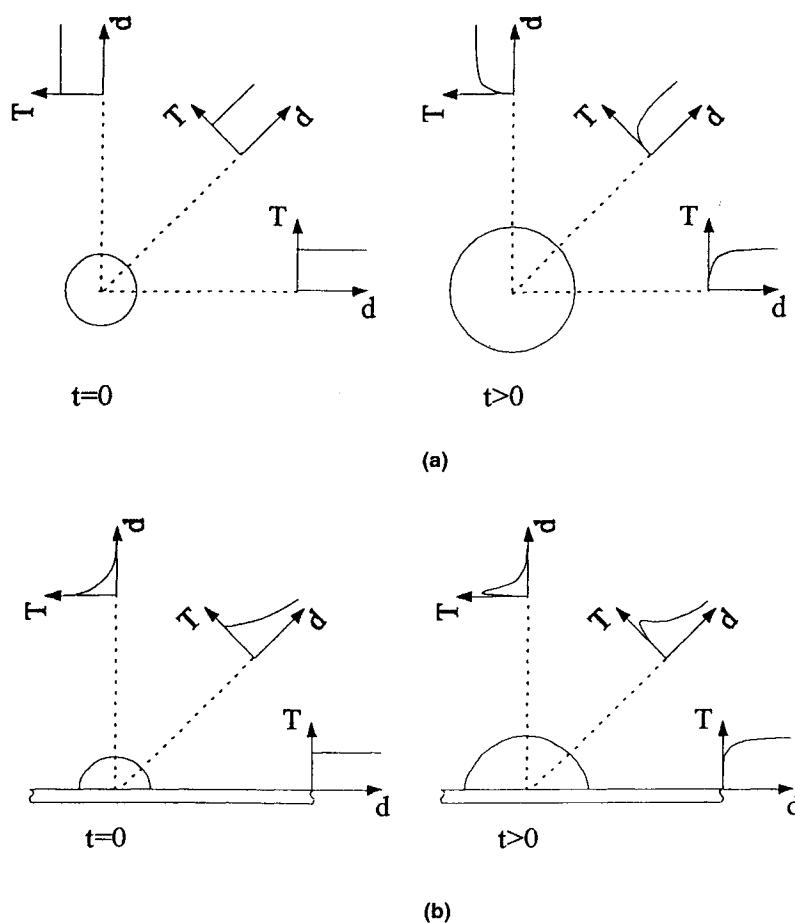

Fig. 1. (a) Spherical vapour bubble growth in an unbounded liquid with a uniform temperature field at $t = 0$ and a spherically symmetric temperature profile for $t > 0$; (b) hemispherical vapour bubble growth at a heated flat surface with a non-uniform temperature field at $t = 0$ and a spherically non-symmetric temperature profile for $t > 0$.

By considering a significant portion of the growth period of a single isolated bubble beginning from inception, the proportional contributions of the various mechanisms which govern growth can be discerned.

2. Formulation of the problem

Fig. 2 shows a sketch of the hemispherical vapour bubble growing at a heated plane surface. Although a viscous boundary layer is known to exist in the liquid above the heated surface, in most practical applications this layer is very thin compared with the size of the bubble so that its overall influence on the bubble as is grows can be neglected. This, coupled with the impermeable wall boundary condition, allows for liquid flow symmetry to be assumed about the r-axis. As a result, hemispherical bubble growth can be modelled as a half segment of the spherical case. In doing so, the equation of motion for the radius, R, of the hemispherical vapour bubble is approximated by the equation for a growing sphere given by

$$P_v(T_v) - P_\infty = \rho_l R \frac{d^2 R}{dt^2} + \frac{3}{2}\rho_l\left(\frac{dR}{dt}\right)^2 + \frac{2\sigma}{R}. \tag{1}$$

Eq. (1) is the extended Rayleigh equation which represents a force–momentum balance between the bubble and surrounding liquid. A detailed derivation of this relationship can be found in Riznic et al. [16]. The initial bubble radius is determined by assuming that the vapour is initially saturated, with $T_v = T_\infty$, and that it exists in unstable equilibrium with the quiescent surroundings. For a stationary vapour bubble with internal pressure $P_{\mathrm{sat}}(T_v)$ at equilibrium with a liquid at pressure P_∞, the Young–Laplace equation gives an initial radius of,

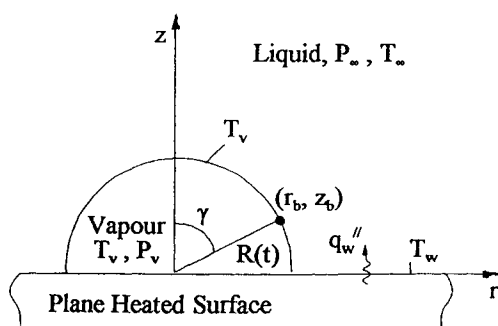$$R_c = \frac{2\sigma}{P_{\mathrm{sat}}(T_v) - P_\infty}. \tag{2}$$

Fig. 2. Hemispherical bubble growing on a plane heated surface.

As a result of the dependence of the vapour pressure on temperature, at least one more equation is required to fully describe this type of bubble growth problem. This expression is obtained by considering an energy balance at the vapour–liquid interface. The energy, Q, required to expand the bubble is supplied by molecular conduction across the thin thermal boundary layer that exists in the liquid around the bubble. Therefore, the rate of change in the energy contained in the vapour bubble is such that

$$\frac{dQ}{dt} = \int_{A_s} k_l\left(\frac{\partial T}{\partial n}\right)_R dA. \tag{3}$$

where A_s is the surface area of the bubble and $(\partial T/\partial n)_R$ is the temperature gradient normal to the interface. Various researchers [1,3,5,10,11] propose different formulations for the term dQ/dt. However, for commonly used fluids well below the critical pressure, the interfacial energy balance can be reduced to

$$h_{fg}\rho_v \frac{dR}{dt} + h_{fg}\frac{R}{3}\frac{d\rho_v}{dt} = \frac{1}{2\pi R^2}\int_{A_s} k_l\left(\frac{\partial T}{\partial n}\right)_R dA. \tag{4}$$

In the above expression, the vapour motion and property variations within the bubble are neglected. Riznic et al. [16] provide a comprehensive derivation of Eq. (4).

Typically, during nucleate pool boiling, energy is continually supplied to the liquid by heat transfer normal to the plane heated surface throughout the entire growth interval of the bubble. Furthermore, an initial liquid temperature distribution which is spherically symmetric around the bubble is not common for most practical boiling applications. These two conditions introduce two-dimensional effects which need to be accounted for in order to adequately describe this type of bubble growth. As a result, the temperature gradient at the bubble wall is obtained by numerically solving the two-dimensional energy equation in axisymmetric cylindrical coordinates for the moving liquid,

$$\frac{\partial T}{\partial t} + U\frac{\partial T}{\partial r} + V\frac{\partial T}{\partial z} = \alpha_l\left(\frac{\partial^2 T}{\partial r^2} + \frac{1}{r}\frac{\partial T}{\partial r} + \frac{\partial T}{\partial z}\right), \tag{5}$$

with initial and boundary conditions given by

$$T(r,z,0) = T_0(r,z),$$

$$T(r_b,z_b,t) = T_v,$$

$$T(\infty,\infty,t) = T_{1D}(z,t),$$

$$\frac{\partial T}{\partial r}(0,z,t) = 0,$$

$$\frac{\partial T}{\partial z}(r,0,t) = \frac{q_w''}{k_l}. \tag{6}$$

The initial condition requires the entire temperature field in the liquid to be specified. A zero flux boundary

condition is assumed at the symmetry boundary (*z*-axis) and a constant heat flux boundary condition is established at the plane heated surface (*r*-axis). Some discussion is warranted concerning the assumption of a constant and uniform heat flux at the solid–liquid interface. Admittedly, this assumption significantly reduces the complexity of the problem by eluding the solution of the energy equation in the solid. However, Gau and El-Genk [17] showed that a constant heat flux can be a reasonable approximation for the case in which energy is supplied to the liquid by resistance heating of a thin metallic coating deposited on a glass substrate, so long as the layer is thin enough to restrict the lateral flow of heat through the metal coating. For the experiments presented in [13–15] a 400 Å transparent gold film was deposited on a polished glass substrate. The thinness of the metallic layer precludes any significant lateral heat flow so that a constant heat flux boundary condition is an adequate representation of the surface for comparison with this data. A third boundary condition is obtained by assuming that the vapour phase is lumped and that the temperature of the liquid at the interface is identical to the temperature of the vapour. Finally, the far-field boundary condition is approximated from the analytic solution for one-dimensional axial conduction in a semi-infinite medium. The axial and radial velocities are determined as functions of the instantaneous bubble radius and interface velocity by assuming that the flow field can be determined by the solution for potential flow around an expanding sphere in an unbounded liquid. The velocity components are

$$U = \frac{\mathrm{d}R}{\mathrm{d}t}\left(\frac{R}{(r^2 + z^2)^{1/2}}\right)^2 \sin(\gamma),$$

$$V = \frac{\mathrm{d}R}{\mathrm{d}t}\left(\frac{R}{(r^2 + z^2)^{1/2}}\right)^2 \cos(\gamma). \tag{7}$$

A brief description of the finite difference solution of the energy equation is set out in Appendix A.

Finally, it is postulated that the vapour is saturated and remains so throughout the bubble growth interval. In this way, the vapour pressure and density can be specified as functions of the saturated vapour temperature,

$$P_\mathrm{v}(T_\mathrm{v}) = a_1 T_\mathrm{v} + a_2 T_\mathrm{v}^2 + a_3 T_\mathrm{v}^3 + a_4 T_\mathrm{v}^4 + a_5 T_\mathrm{v}^5,$$

$$\rho_\mathrm{v}(T_\mathrm{v}) = c_1 T_\mathrm{v} + c_2 T_\mathrm{v}^2 + c_3 T_\mathrm{v}^3 + c_4 T_\mathrm{v}^4 + c_5 T_\mathrm{v}^5. \tag{8}$$

As in [12–14], the property variations with temperature are obtained from a fifth-order polynomial representation of the available property data. With these simplifications, only the rate of change of one state variable, in this case temperature, need be considered given that

$$\frac{\mathrm{d}P_\mathrm{v}}{\mathrm{d}t} = \left(\frac{\mathrm{d}P_\mathrm{v}}{\mathrm{d}T_\mathrm{v}}\right)\frac{\mathrm{d}T_\mathrm{v}}{\mathrm{d}t},$$

$$\frac{\mathrm{d}\rho_\mathrm{v}}{\mathrm{d}t} = \left(\frac{\mathrm{d}\rho_\mathrm{v}}{\mathrm{d}T_\mathrm{v}}\right)\frac{\mathrm{d}T_\mathrm{v}}{\mathrm{d}t}. \tag{9}$$

3. Solution procedure

Eqs. (8) and (9) together with Eqs. (1) and (4) form a set of simultaneous equations for the four unknowns T_v, P_v, ρ_v and R, which were solved numerically using a fourth-order Runge–Kutta method. In order to initiate bubble growth, the equilibrium radius R_c was perturbed by allowing it to increase by a very small amount over an infinitesimally small time interval. This is equivalent to a disturbance in temperature or pressure [10]. A comprehensive discussion on the initial disturbance can be found in [12] and [13]. For this study, the initial time step never exceeded 10^{-7} s, and the radius increase did not exceed 0.05% of the initial radius. Care was taken to ensure that the magnitude of the initial disturbance did not significantly affect the computed growth curve.

4. Comparison with experiment

4.1. Spherical bubble growth

A wealth of experimental data exists for spherical bubble growth in liquids with an initial uniform superheat. This, coupled with the fact that many of the more complex features of heterogeneous growth are absent during homogeneous growth, provides a good test for the present theory and computational procedure. To investigate spherically symmetric growth, the initial
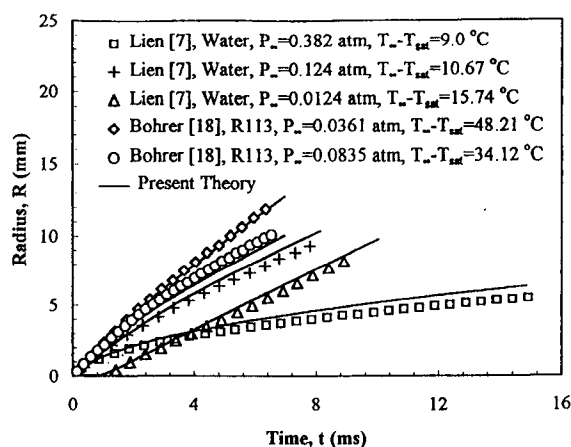

Fig. 3. Comparison of computed results with experimental data for spherical bubble growth in water and refrigerant R113.

temperature distribution is set to be spatially uniform, and symmetry about the r-axis is approximated by setting $q''_w = 0$ to establish a zero temperature gradient.

Fig. 3 shows the comparison of the predictions of the present theory with experimental data of Lien [7] and Bohrer [18]. In the figure, the present theory shows acceptable agreement with the experimental data for homogeneous bubble growth for a range of system pressures and initial liquid superheats for two different fluids. Similar agreement was observed with the bubble growth data provided by Dergarabedian [4] and Board and Duffy [10] for superheated water.

4.2. Hemispherical bubble growth

Heterogeneous bubble growth depends strongly on the amount of energy stored in the thermal boundary layer which forms adjacent to the heater surface. The sensible heat stored in the liquid is converted to latent heat by evaporation into the bubble as it grows. As a result, any predictive model of bubble growth requires that the temperature profile in the liquid be known prior to bubble growth. By heating a quiescent, uniform

temperature liquid in microgravity, Lee [13] was able to show that the solution of the one-dimensional transient heat conduction equation for a constant heat flux boundary condition in a semi-infinite solid did a very good job at predicting the measured mean surface temperature. Consequently, the initial temperature distribution in the liquid could be predicted by the expression

$$T(z, t^*) = T_\infty + \frac{2q''_w \sqrt{\alpha_l t^*/\pi}}{k_l} \exp\left(-\frac{z^2}{4\alpha_l t^*}\right)$$

$$- \frac{q''_w z}{k_l} \mathrm{erfc}\left(\frac{z}{\sqrt{4\alpha_l t^*}}\right). \tag{10}$$

where t^* is the time to the onset of boiling. This expression, together with the assumption of a quiescent liquid, specifies the initial conditions required by the present theory.

Bubble growth predictions for three different test cases are shown in Fig. 4. For each experiment the computational predictions of the two one-dimensional spherically symmetric models, which represent the upper and lower bounds of growth, are given together with the two-dimensional heterogeneous model. As expected, the fully two-dimensional model predicts growth curves
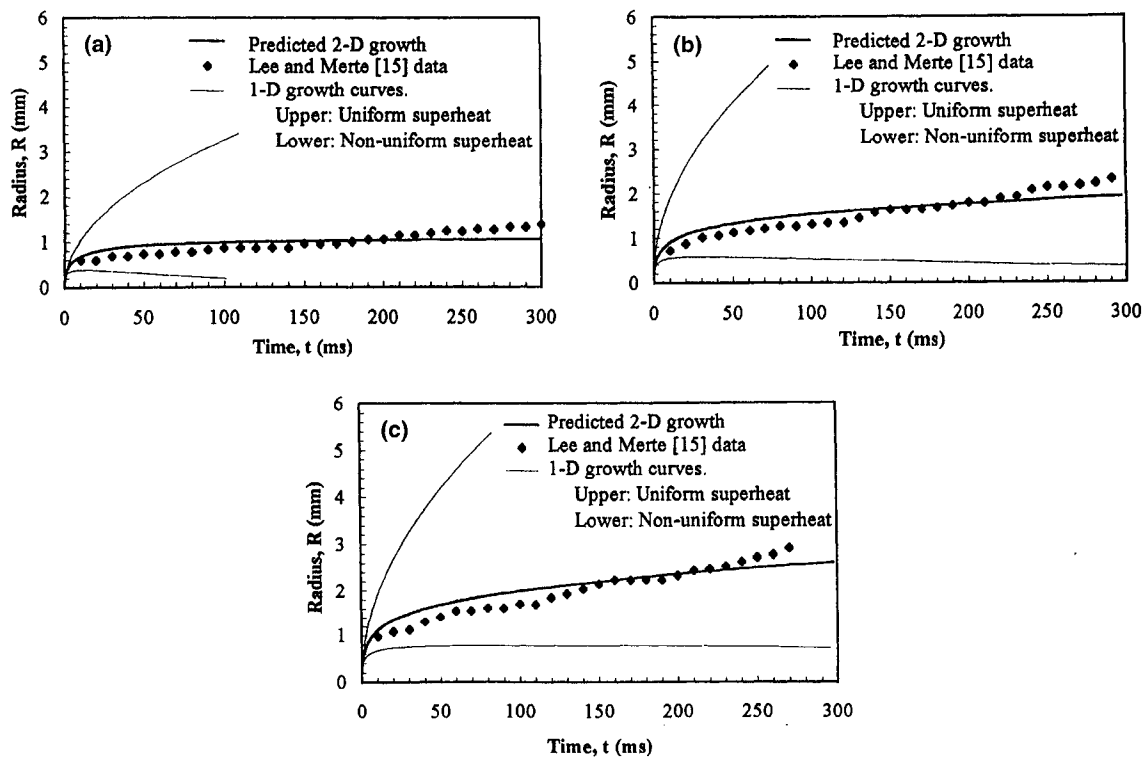
Fig. 4. Comparison of computed results with experiments for hemispherical bubble growth of R113 on a heated plane surface in microgravity, $g_\infty/g = 10^{-4}$ (a) $q'' = 7$ W/cm², $P_\infty = 149.9$ kPa, $T_{sat} = 59.8°C$, $T_\infty = 48.3°C$, $t^* = 0.91$ s, $T^*_w = 85.8°C$; (b) $q'' = 6.5$ W/cm², $P_\infty = 117.3$ kPa, $T_{sat} = 52°C$, $T_\infty = 48.8°C$, $t^* = 0.74$ s, $T^*_w = 86.3°C$; (c) $q'' = 6.95$ W/cm², $P_\infty = 106.8$ kPa, $T_{sat} = 49.1°C$, $T_\infty = 48.35°C$, $t^* = 0.75$ s, $T^*_w = 84.1°C$.

which are positioned somewhere inbetween the upper and lower bounds as depicted in the figure. More importantly, satisfactory agreement is observed between the measured growth curves over a large portion of the respective growth intervals. This lends support to the physical modelling of the problem as well as the numerical techniques utilised in the computations. It can be noted that the agreement between the computed and experimental curves lends support to the assumption that, for these specific test cases, microlayer evaporation did not play a significant role in the bubble growth process.

5. Bubble dynamics

In the following sections, the growth characteristics of a single isolated hemispherical bubble growing at a plane heated surface with negligible effect of an evaporating microlayer will be discussed. The boiling conditions are identical to those of Fig. 4(b). Fig. 5 shows the time variation of the predicted bubble radius and vapour temperature. In the figure, four regions of growth have been demarcated and will be discussed in turn. In Fig. 6 the energy equation for the vapour bubble, Eq. (4), has been decomposed to expose the time varying contributions of its constituent terms. From the figure, it is apparent that the term involving the rate of change of vapour density $(1/3)h_{fg}R(d\rho_v/dt)$, is negligible compared with the interface velocity term, $h_{fg}\rho_v(dR/dt)$. Thus, for discussion purposes, the growth rate can be considered proportional to the area averaged heat flux into the bubble throughout its growth,

$$\frac{dR}{dt} \propto \frac{1}{A_S}\int_{A_S} k_l\left(\frac{\partial T}{\partial n}\right)_R dA = q''_{ave}. \tag{11}$$
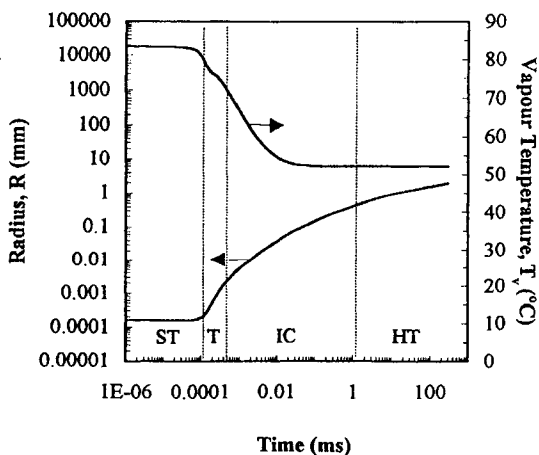

Fig. 5. Bubble radius (R) and temperature (T_v) histories for hemispherical bubble growing atop a heated surface.
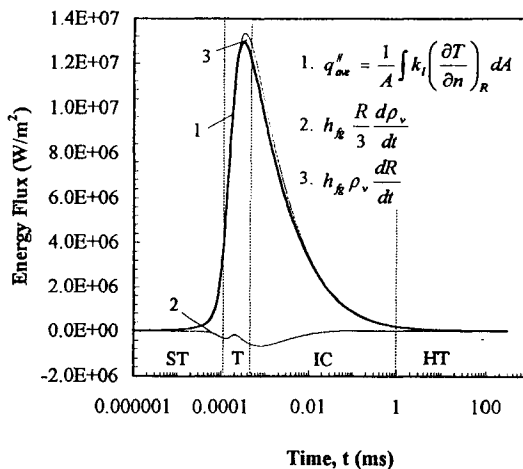

Fig. 6. Decomposition of the energy equation, Eq. (4), showing four growth domains: surface tension controlled (ST), transition (T), inertial controlled (IC), and heat transfer controlled (HT).

In Fig. 7, the constituent components of the equation governing the motion of the interface, Eq. (1), are represented. In the figure, the pressure difference, $P_v - P_\infty$, is balanced by the stress in the interface through the surface tension term, $2\sigma/R$, and the hydrodynamic pressure, P_{hd}, defined as

$$P_{hd} = \rho_l R\frac{d^2R}{dt^2} + \frac{3}{2}\rho_l\left(\frac{\partial R}{\partial t}\right)^2. \tag{12}$$

The hydrodynamic pressure can be regarded as the excess pressure at the bubble interface that is a direct consequence of the bulk motion of the liquid. The total pressure in the liquid at the interface is related to the hydrostatic and hydrodynamic pressures through $P_R = P_\infty + P_{hd}$.

5.1. Surface tension controlled growth (ST)

During the surface tension controlled domain, energy is continuously supplied to the bubble by conduction through the liquid. This is evident from the positive value of q''_{ave} in Fig. 6. However, the average heat flux into the bubble, and thus the growth rate dR/dt, are small enough that the contribution of the hydrodynamic pressure in balancing the equation of motion is insignificant so that it essentially reduces to a static force balance, $P_v - P_\infty \approx 2\sigma/R$, as shown in Fig. 7(a). Because P_∞ is constant, an increase in the bubble radius must occur in conjunction with a decrease in P_v, which of course coincides with a proportional decrease in the vapour temperature, T_v. This is an important effect because the decreasing vapour temperature represents a decreasing interface boundary temperature for the liquid.
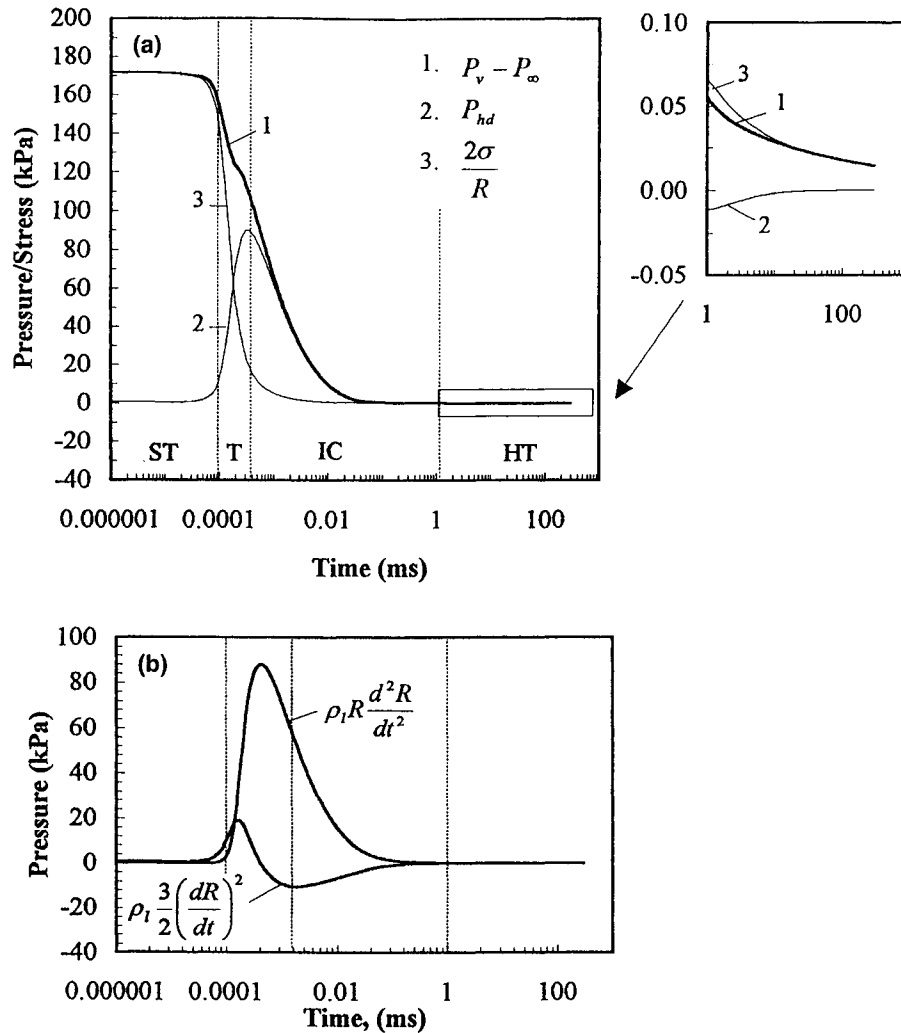
Fig. 7. (a) Decomposition of the equation of motion, Eq. (1) showing the four growth domains: surface tension controlled (ST), transition (T), inertial controlled (IC), and heat transfer controlled (HT); (b) constituent terms of the hydrodynamic pressure term given in Eq. (12).

As the liquid is essentially still, the decreasing interfacial liquid temperature acts to increase the interfacial temperature gradient, $(\partial T/\partial n)_R$. The magnitude of the temperature gradients at the interface can be characterised by considering the tip and base of the bubble as the bounding values. These are shown in Fig. 8. It can thus be said that bubble growth in this domain is accelerated due to a positive feedback effect in which the increase in the radius, R, is related to a decreasing interfacial liquid temperature. This corresponds with an increase in q''_{ave}, through the increase in the magnitude of the local temperature gradient, which feeds back by a proportional increase in the bubble growth rate, dR/dt. In the earliest stage of the surface tension domain, this feedback effect is not significant. However, in the latter

stage, it becomes appreciable as indicated by a noticeable increase in R away from R_c (Fig. 5), a significant decrease in both T_v and P_v (Figs. 5 and 7(a), respectively) and a sharp rise in q''_{ave} (Fig. 6)

5.2. Transition domain (T)

As the bubble interface is accelerating radially outward there comes a point at which the effects of the bulk liquid motion outside the bubble are no longer insignificant. The transition domain is thus distinguished from the surface tension domain by the relative contributions of the surface tension term and the hydrodynamic pressure term in balancing the equation of motion. Fig. 7(a) shows that the excess pressure at the
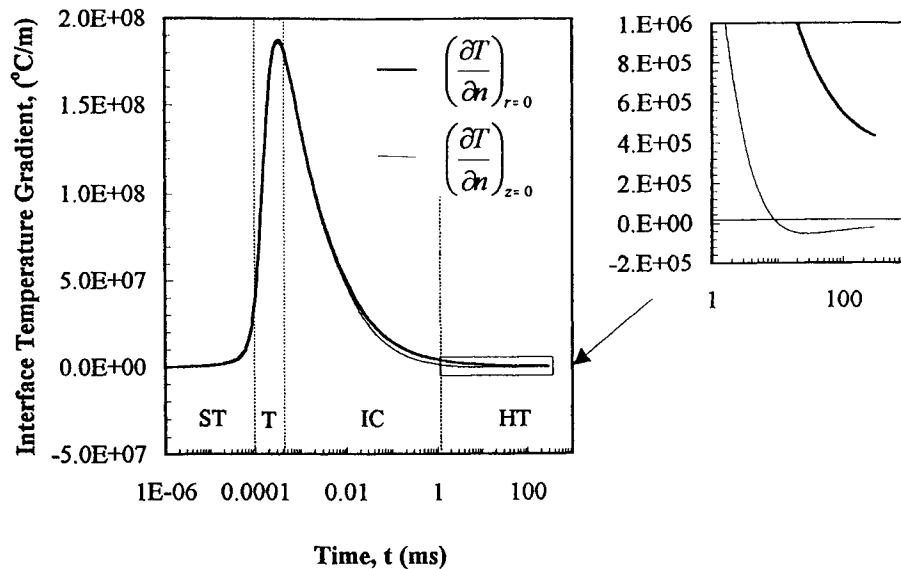
Fig. 8. Interfacial liquid temperature gradient histories at the top of the hemispherical bubble (along z-axis), and the base of the hemispherical bubble (along r-axis).

interface due to flow effects, P_{hd}, rises sharply at the beginning of this region and quickly becomes of the same order of magnitude as the surface tension term, $2\sigma/R$.

At the beginning of the transition domain the effects of liquid motions are still small, so that both q''_{ave} and dR/dt continue to increase rapidly as a result of the positive feedback effect discussed earlier. However, as evident from Fig. 6, the rate of change of q''_{ave} and dR/dt are shown to decrease in the latter stage and reach a maximum value at approximately 3×10^{-4} ms. Because the decreasing vapour temperature tends to have a positive influence on the local temperature gradient and thus q''_{ave}, this signifies that there are mechanisms at work which tend to oppose the increase of q''_{ave}. The most obvious is the fact that, as the growing bubble faces the additional resistance associated with forcing the bulk liquid out radially, the rate at which P_v and T_v decrease becomes less rapid. This tends to adversely affect the rate at which $(\partial T/\partial n)_R$ and q''_{ave} increase. The significant decrease in the slopes are demarcated by the 'inflection' on the T_v and $P_v - P_\infty$ curves shown in Figs. 5 and 7(a), respectively. Secondly, conduction and advection occur in the liquid adjacent to the interface. Each of these heat transfer mechanisms act in such a way as to diminish the temperature gradients in the immediate vicinity of the vapour–liquid interface and thus have a detrimental influence on the rate at which q''_{ave} and dR/dt increase. Advection describes the mechanism by which thermal energy is transported into the bulk of the liquid away from the bubble interface due to outward radial flow. Conduction, on the other hand, is responsible for the

transport of energy into the vapour bubble, and to a lesser extent into the bulk liquid. This is illustrated in Fig. 9, where the temperature profiles along the z- and r-axes are shown.

5.3. Inertial controlled growth (IC)

Inertia controlled growth refers to the interval of bubble growth in which the rate of bubble expansion is considered to be limited by the rate at which the growing interface can push back the surrounding liquid [19]. In this domain, the average heat flux into the bubble is very high, as illustrated in Fig. 6, so that heat transfer to the interface is not the limiting mechanism of growth.

Fig. 7(a) shows that the pressure difference, $P_v - P_\infty$, is now balanced by the hydrodynamic pressure at the interface. The hydrodynamic pressure comprises two 'inertial' terms as given in Eq. (12). These are the acceleration term, $\rho_l R(d^2R/dt^2)$, and the velocity term, $(3/2)\rho_l(dR/dt)^2$. These are plotted in Fig. 7(b). The two terms are of differing sign and thus tend to have an opposite influence on the total liquid pressure, and thus the force of the liquid on the bubble interface. The negative acceleration term accounts for the fact that the fluid body surrounding the bubble is decelerating, causing outward force on the bubble surface. The velocity term is positive because the expanding bubble wall is effectively pushing the fluid outwardly. The reaction force of the liquid on the bubble wall is thus inwardly directed and must be of opposite sign.

This inertial controlled growth domain is characterised by a decreasing average heat flux and decelerating
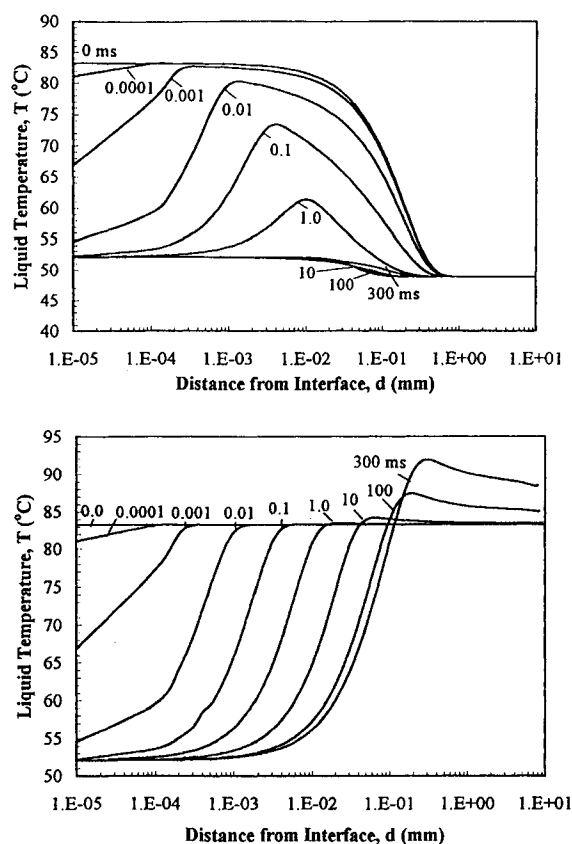
Fig. 9. Computed liquid temperature distribution at (a) the top of the hemispherical bubble (along z-axis), and (b) the base of the hemispherical bubble (along r-axis) at various times.

interface as shown in Fig. 6. This signifies that the positive influence that the decreasing vapour temperature tends to have on the local temperature gradient is not sufficient to compensate for the rate at which advection and conduction serve to decrease the temperature gradient at the interface. Figs. 5 and 8 show that the decreasing vapour temperature occurs in conjunction with decreasing interfacial temperature gradients at the tip and base of the bubble. Fig. 9(a) shows this point more clearly. Here, the interfacial liquid temperature is decreasing. However, due to a net loss of thermal energy by conduction out of the liquid and into the vapour bubble, coupled with conduction and advection of thermal energy away from the bubble and into the bulk liquid, the maximum temperature within the boundary layer decreases and moves further out from the bubble interface. This 'shrinking' and 'stretching' of the thermal boundary layer results in an overall decrease in magnitude of the interfacial temperature gradient, even with a decreasing interfacial liquid temperature. Fig. 9(b) shows a similar effect at the base of the bubble except that the maximum temperature, which is equal to the

temperature of the liquid adjacent to the plane heated surface, remains approximately constant during this domain.

5.4. Heat transfer controlled growth (HT)

Heat transfer controlled growth refers to the interval of bubble growth in which the rate of bubble expansion is considered to be limited by the rate at which liquid is evaporated into the bubble, which is dictated by the rate of heat transfer by conduction through the liquid [19]. In this late stage of bubble growth, the interface velocity has slowed enough so that the hydrodynamic pressure, P_{hd}, becomes insignificant compared with the surface tension term, $2\sigma/R$, in balancing the pressure difference, $P_v - P_x$. This is shown in Fig. 7(a). As a result, the equation of motion is essentially reduced to a balance of static forces acting at the vapour–liquid interface, $P_v - P_x \approx 2\sigma/R$, in much the same way as it did in the surface tension controlled region. However, in contrast with the surface tension controlled region, increases in R do not produce an appreciable decrease in the vapour temperature of the bubble. As shown in Figs. 5 and 9, the vapour temperature remains relatively constant and approximately equal to its minimum value corresponding with the saturation temperature of the system ($T_{v,min} \approx T_{sat}(P_x) = 52.0°C$). Because the liquid temperature at the interface is now constant, the positive feedback effect, responsible for the rapid acceleration of the vapour–liquid interface in the surface tension controlled region, does not occur in this domain of growth. Conversely, the 'shrinking' and 'stretching' of the thermal layer in the liquid due to conduction and advection are responsible for the continuous deceleration of the interface due to the diminishing interfacial temperature gradients. The decrease in the growth rate is compounded by the fact that for $t > 10$ ms the top portion of the bubble penetrates into a region of liquid which is subcooled. This point is illustrated in Figs. 8 and 9(a) by the negative value of the interface temperature gradient for the tip of the bubble. Hence from this time onward, the net energy transfer into the bubble is the difference between that which leaves by condensation and that which enters by evaporation.

It is interesting to note that the maximum temperature in the liquid along the heated surface exceeds that of the far field wall temperature. This is illustrated for $t \geqslant 1.0$ ms in Fig. 9(b). At any point along the heated surface there are three heat transfer mechanisms which act together to transport the imposed heat flux: radial conduction tangent to the heater surface, axial conduction normal to the heater surface, and convection due to the flow of liquid over the surface. The lower temperature in the immediate vicinity of the bubble indicates that the imposed heat flux is being transported away from the surface very efficiently. This region is charac-

terised by a relatively high evaporative heat flux into the bubble together with significant convective heat transfer because it is the region of highest liquid velocity. Moving further away from the interface, the influence of evaporation becomes less and the contribution of convective heat transfer decreases due to the rapidly diminishing liquid velocity ($U(r,0,t) \propto 1/r^2$). The surface temperature increases as the less efficient mode of axial conduction normal to the surface becomes an important mode of heat transfer. One might expect the surface temperature to increase asymptotically to the surface temperature in the undisturbed region at R_∞. However, it is evident from interferometric investigations on growing bubbles that the thermal boundary layer thickness adjacent to the surface can be largest near the bubble and decreases at distances further away [20]. Consequently, in order that axial conduction can accommodate the imposed surface heat flux, the surface temperature must be higher in the region of the thicker boundary layer nearer the interface. This is consistent with the observed overshoot in the liquid temperature profile at the heated surface.

6. Conclusions

In recent years, theoretical developments in nucleate pool boiling have been focussed on isolated bubble growth upon a heated surface. It is hoped that an understanding of the mechanisms which determine the growth of bubbles will offer insight into and perhaps predictions of the increased heat transfer coefficient observed in nucleate pool boiling. However, advances in the state of the art are inhibited by the apparent stochastic nature of boiling due to the rapidly varying thermal and flow fields. As a result of the overwhelming complexities, sufficient testing of the physical modelling and computational procedures has not been afforded in the past.

The present theory overcomes this shortcoming in two ways. First, the theory is simple enough to facilitate comparison with data for homogeneous growth in an unbounded fluid. Second, the theory can accommodate the added complexities of a heated surface and time varying spatially distributed liquid temperature fields for hemispherical bubble growth in microgravity. Overall agreement between the present theory and experimental data is very good, which instills confidence in the physical modelling of the problem as well as the computational procedure which has been utilised.

The complicated thermal and hydrodynamic interactions between vapour, liquid and solid have been manifested for a single, isolated bubble growing on a heated plane surface from inception with the negligible contribution of an evaporating microlayer. It has been shown that early bubble growth away from the initial

radius is restricted by surface tension forces within the bubble wall. However, minuscule increases in radius result in an increase in the local interfacial temperature gradients, which facilitates growth by increasing the area-averaged heat flux into the bubble. Eventually, bubble growth becomes impeded by the fact that it now must force the surrounding liquid out radially. The heat flux increases to such an extent that this becomes the limiting factor to growth. Nevertheless, the growth rate must eventually decrease with increasing time as the thermal energy stored within the boundary layer which surrounds the bubble is consumed by the bubble as well as transported away from the bubble by advection into the bulk of the liquid. Eventually the growth rate slows enough so that liquid inertia no longer plays an important role, and the growth rate becomes limited by the rate at which energy can be transported to the interface through the liquid.

Appendix A. Computational technique for the energy equation

Utilising subscript notation to denote partial differentiation with respect to the subscript variable, the energy equation in axisymmetric cylindrical coordinates can be expressed as

$$T_t + UT_r + VT_z = \alpha_l (T_{rr} + r^{-1} T_r + T_z), \tag{13}$$

where U and V are the axial and radial components of the liquid velocity defined in Eq. (7).

The energy equation was solved numerically on a grid which was constructed using an algebraic grid generation technique proposed by Chen et al. [21]. The grid variables in the physical domain are depicted in Fig. 10. Grid clustering near the vapour–liquid interface as well the moving boundary were facilitated by defining the grid such that
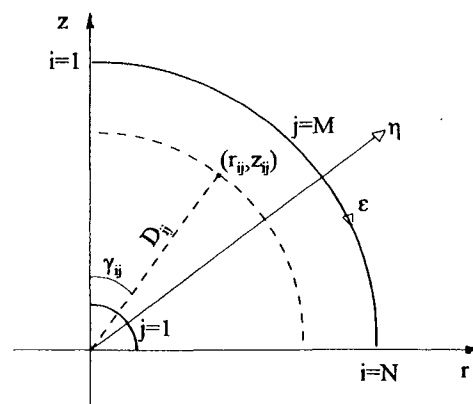

Fig. 10. Grid parameters.

$$r_{ij} = D_j \sin(\gamma_{ij}), \qquad z_{ij} = D_j \cos(\gamma_{ij}), \qquad (14)$$

where

$$\gamma_{ij} = \frac{\pi}{2}\left(\frac{i-1}{N-1}\right),$$

$$D_j = 1 + (R_x - 1)\left(1 - S_R \tan^{-1}\left[\left(1 - \frac{j-1}{M-1}\right)\tan\left(\frac{1}{S_R}\right)\right]\right). \qquad (15)$$

and the term S_R determines the percentage of grid points near the interface. In order that conventional finite difference techniques be utilised, the energy equation was transformed to a stationary grid with uniform grid spacing. The transformation is given by

$$r = r(\varepsilon, \eta, \tau), \qquad z = z(\varepsilon, \eta, \tau), \qquad t = \tau \qquad (16)$$

such that

$$T_r = J^{-1}(z_\eta T_\varepsilon - z_\varepsilon T_\eta),$$

$$T_z = J^{-1}(r_\varepsilon T_\eta - r_\eta T_\varepsilon), \qquad (17)$$

$$T_t = T_\tau - T_r r_\tau - T_z z_\tau.$$

By defining the contravariant velocities as

$$U^c = (U - r_\tau)z_\eta - (V - z_\tau)r_\eta,$$

$$V^c = (V - z_\tau)r_\varepsilon - (U - r_\tau)z_\varepsilon, \qquad (18)$$

the transformed energy equation becomes

$$T_\tau + J^{-1}U^c T_\varepsilon + J^{-1}V^c T_\eta = J^{-2}\alpha_1(aT_{\varepsilon\varepsilon} - 2bT_{\varepsilon\eta}$$
$$+ cT_{\eta\eta} + dT_\varepsilon + eT_\eta)$$
$$+ (Jr)^{-1}\alpha_1(z_\eta T_\varepsilon - z_\varepsilon T_\eta), \qquad (19)$$

where J is the Jacobian and the coefficients a through e are related to the metrics and their derivatives through the following:

$$J = z_\eta r_\varepsilon - z_\varepsilon r_\eta,$$

$$a = z_\eta^2 + r_\eta^2,$$

$$b = r_\varepsilon r_\eta + z_\varepsilon z_\eta,$$

$$c = z_\varepsilon^2 + r_\varepsilon^2, \qquad (20)$$

$$d = J^{-1}(r_\eta \beta_1 - z_\eta \beta_2),$$

$$e = J^{-1}(z_\varepsilon \beta_2 - r_\varepsilon \beta_1),$$

$$\beta_1 = az_{\varepsilon\varepsilon} - 2bz_{\eta\varepsilon} + cz_{\eta\eta},$$

$$\beta_2 = ar_{\varepsilon\varepsilon} - 2br_{\eta\varepsilon} + cr_{\eta\eta}.$$

Eq. (19) was discretised using second-order central difference representations of the spatial derivatives and a fully implicit first order representation of the time derivatives. At a given time step, the temperature field was determined using successive over-relaxation (SOR) by lines. For each line the resulting system of algebraic

expressions were solved utilising the efficient tri-diagonal matrix algorithm (TDMA).

References

[1] J.W.S. Rayleigh, On the pressure developed in a liquid during the collapse of a spherical cavity, Phil. Mag. 34 (1917) 94–98.

[2] M.S. Plesset, S.A. Zwick, The growth of vapor bubbles in superheated liquid, J. Appl. Phys. 25 (1954) 493–500.

[3] H.K. Forster, N. Zuber, Growth of vapor bubbles in superheated liquid, J. Appl. Phys. 25 (1954) 474–478.

[4] P. Dergarabedian, The rate of growth of vapour bubbles in superheated water, J. Appl. Mech. 20 (1953) 537–574.

[5] L.E. Scriven, On the dynamics of phase growth, Chem. Eng. Sci. 10 (1959) 1–13.

[6] B.B. Mikic, W.M. Rohsenow, P. Griffith, On bubble growth rates, Int. J. Heat Mass Transfer 13 (1970) 657–665.

[7] Y.C. Lien, Bubble growth rates at reduced pressure, D.Sc. thesis, MIT, 1969.

[8] T. Theofanous, L. Baisi, H.S. Isben, H. Fauske, A theoretical study on bubble growth in constant and time-dependent pressure fields, Chem. Eng. Sci 24 (1969) 885–897.

[9] A.M. Judd, Analysis of transient boiling of liquid metals, Brit. J. Appl. Phys . 2 (1969) 261–274.

[10] S.J. Board, R.B. Duffy, Spherical vapour bubble growth in superheated liquids, Chem. Eng. Sci. 26 (1971) 263–274.

[11] M. Dalle Donne, M.P. Ferranti, The growth of vapour bubbles in superheated sodium, Int. J. Heat Mass Transfer 18 (1975) 477–493.

[12] H.S. Lee, H. Merte Jr., Spherical vapour bubble growth in uniformly superheated liquids, Int. J. Heat Mass Transfer 39 (1996) 2427–2447.

[13] H.S. Lee, Vapour bubble dynamics in microgravity, Ph.D. thesis, University of Michigan, 1993.

[14] H.S. Lee, H. Merte Jr., Hemispherical vapour bubble growth in microgravity: experiments and model, Int. J. Heat Mass Transfer 39 (1996) 2449–2461.

[15] H. Merte, Jr., H.S. Lee, R.B. Keller, Report on pool boiling experiment flown on STS-47-57-60, report no. UM-MEAM-95-01, Department of Mechanical Engineering and Applied Mechanics, The University of Michigan, Ann Arbor, MI, NASA contract NAS 3-25812, 1995.

[16] J. Riznic, G. Kojasoy, N. Zuber, On the spherically symmetric phase change problem, Int. J. Fluid Mech. Res. 26 (1999) 110–145.

[17] Z. Gau, M. El-Genk, Liquid microlayer evaporation during nucleate boiling on the surface of a flat composite wall, Int. J. Heat Mass Transfer 37 (1996) 1641–1655.

[18] T.H. Bohrer, Bubble growth in highly superheated liquids, M.S. thesis, Purdue University, 1973.

[19] V.P. Carey, Liquid–Vapor Phase-Change Phenomena, Hemisphere, Washington, DC, USA, 1992.

[20] S. Van Stralen, R. Cole, Boiling Phenomenon, Hemisphere, USA, 1979, p. 833.

[21] W. Chen, R. Mei, J.F. Klausner, Vapor bubble growth in highly subcooled heterogeneous boiling, in: Convective Flow Boiling Conference, paper II-4, 1995.

REFERENCES

Abdelmessih, A. H., 1969, "Spherical Bubble Growth in a Highly Superheated Liquid Pool," Cocurrent Gas-Liquid Flow, Plenum Press, pp. 485-495.

Bankoff, S. G., & Mikesell, R. D., 1958,"Growth of Bubbles in a Liquid of Initially Non-Uniform Temperature," ASME paper no. 58-A-105, ASME, New York.

Board, S. J. and. Duffy, R. B., 1971, 'Spherical Vapour Bubble Growth in Superheated Liquids," *Chem. Engng. Sci.* vol. 26, pp. 263-274.

Bohrer, T. H., 1973, "Bubble Growth in Highly Superheated Liquids," M.S. Thesis, Purdue University.

Buyevich, Y. A., and Webbon, B. W., 1996, "Dynamics of Vapour Bubbles in Nucleate Pool Boiling," Mei, R., Chen, W. and Klausner, J. F., "Vapour Bubble Growth in Heterogenoous Boiling-I. Formulation, " *Int. J. Heat Mass Transfer*, vol. 2409-2426, pp. 2409-2426.

Carey, Van P., 1992, Liquid-Vapor Phase-Change Phenomena, Hemisphere Publishing Co. USA

Chen, W, Mei, R., and. Klausner, J. F, 1995, "Vapor Bubble Growth in Highly Subcooled Heterogeneous Boiling," Convective Flow Boiling Conference, Paper II-4.

Cole, R., & Shulman, H. L., 1966,"Bubble Growth Rates of High Jakob Numbers," *Int. J. Heat Mass Transfer*, vol. 9, pp. 1377-1398.

Crank, J., 1984, Free and Moving Boundary Problems, Clarendon Press, New York.

Dalle Donne, M.. and Ferranti, M. P., 1975, "The Growth of Vapour Bubbles in Superheated Sodium," *Int. J. Heat Mass Transfer,* vol. 18, pp. 477-493.

Dergarabedian, P., 1953, "The Rate of Growth of Vapour Bubbles in Superheated Water," *J. Appl. Mech.,* vol.20, pp.537-574.

Florschuetz, L. W., Henry, C. L. and Rashid Khan, 1969, "Growth Rates of Free Vapor Bubbles in Liquids at Uniform Superheats under Normal and Zero Gravity Conditions," *Int. J. Heat Mass Transfer,* vol. 12, pp.1465-1489.

253

Florschuetz, L. W. and Chao, B. T., 1965, "On the Mechanisms of Vapour Bubble Collapse," *J. Heat Transfer*, vol. 87, pp. 209-220.

Forster, H. K. and Zuber, N., 1954, "Growth of Vapor Bubbles in Superheated Liquid," *J. Applied Physics,* vol. 25, pp. 474-478..
Fritz, W. and Ende, W., 1936, "Uber den Verdampfungvorgang Nach Kinematographischen," Phys. Zeitsh., vol. 37, pp. 391-401.

Griffith P., 1965, "Nucleation and Bubble Formation in Boiling," *Proc. Instn. Mech. Engrs.*, vol. 180, Pt.1, pp. 1092-1098.

Guo, Z. and El-Genk, M., 1996, "Liquid Microlayer Evaporation During Nucleate Boiling on the Surface of a Flat Composite Wall, *Int. J. Heat Mass Transfer,* vol. 37, pp.1641-1655.

Han C. and Griffith P., 1965, "The Mechanism of Heat Transfer in Nucleate Pool Boiling," *Int. J. Heat and Mass Transfer*, vol.8, pp.887-903.

Judd, A. M., 1969, "Analysis of Transient Boiling of Liquid Metals," *Brit. J. Appl. Phys.,* vol.2, pp. 261-274.

Kang, S., Bartsch, G., Jai, D., and Chen, X. J., 1993, "Investigation of Bubble Dynamics in Pool Boiling: Part I-A Synthesis Model for Bubble Growth in Terms of Liquid Subcooling and Surface Condsition," National Heat Transfer Conference, Atlanta, Georgia, paper no. 3-HT-36.

Lee, H. S., 1993, "Vapour Bubble Dynamics in Microgravity," Ph.D. Thesis, University of Michigan.

Lee, R. C., and Nydahl, J. E., 1989, "Numerical Calculation of Bubble Growth in Nucleate Boiling from Inception Through Departure," *J. Heat Transfer*, vol. 111, pp. 474-479.

Lee, H. S. and Merte Jr. H., 1996, "Spherical Vapour Bubble Growth in Uniformly Superheated Liquids," *Int. J. Heat Mass Transfer*, vol. 39, pp. 2427-2447.

Lee, H. S. and Merte Jr. H., 1996, "Hemispherical Vapour Bubble Growth in Microgravity: Experiments and Model," *Int. J. Heat Mass Transfer*, vol. 39, pp. 2449-2461.

Lien, Y. C., 1969, "Bubble Growth Rates at Reduced Pressure," D.Sc. Thesis, MIT.

Mei, R., Chen, W. and Klausner, J. F., 1994, "Vapour Bubble Growth in Heterogeneous Boiling-I. Formulation, " *Int. J. Heat Mass Transfer*, vol. 38, pp. 909-919.

Mei, R., Chen, W. and Klausner, J. F., 1994, "Vapour Bubble Growth in Heterogeneous Boiling-II. Growth Rate and Thermal Fields, " *Int. J. Heat Mass Transfer*, vol. 38, pp. 921-934.

Merte Jr. H. , Lee, H. S. and Keller, R. B., 1995, Report on Pool Boiling Experiment Flown on STS-47-57-60. Report No. UM-MEAM-95-01. Department of Mechanical Engineering and Applied Mechanics. The University of Michigan, Ann Arbor, Michigan. NASA Contract NAS 3-25812.

Mikic B.B. & Rohsenow W.M., 1969, " Bubble Growth Rates in Non-Uniform Temperature Fields," *Prog. Heat and Mass Transfer* , vol. II, pp. 283-293.

Mikic, B. B., Rohsenow, W. M.. and Griffith, P., 1970, "On Bubble Growth Rates," *Int. J. Heat Mass Transfer*, vol. 13, pp. 657-665.

Plesset, M. S. and Zwick, S. A., 1954, "The Growth of Vapor Bubbles in Superheated Liquid," *J. Applied Physics,* vol. 25, pp. 493-500.

Prosperetti, A. and Plesset, M. S., 1978, "Vapour-Bubble Growth in a Superheated Liquid," *J. Fluid Mech.*, vol. 85, pp. 349-368.

Lord Rayleigh, 1917, "On the Pressure Developed in a Liquid During the Collapse of a Spherical Cavity," *Phil. Mag.,* vol. 34, pp. 94-98.

Riznic, J., Kojasoy, G. and Zuber, N., 1999, "On the Spherically Symmetric Phase Change Problem," *Int. J. Fluid Mechanics Research*, vol. 26, pp. 110-145.

Robinson, A. J., 2001, " Bubble Growth with Radial Expansion and Vertical Translation," Internal report, McMaster University, Hamilton, Ontario.

Robinson, A. J. and Judd, R. L., 2001, "Bubble Growth in a Uniform and Spatially Distributed Temperature Field," *Int. J. Heat Mass Transfer*, vol. 44, pp. 2699-2710.

Scriven, L. E., 1959, "On the Dynamics of Phase Growth," *Chem. Engng. Sci.*, vol. 10, pp. 1-13.

Son, G., Dhir, V. K., and Ramanujapu, N., 1999, "Dynamics and Heat Transfer Associated with a Single Bubble During Nucleate Boiling on a Heated Surface," *J. Heat Transfer,* vol. 121, pp 623-631.

Theofanous, T. G., Baisi, L., Isben, H. S. and Fauske, H., 1969, "A Theoretical Study on Bubble Growth in Constant and Time-Dependent Pressure Fields," *Chem. Engng. Sci*, vol. 24, pp. 885-897.

Theofanous, T. G. and Patel., P. D., 1976, "Universal Relations for Bubble Growth Rates," *Int. J. Heat Mass Transfer*, vol. 19, pp. 425-429.

Thorncroft, G. E., 1995, "Heat Transfer and Vapour Bubble Dynamics in Forced Convection Boiling," Ph. D. Dissertation, University of Florida, Gainesville, Florida.

van Stralen, J. D., 1966,"The mechanism of Nucleate Boiling in Pure Liquids ans in Binary Mixture, Parts I and II," *Int. J. Heat Mass Transfer*, vol. 9, pp. 995-1046.

van Stralen, S. and Cole, R., 1979, <u>Boiling Phenomenon</u>, Hemisphere Publishing Co.

Welch, S. W. J., 1998, "Direct Simulation of Bubble Growth," *Int. J. Heat Mass Transfer*, vol. 41, pp. 1655-1666.

Zuber, N., 1961,"Vapor Bubbles in Non-Uniform Temperature Fields," *Int. J. Heat Mass Transfer*, vol. 2, pp. 83-98.

Zul, W., Ramakers, F. J. M. and Van Stralen, S. J. D., 1979, "Global Numerical Solutions of Growth and Departure of a Vapour Bubble at a Horizontal Heated Surface in a Pure Liquid and Binary Mixture," *Int. J. Heat Mass Transfer*, vol. 2, pp. 83-98.